

Multiple trap optical tweezers for cell force measurements

Zur Erlangung des akademischen Grades eines

DOKTORS DER NATURWISSENSCHAFTEN

(Dr. rer. nat.)

von der Fakultät für Chemie und Biowissenschaften des
Karlsruher Instituts für Technologie (KIT) - Universitätsbereich
genehmigte

DISSERTATION

von

Melanie Schwingel

aus

Dortmund

Dekan: Prof. Dr. Martin Bastmeyer

Referent: Prof. Dr. Martin Bastmeyer

Co-Referent: Prof. Dr. Ulrich Nienhaus

Tag der mündlichen Prüfung: 20. April 2012

CONTENTS

Summary	IX
Zusammenfassung	XI
1. Introduction: Concepts of Optical Tweezers and Cell-Substrate Interactions	1
1.1 Optical Tweezers	1
1.1.1 Optical Traps: Interaction of Light with Dielectric Particles	2
1.1.2 Calibration Methods: Trap Stiffness and Restoring Forces of Optical Traps	7
1.1.3 Instrumentation of Optical Tweezers and General Design Considerations	10
1.1.4 Force Spectroscopy with Optical Tweezers and Applications in Biology	11
1.2 Cell-Substrate Interaction and Mechanotransduction	13
1.2.1 Cell Morphology and the Actin Cytoskeleton	14
1.2.2 Cell Motility	15
1.2.3 Cellular Forces and Cell-Substrate Adhesions	16
1.2.4 Retrograde Actin Flow	19
1.2.5 The Adhesion-Related Protein Vinculin	20
1.2.6 Mutations in the Vinculin Structure	22
1.3 Objectives of this PhD work	24
2. Methods and Materials	25
2.1 Multiple Trap Optical Tweezers Setup	25
2.1.1 Multiple Trap Operation with Acousto-Optic Deflectors	26
2.1.2 Force and Trap Stiffness Calibration	29
2.2 Bead Functionalization	31
2.2.1 Passive Adsorption	31
2.2.2 Covalent Coupling	31
2.2.3 Ligand Density Quantification	32
2.3 Cell Culture	32
2.3.1 Cell Lines	33
2.3.2 Cell Culture Routine	34
2.3.3 Cell Counting	34
2.3.4 Sample Preparation	34
2.4 Cell Transfection by Electroporation	35
2.4.1 Optimized Electroporation Protocol	35
2.4.2 Plasmid DNA Amplification	36
2.5 Fluorescence Assisted Cell Sorting	37
2.5.1 FACS Sample Preparation	37

2.5.2	Sorting Procedure	37
2.6	Immunohistochemistry and Staining	38
2.7	Experimental Procedures	40
2.7.1	Optical Tweezers Force Spectroscopy	40
2.7.2	Retrograde Transport Assay	40
2.7.3	Cell Migration Assay	40
2.8	Data Analysis and Quantification	41
2.8.1	Traction Force Quantification	41
2.8.2	Migration Velocity	42
2.8.3	Directional Persistence	42
2.8.4	Adhesion Size Quantification	42
2.8.5	Statistical Data Analysis	43
2.8.6	Fast Fourier Transform Filter	43
2.9	Image Acquisition and Software	44
2.9.1	Microscopes	44
2.9.2	Software for Image Acquisition and Analysis	44
2.10	Reagents, Buffers and Chemicals	45
3.	Results	47
3.1	Force Spectroscopy with Multiple Trap Optical Tweezers	49
3.1.1	Geometrical Bead Patterns	49
3.1.2	Functionalized Beads Serve as Local Force Probes	50
3.2	Multi-Parametric Study of Cell-Matrix Adhesion Sites	52
3.2.1	Bead Size Influences Adhesion Reinforcement	52
3.2.2	Integrin Ligand Density Mediates Adhesion Strength	54
3.2.3	Traction Force and Actin Flow Velocity Mapping on the Cell Surface	57
3.2.4	Reinforcement of Neighboring Adhesion Sites	59
3.3	Comparison of Forces and Dynamics in B16, MEF and PCF Cells	62
3.3.1	Cell Morphology on Homogeneously Coated Substrates	62
3.3.2	Traction Force Development	63
3.3.3	Dynamics of Retrograde Actin Flow	65
3.3.4	Cell Migration Characteristics	65
3.3.5	Correlation of Forces and Dynamics in Different Cell Lines	66
3.4	The Role of Vinculin in Cell-Substrate Adhesions	68
3.4.1	Cell Shape and Focal Adhesions in MEF WT and Vinculin Deficient Cells	68
3.4.2	Retrograde Transport in MEF WT and MEF $\text{vin}^{(-/-)}$ Cells	70
3.4.3	Comparison of Cellular Dynamics and Forces in MEF WT and MEF $\text{vin}^{(-/-)}$ cells	74
3.4.4	Traction Force Rescue of MEF $\text{vin}^{(-/-)}$ Cells by Vinculin Reintroduction	75
3.4.5	Effect of Distinct Vinculin Mutants on Force Development	77

4. Discussion	85
4.1 Force Spectroscopy Approaches for Biological Applications	85
4.1.1 Multiple Trap Force Spectroscopy	85
4.1.2 Atomic Force Microscopy	87
4.2 Spatiotemporal Characteristics of Evolving Cell Adhesion Complexes	87
4.2.1 Temporal Development of Adhesiveness in Early Adhesion Sites	87
4.2.2 The Area of Cell Adhesive Contact Sites Mediates Reinforcement	89
4.2.3 Orientation of Spatially-Related Adhesion Sites Controls Adhesion Strength	91
4.2.4 Influence of Integrin Ligand Density on Cell Adhesion Behavior	95
4.2.5 Force and Velocity Mapping: The Interdependence of Adhesion Forces, F-Actin Flow Velocity, and Cell Motility	97
4.3 Influence of Vinculin Recruitment on Actin Flow, Adhesion, and Motility	99
4.3.1 Role of Native Vinculin in Adhesion Reinforcement and Integrin-Actin Coupling	99
4.3.2 Structural Mutations of Vinculin Modify Cell Adhesion Morphology and Force Development	102
4.3.3 Cellular Forces and Cytoskeletal Dynamics: A Comparison of Cell Types	107
4.4 Outlook	110
Appendix	113
A Indirect Labeling of cyclic RGD Peptides	113
B Overview of Forces and Dynamics in All Examined Cell Types	119
Bibliography	121
List of Abbreviations	141
Acknowledgements - Danksagung	143

LIST OF FIGURES

1.1	Illustration of an optical trap in the ray optics regime	3
1.2	Simulation of trap potential and trap force	9
1.3	Structure of fibronectin	13
1.4	Conformation of the RGD cell adhesion motif	14
1.5	Cell morphology and actin cytoskeleton	15
1.6	Maturation process of cell adhesion sites	17
1.7	Schematic model of cell-substrate adhesions	18
1.8	Crystal structure of vinculin	20
1.9	Direct interaction partners of vinculin	21
1.10	Structural mutations of vinculin	23
2.1	Multiple trap optical tweezers setup	25
2.2	Operation principle of acousto-optic deflectors	27
2.3	Amplitude and H/V scan of the AODs	28
2.4	Trap calibration via thermal fluctuations	30
2.5	Force Spectroscopy and Retrograde Flow Assay	41
3.1	Geometrical bead patterns	49
3.2	Force with regard to bead size	53
3.3	Ligand densities mediate cell adhesion strength	56
3.4	Force and RT velocity in MEF WT cells	58
3.5	Velocity mapping in the leading edge of primary chicken cells	59
3.6	Influence of spatial bead separation on force development	60
3.7	Morphology of B16, MEF WT and PCF cells	63
3.8	Force development, retrograde transport and migration velocity	64
3.9	Comparison of B16, MEF WT and PCF cells	66
3.10	Morphology of MEF WT and MEF $\text{vin}^{(-/-)}$ cells and colocalization of vinculin and paxillin	69
3.11	Trajectories in MEF WT and MEF $\text{vin}^{(-/-)}$ cells	71
3.12	Retrograde transport in MEF WT and MEF $\text{vin}^{(-/-)}$ cells	72
3.13	Comparison of MEF WT and MEF $\text{vin}^{(-/-)}$ cells	74
3.14	Forces after vinculin rescue	76
3.15	Expression patterns of vinculin and quantification of focal adhesion morphology	79
3.16	Force development in cells expressing various mutant vinculin proteins	81
3.17	Comparison of MEF WT, MEF $\text{vin}^{(-/-)}$, and vinculin mutant expressing cells	83
4.1	Multiparametric study of force development and retrograde flow	94

4.2	Summary of the effect of vinculin mutations on force development	106
4.3	Comparison of traction forces and actin dynamics in wild type and vinculin knock-out cell lines	108
A.1	Indirect labeling of cRGD peptides	113
A.2	Trifunctional linker synthesis	114
A.3	Coupling of fluorophor and linker	115
A.4	Click chemistry method for peptide-linker coupling	117
A.5	The cyclic RGD peptide cRGDfk	118
B.1	Retrograde transport, cell migration, and traction forces in B16, MEF WT, MEF $\text{vin}^{(-/-)}$, and PCF cells	119

LIST OF TABLES

1.1	Overview of selected force spectroscopy methods	11
2.1	Cell lines and culture conditions	34
2.2	Cell transfection by electroporation	36
2.3	Antibodies and dyes for fluorescent labeling	39
2.4	Statistical data analysis	43
2.5	Reagents, Buffers and Chemicals	46
3.1	Trap stiffness and trap force	50
3.2	B16, MEF WT and PCF: traction forces, retrograde transport, migration	65
3.3	Retrograde transport and persistence in MEF WT and MEF $\text{vin}^{(-/-)}$ cells	73
3.4	Overview of vinculin mutant characteristics	78
A.1	Molecular weight of reactants	116
A.2	Optical properties of Atto610-NHS	117
A.3	CuAAC click reaction equivalents	117
B.1	B16, PCF, MEF WT and MEF $\text{vin}^{(-/-)}$: Force, retrograde transport, migration	120

SUMMARY

Mechanical forces are omnipresent in nature and play an essential role in sustaining connective tissue, in mediating the functionality and morphology of individual cells and in regulating protein conformations on the subcellular scale. In individual cells, highly sensitive mechanosensing mechanisms and spatiotemporal coordinations of the cellular response are prerequisites for physiological processes such as wound healing and proliferation. Cellular malfunction in this regard is a potential cause for pathological developments like metastasis.

A possible approach to characterize cellular mechanosensing is the analysis of cellular force generation. Fibroblast-like adherent cells establish transient cell-substrate adhesion sites that serve as stable anchors of the cell cytoskeleton to the substrate and concomitantly allow for force transduction and cell motility.

In the presented work, a custom-built multiple trap optical tweezers system is established and optimized for non-invasive live cell force measurements at individual adhesion sites. The device employs chemically functionalized microscopic beads as force probes. It allows for a time-resolved study of force development in the initial phase of cell adhesion formation and enables simultaneous measurements at distinct locations. A multiparametric study on adhesion forces was conducted to analyze the impact of bead functionalization, adhesion site area, location, spacing, and orientation. It is demonstrated for the first time that spatially closely related adhesion sites display an orientation specific reinforcement behavior and influence each other, which gives new insights into the spatiotemporal reorganization of the underlying actin cytoskeleton.

The combination of force and actin flow velocity mapping across the cell surface with a systematic analysis of actin dynamics and cell motility elucidates a scale-independent generic relation between traction force generation, actin flow rates, and migration velocity. Force and actin flow correlate linearly in distinct cell surface areas as well as in the different cell lines investigated. The additional evaluation of the cell migration velocity delineates an inverse relation regarding traction forces and actin flow: Cells with a high motility exert low traction forces, concomitant with slow retrograde actin flow dynamics and vice versa.

Vinculin is an adhesion-related protein that is discussed as a key element in adhesion reinforcement and turnover. One focus of this study is the time-resolved analysis of vinculin-mediated force development, which is analyzed by comparing wild type and vinculin deficient cells. Of particular interest is the contribution of specific vinculin domains and conformations on adhesion formation. The predominant importance of vinculin binding to talin (a member of the adhesion plaque) and actin filaments for cell adhesion formation is revealed by expressing various vinculin mutants featuring a suppression of the vinculin inherent conformational switch from the inactive to the active state. For the first time, a significant impact of vinculin expression on retrograde actin flow is observed: Vinculin deficient cells display a doubled actin flow rate compared to wild type cells with a simultaneous two-fold increase in motility and a two-fold decline in adhesion strength. This implicates that the transient interaction of vinculin with actin at adhesion sites does not only mediate reinforcement, but also has a regulatory effect on actin flow rates.

Collectively, the results of this study help to understand the influence of mechanical forces on physiological and pathological processes in biological systems.

ZUSAMMENFASSUNG

Zellen in biologischen Systemen sind einer Reihe von mechanischen Kräften ausgesetzt, die ihre Morphologie und Funktionalität beeinflussen und physiologische Prozesse wie Wundheilung und Proliferation regulieren. Um sich an Veränderungen und Reize aus der extra-zellulären Umgebung anpassen zu können, bilden adhärenente Zellen Rezeptorkomplexe aus, die mechanische Reize in intrazelluläre chemische Signale konvertieren. Adhäsionskomplexe vermitteln die Kopplung des zellulären Zytoskeletts mit der extrazellulären Matrix und sind sowohl für die Signaltransduktion als auch für die aktive Übertragung zellulärer Kräfte von Bedeutung. Der ständige Auf- und Abbau von Adhäsionskomplexen ermöglicht sowohl eine stabile Substratanhaftung als auch eine gerichtete Zellmigration.

In dieser Arbeit wird die Entwicklung von einzelnen Adhäsionskomplexen anhand des zeitlichen Verlaufs der Kraftentwicklung beschrieben. Zu diesem Zweck wird eine optische Pinzette ("optical tweezers") mit multiplen Fallen entwickelt, die Kraftmessungen unter physiologischen Bedingungen in einem Bereich von 10 bis 190 picoNewton zulässt. Diese ermöglicht es eine definierte Anzahl chemisch funktionalisierter Kolloide auf der apikalen Zellmembran zu verteilen und dabei an mehreren Positionen gleichzeitig die zeitliche Entwicklung von Zugkräften in neu entstehenden Kontaktstellen zu messen.

Die Entwicklung zellulärer Zugkräfte wird in Abhängigkeit von Einflussgrößen wie der Fläche, Position und Anordnung von Adhäsionskomplexen sowie der Kolloid-Funktionalisierung charakterisiert. Es wird zum ersten Mal gezeigt, dass sich nah benachbarte Kontakte gegenseitig beeinflussen und ihre räumliche Orientierung zueinander starke Auswirkungen auf die Kraftentwicklung hat.

Des Weiteren werden die Richtungsfelder von Zugkräften und retrogradem Aktinfluss sowie deren Korrelation mit der Migrationsgeschwindigkeit verschiedener fibroblastenähnlicher Zelllinien ermittelt. Dabei ergibt sich eine proportionale Abhängigkeit der Zugkraft und der Aktinflussgeschwindigkeit in Kombination mit einer inversen Relation zur Migrationsgeschwindigkeit.

Ein Schwerpunkt der vorliegenden Arbeit ist die Bestimmung der Rolle von Vinculin, einem Bestandteil von Adhäsionskomplexen, in der Entwicklung zellulärer Zugkräfte. Es wird erstmalig gezeigt, dass die Einbindung von Vinculin in Adhäsionskomplexe nicht nur die Entwicklung von Zugkräften reguliert, sondern auch den retrograden Aktinfluss beeinflusst. Da Vinculin aus mehreren Domänen besteht, ist der Beitrag spezifischer Domänen und Proteinkonformationen zur Kraftentwicklung von besonderem Interesse. Die Expression von modifiziertem Vinculin demonstriert die Bedeutung der Bindung von Vinculin an Talin (eine Komponente von Adhäsionskomplexen) und an filamentöses Aktin sowie der Konformationsänderung von Vinculin von inaktiv nach aktiv.

Insgesamt trägt diese Studie dazu bei, den Einfluss von mechanischen Kräften auf physiologische und pathologische Prozesse in biologischen Systemen besser zu verstehen.



1 INTRODUCTION: CONCEPTS OF OPTICAL TWEEZERS AND CELL-SUBSTRATE INTERACTIONS

In the scope of this work, the development of cellular forces upon substrate interaction was investigated with optical tweezers force spectroscopy. The first part of the introductory chapter gives insights into the working principle of optical tweezers and offers a theoretical background on light forces and optical potentials. Furthermore, a short overview of optical tweezers applications in the biological sciences is presented. In the second part, the fundamentals of the interaction of cells with the extracellular environment are reviewed. Of particular interest is the development of cell-substrate adhesions, their protein composition, their role in mechanosensing and the force generation of the actomyosin system.

1.1 Optical Tweezers

Optical tweezers (also named laser tweezers) give rise to forces that are generated from the electromagnetic properties of light itself. Already in 1619 the astronomer Johannes Kepler proposed that light was able to exert forces. He deduced this from the observation that comet tails always point away from the sun as if they were pushed this way by the radiation of the sun. A theoretical description of the capability of light to exert forces onto encountered objects was presented by James C. Maxwell in 1873. His theory on electromagnetic waves described the generation of radiation pressure perpendicular to a wave front. With the invention of lasers in the 1960s, high intensity coherent light sources became available and it became feasible to experimentally observe light forces on suspended particles [Ashkin 1970]. In 1986, Arthur Ashkin presented the first "single-beam gradient force optical trap" and demonstrated the trapping of nm to μm sized dielectric particles [Ashkin *et al.* 1986], which was the advent of optical tweezers.

Optical tweezers (OTs) use strongly focused laser light to confine and manipulate small objects in a so-called optical trap. These optical traps constitute a potential well for objects with dielectric characteristics and allow for the spatial manipulation of these objects when they are located within the potential well. Particle sizes that can be trapped range from the order of several nm up to more than $100 \mu m$ [Svoboda & Block 1994a, Svoboda & Block 1994b, Grier 2003]. The forces optical tweezers can exert onto a trapped object range from tenth of femtonewton (fN) [Rohrbach 2005] to several hundred piconewton (pN) [Ghislain *et al.* 1994, Rohrbach & Stelzer 2002] and have recently been expanded into the nanonewton (nN) regime [Bormuth *et al.* 2008, Mahamdeh *et al.* 2011].

The most basic way to create optical traps is to pass laser light through a beam expander and couple it into the back aperture of a microscope objective with a high numerical aperture to focus it into a sample. This basic design allows for trapping of small objects in the sample plane and can fixate an objects position by light forces.

Due to the simplicity of the experimental design and the unique force range combined with

non-invasiveness, OTs found a wide range of applications, ranging from biology to chemistry and physics. In biology the study of single motor proteins [Ashkin *et al.* 1990a, Finer *et al.* 1994, Molloy *et al.* 1995b, Molloy *et al.* 1995a, Gross *et al.* 2000, Clemen 2005, Capitanio *et al.* 2007, Bormuth *et al.* 2009, Watanabe *et al.* 2010], the trapping and manipulation of single cells [Ashkin *et al.* 1987, Wu *et al.* 2011], DNA binding and stretching experiments [Dessinges *et al.* 2002, McCauley & Williams 2007, Kegler *et al.* 2007, Farré *et al.* 2010, Wagner *et al.* 2011, Paramanathan *et al.* 2012] and the study of cell membrane and cytoskeleton mechanics [Choquet *et al.* 1997, Kuo 2001, Hormeno & Arias-Gonzalez 2006, Luca *et al.* 2007, Ermilov *et al.* 2007, Fuente *et al.* 2007, Brownell *et al.* 2010] are only a selection of research topics.

In the physical sciences, laser tweezers play an important role in colloidal physics and microfluidics [Baumgartel 2007, Bleil *et al.* 2007, Straube *et al.* 2011], in the manipulation and fusion of air-borne particles [Omori *et al.* 1997, Hopkins *et al.* 2004, King *et al.* 2004, Tang *et al.* 2009], and in optical spectroscopy and force spectroscopy [Fällman *et al.* 2004, Ghislain *et al.* 1994, Kuo 2001, Neuman & Nagy 2008, Fazal & Block 2011].

1.1.1 Optical Traps: Interaction of Light with Dielectric Particles

Optical traps originate from tightly focused laser light and allow to confine dielectric particles in a potential well. In most OT applications, spherical microscopic particles (beads) are trapped and used as interfaces to the objects of interest. In this way, the interaction of the object of investigation with the trapped bead is analyzed.

Thermal Energy of Microscopic Beads in Solution

Microscopic beads feature a typical size of 100nm to $10\mu\text{m}$ and are typically suspended in aqueous solution to serve as force probes for OT force spectroscopy. Particles of this dimension show Brownian motion, which originates from collisions of the bead with the surrounding solvent molecules. This collisions result in a kinetic bead energy U_{kin} that corresponds to a Boltzmann distribution

$$p(U_{kin}) \propto \exp\left(-\frac{U_{kin}}{k_B T}\right) \quad (1.1)$$

with k_B denoting the Boltzmann constant and T (in K) the thermodynamic temperature. In OT force spectroscopy, the beads are exposed to an external potential generated by focused laser light, which defines their potential energy U_{pot} . Due to the virial theorem, the spatial distribution of the potential energy is also described by a Boltzmann distribution with

$$p(U_{pot}(r)) \propto \exp\left(-\frac{U_{pot}(r)}{k_B T}\right) \quad (1.2)$$

and corresponds to the spatial bead distribution.

Interaction with Electromagnetic Fields

Close to the optical trap center, particles are subjected to strong electromagnetic fields originating from tightly focused laser light. In general, particles within a strong external electromagnetic field experience radiation pressure (or scattering forces) and provided that the particles feature dielectric characteristics, the interaction with the electromagnetic field gives rise to an additional type of force: the gradient force. The gradient force enables the confinement ("trapping") of a particle within the laser focus, while the scattering force pushes the particle away from the focus.

A good illustration of particle confinement and the gradient force experienced by a microscopic bead was first presented by Ashkin and considers the ray optics regime, where particle diameters are much larger than the wavelength of light [Ashkin 1992].

In the ray optics approximation, a prerequisite for the generation of a gradient force is that the refractive index of the bead n_b exceeds the refractive index of the solvent n_s ($n_b > n_s$). In figure 1.1 B) and C) the resulting gradient force (\vec{F}) on a dielectric bead is displayed for different locations of the bead with respect to the light focus. Two example rays (a and b) are observed after passing through the objective lens. Upon encounter of an optically transparent bead, incident light is refracted at the refractive index interfaces of bead and solvent. The resulting change in light direction corresponds to a change of photon momentum. Energy conservation leads to a momentum transfer to the bead that generates the forces \vec{F}_a and \vec{F}_b , which result an effective force F that is directed toward the focus of the laser light. If the focus of the incident laser light is not located in the center of a trapped bead but is shifted in axial direction the bead experiences restoring forces, which are directed toward the trap center (figure 1.1 B)). Likewise, a position shift in the transverse plane gives rise to forces that pull the bead back toward the trap center (figure 1.1 C)). In the ray optics

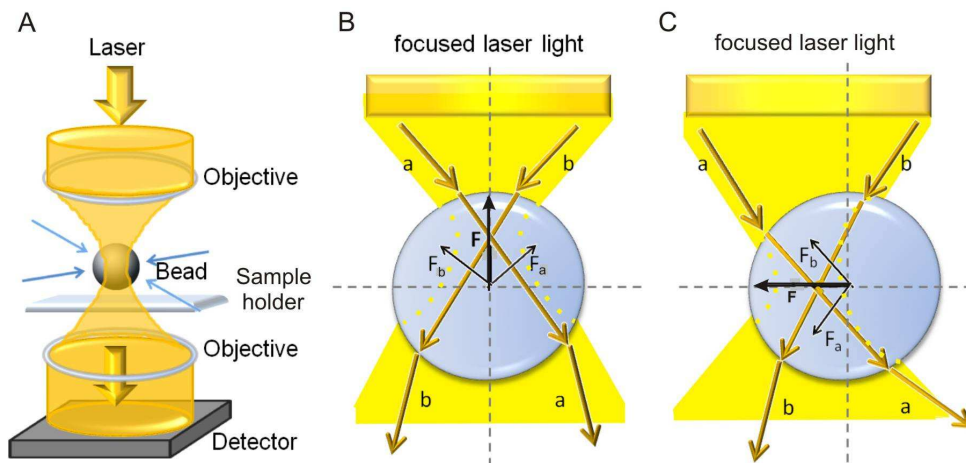


Fig. 1.1: Illustration of an optical trap in the ray optics regime

A) Schematic of an optical trap: The laser light is tightly focused by the first microscope objective and encounters a dielectric bead in suspension. Bead and light focus position are imaged onto a detector by a second objective. A bead in the vicinity of the trap experiences forces that are directed toward the focus. B) Direction of the gradient force F for an axially displaced bead. The gradient force pulls the bead toward the laser focus. C) Lateral displacement of a bead from the laser focus. The forces experienced by the bead restore its position to the trap center.

approximation, the momentum transfer associated with light refraction at the bead-solvent interface accounts for the effect of an optical gradient force on a dielectric bead. However, the overall force on a particle is the contribution of gradient forces and scattering forces, with the scattering force pushing the bead in the direction of light propagation.

In the following the prerequisites for stable trapping of a dielectric bead in an optical potential well are discussed in detail.

Potential Energy and Gradient Forces of Optical Traps

The force a static dielectric bead experiences in an electromagnetic field originates from the electric field and has no contributions from the magnetic field [Jackson 1999]. Hence, the gradient force can be derived for the interaction of a dielectric bead with an external, purely electric field. In the following discussion, a bead size much smaller than the wavelength is assumed, which allows the application of a Rayleigh approximation.

The external field \vec{E}_0 polarizes the spherical bead and generates an internal electric field \vec{E}_{int} , which is a superposition of the external field and the induced electric field (also termed depolarized field \vec{E}_d): $\vec{E}_{int} = \vec{E}_0 + \vec{E}_d$. The dipole moment induced by the external field within the sphere can be described by the polarization density $\vec{P} = \chi \vec{E}_{int}$, where χ is the electric susceptibility. An expression for the electric susceptibility of the internal field \vec{E}_{int} can be derived from the dielectric constants of the bead ϵ_b and of the external solvent ϵ_s , respectively, and yields $\chi = \epsilon_b - \epsilon_s$. An external electric field stores an energy density within dielectric media that is given by $u = -\frac{1}{2} \vec{P} \vec{E}_0$. The potential energy of a bead is given by the integral of the energy density over the volume of a bead with radius r_b , whose center is located at \vec{r} :

$$U(\vec{r}) = -\frac{1}{2} \int_{|\vec{r}-\vec{r}'| \leq r_b} \vec{P}(\vec{r}') \vec{E}_0(\vec{r}') d^3 r' . \quad (1.3)$$

As the particle aims at minimizing its potential energy, it will move toward the maximum strength of the applied external field \vec{E}_0 if $\epsilon_b > \epsilon_s$ is valid. Consequently, relation (1.3) gives evidence for the existence of a gradient force.

To derive the potential energy in dependence of the material characteristics of bead and solvent, the relation between the internal field and the applied external field is considered:

$$\vec{E}_{int} = \frac{3\epsilon_s}{\epsilon_b + 2\epsilon_s} \vec{E}_0 . \quad (1.4)$$

Substituting the polarization density in equation (1.3) with this relation and subsequent integration over the bead volume ($V_b = 4/3 \pi r_b^3$) yields an electrostatic energy of

$$U(\vec{r}) = -\frac{1}{2} 4\pi r_b^3 \epsilon_s \left(\frac{\epsilon_b/\epsilon_s - 1}{\epsilon_b/\epsilon_s + 2} \right) \vec{E}_0(\vec{r})^2 . \quad (1.5)$$

The dielectric constants are related to the refractive index via $n_b \approx \sqrt{\epsilon_b}$ and $n_s \approx \sqrt{\epsilon_s}$ in the case

of a relative permeability of $\mu \approx 1$.

The gradient force \vec{F}_∇ a dielectric particle experiences in the external field is defined by

$$\vec{F}_\nabla(\vec{r}) = -\nabla_{\vec{r}}U(\vec{r}) \quad (1.6)$$

and is termed optical gradient force as it points along the gradient of the external electric field \vec{E}_0 . Substituting the refractive index ratio with $m = n_b/n_s$, the gradient force can be expressed as

$$\vec{F}_\nabla(\vec{r}) = 2\pi r_b^3 n_s^2 \left(\frac{m^2 - 1}{m^2 + 2} \right) \nabla_{\vec{r}} \vec{E}_0^2(\vec{r}) = \frac{1}{2} \alpha \nabla_{\vec{r}} \vec{E}_0^2(\vec{r}), \quad (1.7)$$

where $\alpha = 4\pi r_b^3 n_s^2 (m^2 - 1)/(m^2 + 2)$ denotes the polarizability of a spherical dielectric bead. Equation (1.7) directly reveals that the force vector depends on the gradient of the squared external electric field strength and thus it depends upon the gradient of the focused light intensity ($\nabla \vec{E}_0^2 \propto \nabla I_0$).

The intensity gradient can be externally controlled by the choice of the focusing objective. A high numerical aperture will increase the intensity gradient close to the focal spot and will enhance the forces that are transmitted onto the bead. Equation (1.7) also shows that the radius of the bead contributes with the 3rd power to the gradient force. Furthermore, the refractive indices of bead and solvent define the forces exerted onto the bead. For the typical refractive index range of bead and solvent materials, the relation

$$\left(\frac{m^2 - 1}{m^2 + 2} \right) = \frac{n_b^2 - n_s^2}{n_b^2 + 2n_s^2} = \frac{(n_b - n_s)(n_b + n_s)}{n_b^2 + 2n_s^2} \propto \Delta n \quad (1.8)$$

with $\Delta n = n_b - n_s$, shows that the gradient force is proportional to the difference in the refractive indices of bead and solvent ($F_\nabla \propto \Delta n$).

With the delineated dipole approximation, the interaction of small dielectric objects with light fields can be described. Furthermore, the ray optics approximation allows to characterize the behavior of objects much larger than the wavelength in external fields. For a more accurate, size-independent description of particle/light interaction, the generalized Lorenz-Mie theory is required, which is well described in [Maheu *et al.* 1988, Gouesbet 1994] among others.

Scattering Forces

A bead interacting with an external light field does not transmit all incident light but scatters it partly. This gives rise to a scattering force, also termed radiation pressure, originating from momentum that is transferred from light impinging on the bead surface. For an isotropic scatter, the scattering force acts in the direction of light propagation and thus pushes the beads in axial direction away from the focus of the light field. The momentum of an electromagnetic field \vec{g} is given

by

$$\vec{g} = \frac{\vec{S}}{c^2} = \frac{1}{\mu_0 c^2} (\vec{E}_0 \times \vec{B}_0) = \epsilon_0 (\vec{E}_0 \times \vec{B}_0) \quad (1.9)$$

where \vec{S} is the Poynting vector, which represents the energy flux (energy transfer per unit area), c is the speed of light and \vec{B}_0 is the external magnetic field. To derive the time-averaged transfer of momentum P per unit area (radiation pressure) from the electromagnetic field onto the bead, the relation [Harada & Asakura 1996, Rohrbach & Stelzer 2002]

$$P = \frac{\langle \vec{S} \rangle}{c} = c |g| = c \epsilon_0 \epsilon_s E_0 B_0 \propto I_{scat} \quad (1.10)$$

is applied for a field propagating in a medium of permittivity ϵ_s , with I_{scat} denoting the light intensity scattered on the bead surface. Integration of the scattering intensity across the bead surface area yields the scattering cross section σ_{scat} , which is related to the scattering force F_{scat} and the incident light intensity I_0 by

$$F_{scat} = \frac{n_s}{c} \sigma_{scat} I_0 = \frac{n_s}{c} \frac{128 \pi^5 r_b^6}{3 \lambda^4} \left(\frac{m^2 - 1}{m^2 + 2} \right)^2 I_0. \quad (1.11)$$

This relation demonstrates the linear dependence of the scattering force on the incident light intensity and shows a strong dependence on the bead radius. Furthermore, according to relation (1.8) the scattering force is proportional to the squared refractive index difference ($F_{scat} \propto \Delta n^2$).

The scattering forces experienced by a trapped bead lead to an axial bead displacement from the light focus and leads to a decreased gradient force exerted onto the bead.

In summary, the conditions to be complied with for stable trapping of dielectric particles in external light fields are:

- the refractive index of the particle needs to be larger than the refractive index of the solvent ($n_b > n_s$) to permit the formation of gradient forces
- the gradient force has to exceed the scattering force in all spatial dimensions ($F_{\nabla} > F_{scat}$) to stably restrain the particle to the optical trap.

1.1.2 Calibration Methods: Trap Stiffness and Restoring Forces of Optical Traps

A focused light field creates an optical potential well for a dielectric bead and this potential requires an empirical characterization for force spectroscopy applications. In general, two properties of an optical trap can be calibrated: the trap stiffness of the optical potential and the maximum restoring forces on a confined object. The trap stiffness κ is defined by the shape of the optical potential and can be related to the restoring trap force $F(x)$ via an approximation with Hooke's law: $F(x) = -\kappa\Delta x$, where Δx is the bead displacement from the trap center. As this relation holds true for small displacements only, the maximum trap force $F_{trap,max}$, which equals the force required to remove a bead from the finite potential well, has to be calibrated independently.

Force Calibration: Drag Force Method

Force calibration with the drag force method determines the externally applied escape force, which is required to completely remove a bead from the range of the optical potential: $\vec{F}_{escape} = -\vec{F}_{trap,max}$ [Ashkin *et al.* 1986, Svoboda & Block 1994a, Felgner *et al.* 1995, Oddershede *et al.* 2001, Neuman & Block 2004]. The trapping force is calibrated against the fluid flow of the solvent, which exerts a viscous drag against the bead. The drag force F_{escape} that dislocates the bead from the optical potential is derived from Stoke's law as

$$F_{escape} = \beta v_{escape} = 6\pi\eta r_b v_{escape} \quad (1.12)$$

where β is the viscous drag coefficient, which is composed of the fluid viscosity η and the radius r_b of the bead; v_{escape} denotes the flow velocity required to free the bead from the potential well.

For beads trapped close to a surface (for example the bottom of the measurement chamber), proximity effects have to be considered. This leads to the incorporation of an additional factor, derived from Faxen's law, into equation (1.12):

$$F_{escape} = 6\pi\eta r_b v_{escape} \left[1 - \frac{9}{16} \left(\frac{r_b}{h} \right) + \frac{1}{8} \left(\frac{r_b}{h} \right)^3 - \frac{45}{256} \left(\frac{r_b}{h} \right)^4 - \frac{1}{16} \left(\frac{r_b}{h} \right)^5 \right]^{-1}, \quad (1.13)$$

where h is the distance from the center of the bead to the surface. This equation is valid for $h - r > 0.02r$. For further details on this method it is referred to [Felgner *et al.* 1995, Oddershede *et al.* 2001, Neuman & Block 2004].

Trap Stiffness Calibration: Equipartition Theorem and Optical Potential Analysis

A bead confined within an harmonic potential is subjected to thermal fluctuations. For a one dimensional optical potential well with trap stiffness κ , the equation of motion is, in the simplest case, driven by stochastic thermal forces $F(t)$ (Langevin equation [Langevin 1908]) and is given by

$$\beta \dot{x}(t) + \kappa x(t) = F(t). \quad (1.14)$$

Brownian motion of a bead in a parabolic potential can be characterized by a one-sided Lorentzian position power spectrum [Wang & Uhlenbeck 1945], which translates the bead movement from the time domain into the frequency domain. Expressing the Lorentzian in terms of the corner frequency f_0 gives a power spectrum of

$$S(f) = \frac{k_B T}{\pi^2 \beta (f_0^2 + f^2)} \quad (1.15)$$

where f is the frequency. The frequency where the power of the bead motion has declined to a half is termed corner frequency and relates to the trap stiffness via $f_0 = \kappa(2\pi\beta)^{-1}$. The mean square displacement (or variance) $\langle x^2 \rangle$ of the bead is defined as

$$\langle x^2 \rangle = 2\pi \int_0^\infty S(f) df \quad (1.16)$$

and is related to the trap stiffness through the equipartition theorem with

$$\frac{1}{2} k_B T = \frac{1}{2} \kappa \langle x^2 \rangle . \quad (1.17)$$

With relation (1.15), the trap stiffness can be determined if the viscous drag coefficient from equation (1.12) of the trapped bead is known. From a Lorentzian fit to the measured power spectrum, the corner frequency can be derived, which provides an estimate for the trap stiffness ($\kappa = 2\pi\beta f_0$). Another alternative is the application of the equipartition theorem (1.17), which allows to calculate the trap stiffness from the position fluctuations of the trapped bead by measuring its positional variance.

However, both approaches assume a harmonic potential well, an approximation that is valid for small bead displacements from the trap center but does not describe the shape of the entire potential. An analysis of the actual optical potential can be contrived when the complete position histogram of a trapped bead is recorded. The probability for the bead displacement is given by the Boltzmann distribution in (1.2) and depends on the potential energy. Hence, the effective potential can be deduced by rewriting this relation for the potential $U_{pot}(x)$, which gives

$$U_{pot}(x) \propto -k_B T \ln p(x) . \quad (1.18)$$

From this, the position-dependent restoring forces throughout the potential well can be derived with $F_{\nabla}(x) = -\nabla U(x)$.

Simulation of a Gaussian potential

To simulate the restoring forces a bead experiences in an optical potential, the potential was assumed to be Gaussian shaped with

$$U_{pot}(x) = -U_0 \exp\left(-\frac{x^2}{2\langle x^2 \rangle}\right) \quad (1.19)$$

where U_0 denotes the depth of the potential well. The potential depth is controlled by the applied laser power ($P \propto E^2$) and grows linearly with the laser power as can be derived from relation (1.5). Applying relation (1.6), the force is given by

$$F(x) = -U_0 \frac{x}{\langle x^2 \rangle} \exp\left(-\frac{x^2}{2\langle x^2 \rangle}\right). \quad (1.20)$$

The principal shape of the trap potential and the restoring forces onto a trapped bead are displayed in figure 1.2 A) and B), respectively. In the Gaussian potential well in A), the green dots denote the area that is well-approximated with a parabolic fit ($U(x) = -\frac{1}{2}\kappa x^2$). Correspondingly, the green marked area in B) displays the area of linear force-position dependence ($F(x) = \kappa x$). The simulation used the following values for the parameters: $\langle x \rangle = 500\text{nm}$ and $U_0 = 20 \cdot 10^{-18}\text{J}$.

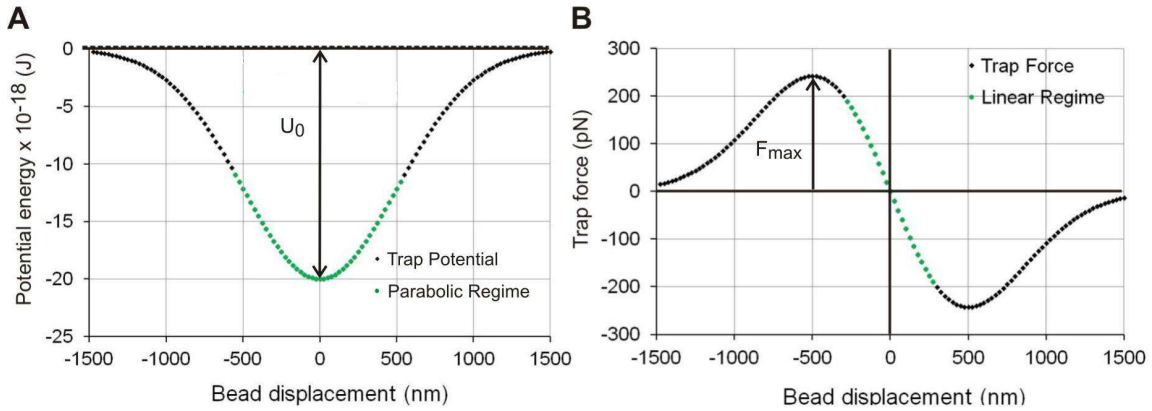


Fig. 1.2: Simulation of trap potential and trap force

A) Gaussian shaped optical potential of depth U_0 . The green dotted line is well approximated by a parabolic fit. B) Simulation of the corresponding restoring trap force on a confined bead. F_{max} denotes the force required to lift a bead from the potential well. The green dotted line marks the area of a linear force-displacement relation.

1.1.3 Instrumentation of Optical Tweezers and General Design Considerations

The most basic OT setup requires the following components for force spectroscopy applications:

- Trapping laser
- Microscope with high numerical aperture objective
- Imaging and position detection

Trapping Laser: The lasers chosen for work with biological samples typically emit light in the infrared regime. As the absorption of most biological materials is low in the infrared, photodamage and heating of the sample are small, allowing to expose the sample for extended measurement times to the radiation without causing hazards. However, the samples are mainly maintained in aqueous solutions and the absorption coefficient of water gains rapidly with wavelength enlargement toward the long-wavelength infrared, causing extensive heating for irradiation in this regime. Low absorption characteristics in both the sample material and water are a prerequisite to apply sufficiently high laser power for the desired trap stiffness and restoring forces of the optical trap. The lowest resulting damage is achieved with sample irradiation at a wavelength of 930 nm , followed by a wavelength of 830 nm and 1064 nm [Gross 2003, Neuman *et al.* 1999, Liang *et al.* 1996].

Microscope objective: The optical gradient force depends on the intensity gradient of the incident light in the sample plane. A Gaussian laser beam can be focused into the tightest diffraction-limited spot compared to other beam profiles. The beam waist w_0 in the focus and the gradient of the light intensity close to the focal spot are controlled by the numerical aperture (NA) of the microscope objective which also defines the angle α between the focused output light and the optical axis:

$$NA = n \sin \alpha \approx \frac{\lambda}{\pi w_0} \quad (1.21)$$

where n is the refractive index of the medium and λ is the wavelength of the laser light in vacuum. A high NA yields a tight beam diameter in the focus, which correlates to a strong electric field ($w_0 \propto |\vec{E}_0|^2$). Hence, an objective of high NA yields the strongest gradient forces and is able to overcome the scattering forces more easily. Due to this, a high NA objective features the highest efficiency of the system in terms of trap stiffness versus laser power.

Imaging and position detection: In optical tweezers force spectroscopy, forces are typically derived from spatial displacement measurements and require accurate position detection. Spherical beads are used as force probes and their position alteration over time has to be monitored with high spatial and temporal resolution. One method typically used is video microscopy, where a CCD (charge-coupled device) camera is used to record images with a frame rate of 25 to 120 Hz. With image processing techniques relying on centroid-finding algorithms a resolution of down to about 5 nm can be achieved and allows for object tracking with subpixel resolution [Cheezum *et al.* 2001,

Thompson *et al.* 2002]. Another commonly applied technique is the additional implementation of a quadrant photodiode [Finer *et al.* 1994, Simmons *et al.* 1996], which offers high precision and high bandwidth particle tracking.

With the basic instrumentation described, a single trap can be generated, allowing for the manipulation of an individual object. With the expansion of OT applications, more complex experimental requirements arose and the availability of an increased number of optical traps together with accurate trap steering became essential. This gave rise to several multiple trap OT approaches, which can be divided into two main categories: holographic OTs [Dufresne & Grier 1998, Reicherter *et al.* 1999, Liesener *et al.* 2000] and time-shared OTs [Visscher *et al.* 1993, Visscher *et al.* 1996, Emiliani *et al.* 2004, Neuman & Block 2004].

1.1.4 Force Spectroscopy with Optical Tweezers and Applications in Biology

To study force development on the single cell and single molecule level, a variety of techniques has been developed over the last decades. Atomic force microscopy (AFM), magnetic tweezers and optical tweezers are among those techniques that found the broadest application range. The general objective of these approaches is the direct study of dynamics on a size scale ranging from individual proteins to single cells. All three methods allow for live cell force measurement under physiological conditions and are thus able to address the questions of *in vivo* dynamics in cell-cell, cell-substrate, and receptor-ligand interactions. Table 1.1 denotes the characteristic force range together with the temporal and spatial resolution of this techniques.

Tab. 1.1: Overview of selected force spectroscopy methods (excerpt from [Neuman & Nagy 2008])

	AFM	Magnetic tweezers	Optical tweezers
Force range (pN)	$10 - 10^4$	$10^{-3} - 10^2$	$10^{-1} - 10^2$
Temporal resolution (s)	10^{-3}	10^{-2}	10^{-4}
Spatial resolution (nm)	$0.5 - 1$	$5 - 10$	$0.1 - 2$

Biological Applications of Optical Tweezers

Owing to their high degree of flexibility and their non-invasiveness, OTs became a versatile tool for the investigation of a variety of force-dependent physiological processes:

- DNA transcription/ RNA polymerase stalling forces and pausing and protein folding [Yin *et al.* 1995, Wang *et al.* 1998, Neuman *et al.* 2003, Woodside *et al.* 2008, Shank *et al.* 2010]
- molecular motors: myosin [Finer *et al.* 1994, Molloy *et al.* 1995a, Coppin *et al.* 1996, Jeney *et al.* 2004] kinesin [Ashkin *et al.* 1990b, Kuo & Sheetz 1993, Svoboda *et al.* 1993, Svoboda & Block 1994b, Visscher *et al.* 1999] and dynein function in cargo transport [Wang *et al.* 1995, Gross *et al.* 2000]
- microrheology: analysis of membrane stiffness by tether formation [Dai & Sheetz 1995, Hochmuth *et al.* 1996, Dai & Sheetz 1999, Titushkin & Cho 2006, Brownell *et al.* 2010]

- Cell adhesion: integrin-cytoskeleton interaction [Schmidt *et al.* 1993, Choquet *et al.* 1997, Nishizaka *et al.* 2000, Galbraith *et al.* 2002, Jiang *et al.* 2003, Petrie *et al.* 2006, Mejean *et al.* 2009, Jeney *et al.* 2010, Bordeleau *et al.* 2011, Brenner *et al.* 2011, Diez *et al.* 2011]

In particular studying the formation of cell adhesions with OTs focusing on cell-substrate interaction sites is of interest as it can help to understand physiological and pathological mechanosensing processes in more detail.

1.2 Cell-Substrate Interaction and Mechanotransduction

The cellular response to the mechanical and biochemical characteristics of the extracellular matrix (ECM) is a crucial process, which influences cellular morphology, proliferation and motility [Choquet *et al.* 1997, Geiger *et al.* 2009]. Adherent cells are capable of forming dynamic contacts with the ECM and these contacts constitute a physical link of the cell cytoskeleton to the substrate and enable force transduction and migration. Cell-substrate adhesions are mediated by transmembrane integrin receptors featuring a binding site for ECM ligands in their extracellular domain and a variety of adhesion-related protein binding sites in the cytosolic domain. The ECM can be constituted by a variety of integrin ligating proteins, including fibronectin, vitronectin, and collagen, which are recognized by different integrin subtypes. Integrins form heterodimers upon activation that are constituted by α and β chains and can combine into 24 different heterodimers [Scales & Parsons 2011].

Extracellular Matrix Components: Fibronectin and the RGD Adhesion Motifs

In the ECM, a variety of integrin ligands build an interactive substrate for cell adhesion. Fibronectin (FN) is an ECM component that plays an important role in cell-substrate adhesion, motility, and proliferation. In addition to its occurrence in the ECM of connective tissue, it can be expressed by the cells themselves and it also exists in a soluble form, for example in blood plasma [Pankov & Yamada 2002].

The FN macromolecule is a dimeric polypeptide that is comprised of two identical strands, with each strand offering binding sites for a variety of integrin types (figure 1.3). At the C-terminus these strands are crosslinked via disulfide bonds [Pankov & Yamada 2002]. Scanning electron microscopy has revealed that each strand has a length of about 61 nm and a width of about 2 nm [Engel *et al.* 1981].

Among the integrin binding sites distributed along the macromolecule, the shortest amino acid se-

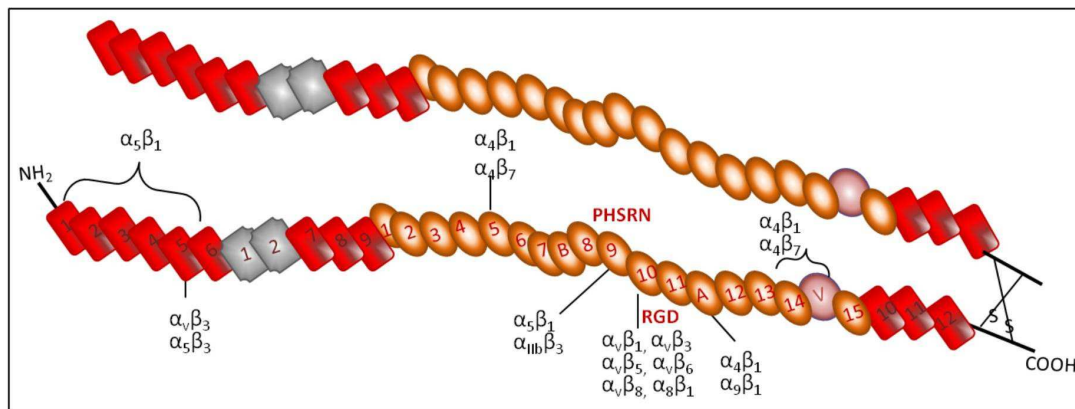


Fig. 1.3: Structure of fibronectin

The macromolecule fibronectin is an extracellular matrix component and ligand to many types of integrins. It is a dimeric protein with a molecular weight of about 230 kDA per strand. Fibronectin contains several adhesion motifs, such as the neighboring RGD and PHSRN amino acid sequences.

quence known to be recognized as adhesion motif is the RGD (Arginine-Glycine-Aspartic Acid) sequence (figure 1.4). This sequence is located in the central region of FN, in the FNIII₁₀ domain, and is a binding site for $\alpha_5\beta_1$, $\alpha_8\beta_1$, $\alpha_{IIb}\beta_3$ and all α_v integrins [Pierschbacher & Ruoslahti 1984, Humphries *et al.* 2006]. Crystal structure analysis revealed a loop-like conformation of the RGD sequence within FN [Leahy *et al.* 1996]. Next to the RGD adhesion motif in the fibronectin macromolecule is the location of a further adhesion site: the amino acid sequence PHSRN (Proline-Histidine-Serine-Arginine-Asparagine) is located in the FNIII₉ domain and is supposed to show synergetic effects with the RGD sequence in mediating cell adhesion based on $\alpha_5\beta_1$ integrins [Aota *et al.* 1994, Leahy *et al.* 1996].

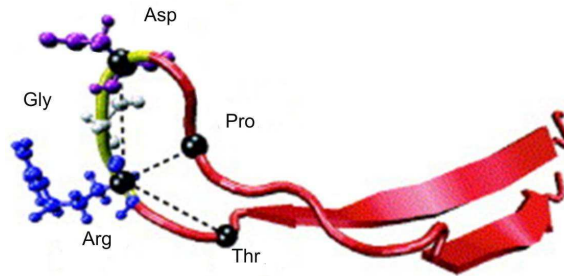


Fig. 1.4: Conformation of the RGD cell adhesion motif

Arginine-glycine-aspartic acid (RGD) peptides constitute the shortest known adhesion motif recognized by integrins. The adhesion motif is located within fibronectin domain III and assumes a loop-like conformation in the native state, but can unfold under the traction forces applied by integrin-mediated adhesion sites (modified and reprinted from Gao *et al.* [Gao *et al.* 2002]).

1.2.1 Cell Morphology and the Actin Cytoskeleton

The biochemical and biomechanical character of the ECM defines the shape of adherent cells. The geometrical distribution of adhesion-mediating ligands [Chen *et al.* 1997, Balaban *et al.* 2001, Lehnert *et al.* 2004, Autenrieth 2008, Klein 2009], as well as the substrate rigidity [Choquet *et al.* 1997, Engler *et al.* 2004, Discher *et al.* 2005, Chan & Odde 2008, Kobayashi & Sokabe 2010, Prager-Khoutorsky *et al.* 2011] and the exposure to external stress and strain [Wang *et al.* 1993, Ingber 1997, Goldyn 2009] regulate cell morphology and polarization. During migration and upon the encounter of mechanical stimuli, cells polarize and assume an elongated shape, which is divided into a leading edge area, oriented into the direction of motion, and a trailing edge at the rear (figure 1.5). The leading edge consists of the lamellipodium in the distal area, which is located right behind the foremost membrane fold, and parts of the lamella in the proximal region.

The cell shape is maintained by the cytoskeleton, a structure that is composed of actin, microtubules, and intermediate filaments [Bao & Suresh 2003, Gardel *et al.* 2008]. Actin forms microfilaments, that originate from the polymerization of globular actin monomers (G-actin) into filaments (F-actin). These actin filaments can assemble into larger structures, so called actin stress fibers. Stress fibers are contractile bundles containing actin filaments [Cramer 1997], myosin II [Fujiwara & Pollard 1976], and several actin associated proteins including α -actinin [Lazarides & Burridge 1975]. They are classified into three categories: ventral actin stress fibers, which are asso-

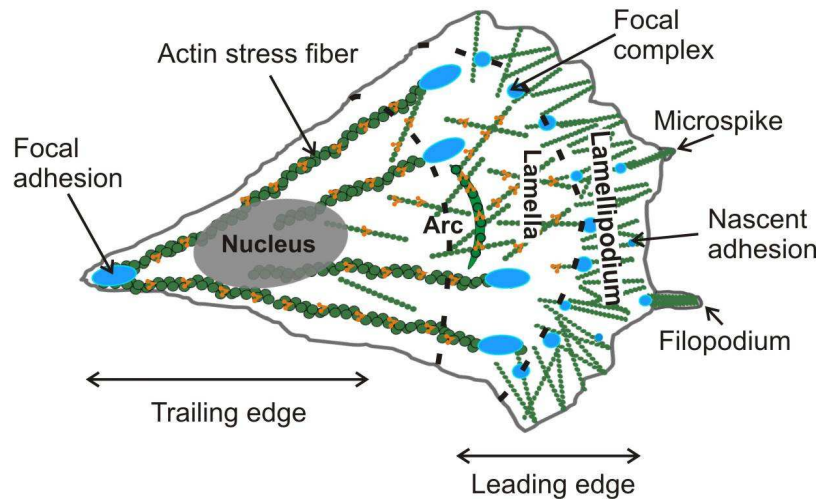


Fig. 1.5: Cell morphology and actin cytoskeleton

Motile cells polarize during migration to form a leading edge and a trailing or retracting edge. The leading edge comprises the lamellipodium, which is interspersed with microspikes and is the origin of filopodia extension. At the proximal boundary, focal complexes emerge and form the transition to the lamella. In the anterior region, the lamella contains a contractile actin network, while the more posterior part displays mature focal adhesions, actin stress fibers and transverse arcs.

ciated with focal adhesions (FAs) at both ends, dorsal actin stress fibers, which are connected to FAs on one end, and transverse actin arcs that are not accompanied by FAs [Small *et al.* 1998, Hotulainen & Lappalainen 2006]. Actin stress fibers and transverse arcs show a periodic spacing of myosin and α -actinin with F-actin, which resembles the morphology of muscle cells [Hotulainen & Lappalainen 2006].

While actin stress fibers are observed in the trailing edge and in the posterior part of the lamella, the anterior lamella and the lamellipodium comprise a different type of actin organization. The lamellipodium is the protruding area of the cell and is formed by rapid actin polymerization, which leads upon interaction with Arp2/3 (actin related protein complex) and cofilin to the emergence of a gel-like actin network of branched and cross-linked filaments [Small 1988, Svitkina & Borisy 1999, Polard *et al.* 2000, Ichetovkin *et al.* 2002, Ponti *et al.* 2004, Small & Resch 2005, Lai *et al.* 2008, Gardel *et al.* 2008]. In the distal part of the lamella, close to the lamellipodium transition, a contractile actin network of interlinked F-actin is prominent, which is riddled with small clusters of myosin II [Verkhovsky *et al.* 1995, Svitkina *et al.* 1997, Gupton & Waterman-Storer 2006].

1.2.2 Cell Motility

Many cell types, such as fibroblasts and neurons, are able to migrate along a substrate. Migration plays an important role physiological processes such as wound healing or embryogenesis. The direction of migration can be influenced by substrate characteristics like rigidity gradients (durotaxis), substrate-bound ligand gradients (haptotaxis), and by soluble chemical cues (chemotaxis).

Migrating cells assume a polarized shape forming the leading edge in the front and the trailing

edge at the rear. A requirement for migration is the spatiotemporal coordination of membrane extension, actomyosin contraction and cytoskeletal remodeling. At the membrane front of the leading edge, the cell starts to form protrusions, which extend the membrane. These protrusions originate from the rapid polymerization of actin monomers into filaments in the lamellipodium (treadmilling), which pushes the membrane outward [Cramer *et al.* 1994, DesMarais *et al.* 2002]. Subsequently forming adhesion sites stabilize the protruding area and allow for the next cycle of extension. In this process, the coupling of the actin filament network to tension bearing adhesion sites is a prerequisite for an increase in cell spreading area [Mitchison & Cramer 1996, Sheetz *et al.* 1998, Giannone *et al.* 2004, Ponti *et al.* 2004, Giannone *et al.* 2007]. However, to effectively migrate, the cell is additionally required to release established substrate adhesions at the rear and allow for the trailing edge to follow.

Contractile forces are generated by the actomyosin system and are transmitted from the cytoskeleton to the cellular adhesion sites and to the ECM. Thus, migration is mainly coordinated by the spatiotemporal interplay of adhesion assembly and disassembly and by cytoskeletal reorganization [Lauffenburger & Horwitz 1996, Small *et al.* 1996, Ballestrem *et al.* 2000, Webb *et al.* 2002, Wehrle-Haller & Imhof 2003, Papusheva & Heisenberg 2010, Parsons *et al.* 2010, Gauthier *et al.* 2011, Lawson *et al.* 2012]. The speed of cell migration depends on both the extension rate of the leading edge and the detachment rate of adhesions in the trailing edge, wherein DeMali and coworkers reported the disassembly speed as the predominant limiting factor [DeMali *et al.* 2002].

During migration, the actin cytoskeleton has to be constantly reorganized. An important mediator of actin nucleation and the formation of a branched actin network in the lamellipodium is the Arp2/3 complex, which has a promoting effect on membrane protrusion [Mullins *et al.* 1998, Machesky *et al.* 1999, Pollard *et al.* 2000, Bailly *et al.* 2001, Welch & Mullins 2002, Pollard 2004]. Cellular traction forces are transmitted to the ECM at integrin-mediated cell adhesion sites. The interactions of integrins with extracellular ligands trigger the activation of signaling pathways, such as the Rho-family GTPases pathway. Among the many downstream effectors regulated by the small GTPases Rho, Rac, and Cdc42 are mDia, WAVE, and WASP, which themselves mediate actin polymerization by activation of Arp2/3 and profilin or inhibition of its counterpart cofilin [Geiger *et al.* 2001, Schwartz 2004, Gupton *et al.* 2007].

1.2.3 Cellular Forces and Cell-Substrate Adhesions

Cells are naturally exposed to forces, which mediate cell morphology and can be generated internally by the actomyosin machinery or externally by shear flow, locomotion, and wound healing [Inger 2004, Wang & Thampatty 2006, Janmey & McCulloch 2007]. As cells are constantly experiencing and generating forces, they require sophisticated mechanosensing and mechanotransduction mechanisms to regulate the adaptation of function and morphology in a sequentially changing environment. The term mechanosensing refers to the recognition and response of cells to extracellular forces, while mechanotransduction relates to the process of mechanical stimuli conversion into intracellular biochemical signals and initializes distinct signal transduction pathways [Alenghat &

Ingber 2002, Bershadsky *et al.* 2003, Nicolas *et al.* 2004, Hoffman *et al.* 2011].

Cells form transient contacts with the ECM to attain stable substrate adhesion and these adhesion sites play an essential role in cellular mechanosensing [Geiger *et al.* 2001, Rivelino *et al.* 2001, Bershadsky *et al.* 2006]. The cell-substrate adhesion sites are comprised of extracellular integrin ligands, transmembrane integrin receptors, and a multi-protein plaque in the cytosolic domain that couples the ligated integrins to the cytoskeleton. In particular, adhesion receptors of the integrin family play a major role in mediating signaling, for example by regulating adhesion-related proteins (paxillin, focal adhesion kinase (FAK), mammalian Diaphanous-related-1 (mDia1)) and by controlling the Rho GTPases signaling pathway [DeMali *et al.* 2003, Ingber 2003, Larsen *et al.* 2006, Gup-ton *et al.* 2007].

Development and Constitution of Adhesive Complexes

In migrating cells, new adhesion sites are continuously formed in the lamellipodium and constitute a mechanical barrier at the transition to the lamella [Bershadsky *et al.* 2006, Alexandrova *et al.* 2008]. The initial formation of adhesion sites is followed by a maturation process, in which adhesion sites grow and change their protein composition (figure 1.6) [Vicente-Manzanares *et al.* 2009, Scales & Parsons 2011].

The origin of a building adhesion site is supposed to be the mutual encounter of membrane-bound proteins with components of the ECM. With the initial clustering of ligated integrins, nascent adhesions assemble, which are comprised of integrins (mainly $\alpha_v\beta_3$), talin, paxillin and probably FAK [Cohen *et al.* 2004, Zaidel-Bar *et al.* 2004, Lawson *et al.* 2012]. In this constitution talin directly mediates the coupling of integrins to the force generating actomyosin filaments [Giannone *et al.* 2003, Jiang *et al.* 2003, Margadant *et al.* 2011]. Integrin $\alpha_v\beta_3$ signaling triggers the activation of Rac and Cdc42, which are involved in stabilizing cellular protrusions [Papusheva & Heisenberg 2010].

The nascent adhesion sites are transient and feature high turnover rates with a life time of about

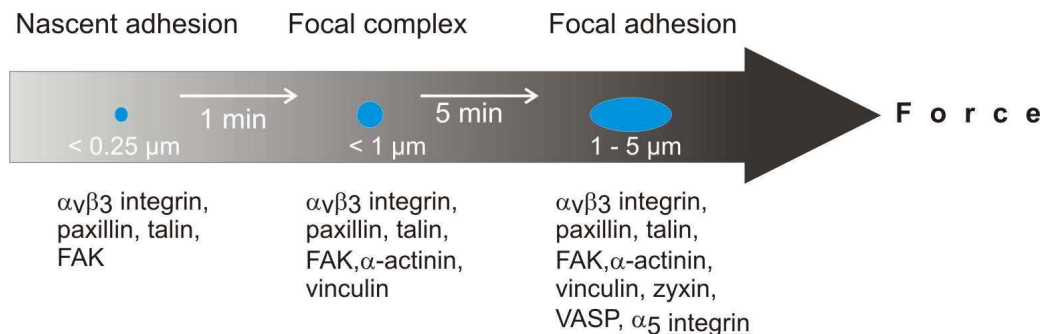


Fig. 1.6: Maturation process of cell adhesion sites

Nascent adhesions evolve in the lamellipodium and undergo a process of growth and reconstitution. The initial formation of nascent adhesions requires the complex formation of $\alpha_v\beta_3$ integrin, paxillin, and talin. With ongoing maturation more adhesion-related proteins are recruited and stabilize the cell adhesion. With increasing size and protein complexity, the tension across the adhesion site is amplified.

one minute [Choi *et al.* 2008], but can stabilize in a tension-dependent manner and grow into focal complexes. Focal complexes are dot-like structures of less than $1\ \mu\text{m}$ diameter that are located in the cell periphery and have accumulated α -actinin, and vinculin in addition to the nascent adhesion components. The interplay of actin with α -actinin is proposed as a major effector of maturation [Choi *et al.* 2008]. Incorporation and phosphorylation of paxillin occurs in the early stage of adhesion formation and precedes the localization of several adhesion-related proteins into adhesion sites.

Focal complexes are transient structures that can experience a force-dependent strengthening and subsequent growth into focal adhesions (FAs) (figure 1.6) [Balaban *et al.* 2001, Rivelin *et al.* 2001, Bershadsky *et al.* 2003]. FAs assume an elongated morphology and are mainly established in the proximal lamella, the center, and the trailing edge of the cell. The reinforcement of FAs is mediated by Rho kinase (ROCK) and is concomitant with a repeated modification of the adhesion plaque composition. Zyxin, VASP and $\alpha_5\beta_1$ integrins are recruited into the focal adhesion, with $\alpha_5\beta_1$ integrin signaling regulating the actomyosin tension and the formation of actin stress fibers [Laukaitis *et al.* 2001, Zaidel-Bar *et al.* 2003, Bershadsky *et al.* 2006, Gardel *et al.* 2010, Pappusheva & Heisenberg 2010]. Actomyosin generated tension is controlled by myosin phosphorylation, which is driven by ROCK via the Rho pathway and by Rac and Cdc42 pathways (figure 1.7) [Burrige & Chrzanowska-Wodnicka 1996, Rottner *et al.* 1999, Rivelin *et al.* 2001, Geiger *et al.* 2001, Schwartz 2004]. For an elaborate schematic model of the components mediating cell substrate adhesions it is referred to Zamir & Geiger [Zamir & Geiger 2001, Wehrle-Haller 2012].

Cell adhesions change their size and composition in a force-dependent manner and thus play an im-

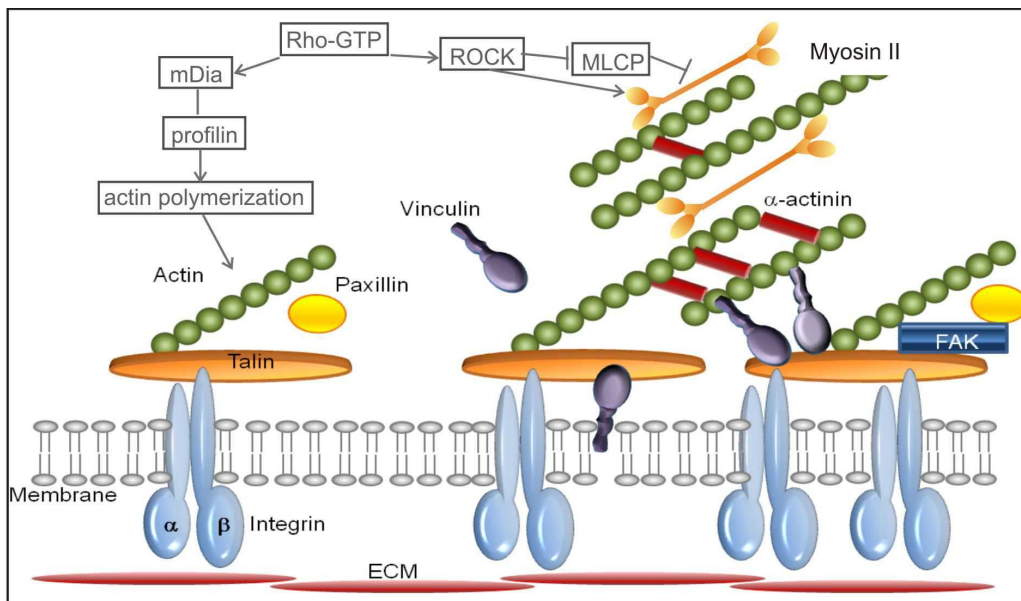


Fig. 1.7: Schematic model of cell-substrate adhesions

Nascent adhesions (left) are constituted by few adhesion-related proteins such as talin and paxillin, which mediate the association of ligated integrins with actin filaments. Focal complexes are bigger and more mature structures (right), featuring additional proteins like vinculin, α -actinin.

portant role in mechanosensing and mechanotransduction. In figure 1.7 the interaction of adhesion constituting proteins with the actin cytoskeleton is illustrated. The nanoscale protein architecture of maturing adhesion sites has been classified into distinct functional layers, with a membrane adjacent integrin signaling layer, an intermediate force transduction layer and an actin regulatory layer, which together bridge a gap of about 40 nm between the cytoplasmic integrin domain and the actin cytoskeleton [Kanchanawong *et al.* 2010].

Although cell-substrate adhesions appear rather stationary over time, there exists a high turnover of proteins within adhesion sites. This leads to a continuous remodeling of the structural morphology and allows for fast adaptations of the protein constitution in response to external or internal stimuli [Wehrle-Haller & Imhof 2002, Brown *et al.* 2006, Lele *et al.* 2008].

The average force transduction in FAs has been estimated to amount to a magnitude of about 0.2 to 15 nN/ μ m, depending on cell type, extracellular ligand, and experimental procedure [Galbraith & Sheetz 1997, Burton *et al.* 1999, Oliver *et al.* 1999, Balaban *et al.* 2001, Beningo *et al.* 2001, Munevar *et al.* 2001, Tan *et al.* 2003].

1.2.4 Retrograde Actin Flow

The locomotion of motile cells is intrinsically coupled to retrograde actin flow in the leading edge [Harris 1994]. During the extension of the leading edge, actin polymerization pushes the foremost membrane outward and the internal actin network rearward, increasing the cell surface [Svitkina *et al.* 1986, Forscher & Smith 1988, Fukui *et al.* 1999, Watanabe & Mitchison 2002]. Concomitantly a rearward flow of actin filaments (retrograde flow), directed centripetally toward the nuclear region, occurs in the lamella and lamellipodium. An inverse correlation was observed between actin flow velocity and the cellular migration speed, with stationary cells exhibiting a rapid actin flow, while motile cells showed a flow velocity that decreased with increasing migration speed [Lin & Forscher 1995, Lin *et al.* 1996, Henson *et al.* 1999]. Small objects placed on the cell membrane were reported to be transported rearward centripetally with the same velocity as the underlying actin network [Forscher & Smith 1988, Schmidt *et al.* 1993, Felsenfeld *et al.* 1996].

In the lamellipodium a dense, randomly organized actin network exists. The actin filaments of this network are oriented with their barbed ends (also termed plus ends or fast growing ends) toward the direction of the membrane tip, and hence assemble actin monomers preferentially at this site [Small *et al.* 1978, Small 1988, Cramer 1997]. This is supposed to play a major role in retrograde actin flow in the lamellipodium.

However, a distinct mechanism is responsible for retrograde flow in the lamella, where forces generated by the motor protein myosin II play an essential role in translocating actin filaments. The activation of the cross-bridge cycle upon actin myosin engagement is the source of the rearward directed forces pulling at the actin filaments [Lin *et al.* 1996, Henson *et al.* 1999, Medeiros *et al.* 2006]. As the lamellar contractile actin network and the lamellipodial gel-like actin network are interconnected, the tension generated in the lamella possibly contributes to the rearward flow in the lamellipodium [Cramer 1997].

1.2.5 The Adhesion-Related Protein Vinculin

Vinculin was discovered by Geiger in 1979 and is a 117 *kDa* protein comprised of 1,066 amino acids [Geiger 1979]. The protein accumulates into adhesion sites and plays an essential role in mediating cell-substrate adhesion and cell-cell adhesion [Volberg *et al.* 1995, Xu *et al.* 1998a]. Vinculin offers binding sites for more than 15 partner molecules and is thus discussed as a key regulator in adhesion strengthening and turnover [Voss & Jockusch 1996, Zamir & Geiger 2001, Saunders *et al.* 2006, Ziegler *et al.* 2006, Carisey & Ballestrem 2011].

Inactivation of the vinculin gene via a "double knockout" in mouse embryos resulted in severe heart and brain defects and was lethal at embryonic day 10 [Xu *et al.* 1998a]. In cultured fibroblasts vinculin deficient cells show a mutant phenotype with a more roundish cell shape, a reduced adhesiveness and a two-fold increased motility compared to wild type cells [Fernández *et al.* 1993, Coll *et al.* 1995, Xu *et al.* 1998b].

Structure and Binding Partners of Vinculin

Scanning electron microscopy analyses revealed an N-terminal globular vinculin head domain of about 8 *nm* diameter and a flexible, proline-rich neck domain that is linked to the C-terminal tail of 20 *nm* length [Milam 1985, Molony & Burridge 1985, Beck 1989, Eimer *et al.* 1993, Winkler *et al.* 1996]. A detailed analysis of the crystal structure of vinculin was derived from diffraction patterns of synchrotron radiation exposure [Bakolitsa *et al.* 2004]. Vinculin comprises five

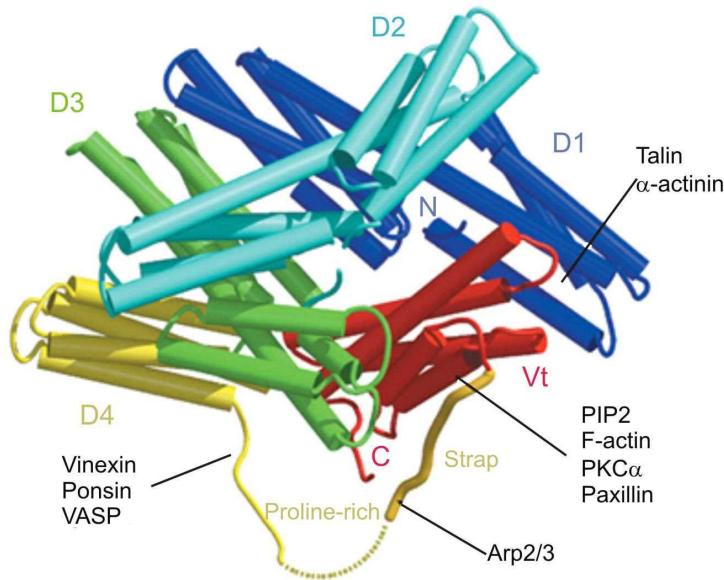


Fig. 1.8: Crystal structure of vinculin

Vinculin is comprised of five helical domains, with domains D1 to D4 constituting the head domain and D5 the tail domain. The resting conformation of vinculin is an autoinhibited state, which is induced by head to tail binding. The arrangement of the helical bundles of domains D1 and D5 in this conformation inhibits binding of talin, α - actinin and F-actin (illustration modified and reprinted from [Bakolitsa *et al.* 2004]).

domains, four head domains (D1-D4) and one tail domain (D5), which are each constituted by distinctive helical bundle conformations (figure 1.8). The head domain features binding sites for talin and α -actinin, the neck domain binds vinexin, ponsin, VASP, and Arp2/3, and the tail domain contains binding sites for PIP₂, F-actin, paxillin, and PKC α [Zamir & Geiger 2001, Ziegler *et al.* 2006, Carisey & Ballestrem 2011]. Talin, PIP₂, and α -actinin are probably involved in the activation of vinculin, which is achieved through helical bundle conversion [Gilmore & Burridge 1996, Bakolitsa *et al.* 2004, Izard *et al.* 2004, Cohen *et al.* 2005, Cohen *et al.* 2006]. The activated vinculin is incorporated into early adhesion sites, where the initial integrin-actin cytoskeleton linkage is mediated by talin, and reinforces the adhesion site [Galbraith *et al.* 2002]. Vinculin recruitment into adhesion sites is proposed to be force-dependent [Galbraith *et al.* 2002, Riveline *et al.* 2001, Pasapera *et al.* 2010] and can stabilize an adhesion if force transmission occurs concurrently [Grashoff *et al.* 2010].

In the passive state, vinculin adopts an autoinhibited conformation where the head domains bind tightly to the tail domain [Johnson & Craig 1994]. The conformation of native vinculin at the location of cell adhesion sites can switch from autoinhibited to active and vice versa [Chen *et al.* 2005]. With the association of head and tail domain, several cryptic binding sites are blocked and vinculin interaction with other proteins is impaired. The autoinhibited cytosolic conformation suppresses binding of talin, α -actinin, and F-actin and anticipates a contribution of vinculin to cell adhesion stabilization [Johnson & Craig 1994, Johnson & Craig 1995, Cohen *et al.* 2005].

An overview of the direct interaction partners of vinculin and the effect of this engagement onto

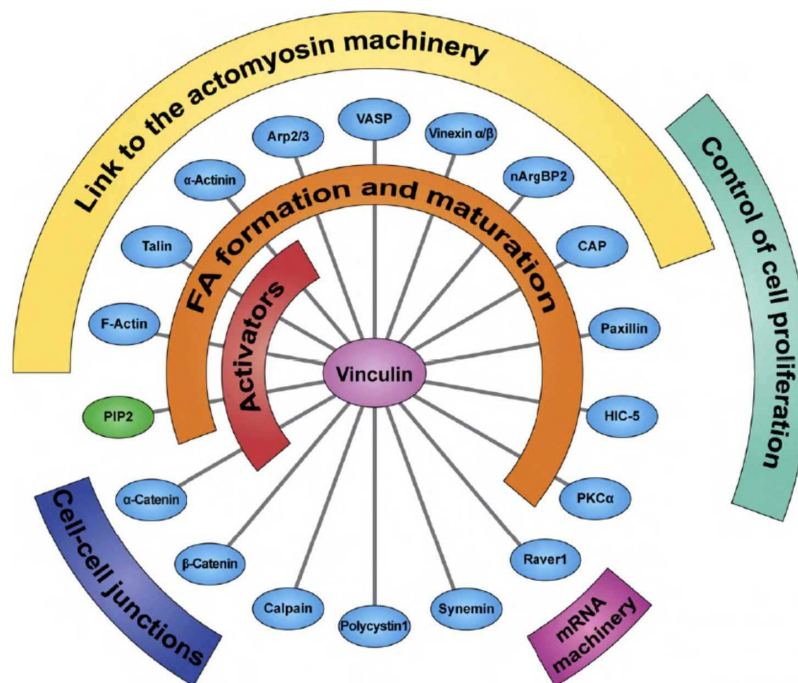


Fig. 1.9: Direct interaction partners of vinculin

Vinculin offers binding sites to a variety of proteins and is involved in the coupling of cell adhesion sites with the actin cytoskeleton, regulation of focal adhesion (FA) formation and cell-cell junctions, and proliferation control (modified from [Carisey & Ballestrem 2011]).

various cell functions is depicted in figure 1.9.

1.2.6 Mutations in the Vinculin Structure

Vinculin is a multi domain protein and thus the question arises, how the distinct vinculin functions are allocated to specific domains and how the conformational switch mediates these functions. Over the last years, several mutations were introduced into the vinculin molecule to study the impact of structural modifications.

The vinT12 mutant

Of particular interest is the role of head-to-tail binding on vinculin function in cell adhesion sites. A mutant vinculin protein was created (termed vinT12) that remains in a constitutively active conformation, as the head-to-tail binding is strongly attenuated (figure 1.10). This attenuation is achieved by point mutations in the tail domain, where five residues in helix 4 are mutated to alanine (amino acids 974 to 978), which decreases the head-to-tail binding to about 10 % of the native binding strength [Cohen *et al.* 2005]. In this constitutively active conformation, all cryptic binding sites are permanently accessible for the binding partners, which increases the residence time of vinT12 in cell adhesion sites by a factor of two compared to the native protein and renders the cell adhesion more stable [Humphries *et al.* 2007].

The vinA50I mutant

As a counterpart to the constitutively active mutant vinT12, a constitutively inactive mutant was designed by exchanging the amino acid alanine for isoleucine at position 50 in the vinculin head domain D1 (vinA50I; figure 1.10) [Bakolitsa *et al.* 2004]. This point mutation strongly enhances the affinity of head-to-tail binding, resulting in a severely inhibited talin binding. However, the talin binding site in vinculin is located in the amino acid sequence at position 167 to 208 and is thus not directly affected by the point mutation [Jones *et al.* 1989]. Furthermore, the constitutively inactive conformation blocks binding sites for α -actinin and F-actin.

The vin880 mutant

To characterize the influence of direct vinculin binding to F-actin on the functionality of cell adhesion sites, tail truncated mutants were constructed. The mutant vin880 is comprised of amino acids 1 to 880, that is it features an intact head and neck domain but lacks the entire tail domain (figure 1.10). This abrogates binding to F-actin, paxillin and PIP₂ and additionally renders the protein constitutively active. Expression of vin880 in fibroblast cells leads to reduced turnover rates of both vin880 and talin in cell-substrate adhesion sites, an effect similar to vinT12 expression [Humphries *et al.* 2007].

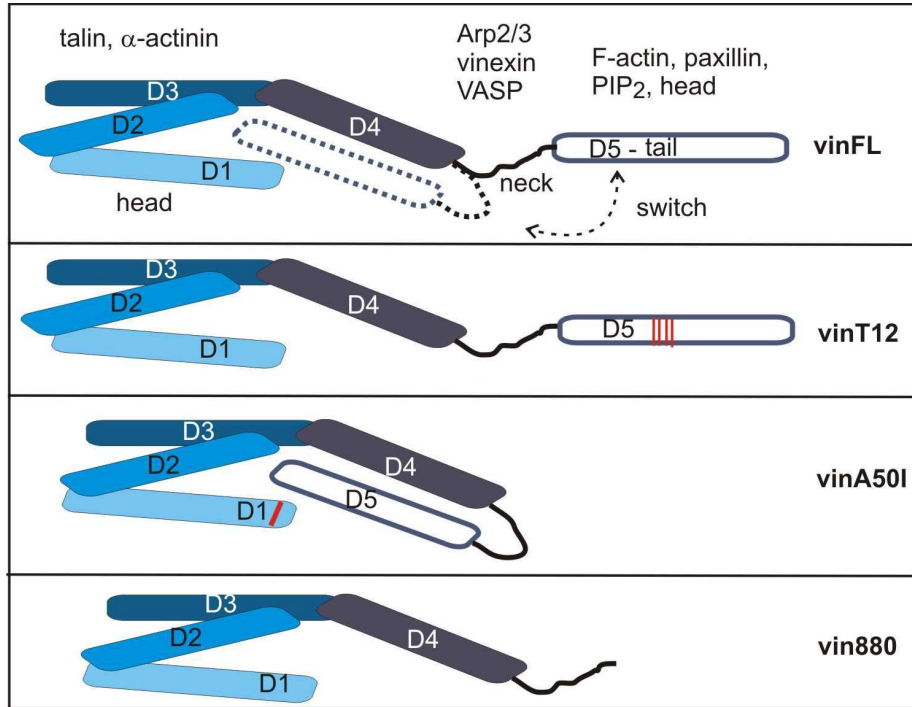


Fig. 1.10: Structural mutations of vinculin

The native full length vinculin protein (vinFL; resembles endogenous vinculin) undergoes a conformational switch upon incorporation into adhesion sites. Mutations (red) in the tail domain can render the protein constitutively active (vinT12), while a point mutation in the D1 head domain can result in a constitutively inactive (vinA50I) conformation. Truncation of the tail (vin880) leads to an active conformation but abolishes the ability of vinculin to bind to the actin cytoskeleton (D1 to D5 denote the vinculin domains).

1.3 Objectives of this PhD work

Optical tweezers use light forces to manipulate small objects in the nano- and micrometer regime and offer non-invasive access to forces on the pN scale. This force range is ideally suited to study the force transmission at individual cell-substrate adhesion sites during their early formation phase (< 300 seconds).

At the outset of this work stood the idea to establish a multiple trap optical tweezers setup in our lab and to apply this device for the investigation of live-cell force development. The task was to design a custom-build microscope based on a solid-state infrared laser system and an orthogonal acousto-optical deflector combination and to adapt it for live-cell imaging requirements.

Upon completion of the experimental setup, the investigation of integrin-mediated cell-substrate adhesion development was started. Optical tweezers force spectroscopy applies integrin ligand-functionalized microscopic beads as interface to the cells. These beads mimic new adhesion sites and allow for the observation of adhesion formation right from their initiation. Of particular interest is the process of adhesion formation with regard to parameters such as adhesion size, integrin ligand density, cell type, and adhesion location. With the multiple trap optical tweezers setup, it is feasible to study the time-resolved force development of several adhesion sites within one cell simultaneously. Hence, the work aims at a force mapping across the cell surface to determine the location of strongest force development.

Another issue of investigation is the correlation of cellular forces, retrograde actin flow and cell motility. A cell-type comprehensive study is conducted to determine this relation in fibroblast like cells (primary chicken fibroblasts, B16 mouse melanoma cells, and mouse embryo fibroblasts).

Of special interest is the contribution of specific adhesion-related proteins to force development and mechanosensing at cell adhesion sites. Vinculin is currently discussed as a key regulator of adhesion turnover and stabilization and one aim of this PhD work is to determine its influence on early adhesion formation. Therefore, a mouse embryonic fibroblast wild type line (MEF WT) is compared to a vinculin-deficient cell line (MEF $\text{vin}^{(-/-)}$). To address the question of the role of specific vinculin domains in vinculin recruitment and force mediation, various vinculin mutants are introduced into MEF $\text{vin}^{(-/-)}$ cells to study the force development in the initial contact formation.

All these might help to understand the mechanosensing and mechanotransduction process and the concomitant cellular response to external stimuli.

2 METHODS AND MATERIALS

2.1 Multiple Trap Optical Tweezers Setup

To measure the forces cells transmit at individual adhesion sites to the extracellular matrix (ECM), an optical tweezers (OT) setup featuring multiple trap operation was established.

The experimental setup was designed in cooperation with the group of Prof. Dr. Clemens Bechinger at the 2nd Institute of Physics of the University of Stuttgart.

A diode pumped solid state laser operating at 1064 nm with a maximum output power of 2W (Compass 1064, Coherent) was the source of the optical traps (figure 2.1). The infrared laser light was passed through a beam expander and was coupled into a custom-built microscope featuring a Plan-Neofluar 63x/1.2 water immersion objective for trap focusing and a Plan-Apochromat 63x/1.2 oil immersion objective for imaging (both from Carl Zeiss). For video rate image acquisition the microscope was equipped with two cameras: brightfield images were recorded with a frame grabber (Falcon/Eagle, IDS) connected to a CCD camera (Hamamatsu), allowing to adapt the video capture rate from 0.5 to 30 frames per second. Image acquisition in the fluorescence channel was performed with a SPOT Insight digital camera (SPOT Imaging Solutions) with the SPOT Advanced imaging

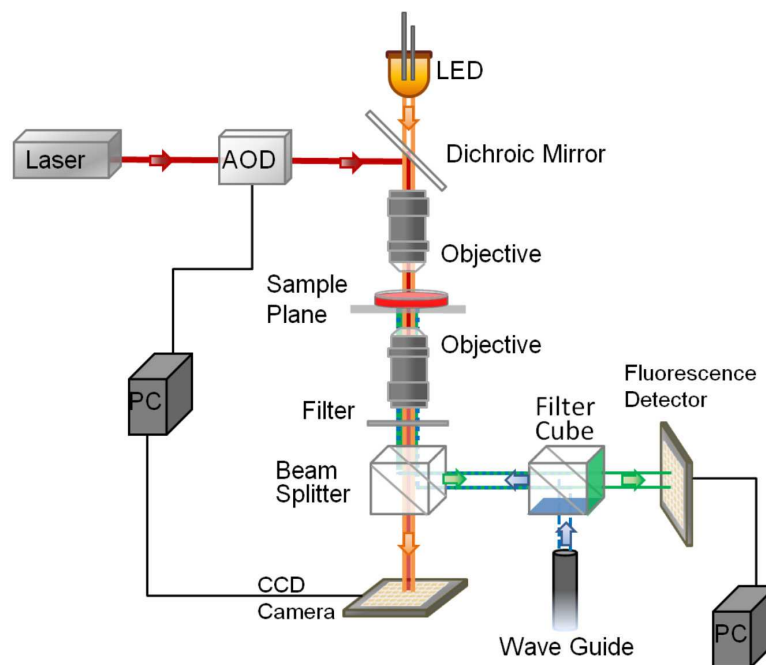


Fig. 2.1: Optical tweezers setup

Infrared laser light is expanded to fill the entrance aperture of the acousto-optic deflectors, which are used to scan the beam rapidly through the sample plane. This allows to operate multiple, quasi-static optical traps. The laser light is coupled into the microscope via telescope optics to maintain collimation and is adjusted to slightly overfill the back aperture of the focusing objective. The setup is equipped with epifluorescence optics and fluorescence illumination. For live cell imaging, a temperature control is inserted to sustain samples at 37°C.

software (SPOT Imaging Solutions). The cameras were mounted to the lower microscope port with a polarizing beam splitter (Laser 2000) dividing the signal to both cameras. Infrared filters were inserted in front of both cameras to protect the optical sensors. The optical tweezers setup featured epifluorescence optics with a GFP excitation/emission optical filter system (AHF Analysentechnik) and a HXP 120 W metal halide light source (Carl Zeiss) for fluorescence illumination. Light from the fluorescence illumination source was coupled into the lower microscope port via a wave guide, while brightfield illumination was aligned through the upper microscope port with a white LED serving as light source (figure 2.1).

To allow for multiple trap operation, acousto-optic deflectors (AODs) with a scan angle of $49 \times 49 \text{ mrad}^2$ (aaOptoelectronics) were inserted into the laser beam path and the laser light was expanded to fill the AOD entrance aperture. Leaving the AODs, the light passed through a telescope for collimation and was coupled into the microscope. The laser light was then directed to the focusing objective where it slightly overfilled the back aperture and was focused into the sample. A control unit (AOD beam steering controller, Aresis) allowed to scan the beam rapidly through the sample plane and provided the user interface Tweez to operate the desired number of quasi-static optical traps.

The sample holder of the setup featured a heating unit to sustain samples at 37° , which enabled cell force spectroscopy measurements over an extended period of time.

2.1.1 Multiple Trap Operation with Acousto-Optic Deflectors

The following paragraph focuses on time-shared multiple optical traps, which are generated by the implementation of acousto-optic deflectors (AODs) into the optical path. Acousto-optic deflectors are optically transparent crystals (here made of TeO_2) that are mounted onto a piezo element. The piezo element allows to transmit acoustic waves into the crystal, which cause density modulations within the crystal material. These density modulations constitute a phase grid (Bragg grid) for the incident laser beam if it enters under the Bragg angle α_B . A laser beam passing through the deflector is split into a component that is transmitted linearly without deflection (0. order) and a component that is deflected by $2\alpha_B$ from the straight pathway (1. order) if the center frequency f_0 is applied to the AOD (figure 2.2). The acoustic frequency applied to the crystal defines the Bragg angle, which is given by

$$\alpha_B = \frac{\lambda f}{2v} \quad (2.1)$$

where λ is the laser wavelength inside the crystal, v is the velocity of acoustic wave propagation in the crystal and f is the acoustic frequency applied to the crystal. Crystals are aligned under Bragg angle for the incident laser light when the center frequency f_0 is applied ($f_0 = 85 \text{ MHz}$). The deflection of the 1. order beam can be manipulated by changing the acoustic frequency to $f = f_0 \pm \Delta f$, which results in a beam deflection of $2\alpha_B \pm \Delta\varphi$ where $\Delta\varphi$ accounts for the additional deflection and is given by the relation

$$\Delta\varphi = \lambda \frac{\Delta f}{v} \quad (2.2)$$

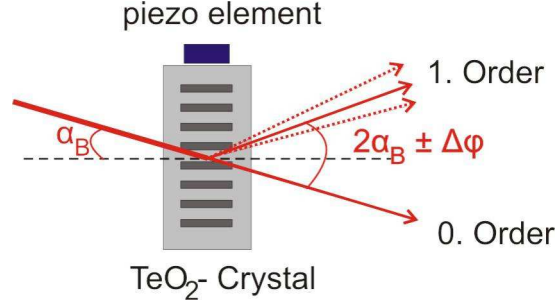


Fig. 2.2: Operation principle of acousto-optic deflectors

The acousto-optic deflectors (AODs) are operated by acoustic waves applied to the crystals via a piezo element. Light incident under Bragg angle passes straight through the crystal (0. order beam). The transmitted 1. order beam is deflected by the angle $2\alpha_B$ from the 0. order beam when the center frequency f_0 is applied. A modification of the applied acoustic frequency to $f = f_0 \pm \Delta f$ changes the deflection of the 1. order beam by the angle $\Delta\phi$. The intensity of the beam is modulated by applying acoustic waves with distinct amplitudes.

where Δf denotes the frequency shift, λ the wavelength of the incident laser light ($\lambda = 1064\text{nm}$) and v denotes the velocity of the acoustic waves inside the crystal ($v = 650\text{m/s}$). Increasing frequency shifts directly results in enlarged deflection angles $\Delta\phi$ of the output light, but reduces the diffraction efficiency. Acceptable losses were obtained for a frequency range of $85 \pm 15\text{MHz}$.

The AODs scan the laser beam through the sample plane and allow to generate a large number of traps from a single incident laser beam. In this case the beam is time-shared between the number of traps by scanning rapidly from one trap position to the next within an accessible area of $\approx 150 \times 150 \mu\text{m}^2$. The limit for this approach is the time scale of diffusion of the particles confined to the traps: as long as the repetition rate of the laser light is far above the diffusion time scale, the particles experience a quasi-static illumination and thus quasi-static restoring forces. The trap stiffness of an individual trap κ_i depends on the number of active traps N and the overall trap stiffness κ_{all} , which is defined by the applied laser power: $\kappa_i = \kappa_{all}/N$. Due to the fast scan rate of the AODs up to 100 traps can be generated simultaneously and each trap can be assigned with a distinct laser power and can be moved individually through the scan area.

For multi trap operation the reaction time of the AOD to the applied acoustic frequencies has to be considered: acoustic waves require a certain time to decline within the crystals and during this reaction time no new frequency can be applied as this would result in signal superpositions. Because of this, the scan rate of the AODs was set to a fixed value of 100kHz (instead of the maximum possible scan frequency of about 150Hz) for all operations to prevent the appearance of "ghost images" or artifacts of optical traps.

AOD Alignment and Calibration

Mounting a set of AODs orthogonally, laser beam steering through the transverse focal plane became feasible. In this system, four output beams were produced with the (1 1) order beam experiencing a deflection in the transverse plane according to the frequency set applied to the crystals.

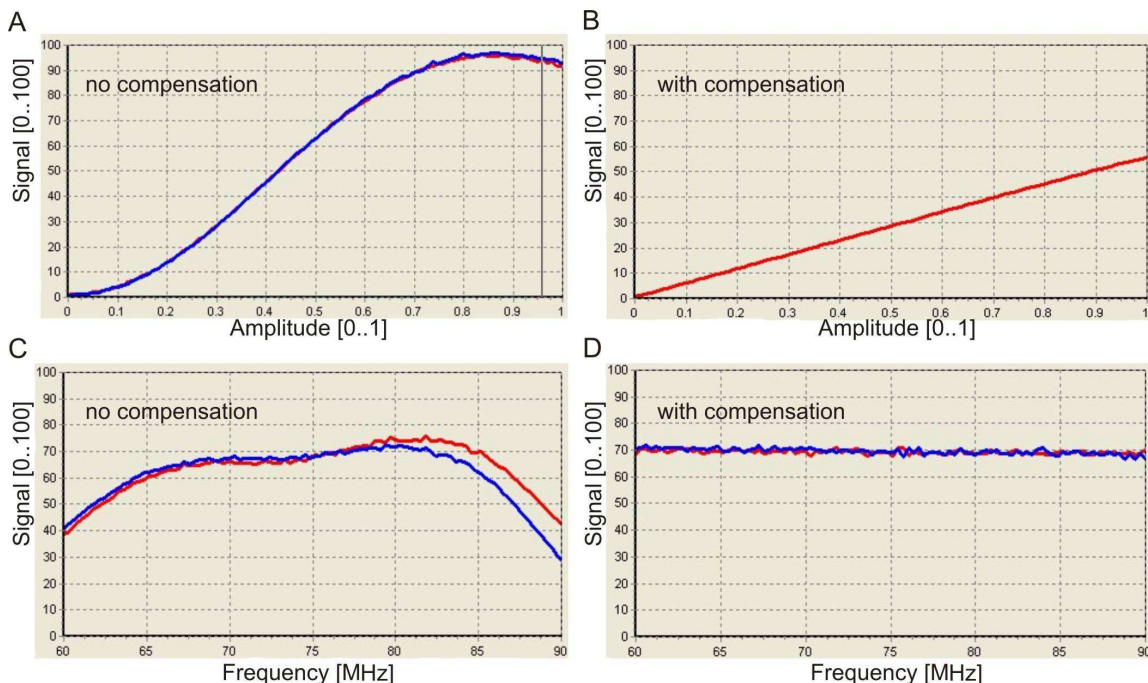


Fig. 2.3: AOD calibration

Screenshots from the AOD calibration toolbar Tweez: Amplitude scan of the crossed AODs with (A) displaying the uncompensated scan and (B) the result after compensation. Horizontal/vertical (H/V) scan of the crossed AODs with (C) displaying the uncompensated scan and (D) the result after compensation (red: horizontal scan, blue: vertical scan).

Each frequency set corresponded to a discrete position in the sample plane and was controlled by the beam steering unit via the user interface of the software Tweez (Aresis). A photo diode was used to control the intensity output of the (1 1) order beam and to adjust the AOD position according to maximum yield. Due to optical nonlinearities of the crystal material, the AOD transmission was not rising linearly with increasing acoustic power but showed the characteristic behavior displayed in figure 2.3 A). To compensate for the nonlinearities, an intensity correction was calculated with the software Tweez and led to the improved intensity profile shown in figure 2.3 B).

Horizontal and vertical scanning (H/V scan) of the beam through the sample plane resulted a deflection-dependent intensity profile (figure 2.3 C)). A compensation of scan angle-dependent losses was calculated with the field flattening tool of the software and was applied to the AODs (figure 2.3 D)).

2.1.2 Force and Trap Stiffness Calibration

For the application of optical tweezers in force spectroscopy, the trap stiffness and the restoring force of the optical traps have to be calibrated empirically (reviewed in [Neuman & Block 2004, Oddershede *et al.* 2001]). Here, the drag force method was combined with optical potential analysis to derive the maximum restoring trap force and the trap stiffness, respectively.

Drag Force Method

With the drag force calibration described in section 1.1.2 the escape force required to free a trapped bead from the optical potential well was determined. For calibration with this method, a bead was trapped and moved with increasing velocity through the sample plane.

The displacement of the confined bead from the trap center in response to the viscous forces of the solvent was recorded with a CCD camera at video rate. Upon trap movement, the bead followed the trap with a particular retardation as long as the viscous resistance of the solvent was lower than the maximum trap force. The trap velocity was increased until the viscous forces exceeded the trap force and the bead escaped from the trap: The drag force F_{drag} on the bead then equaled the escape force F_{escape} and was derived from Stoke's Law

$$F_{drag} = F_{escape} = 6\pi\eta r_b v_{escape} \quad (2.3)$$

where η is the fluid viscosity, r_b is the radius of the trapped bead and v_{escape} is the trap velocity that completely removed the bead from the optical trap.

The maximum trap force equals the escape force and was calculated from the recorded escape velocities, which were in the order of $v_e = 0.13 \text{ m/s}$. For measurements at 37°C the fluid viscosity amounted approximately $\eta = 0.0007 \text{ N s/m}^2$. This resulted in maximum trap forces of $190 \pm 20 \text{ pN}$ for beads of $4.5 \mu\text{m}$ diameter and $120 \pm 15 \text{ pN}$ for beads of $3.0 \mu\text{m}$ diameter, respectively.

Optical Potential Analysis

In thermal equilibrium, a microscopic bead in solution undergoes random movement, called Brownian motion (chapter 1.1.1). For a bead confined within an optical trap the Brownian motion is limited to the width of the optical potential. The thermal position fluctuations of a bead within a trap can be evaluated to determine the shape of the optical potential and subsequently its trap stiffness (section 1.1.2).

The Brownian motion induced position fluctuations of a bead confined to the potential well of an optical trap are described by a Boltzmann distribution with

$$p(x) = C \exp\left(\frac{-U(x)}{k_B T}\right) \quad (2.4)$$

where $U(x)$ is the optical potential, C is a constant, k_B is the Boltzmann constant and T is the absolute temperature in Kelvin. Thus, the potential can be derived from a recording of the position

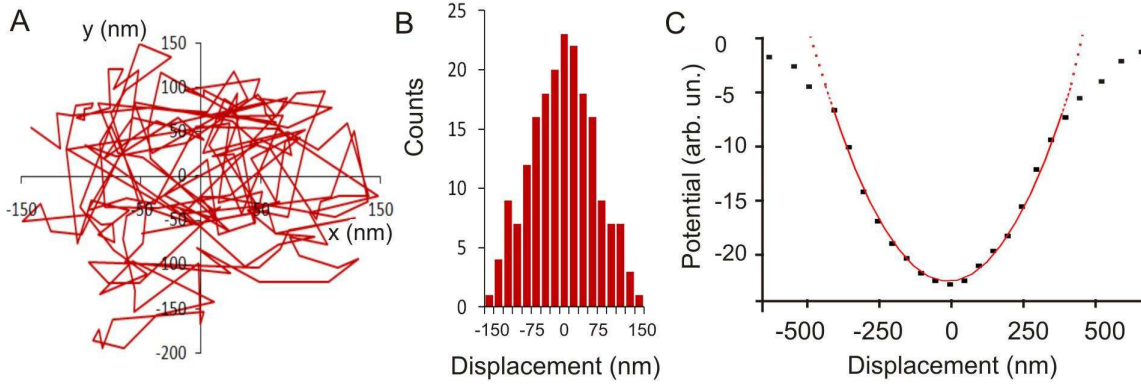


Fig. 2.4: Trap calibration via thermal fluctuations

A) Thermal fluctuations of a bead confined inside a laser trap of 100mW power. B) Position histogram of a $4.5\ \mu\text{m}$ bead in a 100mW optical trap. C) The central area of the optical potential resembles a harmonic potential and is fitted with a parabolic function.

histogram of a trapped bead via the relation

$$U(x) = -\frac{k_B T}{C} \ln(p(x)) . \quad (2.5)$$

A microscopic bead was captured in an optical trap and trap stiffness calibration was performed in single and multiple trap mode to account for possible losses in the quasi static operation mode. The bead position fluctuations were recorded with a CCD camera at an acquisition rate of 30Hz . High resolution position evaluation was performed with image processing techniques: The recorded frames were processed with ImageJ (NIH) and the Metamorph (Visitron) particle detection and tracking algorithms were applied to obtain the bead coordinates in each frame. All bead positions were evaluated with respect to the trap center.

Figure 2.4 A) displays the movement of a trapped $4.5\ \mu\text{m}$ bead in the transverse plane. The optical trap was assigned with a laser power of 100mW in the sample plane and was kept stationary during bead position recording. The bead position histogram (figure 2.4 B)) was derived and from this the shape of the potential well (figure 2.4 C)) was delineated with Matlab (Mathworks). The central area of the potential well resembled a harmonic potential and thus a parabolic fit was applied to this area to determine the trap stiffness κ via the relation

$$U(x) = -\frac{1}{2} \kappa x^2 \quad (2.6)$$

where x is the displacement of the bead from the equilibrium position in the trap center. Consequently, a linear dependence exists between bead displacement and the restoring force experienced by this bead:

$$F(x) = -\nabla U(x) = \kappa x \quad (2.7)$$

For OT force spectroscopy, beads with a diameter of $4.5\ \mu\text{m}$ and $3.0\ \mu\text{m}$ were administered to cell samples kept at 37°C in serum containing medium. The trap stiffness was derived under live

cell imaging conditions with the described approach and amounted to $\kappa = 0.16 \pm 0.02 pN/nm$ for $4.5 \mu m$ diameter beads and to $\kappa = 0.10 \pm 0.01 pN/nm$ for $3.0 \mu m$ diameter beads for the maximum applicable power of $200 mW$. For a stepwise reduction of the applied laser power, a linear decrease in trap stiffness was obtained.

2.2 Bead Functionalization

To mimic new contact sites on the apical cell membrane, microscopic beads were functionalized with the integrin ligand fibronectin (FN), which is a constituent of the extracellular matrix. The FN molecule contains an RGD sequence, which is a well known adhesion motif for a variety of integrin types (chapter 1.2). A cyclic peptide comprising the RGD adhesion motif was chosen as second functionalization agent to compare the cellular response to the two distinct ligands.

2.2.1 Passive Adsorption

Carboxylated polystyrene beads of $3.0 \mu m$ and $4.5 \mu m$ diameter (Polysciences) were homogeneously functionalized either with the extracellular matrix protein FN (human plasma fibronectin, $1 mg/ml$) or with the cyclic RGD peptide c(RGDfk)-(Ahx)₃-N₃ ($1 mg/ml$). Beads were washed 3 times with phosphate buffered saline (PBS) and approximately 10^{12} beads were incubated with $100 \mu l$ poly-l-lysine (PLL, $200 \mu g/ml$) in PBS for 1h at room temperature and with gentle mixing. The solution was centrifuged and resuspended 3 times with PBS to remove residues of unbound PLL. FN and cRGDfk solutions with distinct ligand concentrations were prepared: Varying amounts of FN ($1 \mu l$, $2 \mu l$, $3 \mu l$) or cRGDfk ($2 \mu l$, $4 \mu l$, $5 \mu l$, $8 \mu l$) were added into $100 \mu l$ PBS to obtain distinct coating densities on the bead surface. Subsequently, beads were incubated with the ligand solution with gentle mixing for another hour at room temperature. A surface coverage of 50 %, 80 % and 100 % was prepared for both ligands, FN and cRGDfk, and an additional batch with 150 % coverage was prepared with the cyclic peptide. The functionalized beads were centrifuged 3 times with PBS to remove residual ligands and were finally stored in 1x PBS at $4^\circ C$. Beads were always freshly prepared one day prior to the experiments.

2.2.2 Covalent Coupling

A second method for surface functionalization was employed to test whether a stronger chemical link between ligand and bead leads to different cellular responses. Therefore, the carboxylic groups on the bead surface were activated and covalently crosslinked with free amino groups of the FN macromolecule.

Surface activation: The functional carboxyl groups on the bead surface were activated with EDC (1-Ethyl-3-(3-dimethylaminopropyl)carbodiimid) and sulfo-NHS (N-Hydroxysuccinimid). Approximately 10^{12} beads were diluted with HEPES buffer (4-(2-hydroxyethyl)-1-piperazineethanesulfonic acid) and were mixed with $100 \mu l$ EDC ($40 \mu M$) and $100 \mu l$ sulfo-NHS

(36 μM). The solution was incubated with gentle mixing for 30 min at room temperature and was centrifuged and resuspended twice in 100 μl HEPES buffer (20 mM, pH 9.0).

Coupling of FN: 2 μl FN (2 μM) were diluted in 100 μl PBS and were added to the activated carboxyl beads and incubated for 3 h at room temperature. The functionalized beads were centrifuged and resuspended twice in 100 μl HEPES buffer and stored at 4°C.

The success of the two functionalization approaches, passive and covalent coupling, was checked by fluorescence microscopy. FN-coated beads were immunostained (section 2.6) and fluorescence images were recorded with an Apotome Imager.Z1 (Carl Zeiss) and evaluated with regard to the fluorescence intensity. With this quantification, the samples of the different functionalization methods were indistinguishable and displayed a high degree of homogeneity.

2.2.3 Ligand Density Quantification

After incubation with the ligands cRGDfk or FN, the supernatant from the first centrifugation step was saved for surface density analysis. The amount of ligand attached to the beads was determined spectrophotometrically with UV-VIS spectroscopy (NanoDrop1000, PEQLAB Biotechnologie GmbH).

Optical density measurements were performed at a wavelength of 260 nm on the supernatant of the bead-ligand solution and yielded the concentration of residual ligand c_{residue} . The number of ligands N in the supernatant was derived via the relation $N_{\text{residue}} = c_{\text{residue}} V N_A$ where V is the volume of the solution and N_A is the Avogadro constant. From the amount of substance of initially deployed ligands in the prepared functionalization solution, the total number of deployed ligand molecules N_{ini} was estimated. The number of ligands attached to the surface of a single bead N_b was determined from

$$N_b = \frac{N_{\text{ini}} - N_{\text{residue}}}{n_b} \quad (2.8)$$

where n_b is the number of beads.

To estimate the degree of surface coverage, the size of FN, determined in scanning electron microscopy approaches [Rohde *et al.* 1980, Engel *et al.* 1981], was taken as a measure. The length of a 450 kDa fibronectin molecule was determined as 61 nm and the width as 2 nm [Engel *et al.* 1981], which results in an area of approximately 120 nm² covered by a single molecule. For the 1 kDa cRGDfk peptide, a surface coverage of about 0.24 nm² per molecule was assumed from the ratio of FN to cRGDfk molecular weights. With this approach the appropriate ligand quantity was chosen for the desired surface coverage.

2.3 Cell Culture

In the presented study three cell lines from different organisms plus one vinculin knockout cell line were investigated. All cell lines were maintained in cell culture flasks (greiner bio-one) containing

nutrient media and were kept under humidified atmosphere in an incubator at 37° C with a CO₂ level of 5 % .

2.3.1 Cell Lines

B16 mouse melanoma cells (B16), mouse embryonic fibroblasts (MEF) and primary chicken fibroblasts (PCF) were studied in experiments concerning force development, cell migration and retrograde transport behavior.

B16 cells are malignant murine skin melanoma cells which originated in C57BL/6 mice and produce melanin [Fidler & Kripke 1977]. The cell line in this study is a subclone B16-F1 line (ATCC, CRL-6323) that was derived from pulmonary metastasis in C57BL/6 mice. The subclones originate from the pulmonary injection of clones from the B16-F0 parent cell line and have a low potential to form metastasis [Fidler 1973, Irimura *et al.* 1981, Nakamura *et al.* 2002]. B16 cells are often used as model for malignant human melanoma as they show a similar metastasis process as human cancer cells [Fidler & Kripke 1977].

The cell line was maintained in high glucose Dulbeccos's modified Eagle Medium (DMEM) supplied with 10 % fetal calf serum (FCS).

MEF cells: Two types of mouse embryonic fibroblast were provided by W. Ziegler (Interdisziplinäres Zentrum für Klinische Forschung (IZKF), Leipzig, Germany): a wild type cell line (MEF WT) and a vinculin deficient line (MEF $\text{vin}^{(-/-)}$). MEF cells were obtained from embryos at embryonic day 9. Inactivation of vinculin was achieved by homologous recombination in embryonic stem cells, which were then introduced into mice to gain fertile heterozygous individuals. No living homozygous $\text{vinculin}^{-/-}$ embryos were delivered and between embryonic stage E8 and E10 those embryos did not show a fusion of the midline in the rostral neural tube and developed a deficiency in cranial and spinal nerve evolution. Furthermore, the heart development was strongly impaired in this stage. Cultured MEF $\text{vin}^{(-/-)}$ cells were found to have a reduced binding strength to the integrin ligands fibronectin, vitronectin, laminin and collagen [Xu *et al.* 1998a].

In this study, MEF WT and MEF $\text{vin}^{(-/-)}$ cells were maintained under routine culture conditions in DMEM containing 10 % FCS until passage 25.

Primary chicken fibroblasts were derived from eggs of "white leghorn" hens that were incubated at 37° C and 60% humidity with slow rotation. PCFs were isolated from day 8 chicken embryos that were transferred into 4° C Hanks medium to carefully detach the skin from the spine. After rinsing, the skin pieces were added into a Petri dish containing F-12 medium supplied with 10 % FCS and 2 % chicken serum (CS) and fibroblasts started to grow out from the tissue within one week. The cells were harvested and transferred into cell culture flasks to be maintained under routine conditions [Klein 2009, Autenrieth 2008].

2.3.2 Cell Culture Routine

Cell lines were maintained in cell culture flasks at 37° C and 5 % CO₂ with passaging 3 times per week. For passaging, the culture medium was removed and cells were washed twice with 5 ml PBS. To disable cell-substrate adhesion, 150 μ l trypsin/EDTA diluted in HBSS were added and the flask was placed for 3 to 4 minutes into the incubator. The detached cells were collected into 5 ml culture medium and were centrifuged for 5 minutes at 21° C and 1000 rpm. The supernatant was removed and the cell pellet was resuspended in fresh 37° C culture medium. According to the splitting ratio in table 2.1 the cell suspension was distributed into new culture flasks prepared with 5 ml culture medium at 37° C and was stored in the incubator.

Tab. 2.1: Cell types, culture conditions and sources (HBSS: Hank's balanced salt solution)

Cell type	Culture medium	Trypsin/EDTA in HBSS	Splitting	Provided by
MEF wt	DMEM + 10 % FCS	1:5	1:20	W. Ziegler, IZKF Leipzig
MEF ^{vin-/-}	DMEM + 10 % FCS	1:10	1:20	W. Ziegler, IZKF Leipzig
B16	DMEM + 10 % FCS	1:10	1:10	B. Imhof, CMU Genf
PCF	F12 + 10 % FCS + 5 % CS	1:5	1:20	T. Authenriet, KIT Karlsruhe

2.3.3 Cell Counting

For cell migration, force spectroscopy and retrograde transport studies an optimal cell density in the sample dish was required. To standardize the number of cells transferred into the sample dishes, cells were counted with a haemocytometer. A small volume of cell suspension was loaded into the haemocytometer chamber engraved with a grid structure and cells within a certain grid area were counted. Here, an improved Neubauer haemocytometer (Brand) was used and an area of 1 mm^2 , corresponding to 100 nl suspension, was evaluated. The cell number from four squares was averaged and multiplied with 10^4 to obtain the cell count in 1 ml solution.

The average cell number for MEF cells in 25 cm^2 and 75 cm^2 cell culture flask with 95 % confluency amounted to approximately 5 milion and 15 milion cells, respectively.

For force spectroscopy and retrograde transport measurements approximately 10^3 cells were added into the sample dish to obtain the low cell density required for single cell experiments.

2.3.4 Sample Preparation

As growth substrate for the cells, FN-functionalized glass surfaces were used. The glass inlet of a glass bottom Petri dish (Mattek Inc.) was covered with a solution of 50 μ l poly-l-lysine (200 μ g/ml) in PBS and incubated for 1h at room temperature. After rinsing the dishes twice with PBS, 0.5 μ l FN (1 mg/ml) diluted in 50 μ l PBS were added and dishes were incubated for 1 h at room temper-

ature. Residual FN was removed by rinsing twice with PBS and the culture dishes were stored at 4°C covered with PBS until further use.

2.4 Cell Transfection by Electroporation

MEF WT and MEF *vin*^(-/-) cells were transfected with plasmid DNA encoding for a full length vinculin-GFP fusion protein (vinFL) and a variety of vinculin mutants, all tagged with GFP at the N-terminus. The following proteins were expressed by the cells after transfection (for details on the introduced mutations refer to section 1.2.6):

vinFL	wild type resembling full length vinculin
vinT12	constitutively active: no binding between head and tail domain
vinA50I	constitutively autoinhibited: replacement of alanin by isoleucine at amino acid # 50
vin880	tail domain truncated: no binding sites for F-actin, paxillin, and PIP ₂

2.4.1 Optimized Electroporation Protocol

Cells were grown in cell culture flasks of 25 cm² or 75 cm² with standard culture medium and were harvested at a confluence of about 95 %, which corresponds to approximately 5 and 15 mio cells per flask, respectively. The cells were counted with a Neubauer haemocytometer to standardize cell density and to calculate and optimize the survival rate after electroporation.

Optimal transfection results were obtained with the following protocol:

Flasks chosen for harvesting were washed twice with PBS and 150 or 450 μ l trypsin/EDTA in HBSS were added depending on the flask size. After 3 min of incubation, cells were transferred into 3 ml and 9.5 ml of 4°C cold electroporation buffer, respectively (E-buffer; 120 mM KCl, 10 mM K₂PO₄/KH₂PO₄, 2 mM MgCl₂, 25 mM HEPES, 0.5 % Ficoll 400; pH7.6) and were centrifuged for 5 min with 1000 rpm. Cells were resuspended in 250 μ l E-buffer and were transferred into a 4 mm electroporation cuvette (Gene Pulser cuvette, Bio-Rad) prepared with plasmid DNA (respective quantities for the plasmids are denoted in table 2.2). Plasmid DNA and cells were mixed and the cuvette was incubated on ice for 2 minutes before it was inserted into the electroporator (Gene Pulser Xcell, Bio-Rad) and subjected to an electrical pulse of 250 V and 60 ms duration. Subsequently, the cuvette was incubated on ice for another 2 minutes and the cell suspension was diluted with 200 μ l DMEM plus 10 % FCS.

Depending on the type of experiment, cells were partially transferred onto functionalized coverslips or into glass bottom dishes and incubated for 16 to 20 h to express the vinculin proteins. To determine the survival rate after transfection, electroporated cells were seeded into a cell culture flask and incubated for 2 h to adhere. Cells were washed and trypsinized according to the standard protocol and were counted with a Neubauer haemocytometer. From this, a survival rate of 15 % was estimated.

Tab. 2.2: Optimized conditions for plasmid transfection with vinculin encoding vectors (in pEGFP-C2 vectors (Clonetech)) and GFP encoding vectors.

Plasmid	Confluency	Plasmid DNA [μg] per 25 cm ² flask
vinFL-GFP	> 90 %	1.7
vinT12-GFP	> 95 %	1.0
vinA50I-GFP	> 90 %	2.5
vin880-GFP	> 90 %	2.5
GFP	> 90 %	0.5

2.4.2 Plasmid DNA Amplification

Bacterial Culture Preparations

LB medium (Luria-Bertani medium after Miller) was produced by adding 5 g bacto tryptone, 2.5 g bacto yeast extract and 5 g NaCl into 500 ml deionized water. The pH value was adjusted to 7.5 with NaOH and the solution was autoclaved and stored at 4°C.

To obtain LB agar plates, 500 ml LB medium were mixed with 7.5 g bacto-agar and sterilized by autoclaving. The solution was cooled to 40 to 50°C and kanamycin (50 mg/ml) was added to a final concentration of 50 $\mu\text{g}/\text{ml}$. The solution was poured into sterilized petri dishes and stored at 4°C until further use.

Bacterial Transformation

Competent *Escherichia coli* (E.coli) were thawed on ice for 10 minutes. 30 μl of the bacteria culture were mixed with 0.5 μl plasmid DNA and incubated on ice for 20 minutes. E.coli were heat shocked at 42°C for 30-45 seconds to trigger the uptake of the DNA and placed on ice for 5 minutes. To the bacteria-plasmid solution 200 μl LB medium were added and the solution was incubated for 1 h at 37°C. The bacteria culture was plated on LB agar plates containing the antibiotic kanamycin and incubated overnight at 37°C. A single colony was picked from the plate, transferred into 3 ml of LB medium containing 0.1 % kanamycin and incubated at 37°C overnight with thorough mixing. For high yield amplification, the bacterial culture was mixed into 250 ml LB medium containing 0.1 % kanamycin, stored at 4°C for 10 h and incubated overnight at 37°C with thorough mixing.

Plasmid DNA Purification

The overnight LB culture was harvested by centrifugation (4°C, 4000 rpm, 30 min) and removal of the supernatant. A bacterial lysate was produced and plasmid DNA was extracted by precipitation according to the "QIAGEN EndoFree Plasmid Maxi Kit" protocol. The extracted plasmid DNA was air-dried and redissolved in 200 - 300 μl storage buffer containing 10 mM Tris-Cl and 1 mM EDTA at pH 8.0.

Plasmid DNA Yield Quantification

The amount of plasmid DNA produced by amplification was determined from optical density measurements at 260 nm with a UV-VIS spectrometer (NanoDrop). Usually, plasmid DNA concentrations of 2 - 3 $\mu\text{g/ml}$ were obtained, corresponding to an overall yield of 400 to 600 μg DNA. The plasmid DNA was diluted to a concentration of 1 mg/ml and was stored at -20°C .

2.5 Fluorescence Assisted Cell Sorting

Fluorescence assisted cell sorting (FACS) is a technique to sort fluorescently labeled or transfected cells according to their fluorescence characteristics. For FACS analysis, cells are introduced into a buffer stream through the sorting unit. This stream passes as droplets through the focus of a laser that is surrounded by detectors measuring forward scattering (FCS), side scattering (SSC) and fluorescence (e.g GFP/FITC) intensities of the sample. SSC is related to the granularity of the sample and is used in combination with the FCS signal, relating to the cell size, to sort a live, single cell population from debris and clusters. Sorting according to the fluorescence signal allows to separate autofluorescent cells from fluorescently labeled cells. In general, the sorting is achieved by tagging each droplet passing through the laser focus with a positive or negative charge.

FACS was performed with a FACScan Flow Cytometer (Becton-Dickinson) with the kind support of Dr. Wilko Thiele and Diana Plaumann-Ziegler at the Institute for Toxicology and Genetics (ITG) at KIT campus north.

2.5.1 FACS Sample Preparation

Cell sorting was performed with MEF $\text{vin}^{(-/-)}$ cells transfected to express vinculin-GFP proteins. To calibrate the flow cytometer, two control groups were produced: MEF $\text{vin}^{(-/-)}$ cells expressing GFP and MEF $\text{vin}^{(-/-)}$ cells electroporated without plasmid DNA.

Cells were transfected according to the standard protocol described in chapter 2.4.1 and were incubated for 6 h to express the distinct proteins. Culture flasks were washed with PBS and cells were detached with trypsin/EDTA and suspended in 1 ml PBS+/+ (PBS containing Mg^{2+} and Ca^{2+}). Afterward the cell suspension was centrifuged and resuspended with a density of 10^6 cells per 250 μl in PBS+/+ supplied with 10 % FCS. Until FACS analysis cells were stored on ice.

2.5.2 Sorting Procedure

The flow cytometer was calibrated with empty electroporated cells for autofluorescence using PBS as flow sheet. Subsequently, cells expressing GFP only were inserted to calibrate the fluorescence channel. The actual sorting was performed with cells expressing the various vinculin proteins. On average, the sorts yielded about 500,000 positive cells with a purity of 97 %.

The sampled cells were centrifuged and resuspended in DMEM containing 10 % FCS and 1 % penicilin/streptadivin before transferring them into FN functionalized glass bottom dishes.

2.6 Immunohistochemistry and Staining

Cells were seeded onto FN functionalized glass coverslips and incubated for 2 h. The coverslips were rinsed with 1x PBS to remove residual culture medium and the cells were fixated with 4 % paraformaldehyde (PFA) in PBS for 10 minutes. This was followed by 3 rinsing steps (each for 5 minutes) with 1x PBS containing 0.1 % Triton X-100 to permeabilize the cell membrane for the staining reagents. The samples were transferred onto a hydrophobically covered glass plate and were maintained under humidified atmosphere during the staining procedure. Primary antibodies were selected and diluted in PbS supplied with 1 % bovine serum albumin (BSA) according to the instructions in table 2.3. The sample was either incubated for 1 h at room temperature or over night at 4 °C. Cells were rinsed 3 times for 5 minutes with 1x PBS containing 0.1 % Triton X-100 and were supplied with fluorophor conjugated secondary antibodies to incubate for 1 h at room temperature or over night at 4 °C.

For actin staining, the F-actin binding toxin phalloidin, labeled with a fluorophor, was added together with the secondary antibodies.

To stain the nucleus, DAPI, a molecule forming fluorescent complexes with specific areas of the DNA, was mixed to the secondary antibody solution.

After staining, samples were rinsed 3 more times and were embedded into Mowiol supplied with n-propylgallat before storing them at 4 °C.

Tab. 2.3: Antibodies and dyes for fluorescent labeling (mAB: monoclonal antibodies, host species mouse; pcl: polyclonal antibody, host species rabbit)

ANTIGEN	TYPE/DYE	DILUTION	COMPANY
Primary Antibodies			
Fibronectin	mAB IgG	1:500	BD Biosciences
Fibronectin	pcl IgG	1:400	Sigma Aldrich
Paxillin	mAB IgG	1:500	BD Biosciences
Vinculin	mAB IgG	1:50	Sigma Aldrich
Secondary Antibodies			
Mouse IgG	Alexa488	1:200	Invitrogen
Mouse IgG	Cy3	1:200	Dianova
Mouse IgG	Cy5	1:200	Dianova
Rabbit IgG	Alexa488	1:200	Molecular Probes
Rabbit IgG	Cy3	1:500	Dianova
Rabbit IgG	Cy5	1:200	Dianova
Others			
DAPI		1:1000	Sigma Aldrich
Phalloidin	Alexa488	1:200	Invitrogen
Phalloidin	Alexa543	1:200	Invitrogen

2.7 Experimental Procedures

2.7.1 Optical Tweezers Force Spectroscopy

Functionalized microscopic beads were captured in optical traps and placed on the cell surface to mimic new adhesion sites. The traction forces developed in the newly formed adhesion sites displaced the beads and these bead displacements were recorded with a CCD camera.

About 10^3 cells were seeded into FN-coated glass bottom dishes and were incubated for 2 h under standard conditions (section 2.3) to allow cells to adhere to the substrate and spread. The culture medium was exchanged for transparent CO_2 independent medium containing 20 mM HEPES half an hour prior to experiments. Approximately 10^3 FN-functionalized beads were added to the sample and left for 1 minute to settle before the optical traps were switched on. Beads were captured in the traps and positioned on the apical membrane of an individual, well spread cell (figure 2.5 A)). Over a time course of 300 seconds, bead displacements from the center of the optical traps were recorded with the CCD camera at a frame rate of 1 Hz.

The cellular traction forces displaced the beads from the trap center until a new equilibrium between restoring trap force and cellular traction was reached (figure 2.5 B)). The lateral displacement of the new equilibrium bead position from the trap center is proportional to the applied traction forces, which are approximated by Hooke's law:

$$F(t) = \kappa \Delta x(t) \quad (2.9)$$

where κ is the stiffness of the optical trap and Δx is the bead displacement. With the trap stiffness known from the previous calibration (section 2.1.2), the temporal force development was directly computed from the recorded bead displacements.

2.7.2 Retrograde Transport Assay

To characterize the dynamics of retrograde actin flow, the retrograde transport of microscopic beads was monitored (figure 2.5 C)). Cells and beads were prepared as described in section 2.7.1 and a number of beads was positioned by optical traps on the cell surface. For the retrograde transport assay, traps were switched off instantly after positioning the beads. The bead position was recorded with the CCD camera over a time course of 20 min with a frame rate of 0.5 Hz. The videos were analyzed with MetaMorph to determine the bead position in each frame and the retrograde transport velocity of the beads was calculated from the trajectory data.

2.7.3 Cell Migration Assay

Cell migration of different cell lines was characterized using time lapse microscopy (Colibri/AxioObserverZ1, Carl Zeiss). About 10^4 cells were plated on a glass bottom dish and were incubated for 2 h to allow cells to adhere and spread. The nutrient medium of the cells was exchanged for transparent F12 imaging medium containing 2 % FBS about 30 minutes prior to the

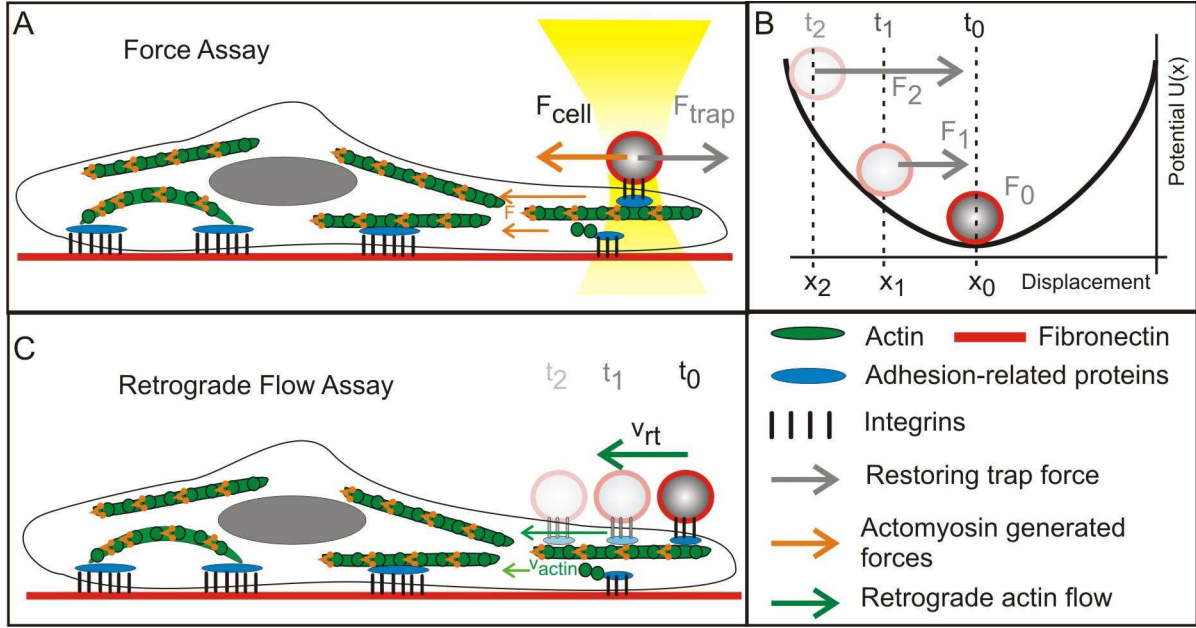


Fig. 2.5: Force Spectroscopy and Retrograde Flow Assay

FN-coated beads were added to a sample of well-spread cells on a FN-functionalized glass substrate. A) Beads were captured with optical traps and were positioned on the apical membrane of the leading edge. In the force spectroscopy assay, the optical traps restrained bead movement by applying a counterforce to the cellular traction forces. B) The cellular traction forces on the bead displace the bead from the bottom of the optical potential well. With increasing distance from the equilibrium position x_0 (restoring force $F_0 = 0$) the restoring force of the optical trap onto the bead grows linearly. C) In the retrograde flow assay, beads were positioned on the leading edge of well-spread cells and subsequently the traps were deactivated. Beads coupled to the retrograde actin flow displayed a rearward translocation toward the nucleus.

start of a measurement. A sample dish was mounted into a time lapse microscope featuring a live cell imaging chamber and cells were monitored for 12 to 16 h. Images were recorded with a 20x/08 Ph2 Plan Apochromate objective (Carl Zeiss) at a rate of one frame per minute.

2.8 Data Analysis and Quantification

2.8.1 Traction Force Quantification

For quantification of bead displacements over time, the recorded force spectroscopy videos were processed with ImageJ for contrast optimization and were further analyzed with MetaMorph. The MetaMorph object tracking algorithm was applied to determine the position coordinates of a bead in each video frame. The obtained position data were evaluated with MS Excel, where the bead trajectory $d(t)$ was derived from the recorded coordinates (x, y) by

$$d(t) = \sqrt{(x(t) - x_0)^2 + (y(t) - y_0)^2} \cdot c_m \quad (2.10)$$

where (x_0, y_0) is position of the trap center and $c_m = 0.13 \mu\text{m}/\text{pixel}$ is the microscope calibration factor for the applied objective.

The bead displacement is linked to the cellular traction force $F(t)$ applied to the beads via the following relation:

$$F(t) = d(t) \kappa . \quad (2.11)$$

2.8.2 Migration Velocity

Migration velocity and directional persistence were derived for different cell types from cell migration assays.

The recorded videos were evaluated with ImageJ using the manual tracking and chemotaxis plugin. With the manual tracking tool the center of the cell nucleus was marked in each frame and the positions were recorded. The data was loaded into the chemotaxis tool, calculating the velocity of the cell and the directional persistence of the movement by means of nucleus motility.

2.8.3 Directional Persistence

The directional persistence of retrograde transported beads was calculated from the bead position data determined with the MetaMorph object tracking algorithm.

The euclidean distance d_{euc} between the bead position in the start frame (x_s, y_s) and end frame (x_e, y_e) of the video was determined by

$$d_{euc} = \sqrt{(x_e - x_s)^2 + (y_e - y_s)^2} . \quad (2.12)$$

Additionally, the actual trajectory length d_t was calculated by summing up the distances the bead moved from one frame to the next. For a total number of n frames, the trajectory length is described by

$$d_t = \sum_{i=1}^n \sqrt{(x_{i+1} - x_i)^2 + (y_{i+1} - y_i)^2} . \quad (2.13)$$

The directional persistence P is defined as the ratio of euclidean distance divided by trajectory length and is given by

$$P = \frac{d_{euc}}{d_t} , \quad (2.14)$$

which yields a value of 1 in case of conformity of trajectory length and euclidean distance.

2.8.4 Adhesion Size Quantification

Fluorescence images of cells expressing GFP-tagged vinculin proteins were evaluated with ImageJ to determine the size and area of a cells focal adhesion sites. A threshold was set to gray scale images before conversion into binary files. The area of the adhesions was marked and evaluated with the region of interest (ROI) manager tool to determine adhesion area, length and width.

2.8.5 Statistical Data Analysis

For all data shown in this thesis, the sample mean \bar{x} and the standard error of the mean (SEM) were calculated. The sample mean is defined as

$$\bar{x} = \frac{1}{n} \sum_{i=1}^n x_i . \quad (2.15)$$

and the SEM was derived by dividing the sample standard deviation σ by the square root of the number of independent experiments n . With a standard deviation of

$$\sigma = \sqrt{\frac{1}{n-1} \sum_{i=1}^n (x_i - \bar{x})^2} \quad (2.16)$$

the SEM is derived from

$$SEM = \frac{\sigma}{\sqrt{n}} . \quad (2.17)$$

To compare the data obtained for two populations, the statistical significance was determined using an independent, two-sided t-test or a Mann-Whitney test with a level of significance of $p \leq 0.05$. The significance was characterized according to table 2.4.

Tab. 2.4: Statistical data analysis

Level of significance	Illustration
$0.05 < p$	n.s. (not significant)
$0.01 < p \leq 0.05$	*
$0.001 < p \leq 0.01$	* *
$p \leq 0.001$	* * *

2.8.6 Fast Fourier Transform Filter

Force curves obtained from the optical tweezers force spectroscopy assay were derived by averaging over the number of examined cells. Afterwards, a fast Fourier transform (FFT) filter was applied with Microcal Origin to smooth the data sets and visualize the primary structure of the force development process. With the FFT filter tool smoothing was accomplished by defining a cutoff frequency F_{cutoff} and removing all frequencies higher than F_{cutoff} from the data sets. The cutoff frequency is defined as

$$F_{\text{cutoff}} = \frac{1}{n \Delta t} \quad (2.18)$$

where n is the number of data points to be considered for smoothing and Δt is the time interval between two recorded video frames.

2.9 Image Acquisition and Software

Force spectroscopy and retrograde transport velocity assays were conducted with the laser tweezer setup described in section 2.1. For cell migration studies and fluorescence image quantification the microscopes and softwares listed below were used.

2.9.1 Microscopes

The following microscopes (Carl Zeiss, Göttingen) were used for fluorescence imaging (a/b), 3D stacks (a) and cell migration studies (c/d).

- | | |
|----------------------------|--|
| a) LSM 510 Meta: | Confocal laser scanning microscope <ul style="list-style-type: none">• Plan-Apochromate 63x/1.4 DIC, oil immersion |
| b) Apotome Imager Z1 | Structured illumination microscope <ul style="list-style-type: none">• Plan-Apochromate 63x/1.4, oil immersion• EC-Plan-Neofluar 40x/1.3 DIC, oil immersion |
| c) Axiovert 200M | Inverse microscope with life cell imaging chamber <ul style="list-style-type: none">• Plan-Neofluar 20x/0.5 Ph2 |
| d) Colibri/AxioObserver.Z1 | Fluorescence microscope with Colibri LEDs, temperature controlled <ul style="list-style-type: none">• Plan-Apochromate 20x/0.8 Ph2 |

2.9.2 Software for Image Acquisition and Analysis

Image Acquisition

Falcon Frame Grabber (IDS)	Laser Tweezer
AxioVision (Carl Zeiss)	Apotome Imager, Axiovert, Colibri microscope
LSM release V4.2 (Carl Zeiss)	LSM 510

Image Processing

MetaMorph V6.2 (Visitron)	Object tracking
LSM release V4.2 (Carl Zeiss)	3D projection of stacks
ImageJ (NIH)	Manual tracking and chemotaxis tool for cell migration assay

Data Analysis

Excel 2007 (Microsoft)	Evaluation of trajectories and visualization of results
Origin 6.0 (Microcal)	Statistical data analysis
MATLAB R2009a (Mathworks)	Calibration algorithm for optical traps

2.10 Reagents, Buffers and Chemicals

Name	Details	Company
Acetonitrile (ACN)		Carl Roth
Agarose		PeqLab
Ampicillin		Carl Roth
Bovine Serum Albumin (BSA)	1 % in PBS	Sigma Aldrich
Chicken Serum (CS)	5 % in F12	Invitrogen
Copper(II) sulfate (CuSO ₄)		Carl Roth
2,5-dihydroxybenzoic acid (DHB)	for MALDI-TOF	ProteoChem
Dimethyl sulfoxide (DMSO)		Sigma Aldrich
Dulbecco's Modified Eagle Medium, high glucose (DMEM)		Invitrogen
1-Ethyl-3-(3-dimethylaminopropyl) carbodiimid (EDC)		Carl Roth
EndoFree Plasmid MaxiPrep Kit		Qiagen
Ethanol (EtOH)	>99.8% p.a.	Carl Roth
F-12K Nutrient Mixture Kaighn's Modification (F-12K)	(+) l-glutamin	Invitrogen
Fetal Bovine Serum "gold" (FBS)	10% in F12/DMEM	Molecular Probes
Fetal Calf Serum (FCS)	10% in F12 /DMEM	Dianova
Fibronectin (FN)	10µg/ml	Dianova
Ficoll 400	0.5 % in E-buffer	Sigma Aldrich
Hanks Balanced Salt Solutiton (HBSS)	-/-: (-)Ca ²⁺ , (-)Mg ²⁺ +/: (+)Ca ²⁺ , (+)Mg ²⁺	Invitrogen
4-(2-hydroxyethyl)-1-piperazine-ethanesulfonic acid (HEPES)	20mM in DMEM	Carl Roth
Kanamycin	0.5%	Carl Roth

Name	Details	Company
Lipofectamin		Invitrogen
Methanol (MeOH)		Carl Roth
Mowiol	20%	Hoechst
Ninhydrin		Carl Roth
Nitrogen	purity 5.0	Linde
n-Propylgallat	1 spatula tip to 10ml Mowiol	Sigma Aldrich
Paraformaldehyde (PFA)	4% in PBS	Sigma Aldrich
Penicillin-Streptadivin	1 % in DMEM	Invitrogen
Phosphate Buffered Saline (PBS)	1x, (-) Ca ²⁺ , (-) Mg ²⁺	Invitrogen
Piperidine	35 % in ACN	Carl Roth
Poly-L-Lysin (PLL)	200µg/ml in PBS	Sigma Aldrich
Triton X-100	0.1% in PBS	Carl Roth
Sodium ascorbate		Carl Roth
Sulfo-N-Hydroxysuccinimid (Sulfo-NHS)		Carl Roth
Trifluoroacetic acid (TFA)		Carl Roth
Trypsin/EDTA	1:5, 1:10 in HBSS-/-	Invitrogen

Tab. 2.5: Reagents, Buffers and Chemicals

3 RESULTS

Cells interact with their environment and are able to sense the biomechanical and biochemical characteristics of their surrounding extracellular matrix (ECM) [Geiger & Bershadsky 2002, Huang *et al.* 2004, Shemesh *et al.* 2005, Geiger *et al.* 2009]. The presence of integrin ligands such as fibronectin or collagen allows cells to establish a link between the intracellular cytoskeleton and the extracellular environment. This link is formed by a variety of adhesion-related proteins and enables cells to explore the rigidity of their surrounding, the availability of cell adhesion-mediating ligands and geometrical substrate characteristics [Chen *et al.* 1997, Balaban *et al.* 2001, Engler *et al.* 2004, Engler *et al.* 2006, Vogel & Sheetz 2006]. Cell-matrix interactions have a substantial influence on cell morphology, motility, and force transmission at adhesion sites. The investigation of adhesion complexes forming on two-dimensional substrates has revealed many insights into their composition, morphology, and dynamics [Zamir & Geiger 2001, Kanchanawong *et al.* 2010, Papushcheva & Heisenberg 2010, Schäfer *et al.* 2010]. It was demonstrated that adhesions also assemble in the more physiological condition of three-dimensional matrices [Cukierman *et al.* 2001, Cukierman *et al.* 2002, Tamariz & Grinnell 2002, Lehnert *et al.* 2004, Klein *et al.* 2010, Fraley *et al.* 2010, Kubow & Horwitz 2011, Hakkinen *et al.* 2011].

Force transmission to the ECM is a crucial process for substrate-attached cells and has been researched over the last decades with various techniques, among them magnetic tweezers, optical tweezers, atomic force microscopy, and elastic substrates [Wang *et al.* 1993, Galbraith & Sheetz 1997, Bausch *et al.* 1998, Sagvolden *et al.* 1999, Balaban *et al.* 2001, Gosse & Croquette 2002, Laurent *et al.* 2002, S. Yang 2005, Franz & Puech 2008, Neuman & Nagy 2008]. However, many details on cell-substrate interactions and cellular force transduction still remain elusive.

In the presented study, fibroblasts-like cells were grown on homogeneously fibronectin (FN)-functionalized substrates and were brought into contact with ligand-coated microscopic beads, together mimicking a 2.5-dimensional environment. Optical tweezers force spectroscopy was used to investigate the force development during the evolution of early adhesion sites at the cell-bead interface. This method uses optical traps to position functionalized beads on the apical cell membrane and deduces force transmission at the emerging adhesion sites from bead-displacement analysis.

Chapter 3.1 gives an introduction to force spectroscopy assays with optical tweezers and elaborates on the general experimental outline.

Chapter 3.2 deals with force transmission in newly formed adhesion sites with respect to the interface size, ligand density and the location of the adhesion sites on the apical cell surface. The cell adhesion-mediating integrin ligand fibronectin and a peptide comprising the adhesion motif Arg-Gly-Asp (RGD) are tested with regard to their force regulating capacity. In addition, the dynamics of retrograde actin flow are studied and correlated to the force measurements.

Chapter 3.3 explores three different cell lines to elucidate a generic correlation between force generation, actin flow and cell migration.

Chapter 3.4 deduces the impact of the adhesion-related adapter protein vinculin: force transmission in vinculin deficient cells and vinculin mutant expressing cells is derived and compared to wild type cells. Complementary data to the adhesion strength of individual cell-matrix contacts, acquired with atomic force microscopy, delineate the overall detachment forces of entire cells from their substrate.

3.1 Force Spectroscopy with Multiple Trap Optical Tweezers

In the recent past, optical tweezers (OTs) were exploited to study cellular mechanical properties and have emerged as a powerful tool to investigate force development with high temporal and spatial resolution. Microrheometry studies with OTs determined membrane elasticity [Kuo & Sheetz 1992, Dai & Sheetz 1995, Raucher & Sheetz 2000, Titushkin & Cho 2006, Jeney *et al.* 2010] and force spectroscopy approaches evaluated the force transmission in distinct cell-matrix adhesion sites [Choquet *et al.* 1997, Galbraith *et al.* 2002, Icard-Arcizet *et al.* 2008, Bordeleau *et al.* 2011]. In addition, optical tweezers have been adopted to study the effect of adhesion-related proteins and have contributed to reveal many details of the cellular force generation processes [Felsenfeld *et al.* 1999, Jiang *et al.* 2003, Wu *et al.* 2005, Giannone *et al.* 2007, Perez *et al.* 2008, Roca-Cusachs *et al.* 2009].

The work presented here employed multiple trap OTs to study force development at individual adhesion sites. In the experimental design described in chapter 2.1, optical traps simultaneously serve as positioning tools for microscopic beads and as force probes.

3.1.1 Geometrical Bead Patterns

With the multiple trap optical tweezers setup described in chapter 2.1 it was feasible to operate a large number of optical traps and to constitute arbitrary geometric patterns with trapped microscopic beads (figure 3.1 A and B). Beads used for trapping were $3.0\ \mu\text{m}$ or $4.5\ \mu\text{m}$ in diameter and were made of polystyrene, a material transparent for the applied laser wavelength of $1064\ \text{nm}$. The generation of multiple traps was contrived by two crossed acousto-optic deflectors (AODs) inserted into the laser beam path, which scanned the laser rapidly (access time: $6.5\ \mu\text{s}$; scan frequency: $100\ \text{kHz}$) through the focal plane granting an accessible area of $150 \times 150\ \mu\text{m}^2$. Each optical trap had the potential to be moved independently from other traps and offered the possibility to be assigned with an individual trap stiffness. As multiple traps were operated in a quasi-static time-shared mode, the maximum trap stiffness allocatable to a single trap was depending on the total number of active traps. By modulating the wavelength of the acoustic frequencies applied

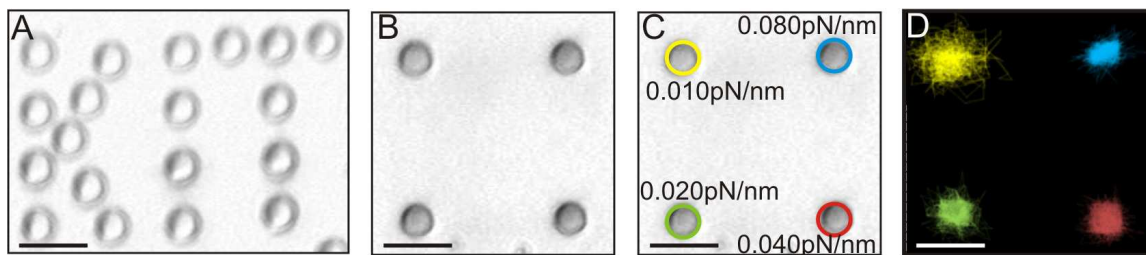


Fig. 3.1: Geometrical bead patterns

A) and B) Polystyrol beads with a diameter of $4.5\ \mu\text{m}$ were positioned in arbitrary geometric patterns by optical traps. C) Each trapped bead was assigned with an individual trap stiffness and was moved through the sample plane independently. D) Trajectories of thermal bead fluctuation at 37°C for beads confined in optical traps featuring the distinct trap stiffness denoted in C).

to the AODs, the laser beam was deflected, while a change of the applied amplitude resulted in a modified light transmission, thus regulating the optical trap stiffness.

An example of multi trap operation with distinct trap stiffness assignments is depicted in figure 3.1 C). The trap stiffness was highest in the blue marked trap (0.08 pN/nm) and was reduced clockwise. In figure 3.1 D) the impact of the trap stiffness on bead confinement is displayed: a high trap stiffness corresponded to the exertion of strong restoring forces onto the bead, keeping it close to the trap center (blue trajectory), while weaker restoring forces allowed the bead to fluctuate along a wider circumference (yellow trajectory).

The trap stiffness κ and the maximum restoring trap force F_{max} were calibrated in multiple trap mode as described in chapter 2.1.2 and yielded the values denoted in table 3.1 for the maximum laser power of 200 mW per trap. All calibrations were conducted with functionalized beads that were administered into cell imaging medium maintained at 37°C to simulate the conditions during the later force spectroscopy experiments.

Tab. 3.1: Trap stiffness and trap force for the maximum available laser power of 200 mW

Bead size	κ [pN/nm]	F_{max} [pN]
$3.0 \mu\text{m}$	0.10 ± 0.01	120 ± 15
$4.5 \mu\text{m}$	0.16 ± 0.02	190 ± 20

3.1.2 Functionalized Beads Serve as Local Force Probes

Beads functionalized with ECM ligands such as FN were employed as local force probes. The high flexibility of the multiple trap OT setup allowed to position a defined number of beads in distinct areas of the apical cell membrane. Positioning was controlled with a closed-loop operation system relying on the brightfield images of a CCD camera. Beads on the cell membrane stimulated the formation of new adhesion complexes at the contact sites. Initially, nascent adhesions assemble at the membrane-bead interface and form a primary link between the cellular actin cytoskeleton and the ECM. The reinforcement of these newly formed adhesion sites requires both a counterforce to the cellular traction and a sufficient contact area between cell membrane and bead. Counterforces were applied to the beads by optical traps: a cell pulling at a trapped bead displaces this bead from the trap center and as the bead is confined within an optical potential well, the deviation from the equilibrium induces restoring optical forces on the bead. The stiffness of the optical trap defines the substrate rigidity experienced by the cell and is adjusted by the laser intensity allocated to the trap. In addition, the applied laser intensity controls the overall magnitude of the restoring force.

The multi-trap mode allows to expose cells simultaneously to a predefined number of beads and in the experiments described in this chapter one to seven beads were arranged on the cell membrane. Due to the fast scanning rate of 100 kHz of the system, cells experience a quasi-static substrate rigidity when applying traction forces to the beads. With the described experimental OT design

(chapter 2.1) the maximum restoring force is continuously adjustable between 10 pN and 190 pN, which is a force regime well suited to measure the force transduction during the early phase of individual adhesion formation.

3.2 Multi-Parametric Study of Cell-Matrix Adhesion Sites

Force development at cell adhesion sites is a complex process depending on a variety of external and internal parameters. Among the externally controllable parameters are the size of adhesions, which can be controlled by the area of ligand patterned substrates [Chen *et al.* 1997, Balaban *et al.* 2001, Lehnert *et al.* 2004, Klein 2009, Tan *et al.* 2003]. The type and amount of available integrin ligands mediate adhesion formation and thereby control of the density and spacing of these ligands constitutes a regulatory mechanism on adhesion strength [Palecek *et al.* 1997, Malmström *et al.* 2010].

In this study, the parameters of adhesion area (controlled by bead size), ligand density (FN and RGD), adhesion location (leading edge/trailing edge), and adhesion spacing were investigated with regard to their influence on force transmission at early adhesion sites.

3.2.1 Bead Size Influences Adhesion Reinforcement

Cells form adhesive complexes when supplied with tension resisting ECM ligands. Adhesion formation starts with the assembly of dot-like nascent adhesions that develop into focal complexes, which reach a maximum size of $1 \mu\text{m}$ in diameter. Mature adhesions (so called focal adhesions) are known to grow into bigger elliptical structures with a diameter of 2 to $5 \mu\text{m}$ along the elongated axis [Gardel *et al.* 2010]. It has been demonstrated that the development of mature adhesion sites requires a certain contact area between bead and cell, with bead diameters of about $3 \mu\text{m}$ probably offering enough space for the formation of more than one focal complex per bead [Galbraith *et al.* 2002]. A relation between adhesion size and force development has also been shown in cells cultured on elastic substrates [Beningo *et al.* 2001].

In the presented study, the dependence of adhesion strength at the cell-substrate interface area is tested by applying beads of diverse diameters to fibroblast cells.

To determine the optimal conditions for the optical tweezers force spectroscopy assay, beads of $3.0 \mu\text{m}$ and $4.5 \mu\text{m}$ diameter were administered to the leading edge of mouse embryonic fibroblasts (MEF WT) and the force development in the evolving adhesion sites was monitored by video microscopy (figure 3.2 A)). The formation and development of adhesion sites was analyzed with regard to the available contact area between the cell membrane and the bead. A bead placed on the cell surface slightly indents the membrane (figure 3.2 B)), forming an effective contact area that is defined by the contact angle α , related to the indentation height h by

$$h = \frac{1}{2}d(1 - \cos(\alpha)) \quad (3.1)$$

where d is the diameter of the bead. Estimates for the indentation depth of micron sized beads on fibroblast cells have been derived in previous studies by atomic force microscopy and scanning electron microscopy and typically amounted $h = 0.05 \mu\text{m}$ to $h = 0.2 \mu\text{m}$ [O'Callaghan *et al.* 2011, Galbraith *et al.* 2002, Laurent *et al.* 2002]. The effective contact area between microscopic beads

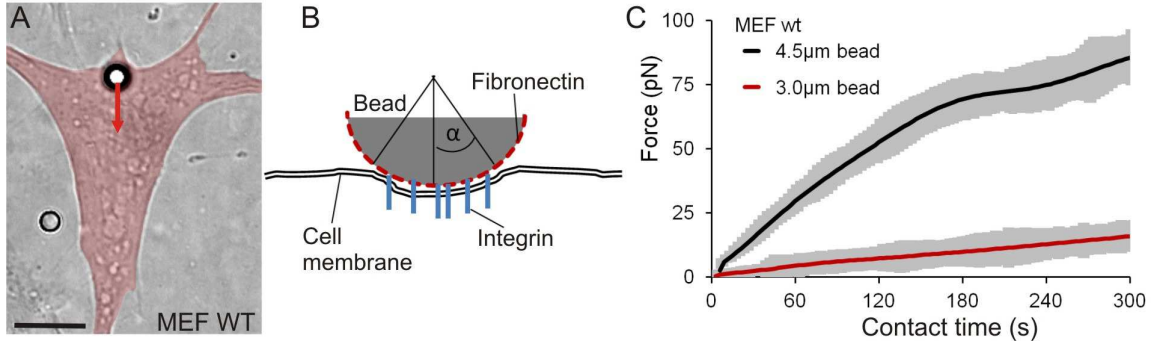


Fig. 3.2: Traction force in relation to bead size

A) DIC image of a MEF WT cell with a bead placed on the leading edge. The arrow denotes the direction of the cellular traction force (scale bar = $10 \mu\text{m}$). B) Sketch of the effective contact area between bead and cell membrane. The bead is slightly indenting the membrane and integrins are recruited to the membrane-bead interface. C) Force curves measured for beads of $3.0 \mu\text{m}$ and $4.5 \mu\text{m}$ diameter with increasing contact time. The force curves were averaged over the number of experiments ($n_{3.0\mu\text{m}} = 17$ and $n_{4.5\mu\text{m}} = 14$) and were smoothed with the Origin FFT filter (SEM denoted in gray).

and the cell membrane resembles the surface area A of a spherical cap of height h that is defined as

$$A = \pi dh . \quad (3.2)$$

From this, an average contact area of $A \approx 1.2 \mu\text{m}^2$ for $3.0 \mu\text{m}$ diameter beads and an area of $A \approx 1.8 \mu\text{m}^2$ for beads of $4.5 \mu\text{m}$ was estimated. Thus, the effective membrane-bead contact area should be large enough to accomplish focal complex formation with both bead dimensions. However, the accuracy of this estimate is rather low as the actual contact area is hard to determine.

FN-functionalized beads were placed with optical traps on the apical cell membrane of MEF WT cells spread on a homogeneously FN-coated substrate to mimic new contact sites. A counterforce to the cellular traction amounting $F_{max} = 120 \text{ pN}$ for $3.0 \mu\text{m}$ beads and $F_{max} = 190 \text{ pN}$ for $4.5 \mu\text{m}$ beads, was applied by the optical traps to the beads to induce a reinforcement of adhesion sites at the membrane-bead interface. The process of force development in early adhesion sites forming during the initial 300 s of bead contact was recorded with a temporal resolution of 1 s.

As shown in figure 3.2 C), force transmission at the interface with beads of $3.0 \mu\text{m}$ diameter amounted $F_{3.0\mu\text{m}} = 16 \pm 1 \text{ pN}$ after 300 s ($n = 17$). Adhesion complexes evolving at the contact sites with $4.5 \mu\text{m}$ diameter beads transmitted an average force of $F_{4.5\mu\text{m}} = 83 \pm 4 \text{ pN}$ ($n = 14$). Hence, force transduction onto $4.5 \mu\text{m}$ beads was about 5-fold stronger than onto $3.0 \mu\text{m}$ beads, whereas the effective contact area was only 1.5 times larger. This reveals a nonlinear correlation between the adhesion size and the transmission of contractile forces.

The dependence of adhesion formation on the available contact area has also been discussed by Galbraith and coworkers, who demonstrated that focal complex evolution relies upon a sufficient bead size [Galbraith *et al.* 2002]. The results obtained from the OT force spectroscopy on different bead sizes suggest that only the larger contact area of $4.5 \mu\text{m}$ diameter beads is adequate for focal

contact maturation under the chosen experimental conditions.

For all following force studies, functionalized $4.5\ \mu\text{m}$ beads were employed to mimic new contact sites as they geometrically enable the maturation of adhesion sites and thus experience higher traction force transmission.

3.2.2 Integrin Ligand Density Mediates Adhesion Strength

The amount and density of available integrin ligands in the extracellular environment has been shown to influence cell spreading and motility as well as adhesion morphology and strength. Previous studies reported that cells plated on substrates functionalized with high FN concentrations responded with a modification of their motility as well as with an enhanced proliferation rate and stronger adhesiveness [Palecek *et al.* 1997, Petrie *et al.* 2006, Walter *et al.* 2006]. The shortest amino acid sequence known to be recognized as adhesion motif is the RGD sequence located in fibronectin domain III. A comparison of substrates prepared with either the RGD adhesion motif or the FNIII₇₋₁₀ segment revealed that cellular adhesion was improved when the FN segment was provided [Petrie *et al.* 2006]. Low density experiments with adhesion-mediating ligands demonstrated that the spatial separation of individual ligands strongly influences adhesion formation. For example, a separation length of 69 nm was defined as upper limit for focal complex formation [Walter *et al.* 2006] and the number of ligands required to establish an integrin mediated link to the cytoskeleton was determined to amount to a trimeric cluster [Coussen *et al.* 2002]. As these studies addressed the overall adhesiveness of cells in response to distinctive amounts of ligands, the question was raised how force transduction advances in individual adhesion sites in a time-dependent manner.

In the following, the force development in early cell adhesion sites mediated by the ECM constituent FN and the RGD adhesion motif is presented. The cyclic peptide cyclo(Arg-Gly-Asp-Phe-Lys) (cRGDfk) was chosen as integrin ligand as its cyclic shape resembles the native loop-like RGD conformation better than a linear RGD sequence. To determine the effect of ligand density on cell adhesion formation, beads were functionalized with distinct surface coverages of FN. A second bead batch was prepared with varying amounts of the cyclic peptide cRGDfk to test the cellular response to different ligands. Beads were coated with a surface coverage ranging from 50 % to 100 % for both ligands and an additional batch with a coverage of 150 % was contrived for the cRGDfk peptide. The ligand density on the bead surface was controlled spectrophotometrically as described in chapter 2.2.3. With this method the mean coverage of all bead batches was determined. Due to the limited sensitivity of the photospectrometric analysis, it was only feasible to determine the mean surface coverage of an entire batch with an accuracy of about $\pm 25\%$. As merely the mean coverage of an entire batch was derived, it was not possible to account for the individual variabilities in surface coverage of beads within the same batch, which further reduced the precision of the actual ligand density estimation.

However, the formation of integrin-mediated cell-substrate adhesion sites is highly sensitive to the amount of extracellular ligands and thus the limited control of the ligand coverage on beads introduced a significant level of uncertainty into the system. Hence, a well-controlled bead functionalization is desirable for the study of traction force development at emerging cell adhesion sites.

To provide the means to determine the actual density on a specific bead, a fluorescent 1:1 labeling of a single ligand molecule with an individual fluorophor is crucial. Ligand density can then be derived from the evaluation of confocal microscopy fluorescence images. By attaching fluorophores with distinct excitation and emission spectra to beads of different ligand coverage, it becomes feasible to simultaneously expose an individual cell to distinctive ligand densities. With this, an enhanced degree of flexibility arises, allowing to investigate in detail the cellular response to a matrix containing ligand density gradients.

To address this task, a cooperation with the Nano-Devices group of Dr. Ljiljana Fruk at the Center for Functional Nanostructures (CFN) was established. In the scope of this cooperation, a trifunctional lysine linker, allowing to attach a fluorophor on one terminus and a ligand on the second terminus was developed. The residual functional group remained to crosslink the construct to the microscopic beads. Conceptual details and the chemical production process are described in appendix A.

The experiments presented here exposed cells to only one batch of surface densities per sample and did not test the described fluorescently labeled peptides, as the optimization of the production process is still in progress. Nonetheless, the experiments described in the following paragraph are able to clearly delineate the relation between traction force generation and bead coverage.

With optical traps beads of $4.5 \mu\text{m}$ diameter were placed on the leading edge of MEF WT cells and the displacement of beads from the trap center was monitored for 300 s with an image acquisition rate of 1 Hz. For FN-functionalized beads, a surface coverage of 50 %, 80 % and 100 % was prepared and force-time curves were recorded (figure 3.3 A)). The shape of the force curves was similar for all prepared FN densities: in the initial contact phase, force transmission grew rapidly and decelerated subsequently. The duration of swift reinforcement was identified to depend on the amount and density of available ligands. Contacts to low density beads were first to reach the deceleration phase after about 120 s while adhesions formed to beads with 80 % FN coverage displayed a slowdown after 180 s. Analyzing beads offering a complete ligand monolayer, a linear adhesion reinforcement was accomplished over the entire time course of 300 s.

At the end of the measurement interval of 300 s, adhesion sites were able to transmit a force of $F_{\text{FN},50\%} = 49 \pm 3 \text{ pN}$ ($n=13$) to beads with the lowest coverage of 50 %. Beads prepared with a medium ligand density of 80 % experienced traction forces of $F_{\text{FN},80\%} = 81 \pm 5 \text{ pN}$ ($n=9$) and onto beads coated in a complete monolayer (100 %) forces of $F_{\text{FN},100\%} = 134 \pm 13 \text{ pN}$ ($n=8$) were applied. The different force developments on beads with distinct FN densities were clearly distinguishable after 180 s of contact time ($p < 0.001$, t-test).

Plotting the magnitude of force transmission against the ligand density, a proportional dependence

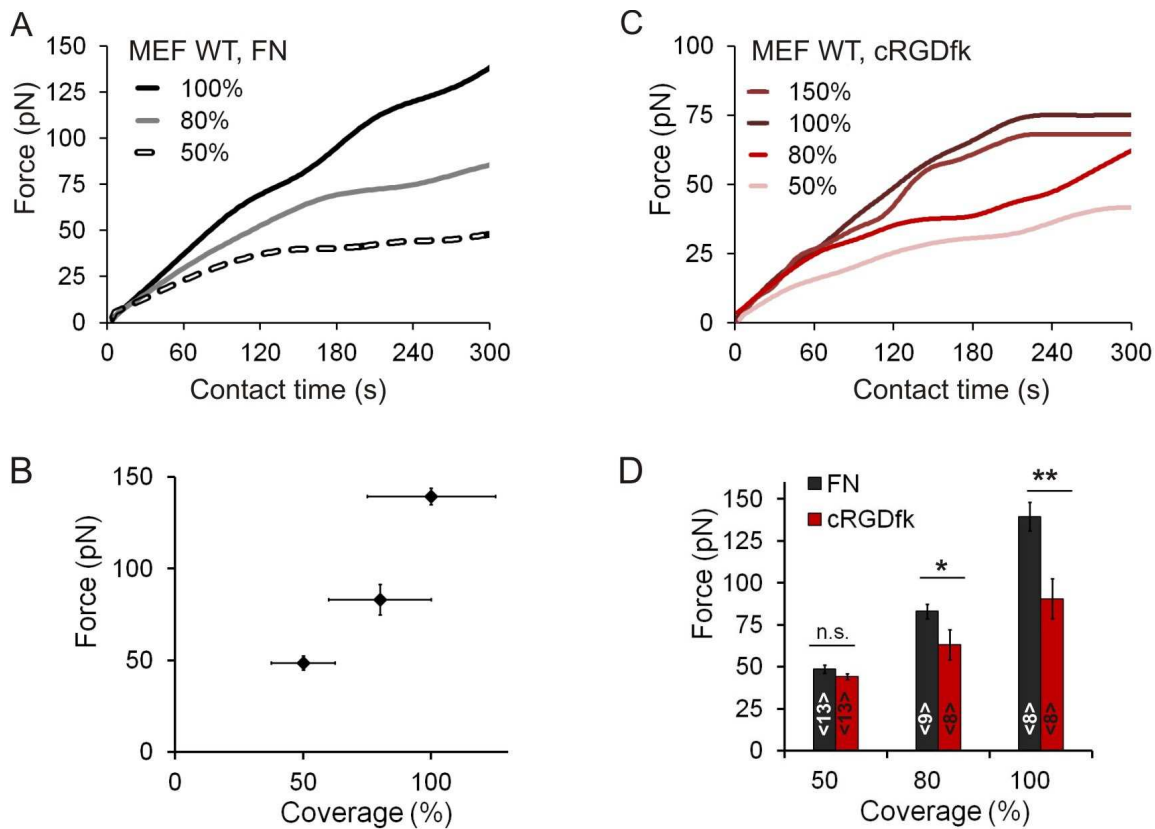


Fig. 3.3: Ligand densities mediate cell adhesion strength

Beads were coated with different densities of the ligands FN and cRGDfk. A) Traction forces on FN beads functionalized with different ligand densities. B) The force transduction on FN beads is plotted against the surface coverage (mean \pm SEM). C) In addition to beads covered in a complete ligand monolayer (100%), a sample with bilayer formation was prepared (150%). Force transmission onto these beads resembled the monolayer magnitude, indicating a saturation effect. All force curves were smoothed with the Origin FFT filter tool. D) Comparison of forces transmitted on FN and cRGDfk beads, respectively (mean \pm SEM, numbers in bars denote the number of examined cells)

of traction force exertion and ligand coating was observed (figure 3.3 B)). This relation supposedly originated from enhanced integrin clustering mediated by the increase of ligand availability.

The same measurements were performed with beads functionalized with different densities of the cRGDfk peptide. Here, an additional coating density of 150% coverage was prepared to test if a saturation effect regarding adhesion reinforcement can be observed. Beads with 150% coverage contained more ligand on the surface than required to form a complete monolayer (chapter 2.2.3). Thus a second peptide layer started to form on this beads. Force curves for distinct cRGDfk densities (50%, 80%, 100%, and 150%) are displayed in figure 3.3 C). The evaluation of adhesion forces after 300 s of bead contact yielded the weakest force transduction onto beads with a coverage of 50%: $F_{\text{cRGD},50\%} = 33 \pm 3 \text{ pN}$ ($n = 13$). Cells establishing contacts with beads featuring a ligand density of 80% transmitted forces of $F_{\text{cRGD},80\%} = 63 \pm 9 \text{ pN}$ ($n = 8$). Beads coated with a ligand monolayer (100% coverage) experienced traction forces of $F_{\text{cRGD},100\%} = 92 \pm 11 \text{ pN}$ ($n = 8$). The formation of a second ligand layer on beads with 150% coverage did not lead to an increased force transmission but resulted in similar adhesion forces as determined for 100% bead coverage

($F_{\text{cRGD},150\%} = 90 \pm 16 \text{ pN}$ ($n=8$)).

In general, reinforcement of adhesion sites formed to distinct cRGDfk densities was discernible after 120 s of membrane-bead contact ($p < 0.001$), only the 150 % coverage was indistinguishable from 100 % coverage. Analyzing the cellular response to distinct cRGDfk densities, a proportionality between ligand density and force development was deduced for up to 100 % bead coverage. In figure 3.3 D) a comparison of cellular traction forces applied to beads covered with different densities of FN and cRGDfk is depicted. At contact sites formed with FN-functionalized beads an enhanced force transmission occurred and became more pronounced with increasing ligand densities.

Summarizing the results of this paragraph, a proportional relation between surface coverage and adhesion strength was found for both ligands for up to 100 % bead coverage. With sufficient ligand to induce bilayer assembly a saturation effect was observed, as the force transmission did not increase but remained on the same level as for a completed monolayer.

The comparison of force development with the two ligands, FN and cRGDfk, showed stronger traction forces at adhesion sites with FN beads.

An interesting perspective for future experiments is the simultaneous exposure of cells to beads functionalized with distinct ligands and distinct surface coverages, which will be feasible with the newly designed trifunctional, fluorescent linker approach.

3.2.3 Traction Force and Actin Flow Velocity Mapping Across the Cell Surface

Retrograde actin flow is a process found in all migrating cells and has been investigated in a variety of studies. For more than two decades, the mechanisms driving cytoskeletal actin flow have been investigated, revealing several resources generating the rearward directed translocation, but the exact regulation of the process is not yet completely understood [Svitkina *et al.* 1986, Symons & Mitchison 1991, Cramer 1997, Caspi *et al.* 2001a]. Approaches with FN-functionalized beads positioned on the cell membrane were employed to study the response of the cellular cytoskeleton, as was first discussed by Grinnell and Geiger [Grinnell & Geiger 1986]. It was demonstrated that the complex formation of integrins with the FN ligands of functionalized beads induced the assembly of actin cytoskeleton beneath the membrane-bead contact [Grinnell & Geiger 1986, Miyamoto *et al.* 1995b, Miyamoto *et al.* 1995a] and that the coupling of FN-functionalized beads to the actin flow was mediated by integrins [Felsenfeld *et al.* 1996]. Furthermore, it was shown that FN-functionalized beads coupled to the rearward flow were not attached strongly to the cell membrane but could be pulled off easily or were released self-induced [Schmidt *et al.* 1993, Choquet *et al.* 1997, Nishizaka *et al.* 2000].

In the work presented here, an actin flow mapping across the cell surface is combined with a contractility mapping to correlate cellular dynamics and force generation in distinct cellular areas. The custom-built optical tweezers setup featured a multiple trap mode allowing to simultaneously measure force transmission at distinct locations (figure 3.4 A)). This enabled force mapping over

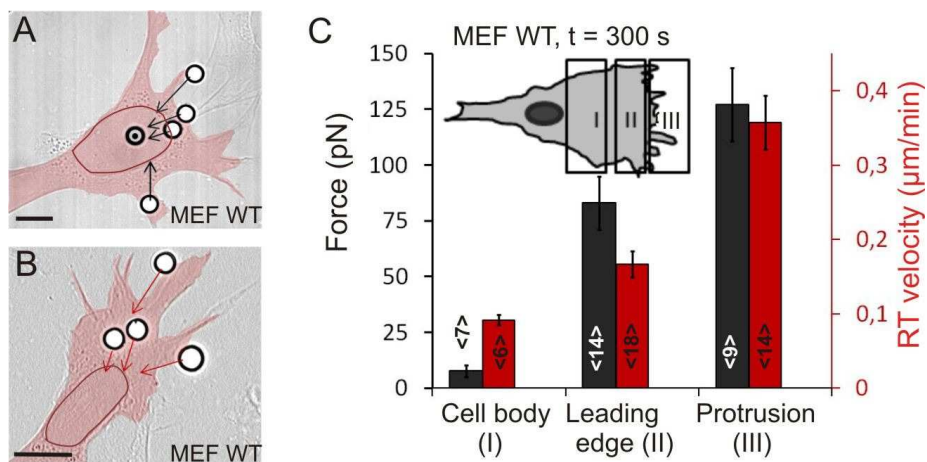


Fig. 3.4: Force and RT velocity mapping in MEF WT cells

A) and B) DIC images of MEF WT cells with 4.5 μm diameter FN-functionalized beads distributed across the cell surface. The vectors point in the direction of A) the traction force and B) the retrograde transport (RT) and scale with the magnitude of force and velocity, respectively. A colored overlay was added to highlight the outline of the cell and the nucleus was traced by a red line with Adobe Photoshop (scale bars = 10 μm). C) Forces (black) were evaluated after a contact time of 300 s and grow proportionally to the RT velocity (red). The inset shows a schematic definition of the distinct cellular areas. (Histogram: mean ± SEM; numbers in bars denote the number of experiments)

the whole surface of a single cell. A predefined number of beads was placed on the cell body (area I), the leading edge (area II) and on cellular protrusions (area III) to investigate the dynamics and adhesion strength arising in the linking process to the bead. The distinct cellular areas are illustrated schematically in the inset of figure 3.4 C).

Figure 3.4 A) depicts a cell where five beads are distributed across the surface with one bead in area I, two beads in area II and two beads placed in area III, one at a forward directed protrusion and one at a lateral directed protrusion. The force vectors attributed to the bead in area III denote the highest forces in this area relative to areas I and II. Beads located in the leading edge experienced cellular traction forces in an intermediate force regime while hardly any force development was observed for beads placed in the perinuclear area I. In addition, the force mapping approach demonstrated that adhesion sites located in area II with equal distance to the membrane tip of the leading edge exerted similar traction forces.

The adhesion forces on FN-functionalized beads of 4.5 μm diameter, derived after 300 s of membrane-bead contact, are displayed in figure 3.4 C). Measurements revealed that traction forces were highest in the foremost protrusions ($F_{III} = 127 \pm 15 \text{ pN}$), decreased rearwards within the lamella ($F_{II} = 83 \pm 6 \text{ pN}$) and became negligible when placed in the nuclear region or the rear of the cell ($F_I = 8 \pm 3 \text{ pN}$) (figure 3.4 C)).

Complementary measurements were conducted regarding retrograde transport behavior at different locations. Retrograde transport velocity (v_{rt}) mapping presented an elevated bead flow in the exceptionally dynamic protrusions with $v_{rt,III} = 0.36 \pm 0.04 \text{ μm/min}$ in MEF WT cells. This is also depicted in figure 3.4 B), where the vectors denote the direction and velocity of retrograde transported beads. Beads placed on the cell membrane close to the lamellipodium (area II) were

translocated with an average velocity of $v_{rt,II} = 0.16 \pm 0.02 \mu\text{m}/\text{min}$, which decreased toward area I to $v_{rt,I} = 0.09 \pm 0.01 \mu\text{m}/\text{min}$.

Of particular interest was the development of transport velocities close to the membrane tip of the leading edge and their alteration at the transition region to the lamella. To obtain detailed spatial information about this area, cells with an extended leading edge region were required. A cell line satisfying this demand were primary chick fibroblasts (PCFs).

PCF cells were exposed to functionalized beads that were arranged at various distances from the tip of the leading edge. In figure 3.5 the retrograde flow velocity is plotted against this distance. The acquired data were fitted with a power law regression ($y(x) = ax^b$ with the parameters $a=0.5$ and $b=-0.3$), and showed a steep decline of velocity with increasing distance that eventually turned into a steady, position-independent translocation speed.

Altogether, the dynamics of retrograde bead flow displayed the same behavior as traction forces in the corresponding cellular areas: In protrusions, retrograde transport was fastest and traction forces were strongest. This was followed by medium transport rates and medium adhesion strength in the leading edge, which decreased further toward the nuclear region. From this analysis a proportional relation between the actin flow dynamics and the strength of adhesion sites was concluded.

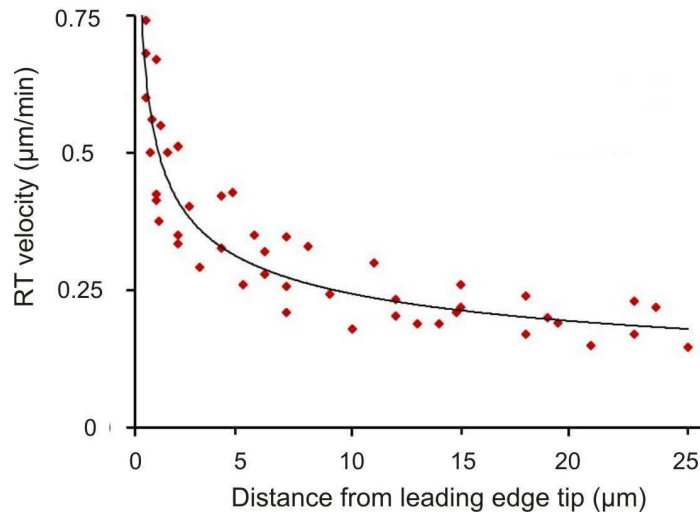


Fig. 3.5: Velocity mapping in the leading edge of primary chicken cells

Development of the retrograde transport (RT) velocity in primary chicken fibroblasts (PCFs) with regard to the tip of the leading edge. Data were fitted with a power law regression.

3.2.4 Reinforcement of Neighboring Adhesion Sites

The force mapping approaches presented in the previous section characterized the adhesion strength in distinct cellular areas. As yet, it has not been investigated how the spatial relation of neighboring adhesion sites influences their force transmission properties. In the cell periphery, cell matrix adhesion sites are often spatially closely related. This raises the question if cells reinforce a set of neighboring adhesion sites similar to individual adhesions and if both adhesions then experience an equal magnitude of force transmission.

The results presented so far all dealt with individual adhesion sites that were spatially well separated. In the force mapping assay, multiple beads were placed on the cell surface but were separated by distances $d > 10 \mu\text{m}$ and therefore were regarded as independent. Now, the influence of spatially closely related beads on force transmission in evolving adhesions is examined. The beads mimicking new contact sites for the cells were placed with a center-to-center distance of $d = 5 \mu\text{m}$ on the leading edge of the cell. Control measurements were conducted with bead spacings larger than $10 \mu\text{m}$ and yielded comparable results to forces observed on single beads. In figure 3.6 A) two examples of bead spacing are depicted: (i) two beads are placed in parallel to the boundary of the leading edge (black) and (ii) beads are placed in successive order and are oriented perpendicular to the border of the leading edge (red). The organization of the cellular actin cytoskeleton and a close-up on structural proportions in the leading edge are illustrated in figure 3.6 B) and C), respectively.

In case (i), with parallel beads, a diminished force transmission was observed when the spatial separation between two beads was reduced to $5 \mu\text{m}$ (figure 3.6 D)). With a spacing of $5 \mu\text{m}$ cells

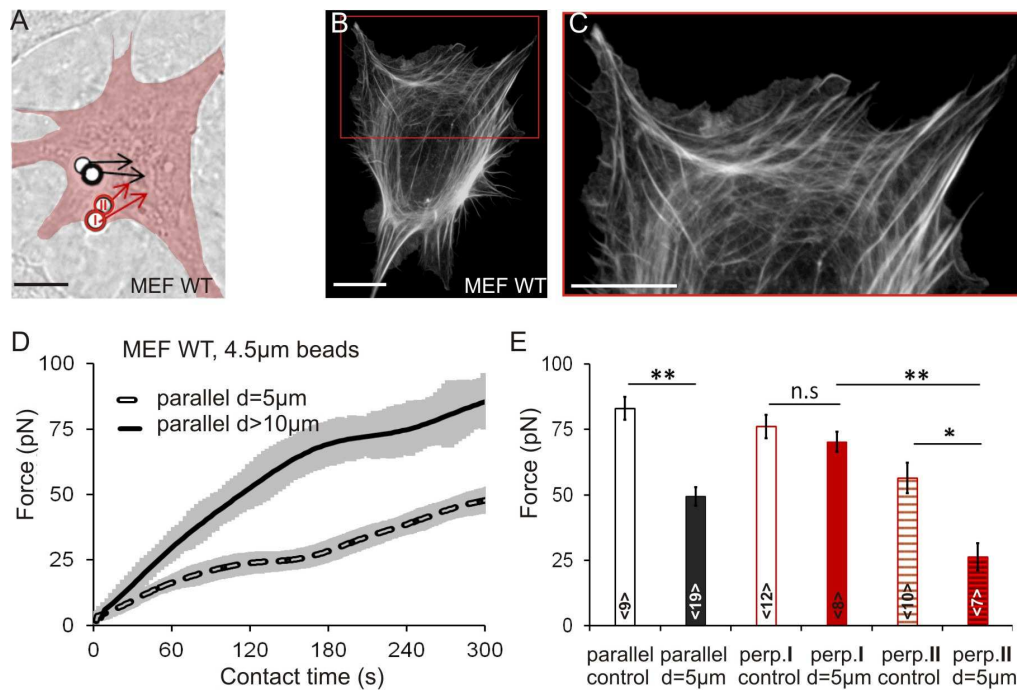


Fig. 3.6: Influence of spatial bead separation on force development

A) Beads were arranged in close spatial relation on the cell membrane of MEF WT cells. Vectors denote the force transmission on a pair of parallel oriented beads (black) and successive beads oriented perpendicular to the leading edge (red) (cell outline is highlighted by a colored overly; all scale bars = $10 \mu\text{m}$). B) Actin cytoskeleton of MEF WT cell marked by phalloidin staining. C) Close-up on the boxed area. The actin cytoskeleton assumes a gel-like shape in the lamellipodium that undergoes a transition into a network like structure at the interface to the lamella and is interspersed with actin fibrils. D) Force evolution over a time interval of 300 s for beads placed parallel with center-to-center distances of $d = 5 \mu\text{m}$ or $d > 10 \mu\text{m}$ (FFT smoothed force curves, SEM denoted in gray). E) Comparison of traction forces observed on parallel and successive oriented beads after a contact time of 300 s (mean \pm SEM; number in bars = number of experiments).

applied a traction force amounting to about 60 % of the strength they exerted on spatially well separated beads: $F_{=5\mu\text{m}} = 49 \pm 4 \text{ pN}$ ($n = 19$) compared to $F_{>10\mu\text{m}} = 83 \pm 4 \text{ pN}$ ($n = 9$). As indicated by the black arrows in figure 3.6 A), force transmission on both beads was equally strong. The force development over a time course of 300 s is shown in figure 3.6 D), where the two force curves become divergent already after 30 seconds of contact time ($p = 0.02$). This shows that the decision to reduce adhesion reinforcement occurs in a very early state of adhesion development.

The histogram in figure 3.6 E) depicts the contractile forces transmitted at a contact site after 300 s for both examined cases. As force transmission on parallel oriented neighboring beads (i) was distributed equally onto each, the results were combined into one bar (black) and were compared to the control group of enlarged bead distances (white; $p < 0.0001$, t-test).

For beads placed in successive order and perpendicular to the leading edge boundary (ii), the blank red bar illustrates the control group for the anterior bead (I) with bead spacings of $d > 10 \mu\text{m}$ (figure 3.6 E)). In this case, a clearly distinctive force administration to each bead was observed when the spacing equaled $d = 5 \mu\text{m}$. Compared to the control group, the anterior bead (solid red bar) did not show any decrease in adhesion strength, while the posterior bead (II) experienced strongly reduced force development. Contacts formed at this bead generated only 38 % of the forces applied to the anterior bead ($F_{\text{I}} = 67 \pm 6 \text{ pN}$ ($n = 8$) and $F_{\text{II}} = 26 \pm 5 \text{ pN}$ ($n = 7$)). This is also marked by the red arrows in figure 3.6 A), which denote a similar direction of traction but diminished forces on the bead located closer to the nucleus. It is well established that traction force generation depends on the location of the adhesion site with regard to the leading edge tip. Here, control measurements was conducted with individual beads placed in the location of the posterior bead (red hatched bar in figure 3.6 E)). These controls resulted a traction force reduction of 20 % compared to the anterior bead position. Thus, the overall force reduction at the posterior adhesions site of a successively oriented pair of adhesion sites cannot exclusively be attributed to the more posterior location.

Recapitulating the obtained force curves, reinforcement of adhesion sites did not only depend on the parameters of the contact directly concerned but also relied on neighboring adhesions. Laterally closely related adhesion complexes experienced equal force transduction. The adhesion strength of these contacts was reduced by about 40 % compared to independent adhesion sites. In contrast to this, beads placed in successive order did not develop similar adhesion forces in both contact sites. The anterograde bead was clearly favored and displayed similar force transmission as an individual contact site. Adhesion reinforcement on the retrograde adhesion site was reduced by more than 60 %.

Analyzing the two types of neighboring adhesions, force transmission on a successive bead was reduced by about 50 % compared to beads placed in parallel.

3.3 Comparison of Forces and Dynamics in B16, MEF and PCF Cells

Cellular traction forces have been examined in a number of studies and in various cell types using multitudinous approaches such as AFM, magnetic tweezers, optical tweezers or elastic substrates [Aratyn-Schaus & Gardel 2010, Fournier *et al.* 2010, Prass *et al.* 2006, Balaban *et al.* 2001, Wang *et al.* 1993, Svoboda & Block 1994a, Dai & Sheetz 1995, Bao & Suresh 2003]. The resulting insights on cell mechanics varied strongly depending on the examined cell type and were not readily comparable due to the diversity of the applied experimental methods.

Within this PhD work, three cell lines were studied with the same optical setup and with exactly the same sample preparation and imaging conditions to allow a comparison of force development throughout cell lines. In addition, the dynamics of retrograde actin flow and cell migration were characterized with the aim to define a general relationship between force and cellular dynamics.

Mouse embryonic fibroblasts (MEFs), mouse B16 melanoma cells (B16) and primary chicken fibroblasts (PCFs) were studied with regard to force transmission in individual adhesion complexes, retrograde actin flow velocity, and cell migration velocity. All cell lines were cultured on homogeneously FN-functionalized glass substrates. FN-functionalized beads with a diameter of $4.5 \mu\text{m}$ were prepared with a surface coverage of 80 % (section 3.2.2) and were positioned on the apical cell surface, creating flexible patterns of new possible adhesion sites with optical traps.

3.3.1 Cell Morphology on Homogeneously Coated Substrates

Two immortalized cell lines and one primary cell line were chosen for investigation. In figure 3.7 A) to C) phase contrast images of the three cell lines are displayed. While B16 and MEF WT cells showed a similar size and a typically elongated shape, PCF cells were much larger and adopted a more compact shape. The morphology of the cellular actin cytoskeleton was visualized by actin staining (green) depicted in figure 3.7 A') to C'). In B16 melanoma cells, the actin cytoskeleton in the leading edge developed into a meshwork with random organization (figure 3.7 A')). A characteristic feature of this cell line was the formation of arc-like actin fibrils that connected spatially separated peripheral adhesion sites (marked in red by immunostaining for vinculin). In comparison to that, MEF WT cells showed more pronounced actin stress fibers originating from the adhesion sites in the cell periphery and running toward the cell center (figure 3.7 B')). The morphology of the vinculin marked adhesion sites was similar in both B16 and MEF WT cells but the membrane sections between adhesive complexes were more stretched in the latter and did not display a prominent actin enrichment. The primary cells derived from chicken skin maintained a less polarized shape than the two other cell lines (figure 3.7 C')). In the periphery of PCF cells a clustering of cell adhesion sites was observed, whereas in the cell center individual, smaller adhesion complexes were apparent. The primary fibroblasts formed an extensive actin stress fiber system spanning the entire length of the cell.

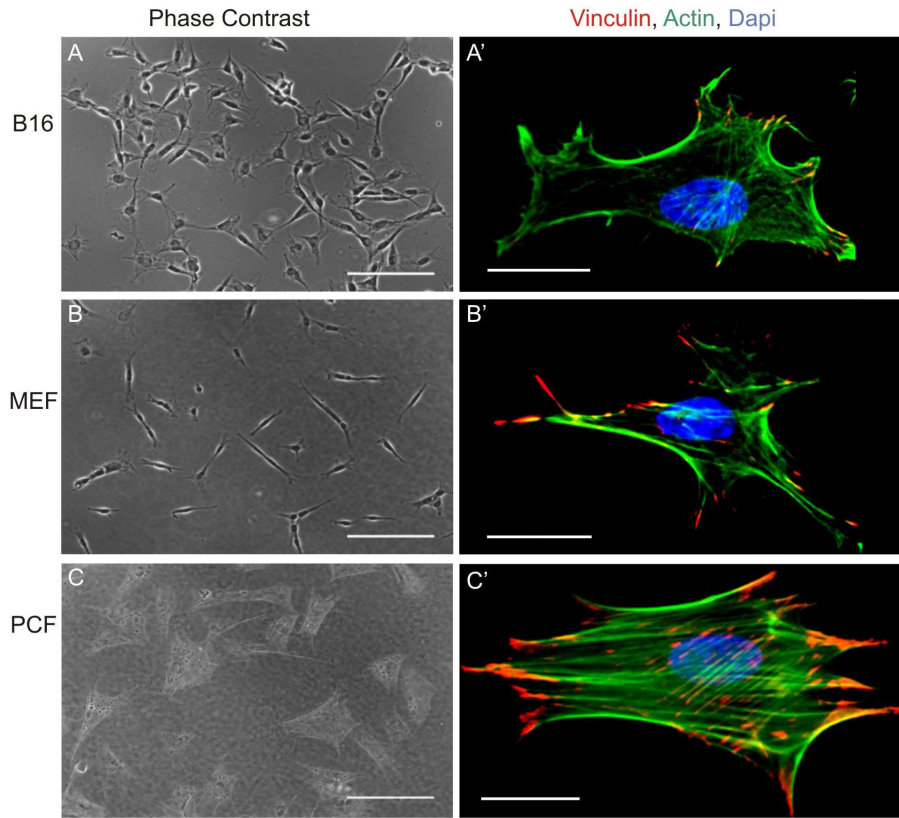


Fig. 3.7: Morphology of B16, MEF WT and PCF cells

(A-C) Phase contrast images of B16, MEF WT and PCF cells show a different cell size and morphology (scale bars = $100 \mu\text{m}$). (A'-C') Fluorescence images of the immunostained actin cytoskeleton (green), cell adhesion sites (vinculin, red) and the nucleus (blue) (scale bars = $20 \mu\text{m}$)

3.3.2 Traction Force Development in Different Cell Lines

Force transduction at early adhesion sites forming at membrane-bead interfaces was monitored over a time course of 300 s. FN-functionalized beads with a diameter of $4.5 \mu\text{m}$ were deposited on the leading edge of the cells and images were acquired with a frame rate of 1 Hz.

In figure 3.8 A) the recorded force curves for B16, MEF WT and PCF cells are depicted. The forces transmitted during the formation of adhesive contacts were clearly divergent for the three investigated cell lines. Maximum forces were observed for all cell lines at the end of the measurement interval of 300 s, signifying that the growth and maturation of the adhesion sites was not yet completed. After 300 s of membrane-bead contact, PCF cells exerted the strongest adhesion forces with $F_{\text{PCF}} = 151 \pm 10 \text{ pN}$ ($n = 20$). Force transmission in MEF WT cells resulted an average force of $F_{\text{MEF}} = 83 \pm 4 \text{ pN}$ ($n = 14$), while beads placed on B16 cells experienced the weakest traction forces with $F_{\text{B16}} = 42 \pm 2 \text{ pN}$ ($n = 12$) (figure 3.8 A)). Over the entire course of measurements, B16 cells showed a diminished increase in traction force and already after 60 s a significant difference regarding adhesion reinforcement was observed in comparison to MEF WT and PCF cells ($p < 0.01$, t-test). Both, B16 and MEF WT traction forces evolved in a two-step process with a steep force increase during the early adhesion formation (initial 60 to 120 s). This was followed by

a deceleration of reinforcement toward the end of the measurement interval (figure 3.8 A)). During the first 120 s of bead contact, traction force evolution in PCF cells was similar to MEF WT cells. While MEF WT adhesion reinforcement slowed in the following, PCF cells remained in a state of linear adhesion strengthening and exerted exalting forces onto the beads. Due to this, PCF cells gained significantly stronger traction forces after 180 s and were clearly distinguishable from MEF WT cells ($p < 0.05$, t-test) (figure 3.8 A)). The measurement duration was extended to 10 minutes to determine whether PCF reinforcement continued at the same rate. Nonetheless, no decline in adhesion strengthening was found within the increased measurement interval. Instead, after 8 minutes the cells overcame the maximum optical counterforce of 190 pN and pulled the beads out of the traps. Beads were then coupled to the retrograde actin flow and were transported toward the nuclear region.

In summary, regarding the three cell lines, PCF cells were found to develop the fastest reinforcement of cell adhesion sites over the observed time course of 300 s and showed a near four-fold amplification of force transduction compared to B16 melanoma cells.

In B16 and MEF WT cells a step-wise force evolution was observed. With the advancing contact strengthening at the bead interface came a spatial expansion of the adhesion site. The deceleration of adhesion strengthening after a specific interaction time was supposedly due to a decline of available bead space or a diminished number of non-complexed FN ligands. As has been demonstrated in section 3.2.2, a low amount of unbound adhesion-mediating ligands leads to a diminished reinforcement rate at the evolving adhesion sites.

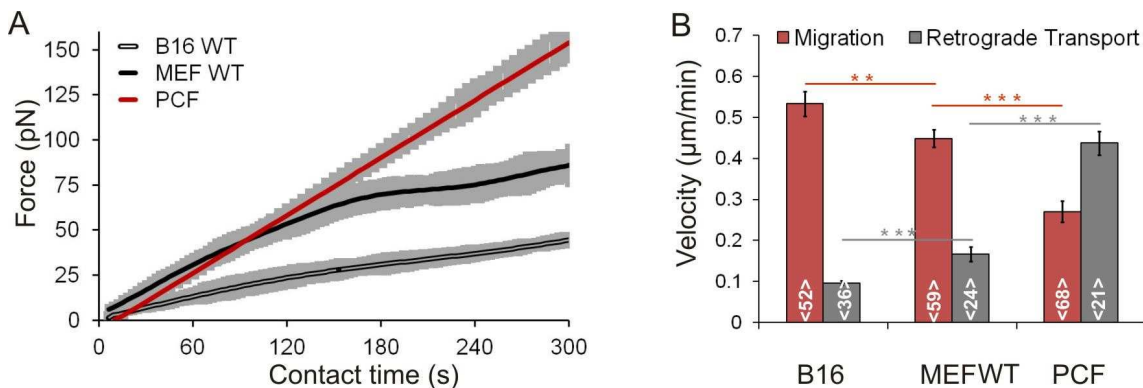


Fig. 3.8: Force development, retrograde transport and migration velocity

A) Force development in the leading edge of B16, MEF WT and PCF cells at the membrane-bead interface of $4.5 \mu\text{m}$ diameter FN-functionalized beads (force curves were smoothed with an FFT filter; SEM denoted in gray). B) The retrograde transport velocities of microscopic beads placed on the leading edge of B16, MEF WT and PCF cells were compared to the migration velocity of these cell lines. The histogram displays a reciprocal relation between retrograde flow and migration velocity (numbers in bars denote the number of examined cells).

3.3.3 Dynamics of Retrograde Actin Flow in Different Cell Lines

To study retrograde transport in B16, MEF WT and PCF cell lines, the optical traps were used to position FN-functionalized beads of $4.5 \mu\text{m}$ diameter on the apical cell surface. As soon as the beads were attached, the optical traps were removed. Lacking a restoring force from the optical traps, beads placed on the cell surface were coupled to the underlying retrograde actin flow and started to move rearward toward the nucleus. The bead translocation was recorded with a frame rate of 0.5 Hz over an interval of 20 min. Beads were always placed on well spread cells with a defined leading edge.

Analysis of the retrograde transport velocity v_{rt} resulted the fastest transport dynamics in PCF cells with a bead translocation rate of $v_{rt,PCF} = 0.44 \pm 0.03 \mu\text{m}/\text{min}$ ($n=21$). This was followed by moderate bead transport for MEF WT cells with $v_{rt,MEF} = 0.17 \pm 0.02 \mu\text{m}/\text{min}$ ($n=24$). The slowest dynamics regarding actin flow and bead locomotion were observed in B16 cells and resulted a velocity of $v_{rt,B16} = 0.097 \pm 0.006 \mu\text{m}/\text{min}$ ($n=36$). In figure 3.8 B) the gray bars of the histogram display the retrograde transport velocity of FN-functionalized beads coupled to the cytoskeletal actin flow. Controls with non-functionalized beads did not show a directed transport but were observed to move randomly across the membrane, a phenomenon that is probably due to thermal fluctuations, or to detach completely. The statistical analysis with a two-sided t-test demonstrated a significant difference between the retrograde transport velocities in the three examined cell types ($p < 0.0001$ for all cell lines).

3.3.4 Cell Migration Characteristics

With the retrograde actin flow characterization, dynamics within the cellular cytoskeleton were evaluated. In the following, the dynamics of individual cells are studied by monitoring their motility. It was demonstrated in previous studies, that the rearward directed F-actin flow contributes to cellular locomotion [Forscher *et al.* 1992, Fukui *et al.* 1999] and that retrograde flow of adhesion-related proteins occurs in adhesion sites as a response to cell migration [Guo & Wang 2007, Möhl *et al.* 2012].

B16, MEF WT and PCF cells were plated onto Petri dishes and were incubated for 2 h to allow cells to adhere and spread. The migratory behavior of the cell lines was monitored with time lapse microscopy. Phase contrast images were acquired every minute over a time course of 12 to 16 h.

Tab. 3.2: Traction forces, retrograde transport velocity v_{rt} and migration velocity v_m in B16, MEF WT and PCF cells. Forces were evaluated after a membrane-bead contact time of 300 s.

Cell type	Force [pN]	v_{rt} [$\mu\text{m}/\text{min}$]	v_m [$\mu\text{m}/\text{min}$]
B16	42 ± 2	0.097 ± 0.006	0.53 ± 0.03
MEF WT	81 ± 7	0.17 ± 0.02	0.45 ± 0.02
PCF	155 ± 10	0.44 ± 0.03	0.27 ± 0.03

The cell migration velocity v_m was derived by manual tracking of the nucleus and evaluation of the obtained trajectories.

Studies with PCF cells revealed a low motility of this cell line with typical migration velocities of $v_{m,PCF} = 0.27 \pm 0.03 \mu\text{m}/\text{min}$ ($n = 68$). Faster migration rates were observed for MEF WT cells, migrating with a velocity of $v_{m,MEF} = 0.45 \pm 0.02 \mu\text{m}/\text{min}$ ($n = 59$). The highest motility of the investigated cell lines was displayed by B16 cells with $v_{m,B16} = 0.53 \pm 0.03 \mu\text{m}/\text{min}$ ($n = 52$) (table 3.2 and figure 3.8 B)).

In figure 3.8 B) the migration velocities for the three cell lines are denoted in red, showing a reciprocal relation toward retrograde transport velocities. The enhanced migration rates in B16 cells correlated with the lowest retrograde bead translocation of all cell lines. Conversely, PCF cells displayed a minor motility concomitant with a rapid retrograde transport rate (table 3.2 and figure 3.8 B)).

3.3.5 Correlation of Forces and Dynamics in Different Cell Lines

Identical, standardized experimental conditions were realized for all force, actin flow and motility experiments in the cell line comprehensive study. As a consequence, the presented study allows to compare the relation of adhesion forces of three distinct cell lines with their retrograde actin flow dynamics and their motility. A correlation of traction forces and retrograde actin flow has been demonstrated with isolated cell lines in previous studies [Jurado *et al.* 2005, Gardel *et al.* 2008, Fournier *et al.* 2010] as well as an inverse relation of retrograde flow and cell motility [Guo & Wang 2007, Shih & Yamada 2010]. Here, results derived for all three parameters are compared for the three investigated cell lines.

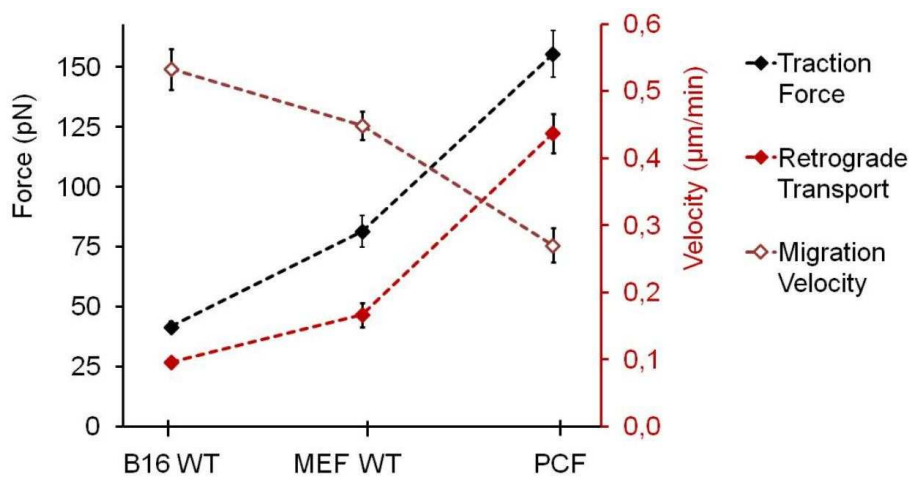


Fig. 3.9: Comparison of B16, MEF WT and PCF cells

Traction force, retrograde transport velocity, and cell motility of the investigated cell types showed a characteristic correlation: Cell lines were ordered with regard to their retrograde transport velocity and a linear relation was found between transport velocity and traction force. Migration velocity behaved reciprocal to the two other quantities. The membrane-bead contact time for force evaluation was 300 s

The results of the data analysis of all cell lines regarding force, actin flow, and migration velocity are illustrated in figure 3.9. Cells were aligned in ascending order according to the traction forces they exerted after 300 s of bead contact (denoted in black). Velocities are marked red, with the retrograde transport velocity displayed in solid squares and the migration velocity denoted with empty squares.

A comparison of B16, MEF WT and PCF cells identified a linear correlation of force and retrograde transport velocity for all cell lines: A high retrograde transport velocity was coinciding with strong cellular traction forces (compare table 3.2). In section 3.2.3, the adhesion strength and actin dynamics within distinct areas of a single cell were evaluated and resulted an analogous linear dependence. There, cellular areas with high dynamics, such as protrusions, were observed to exert the highest traction forces.

In contrast to this, a reciprocal behavior of migration velocity with respect to adhesion force and retrograde transport dynamics was observed. For instance, B16 cells exhibited low adhesion forces and featured a slow retrograde actin flow, whereas their motility was enhanced.

Summarizing these findings, the presented measurements are in good agreement with data previously published in the literature and confirm these results in a multiple cell line study [Jurado *et al.* 2005, Guo & Wang 2007, Gardel *et al.* 2008, Fournier *et al.* 2010, Shih & Yamada 2010, Möhl *et al.* 2012].

3.4 The Role of Vinculin in Cell-Substrate Adhesions

In the previous section, several WT cell lines have been studied with regard to their force transmission at cell-substrate adhesion sites, their retrograde actin flow rates, and their motility. The following investigations consider the effect of vinculin on cellular traction, motility, and retrograde actin flow.

Focal adhesions are multi-protein complexes formed to connect the cellular cytoskeleton with the surrounding ECM (for details see chapter 1.2.3). One of the many proteins accumulating into those adhesion sites is vinculin. Vinculin is a multi-domain protein and offers binding sites for a variety of other proteins contributing to the formation of the protein adhesion plaque [Chen & Singer 1982, Humphries *et al.* 2007, Carisey & Ballestrem 2011]. The interactions of adhesion plaque-constituting proteins have been researched in a large number of studies. However, many causal connections relating protein interaction with force transmission and cellular dynamics still remain elusive.

With the *in vitro* study of a vinculin knockout cell line (MEF $\text{vin}^{(-/-)}$) and a MEF WT cell line, this work aims at investigating the role of vinculin in the constitution of adhesion sites and the complex process of traction force development and cell migration.

In the following, retrograde transport dynamics, cell motility, and cellular force development were studied in MEF $\text{vin}^{(-/-)}$ and MEF WT cells to characterize the influence of vinculin. The re-expression of native, full length GFP-tagged vinculin (vinFL) in vinculin deficient cells induced a rescue toward a WT phenotype. To determine the effect of specific vinculin domains on force development, MEF $\text{vin}^{(-/-)}$ cells were transfected to express GFP-fused vinculin proteins with mutations in various protein domains which induce well-defined conformational changes. Among the mutants studied here was a constitutively active protein conformation caused by attenuated head-to-tail binding (vinT12). A counterpart to this protein was a mutant with enhanced head-to-tail binding, enforcing a default autoinhibited conformation and thereby impairing talin binding (vinA50I). Another mutant protein lacking the entire tail domain (vin880) and thus binding sites for paxillin and F-actin was investigated to deduce the importance of these binding sites for vinculin recruitment into adhesion sites. With the comparison of these mutant proteins, the impact of the active versus inactive vinculin conformation on force development was studied. Furthermore, the specific influence of talin binding and the ability of vinculin to connect directly via its tail domain to the actin cytoskeleton was investigated (all mutations are described in detail in chapter 1.2.6).

3.4.1 Cell Shape and Focal Adhesions in MEF WT and Vinculin Deficient Cells

Compared to MEF WT cells, MEF $\text{vin}^{(-/-)}$ cells cultured on homogeneously FN-coated substrates showed a more roundish phenotype, enhanced motility, and smaller adhesion sites located mostly in the periphery (figure 3.10 A) and B); compare [Fernández *et al.* 1993, Coll *et al.* 1995, Baumann 2010]).

For a comparison of the morphology of adhesion sites in MEF WT and MEF $\text{vin}^{(-/-)}$ cells, both

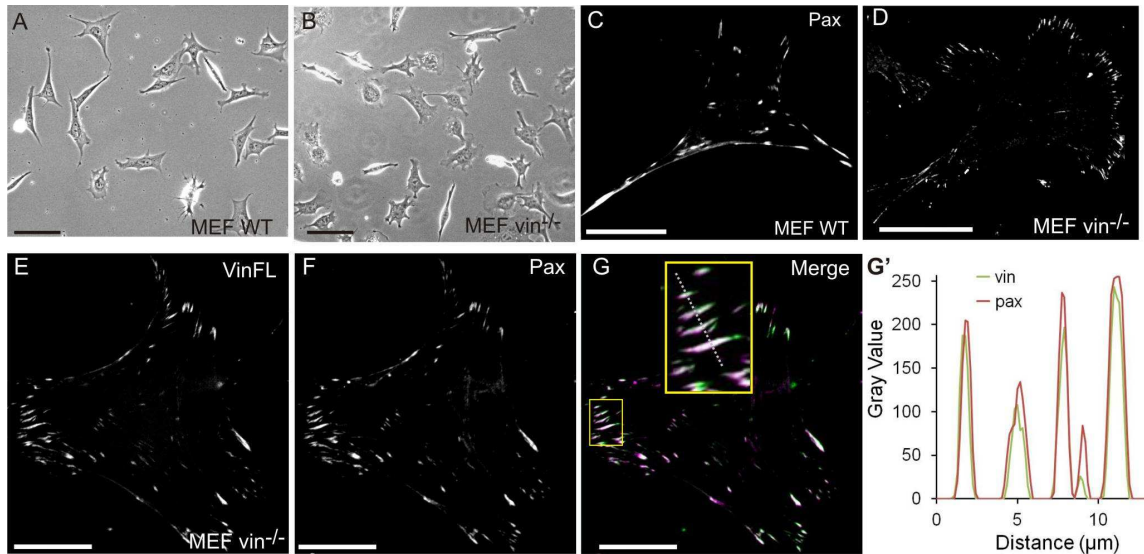


Fig. 3.10: Morphology of MEF WT and MEF *vin*^(-/-) cells and colocalization of vinculin and paxillin

A) Phase contrast images of MEF WT and B) MEF *vin*^(-/-) cells spread on a homogeneously coated FN substrate (scale bars = 70 μm). C) Immunostaining of paxillin in MEF WT cells and D) in MEF *vin*^(-/-) cells. E) MEF *vin*^(-/-) cells transfected to express native full length vinculin (vinFL) and F) immunostained for paxillin after fixation. G) A merger of vinculin (green) and paxillin (magenta) fluorescence images shows the colocalization of the two proteins within focal adhesion sites. G') Histogram of fluorescence intensities in the magenta and green channel (scale bars = 20 μm).

cell lines were immunostained for paxillin (figure 3.10 C) and D)). Paxillin is a protein that accumulates early into adhesion sites. To derive whether paxillin and vinculin retrace the focal adhesion shape identically, MEF *vin*^(-/-) cells were transfected to re-express vinculin and were subsequently subjected to paxillin staining. Paxillin is known as a marker for adhesion sites, including nascent adhesions, focal complexes, and focal adhesions, and binds to the C-terminal tail domain of vinculin.

The localization pattern of native full length vinculin (vinFL) in MEF *vin*^(-/-) cells is depicted in figure 3.10 E). The localization of immunostained paxillin (figure 3.10 F)) was compared to vinculin-GFP marked adhesions and the merger of the two fluorescence channels (figure 3.10 G)) was analyzed to deduce the overlap of vinculin (green) and paxillin (magenta) containing adhesion sites. To determine the colocalization of both proteins, intensity line profiles along focal adhesion sites were evaluated in the two respective channels for vinFL and paxillin with ImageJ. A close-up on a series of adhesion sites in the cell periphery is displayed in the inset of the merged image (figure 3.10 G)), with the dashed line marking a typical region of interest. As a measure for colocalization, the Pearson correlation coefficient was determined [Manders *et al.* 1992, Adler & Parmryd 2010]. The overlay of the intensity profiles in the marked area is presented in figure 3.10 G') and shows that vinculin and paxillin colocalize within adhesion sites. A slight color shift occurred in the overlay image of paxillin and vinculin channels, which might indicate an association of these proteins to different locations within individual adhesion sites. Further investigation with

high resolution microscopy is required to elucidate the observed effect. However, the colocalization is well-defined enough to assume that a paxillin staining reproduce focal adhesion morphology similar to vinculin, allowing a comparison of the two adhesion markers within the two cell types MEF WT and MEF $\text{vin}^{(-/-)}$.

The fluorescence images obtained for immunostained paxillin in MEF WT cells show elliptical adhesion sites located mainly in the cell periphery (figure 3.10 C)). In MEF $\text{vin}^{(-/-)}$ cells, paxillin staining reveals smaller and thinner adhesions as well occurring mainly in the cell periphery (figure 3.10 D)). Comparing adhesion sites of MEF $\text{vin}^{(-/-)}$ cells expressing vinFL and MEF WT cells, an identical adhesion morphology was found (compare figure 3.10 C) and F) and figure 3.15 F) and G) for a quantification). This gave evidence that the reintroduction of vinculin into MEF $\text{vin}^{(-/-)}$ cells was successful and restored adhesion site morphology to WT characteristics.

3.4.2 Retrograde Transport in MEF WT and MEF $\text{vin}^{(-/-)}$ Cells

FN-functionalized beads ($4.5 \mu\text{m}$ in diameter) were positioned on the apical cell membrane of the leading edge of MEF WT and MEF $\text{vin}^{(-/-)}$ cells and brightfield images were recorded with a frame rate of 0.5 Hz over a time course of 20 min. Figure 3.11 A) and C) depict phase contrast images of both cell lines and illustrate the different morphologies of MEF WT and MEF $\text{vin}^{(-/-)}$ cells, with MEF WT cells demonstrating a generally larger and more elongated shape than MEF $\text{vin}^{(-/-)}$ cells. The beads observed in the leading edge of the two cell lines showed distinct retrograde transport trajectories as indicated by the red lines in figure 3.11 A) and B). Bead movement on MEF WT cells (figure 3.11 A)) followed a straight trajectory from the leading edge to the nuclear region, while beads on MEF $\text{vin}^{(-/-)}$ cells (figure 3.11 B)) followed a zigzag course toward the nucleus. Additional examples of bead trajectories on vinculin expressing and vinculin deficient cells are illustrated in figure 3.11 A') and B'), respectively. The nonlinear trajectories were observed in 85 % of tested MEF $\text{vin}^{(-/-)}$ cells. In about 50 % of MEF $\text{vin}^{(-/-)}$ cells showing a zigzag trajectory, the lateral deviations from a linear path occurred only temporarily and alternated with partially straight transport trajectories. This is also displayed in figure 3.11 B) where the highly persistent trajectory in the beginning of the transport process was followed by a path of strong lateral deviations, which was followed again by a straight path.

The trajectories of beads on MEF WT ($n = 20$) and MEF $\text{vin}^{(-/-)}$ ($n = 18$) cells were analyzed in detail and typical examples of spatially resolved trajectory profiles are displayed in figure 3.12 A). Full length trajectories, recorded over the entire 20 min of measurement, are depicted with the blue inlets showing a close-up into the trajectory paths of the two cell lines. For MEF WT cells the bead trajectory remains highly linear even when analyzed with higher spatial resolution, indicating that the bead is stably linked to the underlying retrograde actin flow. In MEF $\text{vin}^{(-/-)}$ cells the zigzag course mentioned above was not only found in the long range transport over distances bigger than $1 \mu\text{m}$, but also in short distance traveling of the beads (shown in the blue inlet). This hints at an impaired linkage of the FN-functionalized bead to the retrograde actin flow or at an altered actin flow within the cell.

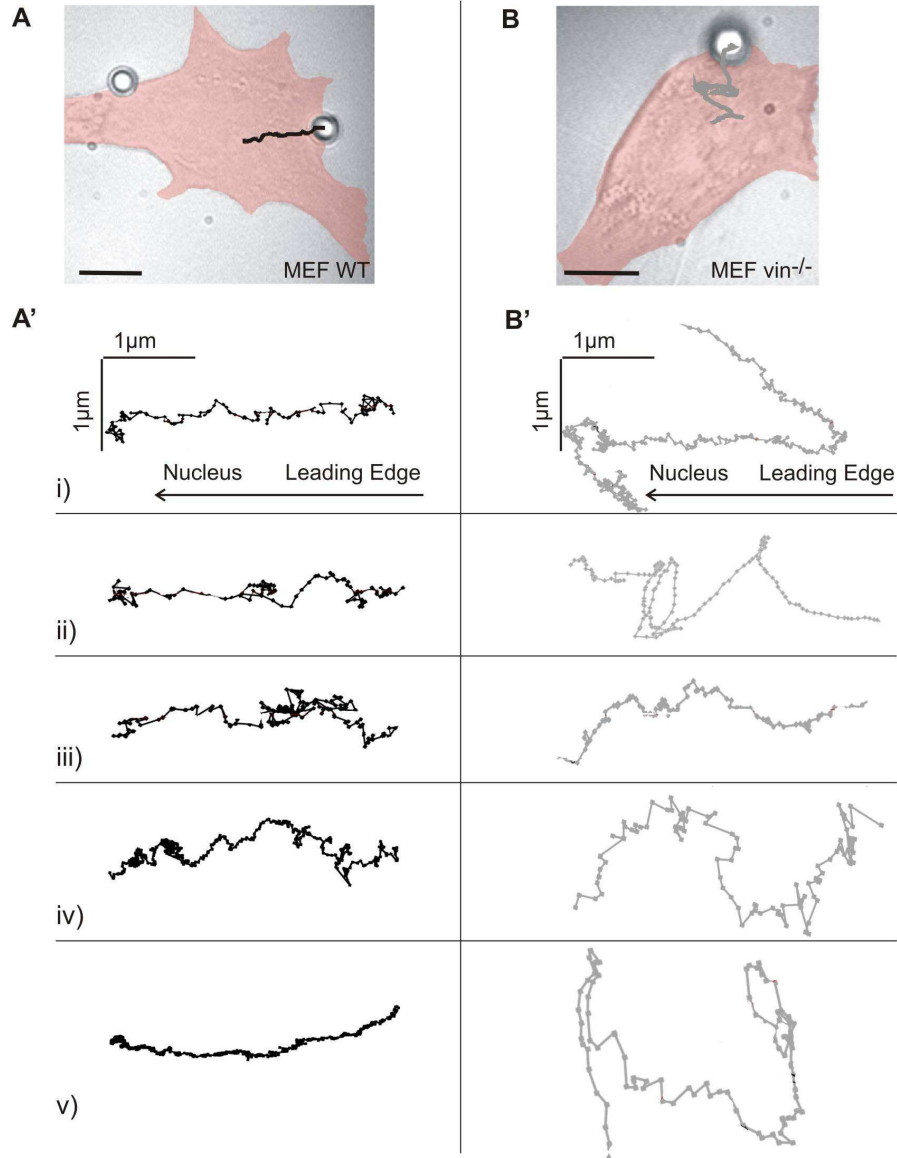


Fig. 3.11: Trajectories in MEF WT and MEF $vin^{(-/-)}$ cells

A) MEF WT and B) MEF $vin^{(-/-)}$ cell with a $4.5 \mu m$ diameter FN-coated bead locating to the leading edge. The black and gray traces denote the bead trajectories (cell bodies are visualized with a red overlay; scale bars = $10 \mu m$). A') and B') Example trajectories of beads displaying retrograde movement in MEF WT and MEF $vin^{(-/-)}$ cells.

The recorded retrograde transport trajectories were evaluated in regard to the bead velocity and directional persistence (figure 3.12 B)). For beads coupled to the retrograde flow in the lamella, the retrograde transport velocity amounted to $v_{rt,WT} = 0.17 \pm 0.02 \mu m/min$ in MEF WT cells and to $v_{rt,KO} = 0.34 \pm 0.06 \mu m/min$ in MEF $vin^{(-/-)}$ cells. Thus, when using the beads as readout the retrograde actin flow rate appeared doubled in MEF $vin^{(-/-)}$ cells compared to wild type cells.

A quantitative analysis of the directional persistence P of retrograde bead transport was performed for both cell lines (details are described in chapter 2.8.3). The directional persistence of the MEF WT cell line was determined as $P = 0.24 \pm 0.02$ and for the MEF $vin^{(-/-)}$ cells an aver-

age directional persistence of $P = 0.07 \pm 0.01$ was derived. As expected from the outline of the trajectories, the directional persistence in MEF WT cells was significantly higher compared to MEF $\text{vin}^{(-/-)}$ cells (figure 3.12 B)).

To test whether the rearward translocation characteristics of beads were position-dependent, the retrograde transport velocity in both cell lines was studied at more anterograde locations in cellular protrusions. Protrusions are formed in the foremost area of the leading edge and are a prerequisite for cell migration. The results for beads placed in this highly dynamic area are displayed in table 3.3: the retrograde actin flow was twice as fast in protrusions than in the leading edge and lamella. This correlation held true for both cell lines. As already seen in the evaluation of v_{rt} in the lamella, bead transport in protrusions of MEF $\text{vin}^{(-/-)}$ cells was also about twice as fast as in MEF WT cells. This indicates that the actin polymerization in the leading edge area is subjected to alterations, which are possibly due to the lack of vinculin.

The observed changes in retrograde transport characteristics of microscopic beads suggest that

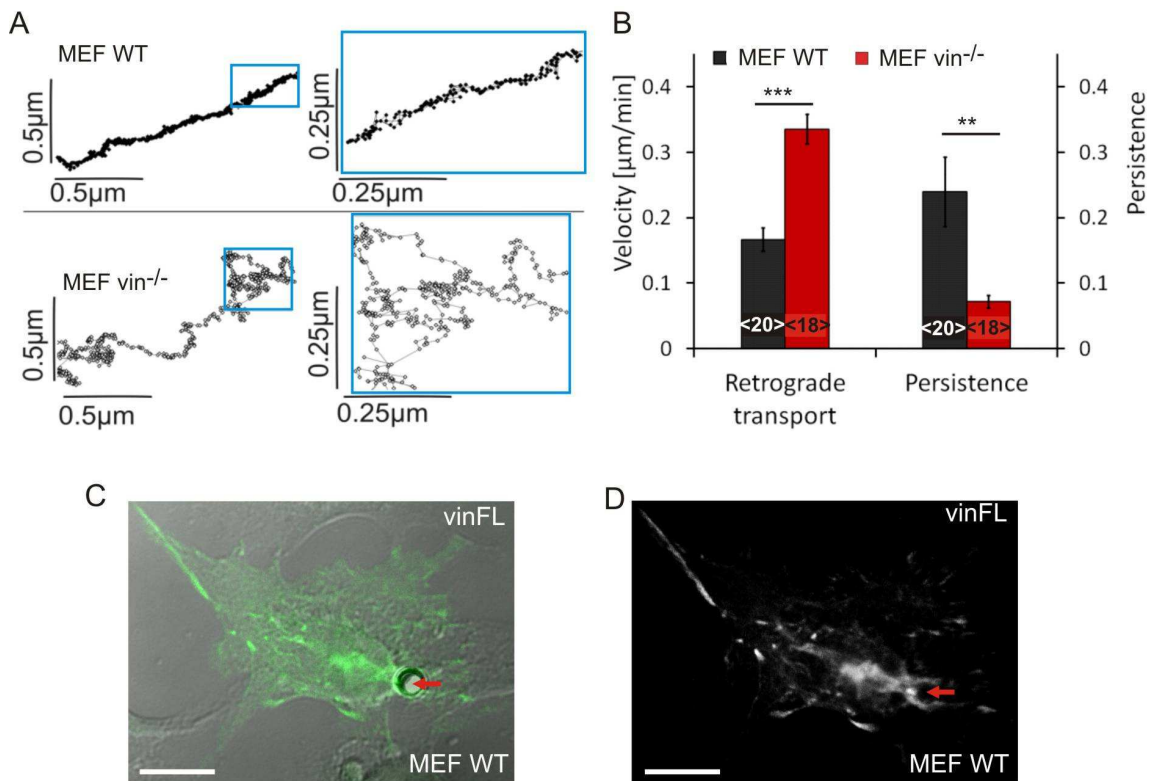


Fig. 3.12: Retrograde transport in MEF WT and MEF $\text{vin}^{(-/-)}$ cells

A) shows the retrograde transport trajectories of MEF WT and MEF $\text{vin}^{(-/-)}$ cells with a close-up of the marked area. Beads positioned on MEF WT cells were transported rearward with a high directional persistence while transport on MEF $\text{vin}^{(-/-)}$ cells followed a zigzag course toward the nucleus. B) Retrograde transport in MEF $\text{vin}^{(-/-)}$ cells was enhanced by a factor of two, while the directional persistence was reduced by a factor of three. C) Overlay of DIC and fluorescence channel of an LSM image showing a FN-functionalized bead of $4.5 \mu\text{m}$ diameter on the leading edge of a MEF WT cell expressing vinFL . D) shows a 3D projection of vinculin-GFP localization and depicts a ring-like accumulation of the protein along the bead perimeter. Red arrows indicate the membrane-bead interface area (scale bars = $10 \mu\text{m}$).

vinculin does play a considerable role in mediating the linkage of the ligated integrins to the intracellular actin flow. As vinculin recruitment is proposed to require a certain tension across an adhesion cluster, this result was unanticipated. Therefore, it was tested if the effect of vinculin on retrograde flow could be due to a direct interaction of vinculin in the adhesion site forming at the bead-membrane interface. The accumulation of vinculin at membrane-bead contact sites without the application of external forces was analyzed in MEF WT cells that were transfected to express vinFL and were supplied with FN-functionalized beads. The beads were not positioned with optical traps but were allowed to float down onto the cell surface. For an attachment time of 20 minutes the cells were incubated with the beads under standard culture conditions (chapter 2.3.2) and were subsequently fixed and embedded in mounting media for confocal microscopy analysis. Figure 3.12 C) is an overlay of the DIC and fluorescence imaging channels and displays a vinFL expressing MEF WT cell with a bead positioned on the lamella. In 3.12 D), the formation of a circular vinculin structure around the bead perimeter is depicted. The localization of vinculin at bead contact sites without application of external forces was found in about 50 % of examined cells and shows that vinculin can accumulate without the prerequisite of external forces. A potential explanation for this is the mechanical inertia of the beads which possibly offers enough resistance for the application of low cellular traction forces. These findings suggest that vinculin recruitment to membrane-bead contact sites is not negligible even if no external forces are applied.

Tab. 3.3: Retrograde transport velocity and directional persistence in MEF WT and MEF $\text{vin}^{(-/-)}$ cells

Cell Type	v_{rt} [$\mu\text{m}/\text{min}$] Lamella	v_{rt} [$\mu\text{m}/\text{min}$] Protrusion	Directional Persistence
MEF WT	0.17 ± 0.02	0.36 ± 0.04	0.24 ± 0.02
MEF $\text{vin}^{(-/-)}$	0.34 ± 0.06	0.64 ± 0.09	0.07 ± 0.01

3.4.3 Comparison of Cellular Dynamics and Forces in MEF WT and MEF $\text{vin}^{(-/-)}$ cells

In section 3.3.2 the relation of force, retrograde transport velocity, and cell motility has been characterized for the wild type cell lines MEF WT, B16 and PCF. For these three cell lines it was shown that a monotone relation exists between the tension exertion in adhesion sites and the retrograde actin flow velocity. Furthermore, the cell migration velocity was found to behave reciprocal toward force and retrograde transport dynamics. These correlations held true for all three WT cell lines. Here, the relation of dynamics and force generation is examined for the vinculin deficient MEF $\text{vin}^{(-/-)}$ cell line and is compared to the results obtained for the respective MEF WT cell line to determine the relevance of vinculin expression for the observed correlations.

Cellular traction forces were measured over a time course of 300 s in both MEF WT and MEF $\text{vin}^{(-/-)}$ cells. In figure 3.13, forces transmitted after a bead contact interval of 300 s are displayed, showing traction forces of $F_{WT} = 84 \pm 4 \text{ pN}$ for MEF WT cells. The contractility of MEF $\text{vin}^{(-/-)}$ cells amounted to $F_{\text{vin}^{(-/-)}} = 34 \pm 4 \text{ pN}$, corresponding to a force reduction of more than 50% compared to the WT cell line. The reduction of traction force onto the ECM was an expected effect of vinculin deficiency, as vinculin is known to be required for reinforcement of adhesion sites by interlinking the membrane-adjacent proteins with the actin cytoskeleton [Alenghat *et al.* 2000, Humphries *et al.* 2007, Möhl *et al.* 2009, Peng *et al.* 2011].

The migration velocity v_m of MEF WT and MEF $\text{vin}^{(-/-)}$ cells was derived from time lapse imaging over 12 h to 16 h with a recording rate of 1 frame per minute. With a migration rate of $v_m = 0.84 \pm 0.05 \mu\text{m}/\text{min}$, MEF $\text{vin}^{(-/-)}$ cells displayed a two-fold increase in motility compared to MEF WT cells with $v_m = 0.45 \pm 0.02 \mu\text{m}/\text{min}$.

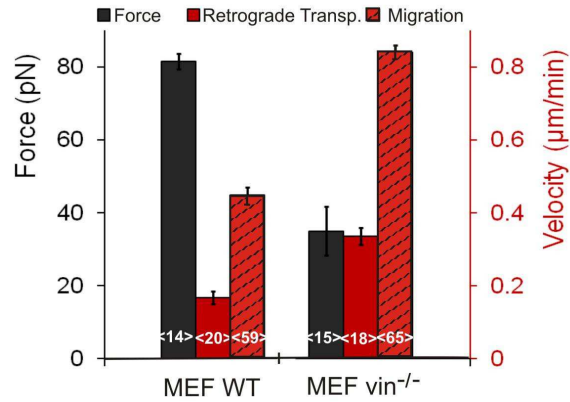


Fig. 3.13: Comparison of MEF WT and MEF $\text{vin}^{(-/-)}$ cells

Force, retrograde transport velocity v_{RT} and migration velocity v_m in MEF WT and MEF $\text{vin}^{(-/-)}$ cells. Force transmission was evaluated after 300 s of bead contact and was about 50% reduced in MEF $\text{vin}^{(-/-)}$ cells (numbers in bars denote the number of experiments).

These results are consistent with the reciprocal relation regarding force and migration described in section 3.3.2 for wild type cell lines. On the contrary, retrograde transport dynamics of FN-functionalized beads in the leading were enhanced, coinciding with accelerated retrograde flow rates in MEF $\text{vin}^{(-/-)}$ cells. In this respect, no validation of the correlation between traction force and actin-related dynamic characteristics found in wild type cell lines was obtained.

3.4.4 Traction Force Rescue of MEF $\text{vin}^{(-/-)}$ Cells by Vinculin Reintroduction

Vinculin deficiency leads to cellular malfunction with regard to force development, retrograde actin flow and cell migration. To assess whether these defects were purely due to the vinculin deficiency and did not originate from side-effects of the knockout procedure itself, MEF $\text{vin}^{(-/-)}$ cells were transiently transfected to express a native full length vinculin-GFP (vinFL) fusion protein. It was first proven by Xu et al. that re-expression of intact full length vinculin in knockout cells restores wild type characteristics with regard to cellular locomotion and adhesiveness [Xu *et al.* 1998b].

In this work, force transduction in MEF WT, MEF $\text{vin}^{(-/-)}$, and vinFL expressing MEF $\text{vin}^{(-/-)}$ cells was studied with a focus on adhesion forces at different time points. The force development in individual adhesion sites was deduced with optical tweezers force spectroscopy and compared to the overall adhesion strength of single cells derived from AFM measurements. AFM single-cell force spectroscopy (SCFS) was conducted and evaluated by Dr. Clemens Franz and his group (Young Scientist Group Nanobiology of the DFG-Center for Functional Nanostructures (CFN) at the KIT, Karlsruhe).

To induce a rescue, MEF $\text{vin}^{(-/-)}$ cells were transfected by electroporation and incubated under routine conditions for 16 h to 20 h to express the vinFL protein. As displayed in figure 3.10 A), vinFL expressing MEF $\text{vin}^{(-/-)}$ cells developed a similar focal adhesion morphology as MEF WT cells, indicating the expression of fully functional vinculin proteins.

The recording of optical tweezers (OT) force curves in MEF WT, MEF $\text{vin}^{(-/-)}$, and vinFL expressing MEF $\text{vin}^{(-/-)}$ cells was conducted with 4.5 μm diameter FN-coated beads placed on the leading edge of the cells. MEF $\text{vin}^{(-/-)}$ cells expressing vinFL exerted the same forces over the complete course of measurements as MEF WT cells (figure 3.14 A)). The statistical evaluation of the two force curves yielded no significant differences in force transmission and confirmed the success of the vinculin rescue in MEF $\text{vin}^{(-/-)}$ cells expressing vinFL.

Regarding MEF $\text{vin}^{(-/-)}$ cells, force transmission initially (first 30 s) developed similar to MEF WT cells as can be deduced from the force curves in figure 3.14 A) and the histogram in B). After 60 s of bead contact, traction forces in MEF $\text{vin}^{(-/-)}$ cells started to deviate from MEF WT cells and hardly continued the reinforcement of cell adhesion sites. Force transduction measured after 120 s was 50 % reduced compared to MEF WT and vinFL expressing MEF $\text{vin}^{(-/-)}$ cells, a relation that remained almost constant until the end of the investigated time course of 300 s (figure 3.14 B)).

Complementary experiments were conducted by Dr. C. Franz with AFM-SCFS (setup described in [Franz *et al.* 2007]) to derive the overall adhesion strength of an isolated cell to the substrate. The substrate was FN-coated and a cantilever was used to pick up a cell for the experiment (figure 3.14 C)). The cell was then lowered to the substrate (phase I; figure 3.14 D)) and brought in contact with it for a defined period of time (phase II). Subsequently, the cantilever was slowly retracted and the cell was forced to detach from the substrate (phase III).

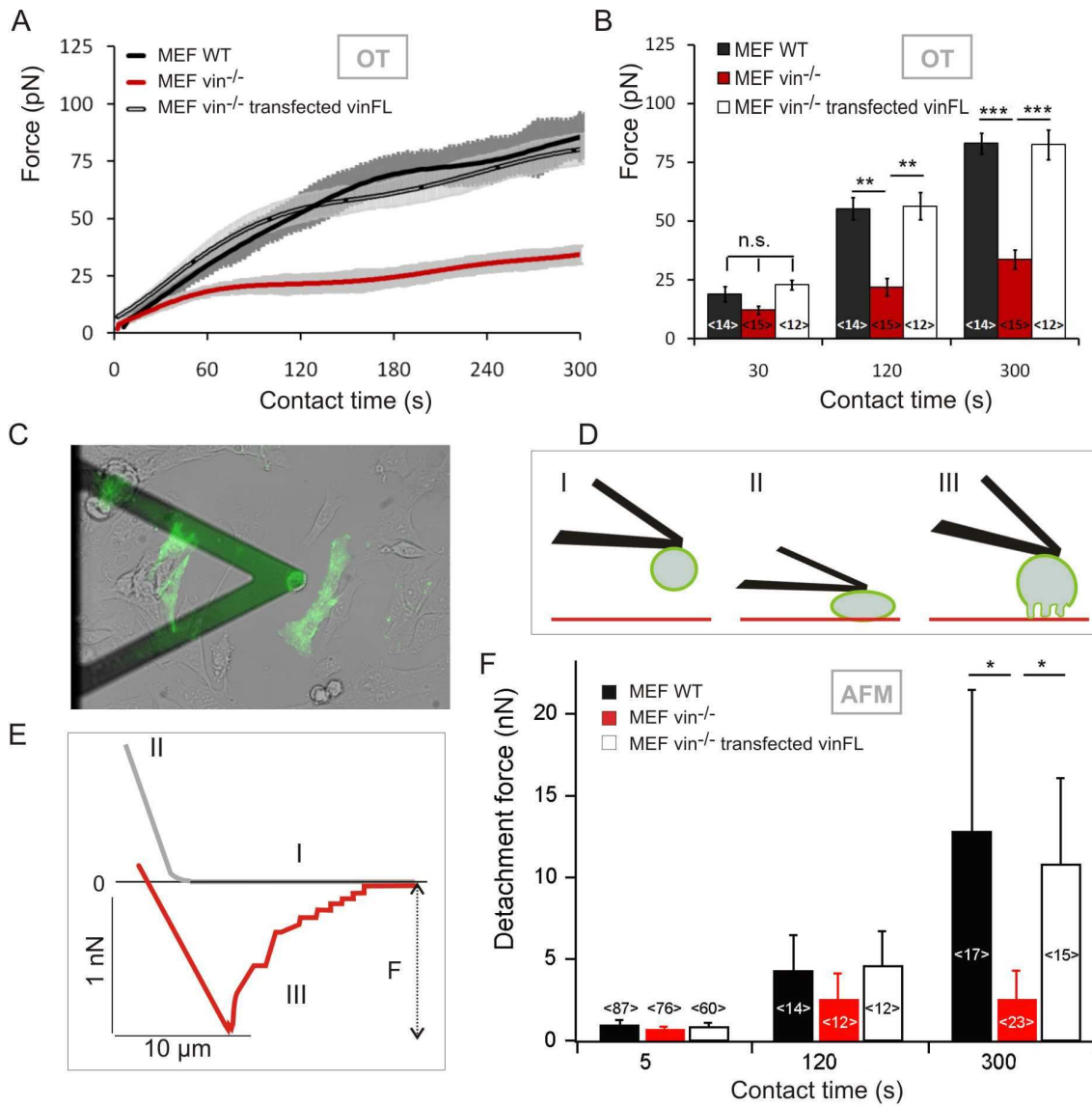


Fig. 3.14: Force development after vinculin rescue

MEF $vin^{-/-}$ cells were transfected to express the native full length vinculin protein vinFL. A) Optical tweezers (OT) derived force development over a time course of 300 s in MEF WT, MEF $vin^{-/-}$ and vinFL expressing MEF $vin^{-/-}$ cells; MEF $vin^{-/-}$ cells transfected to express vinFL showed the same behavior as MEF WT cells during the entire measurement time (force curves were smoothed with the FFT filter tool in Origin, gray background denotes the SEM). B) Histogram of force transmission at distinctive contact times (mean \pm SEM; numbers in bars denote the number of experiments). C) Overlay of a DIC with a fluorescence image showing an AFM cantilever with a vinculin-GFP expressing cell attached to the tip (image courtesy of Dr. C. Franz). D) Sketch of the atomic force microscopy (AFM) single cell force spectroscopy method: I. Approach phase: a single cell is picked up with the cantilever and is lowered to the substrate; II. Contact phase: the cell is brought into contact with the substrate for a predefined time; III. Detachment phase: the cantilever is retracted and the cell detaches from the substrate. E) Schematic of a typical AFM force-distance curve for cantilever approach (gray) and retraction (red) with F denoting the detachment force of an entire cell. F) Detachment forces of single cells measured for MEF WT, MEF $vin^{-/-}$ and MEF $vin^{-/-}$ cells expressing vinFL (mean \pm mean absolute error; histogram courtesy of Dr. C. Franz).

A typical force-distance curve obtained with AFM-SCFS is displayed in 3.14 E), where the three phases of approach (I), contact (II) and detachment (III) are denoted (gray: cantilever approach, red: cantilever retraction). The force steps occurring during the retraction of the cantilever are due to the rupture of individual cell-surface contacts and add up to the overall detachment force. The histogram in figure 3.14 F) depicts the overall detachment forces of MEF WT, MEF $\text{vin}^{(-/-)}$ and vinFL expressing MEF $\text{vin}^{(-/-)}$ cells for cell-surface contact times of 5 s, 120 s and 300 s. After 5 s, the detachment forces were low (about 1 nN) for all cell types as the cells were only able to form small initial contacts with the substrate. Increasing the contact time to 120 s, detachment forces were slightly larger for MEF WT and vinFL expressing MEF $\text{vin}^{(-/-)}$ cells compared to MEF $\text{vin}^{(-/-)}$ cells. A lack of adhesion reinforcement in MEF $\text{vin}^{(-/-)}$ cells became obvious after 300 s of cell-substrate contact: Here, the overall adhesion strength of MEF $\text{vin}^{(-/-)}$ cells was about four-fold reduced compared to MEF WT and vinculin rescued cells. This was also demonstrated by Baumann in her diploma thesis [Baumann 2010].

Comparing the data obtained with AFM-SCFS and OT force spectroscopy, two different size and force regimes were accessible and the similarities of the results derived from the two methods were striking: Both approaches deduced a fast increase in adhesion strength in the initial 120 s of cell-substrate contact and both showed a strong reduction of MEF $\text{vin}^{(-/-)}$ force transduction. In the early phase of cell-substrate contact formation examined in this two studies, individual contacts showed the same characteristics in force development as the entire cell. The overall adhesion strength of a single cell, measured by AFM-SCFS, was found to be about 150 times larger than the adhesion strength in an individual contact site, measured by OT force spectroscopy. Both studies showed that the reintroduction of a fully functional vinculin protein restores the force transmission characteristics of the vinculin deficient cell line and renders it indistinguishable from wild type cells.

3.4.5 Effect of Distinct Vinculin Mutants on Force Development

Earlier studies on mutant vinculin expressing cells have revealed a variety of interaction partners of the macromolecule and have discussed their involvement in focal adhesion formation [Humphries *et al.* 2007, Diez *et al.* 2011]. The crystal structure of the protein has been described by Bakolitsa and coworkers, who also performed a calorimetric analysis of vinculin and ligated complexes and determined possible binding sites and activation processes for several ligands [Bakolitsa *et al.* 2004]. While some studies addressed the question of the rheological characteristics of native and mutant vinculin expressing cells [Diez *et al.* 2011] others discussed the rupture forces of mature adhesion sites [Mierke & Kollmannsberger 2008].

The work presented here aims at allocating specific functions of vinculin during early cell adhesion formation to distinct structural domains of the macromolecule. Of special interest was the impact of the vinculin conformation on force transduction to the ECM.

To study the influence of specific vinculin domains on adhesion formation and force regulation, MEF $\text{vin}^{(-/-)}$ cells were transfected to express vinculin proteins featuring mutations in various func-

tional domains. Native vinFL was expressed to induce the vinculin rescue in MEF vin^(-/-) cells as described in section 3.4.4 and was compared to cells expressing the GFP-fusion proteins vinT12, a constitutively active full length mutant (a schematic of the mutants is given in figure 3.15 E)). To test the importance of vinculin-talin binding, vinA50I, a protein with point mutations amplifying the head-tail association and thereby reducing the talin binding affinity, was introduced into MEF vin^(-/-) cells. The mutant vin880, a protein lacking the tail domain and thus binding sites for F-actin, paxillin, PIP₂, PKC α , and the vinculin head domain, was expressed to investigate the effect of inhibited binding to the cytoskeleton (for more detailed information on vinculin mutants refer to chapter 1.2.6). In figure 3.15 A) to D) fluorescence images of MEF vin^(-/-) cells expressing the described proteins are depicted.

Tab. 3.4: Overview of vinculin mutant characteristics

vinFL	native, full length vinculin
vinT12	constitutively active: no binding between head and tail domain
vinA50I	constitutively autoinhibited: reduced binding to talin, α -actinin, F-actin
vin880	tail truncated mutant: no binding to F-actin, paxillin, PIP ₂

Adhesion Morphology of MEF vin^(-/-) Cells Expressing Mutant Vinculin

Adhesion sites containing the vinFL protein displayed the same morphology as focal adhesions in MEF WT and were similarly located in the cell periphery (figure 3.15 A)).

In cells expressing constitutively active vinT12, the same adhesion morphology was found, but the number of adhesion sites was increased and uniformly distributed throughout the basal cell surface (figure 3.15 B)). Cell adhesions in the periphery were larger and more elongated than those found in the central area. The uniform distribution and the small, roundish shape of adhesion sites in the cell center might be due to the permanent exposure of binding sites in the active vinculin conformation: usually the cytoplasm contains an inactive vinculin pool but as a result of the permanent accessibility of vinT12 binding sites [Cohen *et al.* 2005], the constitution of new adhesion sites might be induced from cytoplasmic vinculin.

VinA50I localized with a high cytosolic fraction and only few cell-substrate adhesions were formed, all of them in the cell periphery (figure 3.15 C)). The morphology of the limited number of adhesion sites constituted by this protein resembled MEF WT adhesions. As the vinA50I mutant is known to have a reduced talin affinity [Bakolitsa *et al.* 2004], the high cytosolic concentration of this protein indicated that talin is required to successfully incorporate vinculin into adhesion sites. This was also demonstrated by Humphries and coworkers [Humphries *et al.* 2007]. Talin is an adhesion-related protein and has been proposed as a mediator of the initial coupling of the cytoplasmic integrin domain to the actin cytoskeleton and allows for low force transmission [Jiang *et al.* 2003, Margadant *et al.* 2011].

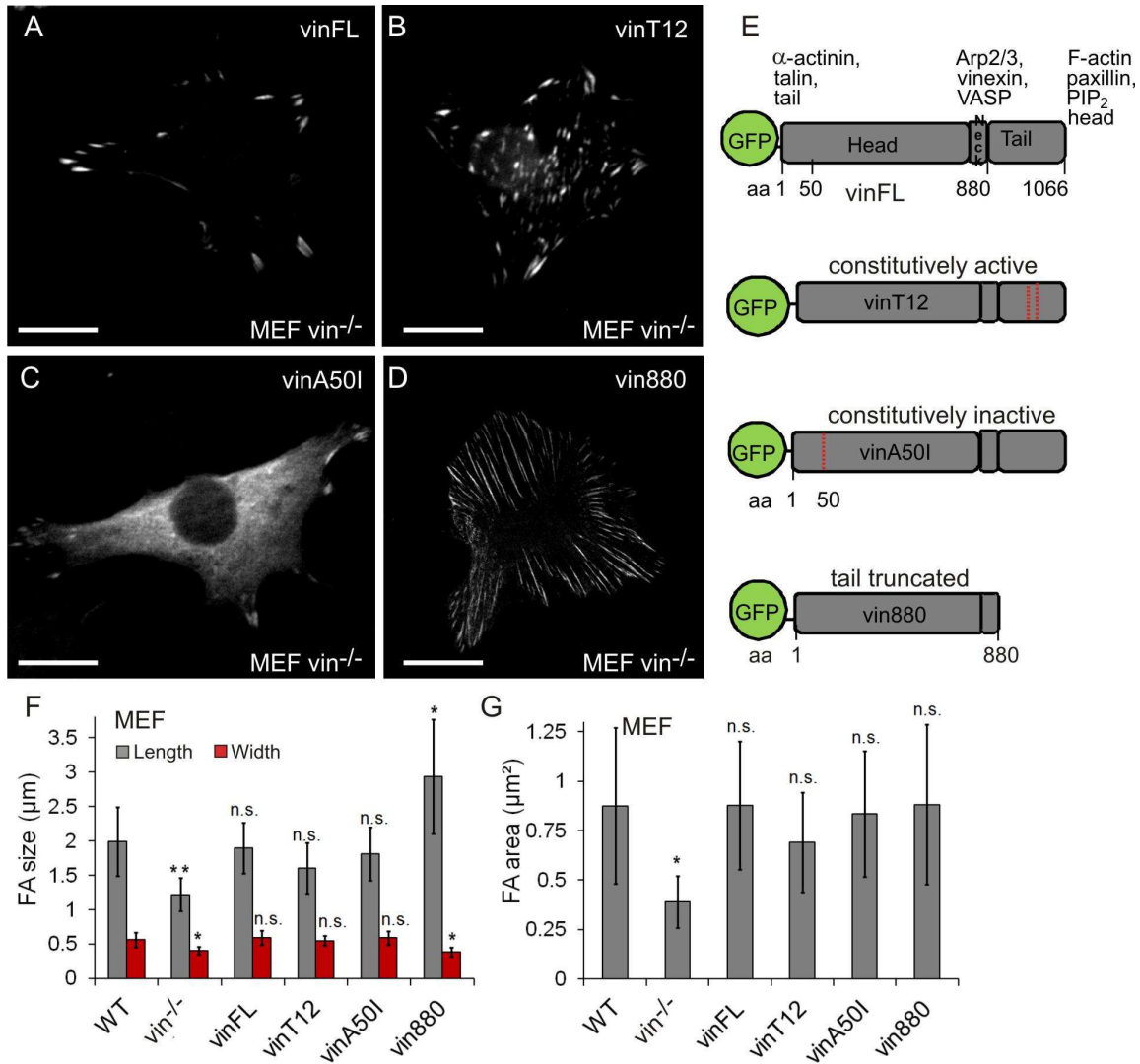


Fig. 3.15: Expression patterns of vinculin and quantification of focal adhesion morphology
 MEF $\text{vin}^{-/-}$ cells were transfected to express A) native full length vinculin (vinFL), B) constitutively active full length vinculin (vinT12), C) constitutively autoinhibited vinculin (vinA50I) and D) tail domain truncated vinculin (vin880). E) Schematic of the expressed vinculin proteins; point mutations are denoted in red. F) and G) show the quantification of focal adhesion (FA) morphology (t-test in comparison to WT cells). FA size was quantified with regard to GFP-tagged vinculin localization and immunostained paxillin (the latter in MEF $\text{vin}^{-/-}$ cells only) (error bars denote the SEM, number of evaluated cells $n=10-15$).

MEF $\text{vin}^{-/-}$ cells expressing vin880 exhibited strongly elongated adhesion sites (figure 3.15 D)). Although this protein did not comprise any binding sites for paxillin or actin, it accumulated normally into adhesion sites, indicating that a direct interaction with paxillin is not required for vinculin recruitment. Neither does a direct connection to the actin cytoskeleton play a role for the association of vinculin with adhesion sites. This indicates that the tail domain is not involved into vinculin recruitment; instead, recruitment is mediated by the head and/or neck domain of the protein.

The size of cell-substrate contacts for the expression of various vinculin proteins was quantified and compared to MEF WT cells (figure 3.15 F) and G)). The data given in F) represent the width and length of the elliptical adhesion complexes. In general, a large size variation was found within each cell type as the elongation of adhesion sites strongly depended on the state of maturation of the individual contact sites. However, a significant reduction of adhesion length and width was found in paxillin labeled MEF $\text{vin}^{(-/-)}$ cells. In MEF $\text{vin}^{(-/-)}$ cells expressing $\text{vin}880$, a considerable elongation of adhesion sites was concomitant with a thinning of the structures. Adhesion sites in MEF WT cells, vinFL , vinT12 , and vinA50I expressing MEF $\text{vin}^{(-/-)}$ cells showed the same morphology with regard to the length and width of the elliptical accumulation patterns.

The evaluation of the area covered by an individual adhesion site revealed a reduced adhesion area in MEF $\text{vin}^{(-/-)}$ cells, compared to MEF WT adhesion sites. In contrast, all vinculin expressing cells were indistinguishable from the wild type adhesion characteristics (figure 3.15 G)). The small adhesion area in MEF $\text{vin}^{(-/-)}$ cells signified that vinculin is required for the maturation process of the adhesion sites and for the recruitment of additional adhesion-related proteins. The mutant $\text{vin}880$ protein induced elongated but thinner adhesions compared to MEF WT cells, which resulted in the same adhesion area as observed in all vinculin expressing cell lines.

The expression patterns of the various vinculin proteins allowed the allocation of different functions to the vinculin domains:

- Talin binding to the head domain is essential to attract vinculin into the protein adhesion plaque [Johnson & Craig 1994].
- Head to tail binding, converting vinculin into its inactive conformation, regulates the spatial distribution of adhesion sites and possibly prevents the formation of extensive matrix contacts away from the periphery.
- The C-terminal tail domain mediates the morphology of adhesion sites with its absence leading to strongly elongated and thinned adhesions.
- A direct interaction between the vinculin tail domain and paxillin or actin is no prerequisite for vinculin recruitment into adhesion sites.

Force Transmission in Cells Expressing Various Mutant Vinculin Proteins

Contractile forces applied to FN-functionalized beads simulating individual contact sites were analyzed with OT force spectroscopy to characterize MEF $\text{vin}^{(-/-)}$ cells expressing the described vinculin mutants. The results obtained with this method were compared to data on the overall detachment force of an entire cell from its substrate. These measurements were conducted with AFM-SCFS by Dr. Clemens Franz and his group, who also processed the raw data.

In figure 3.16 A), the force transmission of transfected cells onto a FN-functionalized bead, measured by OT force spectroscopy, is depicted over a time course of 300 s. In the initial formation

phase of new adhesion sites (first 30 s of membrane-bead contact), the force development was similar for all vinculin mutant expressing MEF $\text{vin}^{(-/-)}$ cells. This is also shown in the histogram in figure 3.16 B) where the data from the force curves are statistically analyzed for a particular contact time. With advancing contact time, the force curves for the distinct vinculin proteins became distinguishable: after 60 s, force transmission at vinFL incorporating adhesion sites was stronger than at all other vinculin mutant containing adhesion sites and after 120 s force development was clearly discriminable for each mutation. The vin880 protein developed the lowest reinforcement of adhesion sites over the entire time course of 300 s while the adhesion strength of vinFL and vinT12 expressing cells was highest. VinA50I expressing MEF $\text{vin}^{(-/-)}$ cells remained in an intermediate force range: they developed stronger adhesions than vin880 expressing cells but did not match the force transmission of the native protein (figure 3.16 A) and B)).

A surprising finding was that the constitutively active vinT12 protein matched the vinFL adhesion

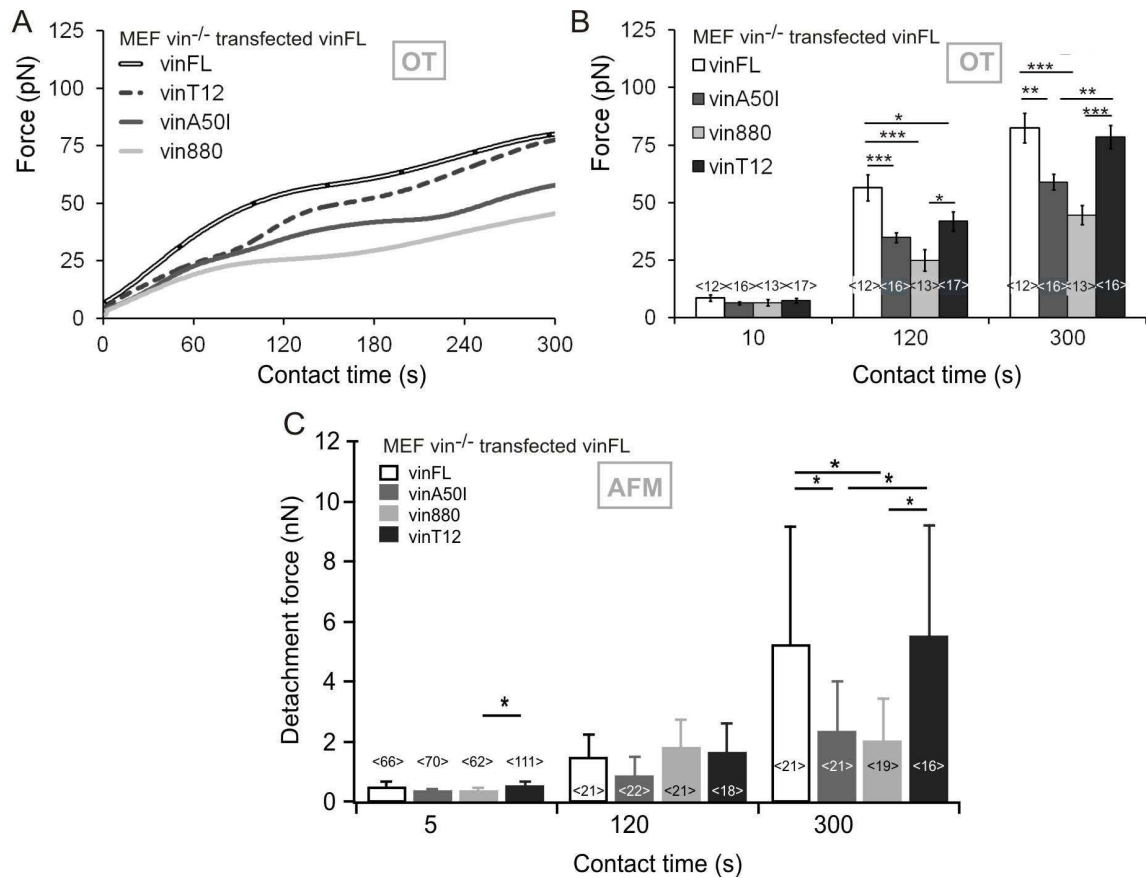


Fig. 3.16: Force development in cells expressing various mutant vinculin proteins

A) Optical tweezers (OT) force curves for MEF $\text{vin}^{(-/-)}$ cells transfected to express the proteins vinFL, vinT12, vinA50I, and vin880. The constitutively active vinT12 mutant showed a complete force recovery after 300 s. In the early force transmission phase, vinT12 behavior tended more toward MEF $\text{vin}^{(-/-)}$ cell behavior than to the vinFL rescue. B) Analysis of the OT force curve data at a particular time (mean \pm SEM). No rescue was obtained for vin880 expressing cells over the entire measurement while force transmission in vinA50I expressing cells reached an intermediate force level between rescue and MEF $\text{vin}^{(-/-)}$ cells. C) Overall detachment force of isolated cells on vitronectin substrates determined by atomic force microscopy (AFM) (histogram courtesy of Dr. C. Franz).

strength only after about 240 s. In the early membrane-bead adhesion phase of the first 90 s the protein described the same force curve as the less reinforced mutants *vin880* and *vinA50I*. Between 90 and 240 s the force transmission of *vinT12* comprising adhesion sites was gaining fast until it reached the same strength as *vinFL* expressing cells (figure 3.16 A) and B)).

The overall detachment force of cells expressing the different vinculin mutants was measured by AFM-SCFS and is depicted in figure 3.16 C). As in the OT measurements, force development for short cell-substrate contact times (5 s) was low for all mutants. Detachment forces of the cells after 120 s of substrate contact were increased but all mutants still showed similar adhesion strength. Only after a contact time of 300 s did the *vinFL* and *vinT12* proteins develop stronger detachment forces, which were about twice as strong as those measured for *vin880* and *vinA50I* expressing cells. The *vinFL* and *vinT12* expressing cells showed similar adhesion forces of about 5 nN while *vin880* and *vinA50I* expressing cells exhibited an equally reduced adhesion strength of about 2 nN.

Comparing the results obtained for the traction forces of individual adhesion sites and the detachment forces of entire cells, a general correlation was found inasmuch as the *vinFL* and *vinT12* proteins exhibited the strongest forces after 300 s. This exceeded force transmission of *vin880* proteins by about 100 %. Although the OT measurements revealed a considerable increase in adhesion strength of *vinA50I* expressing cells compared to *vin880*, this behavior was not explicitly seen with the AFM experiments.

Collectively, the results from OT and AFM force spectroscopy expose well-defined adhesion characteristics for the distinct mutations in the vinculin helical domains. None of the mutations has an effect on the initial force transmission at adhesion sites, correlating with the finding that vinculin is recruited with a retardation and in a force-dependent manner into newly formed adhesion sites [del Rio *et al.* 2009, Galbraith *et al.* 2002, Bershadsky *et al.* 2003, Pasapera *et al.* 2010, Yu *et al.* 2011]. Instead, the effect of vinculin-mediated reinforcement of adhesion sites emerged within a time interval between 30 s and 90 s after contact initiation. Within this initial time frame, the adhesion strength of the contact site gained exceptionally fast. Subsequently, the adhesion reinforcement entered a phase of slowed increase, which occurred after 90 s to 180 s and was superseded by a phase of moderate reinforcement maintained for the residual measurement time.

Overview of adhesion forces in MEF WT, MEFvin^(-/-), and MEFvin^(-/-) cells expressing mutant vinculin

To allow for a comparison of the maximum traction forces developed in all examined cells types (mutant vinculin expressing MEF vin^(-/-) cells, MEF WT, and MEF vin^(-/-) cells), the data obtained with OT force spectroscopy for a contact time of 300 s are depicted in figure 3.17. The histogram shows the adhesion strength of the studied cell types in ascending order with the corresponding force values available in the table of figure 3.17. As expected, MEF vin^(-/-) cells featured the least adhesion reinforcement (amounting to 40 % of MEF WT traction forces), while vinFL and vinT12 matched the force transmission of MEF WT cells. Cells expressing the vin880 protein did not diverge significantly from MEF vin^(-/-) cells with regard to their adhesion reinforcement and the expression of vinA50I resulted in a slight increase of adhesion forces compared to MEF vin^(-/-) cells, which amounted to about 70 % of MEF WT force transmission.

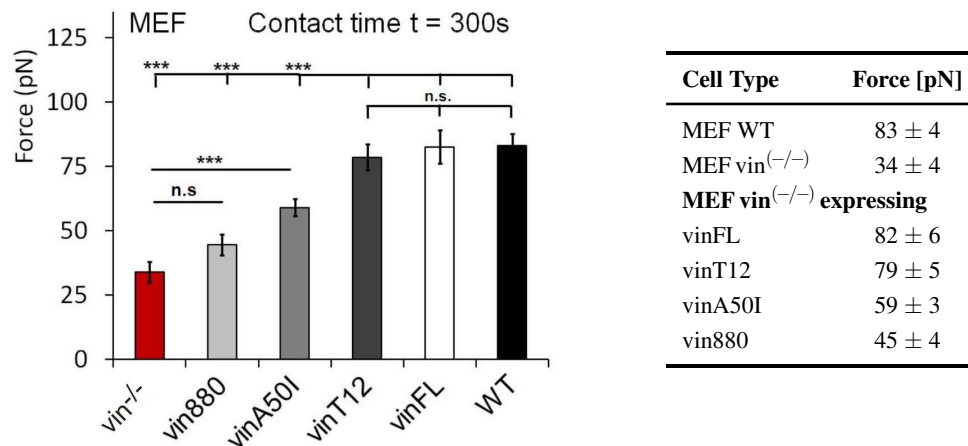


Fig. 3.17: Comparison of MEF WT, MEFvin^(-/-), and vinculin mutant expressing MEF vin^(-/-) cells

After 300 s contact time, a complete traction force rescue was achieved for vinFL and constitutively active vinT12 expressing cells. Cells expressing vinA50I demonstrated a force reduction of 25 % compared to MEF WT cells, while vin880 expressing cells did not show any force recovery (mean ± SEM).

4 DISCUSSION

4.1 Force Spectroscopy Approaches for Biological Applications

In the past decades, the question of force generation by the actin cytoskeleton and force transmission at cell-matrix interfaces was addressed in many research studies. However, the fundamental processes behind mechanotransduction, the translation of external mechanical signals into intracellular signals, and the cellular response in terms of adhesive interactions and structural reorganization are not yet completely understood [Hamill & Martinac 2001, Gillespie & Walker 2001, Alenghat & Ingber 2002, Wang & Thampatty 2006, Janmey & McCulloch 2007, Boccafoschi *et al.* 2010, Brownell *et al.* 2010, Levayer & Lecuit 2012]. Comprehension of the mechanotransduction pathway would provide insights into many physiological processes such as cell proliferation, motility, and apoptosis. Additionally, cell adhesion strength and traction force generation are discussed as possible factors contributing to pathologic cellular behavior such as metastasis and invasiveness. Thus, the mechanical interaction of a cell with its environment plays a decisive role in both individual cell and tissue fate.

To investigate the mechanism of cellular response and reorganization to mechanical stimuli, a variety of force spectroscopy approaches has been established, among others atomic force microscopy (AFM), optical tweezers (OT), magnetic tweezers, cell stretching devices, and 2D or 3D elastic substrates [Binnig *et al.* 1986, Ashkin *et al.* 1986, Wang *et al.* 1993, Burton & Taylor 1997, Balaban *et al.* 2001, Goldyn 2009, Klein *et al.* 2010, Friedrichs *et al.* 2010, Müller & Dufrêne 2011, Stewart *et al.* 2011, Schönherr 2012]. The work presented here, focuses on the application of laser optical traps with the aim to access the early development of cell-substrate adhesion sites. Data from AFM studies were included to allow for a comparison with a distinctively higher force regime.

4.1.1 Multiple Trap Force Spectroscopy

Optical tweezers (OTs) were invented in 1986 [Ashkin *et al.* 1986] and have been engineered in the recent past to access force regimes ranging from femtoNewton to several hundred picoNewton [Rohrbach 2005, Schäffer *et al.* 2007, Bormuth *et al.* 2008]. In addition, approaches were developed to simultaneously generate a large number of optical traps, adding a high degree of flexibility to the system [Dufresne & Grier 1998, Emiliani *et al.* 2004].

In the scope of this project a multiple trap optical tweezers setup was established with the experimental design adapted to allow live cell imaging under physiologically relevant conditions (chapter 2.1). The multiple traps originated in the ultra-fast laser beam scanning capability of a pair of acousto-optic deflection devices. With the assigned software interface a measure for real time manipulation was provided, allowing to modify the spatial coordinates and force characteristics of each trap independently. As optical tweezers offer a non-invasive force spectroscopy approach and

are not restrained by live cell imaging conditions, they are ideally suited to study cell-matrix interactions. In contrast to AFM and magnetic tweezers, OTs allow for a continuous, time-resolved study of force development. The force regime of the setup designed in the scope of this thesis work is in the range of 10 pN to 190 pN, and is thus providing insights into the evolution of early individual adhesion sites.

Microscopic Beads as Interfaces to the Cell

In optical tweezers force spectroscopy, micrometer sized dielectric spheres (beads) are commonly administered as local force probes. As the beads act as passive sensors and do not actively apply forces to the cell, OT assays are characterized as indirect force spectroscopy approach. This offers the advantage that the cell response to ligand stimuli is not disturbed by active external mechanical interferences. Instead, the optical traps provide a resistance to cellular traction forces and allow for a noninvasive study of force transmission at evolving cellular adhesion sites. The adjustment of trap intensity makes it feasible to modify the compliance of the force probe and provides a control of the matrix rigidity experienced by the cell. Substrate rigidities mimicked by trap confined beads are much softer than the glass substrates the cells are plated on and therefore reflect physiological conditions more closely. The laser intensity allocated to the trap is deflected by the beads and thus the focused laser radiation does not interfere directly with the examined biological samples. This permits the application of comparatively high laser intensities to the beads without causing damage by superheating the sample. The risk for hazards was further diminished by the choice of an infrared laser wavelength (1064 nm), which features low absorption rates for the tissue and the surrounding aqueous culture medium as well as for the beads.

The small polystyrol beads applied for force spectroscopy supply a flexible, readily alterable and easy to handle system to accurately control adhesive conditions in a spatiotemporally resolved manner. Optical traps serve as positioning tool for the beads and simultaneously act as force probes. With the selective chemical functionalization of the bead surface, specific integrins can be targeted to form adhesive complexes between the cell and the bead, thus revealing details about their expression patterns. By modifying the ligand density on the bead surface, the quantitative perception of integrin mediated adhesion sites can be assessed. Furthermore, the size of the force probe plays an essential role in inducing adhesion formation and force transduction. The choice of bead size provides defined geometrical constraints for the evolution of adhesions and allows to externally regulate the cellular force response.

Altogether, optical tweezers offer a highly flexible, spatially well-controlled system to induce the formation of new adhesion complexes. Adjusting the trap stiffness of the optical traps, a predefined counterforce is applied to the assembling adhesion sites, its magnitude specifying the matrix rigidity experienced by the cell. The variability of substrate rigidity allows to study cellular mechanotransduction within an accurately defined model system.

4.1.2 Atomic Force Microscopy

Atomic force microscopy (AFM) has emerged as a sensitive force probe to study cellular adhesion forces. Invented by Binnig and coworkers it has developed into a versatile tool to investigate cell mechanics and offers the unique perspective to address forces in an order of magnitude ranging from 10th of pN up to roughly 100 nN [Binnig *et al.* 1986, Franz & Puech 2008, Helenius *et al.* 2008, Friedrichs *et al.* 2010, Müller & Dufrêne 2011, Schönherr 2012]. The core element of the AFM is a cantilever of accurately defined mechanical properties, which serves as force probe. In AFM single-cell force spectroscopy (SCFS) a tipless cantilever is functionalized to stably attach a single cell. This cell is then lowered to the substrate and remains in contact for a defined contact time. Subsequently, the cell is removed by retracting the cantilever and a force-distance curve is recorded. Analysis of the force curves provides information of the detachment force required to completely separate the cell from the underlying substrate.

In the work presented here, SCFS measurements were performed in the Nano-Biology group of Dr. Clemens Franz at the Center for Functional Nanostructures of the KIT. The obtained AFM force-distance curves revealed the adhesion strength of single cells to their growth substrate and provided complementary data to the conducted OT force spectroscopy measurements.

The combination of the two force spectroscopy approaches, OT and AFM, offered the unique potential to analyze cellular adhesion forces at individual contact sites (in the pN regime) and compare them directly to the overall adhesion strength of an entire cell.

4.2 Spatiotemporal Characteristics of Evolving Cell Adhesion Complexes

Force transmission at cell-matrix interaction sites is a crucial process known to be mandatory for example for cell motility. Although the process of force generation has been studied with various approaches, many details about the interaction of the intracellular cytoskeleton with the extracellular surrounding remain elusive. The presented work is a multi-parametric study surveying biomechanical and biochemical environmental effects influencing cellular mechanotransduction. Cell systems originating from distinct organisms were investigated and compared with regard to their force development in adhesion sites. Cytoskeletal F-actin flow dynamics and cellular motility were analyzed, complementing the information on adhesion forces obtained for the distinct cell lines.

4.2.1 Temporal Development of Adhesiveness in Early Adhesion Sites

A specific characteristic of the presented study is its focus on a time-resolved force analysis in the formation of early cell adhesion sites. The initial phase of cell-matrix interaction is of particular interest as in this period of time a remarkable reorganization of membrane adjacent proteins and

cytoskeletal components occurs. The process of adhesion formation is initiated by integrin binding to ECM ligands. This is likely followed by Rac activation, which itself activates the aggregation of the dynamic actin network in the lamellipodium. As a next step, focal complex maturation is induced by Rho activation, which is an effector of Rho-associated kinase (ROCK) and diaphanous proteins (Dia). An increase of actin polymerization is attributed to the activation of Dia, while ROCK is reported to play a role in the augmentation of myosin II-mediated contractility. A detailed discussion on cell adhesion initiation and assembly is provided by [Geiger & Bershadsky 2001, Cohen *et al.* 2004, Yamada & Nelson 2007, Parsons *et al.* 2010, Levayer & Lecuit 2012]. With ongoing integrin clustering, cell adhesion-related proteins are accumulated into the adhesion sites, inducing the association of the cytoplasmic integrin domain to the actin cytoskeleton. Vinculin is one of the proteins that is recruited to adhesion sites in a force dependent manner and is proposed to be a key regulator of adhesion reinforcement. In immature adhesion sites the actin-related protein complex Arp2/3, a complex attributed with actin polymerization and F-actin bundling or branching, is attracted by vinculin [Welch *et al.* 1997, Svitkina & Borisy 1999, Robinson *et al.* 2001, DeMali *et al.* 2002, Gardel *et al.* 2010, Levayer & Lecuit 2012, Wu *et al.* 2012]. It is speculated that this interaction is potentially able to allocate actin assembly to adhesion sites and enhances the initial coupling of actomyosin contractility to the adhesion complex and the ECM.

OT force spectroscopy assays were conducted with different cell lines (mouse embryonic fibroblasts, B16 mouse melanoma cells and primary chicken fibroblasts), which were subjected to varying experimental conditions. For instance, the bead-administered integrin ligands and ligand densities were altered or a change in bead size reduced the available adhesion area. A general outline of temporal adhesion reinforcement in the initial 300 seconds of membrane-bead contact in the lamellar region was derived with a temporal resolution amounting to 1 Hz. The force-time curves acquired under the varying experimental conditions all conformed with a clearly defined multi-step adhesion reinforcement process.

All acquired force-time curves displayed a rapid increase in force transduction right after contact initiation that continued up to 120 to 180 seconds (illustrated i. e. in figure 3.3). Following, a gradual transition to a shallow but steady reinforcement was observed and continued over an additional interval of 60 to 120 seconds of the recording period. This reinforcement plateau was subsequently replaced by a moderately increased reinforcement rate, which was sustained over the entire time of the remaining measurement interval.

From the temporal development of force transmission at cell adhesion sites, inferences on the formation of the adhesion protein plaque and its association to the actin cytoskeleton can be deduced. Previous studies reported the time-dependent recruitment of adhesion-related proteins on the time scale of seconds, with $\alpha_v\beta_3$ integrins initiating complex formation, followed by paxillin, talin, and FAK incorporation and subsequently vinculin and α -actinin recruitment [Laukaitis *et al.* 2001, Balaban *et al.* 2001, Zaidel-Bar *et al.* 2003, Gardel *et al.* 2010, Papusheva & Heisenberg 2010, Scales & Parsons 2011, Lawson *et al.* 2012]. Thus the fast increase in traction force transmission in the

beginning of membrane-bead interaction is probably attributed to the rapid assembly of integrins and adhesion-related proteins from the cytoplasmic pool to the adhesion site. Their crosslinking to the filaments of the underlying actin network in the lamella constitutes the mechanical precondition for force transduction.

Close to the lamellipodium, the lamella features a contractile actin network. The actin filaments within this network are randomly organized and are supplied with localized myosin II aggregations [Verkhovsky *et al.* 1995, Gardel *et al.* 2008, Silva *et al.* 2011]. The fast initial binding of proteins to F-actin at cell adhesion sites is followed by a remodeling of the F-actin network, including enhanced actin polymerization as well as bundling and cross-linking of individual filaments that is induced by myosin II generated contractile stress [Johnson & Craig 1995, Verkhovsky *et al.* 1995, Goldmann *et al.* 1998b, Hotulainen & Lappalainen 2006, Pollard 2007, Sun *et al.* 2010]. This results in a continuous transition from the randomly organized actin network to the highly aligned structures of actin stress fibers [Verkhovsky *et al.* 1995, Aratyn-Schaus *et al.* 2011]. The process of spatiotemporal reorganization has recently been simulated with a theoretical model based on biological friction and mechanochemical interaction [Walcott & Sun 2010]. Aratyn-Schaus and coworkers have demonstrated that the reorganization of the actin network involves processes on distinctive time scales: the formation and thickening of actin bundles is completed within 60 to 120 seconds, whereas the remodeling of the actin network into linear bundles proceeds on a time scale in the order of 10 minutes with actin stress fiber formation after 10 to 20 minutes. Cellular traction force on a polyacrylamide substrate was also reported to occur on two distinctive time scales with a rapid reinforcement in the initial 60 seconds followed by moderate reinforcement over 20 minutes. In this study adhesion sites reached a constant length after a few minutes and did not continue enlargement [Aratyn-Schaus *et al.* 2011]. Regarding this context, the evolution of reinforcement deduced from the optical tweezers force spectroscopy assay can be interpreted as a temporal overlap of short term actin bundle formation and long term structural reorganization, accompanied by linear alignment of the actin filaments. The observed reinforcement plateau, occurring after 120 to 180 seconds of membrane-bead interaction possibly corresponds to the period of both actin thickening and adhesion growth deceleration and completion. The subsequent increase in reinforcement rate is potentially mediated by the commencement of F-actin bundle alignment.

Altogether, the study of force development in early adhesion complexes confirms the previously reported dynamics of adhesion formation and provides versatile additional information regarding temporal sensitivity.

4.2.2 The Area of Cell Adhesive Contact Sites Mediates Reinforcement

One of the crucial parameters for traction force exertion is the available contact area to which the cell can establish an adhesion complex. Following the initial integrin aggregation upon ligand interaction, nascent cell adhesions form and evolve into focal complexes by recruitment of adhesion-related molecules [Burrige & Chrzanoska-Wodnicka 1996, Rottner *et al.* 1999, Laukaitis *et al.* 2001, Webb *et al.* 2002, Zaidel-Bar *et al.* 2003, Zaidel-Bar *et al.* 2004, Liu *et al.* 2010, Rape

et al. 2011]. Coinciding with this process, the immature adhesion sites expand and experience the application of contractile tension, conveyed by the association to the actin cytoskeleton. Mechanical tension, applied internally or externally, induces changes in the protein constitution of the intracellular adhesion plaque [Balaban *et al.* 2001, Riveline *et al.* 2001, Bershadsky *et al.* 2003, Choi *et al.* 2008, Parsons *et al.* 2010, Levayer & Lecuit 2012]. While Balaban and coworkers described a linear dependence of force and adhesion area for mature focal adhesions, other groups determined a non-proportional behavior of size and force exertion for small and nascent adhesions [Beningo *et al.* 2001, Tan *et al.* 2003] and for mature adhesion sites [Stricker *et al.* 2011]. In these studies, the nascent adhesions were found to exert stronger propulsive forces than expected from their small size ($< 1 \mu\text{m}$).

In the force spectroscopy assays presented here, the expansion of adhesion area was controlled by the selection of the force probes. As force probes beads with a diameter of $3.0 \mu\text{m}$ and $4.5 \mu\text{m}$, respectively, were applied. This correlates to a membrane-bead contact area of $A \leq 1.8 \mu\text{m}^2$ and $A \leq 2.7 \mu\text{m}^2$, respectively (chapter 3.2.1). The present study investigated the contractile response of mouse embryonic fibroblasts to fibronectin (FN)-functionalized beads. Evaluation of the cellular forces was conducted with a focus on cell adhesion development within the initial 300 seconds of membrane-bead interaction. Contact formation was monitored with a video rate of 1 Hz, allowing to pursue the temporal development of early cell adhesions.

At small contact sites of less than $1.8 \mu\text{m}^2$ FN-beads experienced an average force transmission of $F_s = 16 \pm 1 \text{ pN}$ after 300 seconds of contact formation (figure 3.2). Expansion of the contact area by a factor of 1.5 led to contractile force transmission of $F_l = 83 \pm 4 \text{ pN}$ onto the beads within the same time interval. Although the traction force resistance of the smaller $3.0 \mu\text{m}$ beads, regulated by the optical trap intensity, was of the same magnitude as for the $4.5 \mu\text{m}$ beads, the contact sites were not reinforced accordingly. Instead, the 1.5-fold enlargement of adhesive contact area caused an increase in force transmission by a factor of 5 (figure 4.1 A1)). This identifies the geometrical restriction of adhesion areas as a primary cue to control contractile stress generation.

A size-dependent reinforcement of cell-substrate contacts has been proposed by Beningo and coworkers, who reported an enhanced force transmission during the early formation and enlargement process of focal adhesions [Beningo *et al.* 2001]. With GFP-zyxin as cell adhesion marker this group demonstrated that adhesion strengthening and adhesion growth both advanced during the initial five minutes of focal complex formation. Nevertheless, with continuing maturation and growth, the force transmission at adhesion sites declined. However, that study did not temporally resolve the force development during initial adhesion assembly (300 seconds) but focused on longer time scales (45 minutes).

The work presented in this thesis addressed the intriguing aspect of force development during the initial focal complex formation by analyzing early membrane-bead interactions of distinct diameters. The nonlinear relation between force and adhesion area detected for the examined geometrical restrictions implies that adhesion reinforcement rates exceed the growth rate of adhesion sites.

A possible interpretation of the nonlinear dependence of reinforcement on adhesion area is a size dependent change in the protein constitution of the adhesion sites. This indicates that in addition to the traction resisting counterforce a sufficiently large contact area has to be established to develop high cellular traction forces. These findings correspond to previous studies that discussed the role of force application to adhesion sites in mediating the conversion of nascent adhesions into more mature focal complexes by rearranging the protein constitution [Galbraith *et al.* 2002]. The same study reported that without counterforces, a certain bead size was required to trigger the maturation of nascent adhesions into focal complexes.

Analyzing cellular traction response to distinct adhesion areas it was concluded that the membrane contact area of $4.5 \mu\text{m}$ beads was best suited for the experimental purpose of further studies. With the available contact area on this beads, maturation of nascent adhesion into more mature adhesion complexes was feasible.

4.2.3 Orientation of Spatially-Related Adhesion Sites Controls Adhesion Strength

The available contact area for an adhesion site has been demonstrated to be of predominant importance for the transduction of contractile stress. These studies were considering the force development in isolated cell-matrix contact sites. In the lamellipodium, cells form membrane extensions to probe their environment and in this highly dynamic area a large number of adhesion sites is constantly formed and remodeled. This leads to the emergence of tightly arranged adhesion patterns at the proximal boundary of the lamellipodium to the lamella. Hence, the evolution of tensile stress in neighboring adhesion sites and the coordination of their reinforcement is of particular interest. With spatially closely related adhesion sites, the question arises whether both adhesions are treated equally or if a certain adhesion orientation is reinforced preferentially. With the objective of gaining insights into the spatiotemporal coordination of neighboring adhesion sites, force development in early adhesions formed to microscopic beads was investigated in this study.

To stimulate the formation of spatially closely related adhesion sites, FN functionalized beads with a diameter of $4.5 \mu\text{m}$ were administered to the apical membrane of mouse embryonic fibroblasts. With optical traps a pair of beads was positioned with a center to center distance of $d = 5 \mu\text{m}$. As a control, measurements with a bead spacing of $d > 10 \mu\text{m}$ were conducted. Beads were arranged in the leading edge of well spread cells and each bead was confined by identical trap intensities.

In chapter 3.2.4 two case studies were described concerning the orientation of neighboring adhesion sites. In the first case (i) a pair of beads was aligned parallel to the membrane tip of the leading edge. The second case (ii) was constituted with a pair of beads positioned in successive order and perpendicular to the leading edge boundary (figure 3.6).

Force-time curves were recorded for both cases and their evaluation revealed an orientation-dependent adhesion reinforcement (figure 4.1 A2)). In case of parallel beads, both adhesion sites were strengthened equally, the average traction force at the interface site amounting $F_{||5\mu\text{m}} =$

$49 \pm 4 pN$ after 300 seconds. This corresponded to a force reduction of 40 % compared to isolated cell-bead adhesion reinforcement. A spacing-dependent divergence of force curves was observed already 30 seconds after adhesion initiation, with a significant reinforcement gain for widely spaced adhesion sites. This indicates that an early communication between neighboring adhesion complexes exists.

Analysis of force curves for case (ii) with successive beads oriented perpendicular to the leading edge revealed distinctive reinforcements on the anterior and posterior contact site. At the anterior contact, a force transmission of $F_{\perp 5\mu m}^a = 67 \pm 6 pN$ was observed, whereas forces at the posterior contact were diminished to $F_{\perp 5\mu m}^p = 26 \pm 5 pN$. In this case the anterior membrane-bead contact was treated similar to isolated adhesion sites and reinforcement there was strongly favored over the posterior contact site which experienced a force decrease of more than 60 %. Generally, a reduced force transmission is expected for increasing distances to the leading edge. However, control measurements with individual beads placed at the posterior bead position revealed a force reduction of about 20 %, compared to beads positioned $5 \mu m$ closer to the leading edge. Thus, the diminished traction forces at the posterior bead can not be attributed exclusively to the location itself.

Closely spaced parallel adhesion sites featured equal force transmission that was reduced by 40 % compared to independent adhesion sites. To derive a hypothesis for the impact of the orientation of neighboring adhesion sites on adhesion strength, the outline of the underlying actin network has to be considered. Motile cells are polarized and have a leading edge and retracting tail. The leading edge consists of lamella and lamellipodium, with the lamella presenting a radial orientation of actin bundles associated with adhesion sites in the proximal region and a contractile actin network in the distal area. This is followed by a randomly organized, gel-like actin network in the lamellipodium [Verkhovskiy *et al.* 1995, Verkhovskiy *et al.* 1997, Svitkina *et al.* 1997, Small *et al.* 1998, Ponti *et al.* 2004, Urban *et al.* 2010, Zimmermann *et al.* 2010, Zimmermann *et al.* 2012]. With the presentation of bead-attached integrin ligands close to the leading edge, cells start to accumulate adhesion-related proteins that mediate the link between integrins and actin cytoskeleton. Simultaneously, a reorientation of the actin network is induced and coincides with the formation of a rearward extending actin tail at the adhesion site.

In principle, it is conceivable that the close spatial relation of the two adhesion sites forces a competition for actin and adhesion-related proteins, rendering neighboring adhesions unable to recruit these as fast as isolated adhesion sites. This would imply that the pool of unbound adhesion- and actin-associated proteins can be easily depleted and is contradictory to the reported dynamics and turnover rates of these components. A number of studies applied fluorescent speckle microscopy and fluorescence recovery after photobleaching and demonstrated that adhesion-related proteins feature both turnover rates on a time scale of tenth of seconds and high diffusion coefficients [Wang 1985, McGrath *et al.* 1998, McGrath *et al.* 2000, Zicha *et al.* 2003, Iwasa & Mullins 2007, Choi *et al.* 2008, Lai *et al.* 2008]. Typical half times of fluorescence recovery after photobleaching were estimated to amount about 10 to 40 seconds for actin, Arp2/3, paxillin, FAK,

talin, and zyxin, and about 80 seconds for vinculin [Theriot & Mitchison 1991, Ponti *et al.* 2004, Lai *et al.* 2008, Pasapera *et al.* 2010, Cortesio *et al.* 2011]. Hence, it is unlikely that a depletion of the actin and adhesion-related protein reservoir is responsible for the observed force decline in the considered time frame.

Considering the presence of radially aligned F-actin bundles in the leading edge, parallel oriented adhesion sites could be established on parallel fibrils of the underlying actin cytoskeleton. The proximity of these fibrils could give rise to rather identical contractility conditions and thus account for the identical reinforcement of neighboring adhesions. However, if the adhesions are associated to distinct actin fibrils this would resemble the conditions met by isolated contacts and should allow for force generation identical to individual adhesion sites. Internal feedback and crosstalk between the neighboring adhesion site could potentially synchronize force transmission and reduce reinforcement to ensure dynamic efficiency.

Another hypothesis for the force reduction in parallel adhesion sites is that the actin filaments associated to the two neighboring contacts extend rearward and merge into one single actin fibril. This could possibly explain the partition of force transduction onto both adhesion sites and would also account for the similarity of force magnitudes.

Altogether, the mechanisms behind the synchronization and traction force reduction remain speculative and require additional investigation of the reorganization processes of the actin cytoskeleton at emerging adhesion sites.

The force spectroscopy data for neighboring beads arranged successively revealed a decline of adhesion reinforcement on the posterior adhesion site. In contrast, the reinforcement of the anterior bead, located in the more dynamic area close to the leading edge, is not affected by the appearance of a successive bead. A possible explanation for this phenomenon is the decrease of protein turnover rates with increasing distances from the leading edge tip [McGrath *et al.* 2000, Iwasa & Mullins 2007, Lai *et al.* 2008, Vicente-Manzanares & Horwitz 2011, Wolfenson *et al.* 2011, Möhl *et al.* 2012]. It is generally accepted that this leads to a decline of force transmission with advancing distance of the adhesion from the tip. Still, by itself this effect does not account for the entire decrease in adhesion strength detected with OT force spectroscopy. Control measurements at isolated adhesions in the more posterior positions revealed only a slight force reduction.

To derive an assertion for the observed phenomenon, the interaction of the emerging adhesion sites with the actin cytoskeleton were considered. Both adhesions were established in a lamellar region that is riddled with a contractile actin network. It has been proposed that adhesion sites constitute a barrier for the retrograde actin flow that induces friction and thus leads to the deceleration of flow dynamics [Lin & Forscher 1995, Hu *et al.* 2007, Wang 2007, Alexandrova *et al.* 2008, Barnhart *et al.* 2011, Möhl *et al.* 2012]. Recently, a model for F-actin flow at adhesion sites has been computed by Shemesh and coworkers, suggesting that the actin network is stretched upon encounter of adhesion sites. This induces a stress-dependent partial actin disintegration of the F-actin network [Ponti *et al.* 2004, Vallotton *et al.* 2004, Shemesh *et al.* 2009, Maruthamuthu *et al.* 2010, Hoffman *et al.* 2011, Rottner & Stradal 2011]. The model predicts the appearance of "shadows" of low

actin density behind adhesion sites. In addition, the emergence of a single dorsal actin tail, generated from the actin flow through or above the adhesion site is projected, which might function as a template for actin bundle formation [Shemesh *et al.* 2009]. The actin tail had also been experimentally observed in a previous study [Choi *et al.* 2008] and was proposed as a mandatory mediator (in addition to tension) for adhesion maturation [Oakes *et al.* 2012]. Together, the dynamics and forces arising from friction between actin flow and adhesions appear well capable of diminishing force transmission onto an adhesion site arising in the shadow of more anterior adhesion. The reduction of F-actin flow at the posterior adhesion, might limit the access to the pre-existing actin network and delay the nucleation of a dorsal actin bundle, which is required for transmission of myosin contraction. Additionally, the reduced friction might act as a trigger for adhesion disintegration. Altogether, the force spectroscopy data on successive adhesions fit well into the described model and give experimental evidence for the reduction of actin density at the rear of adhesion sites. However, a closer investigation of the actual F-actin reorganization at a doublet adhesion is required to confirm this assumptions.

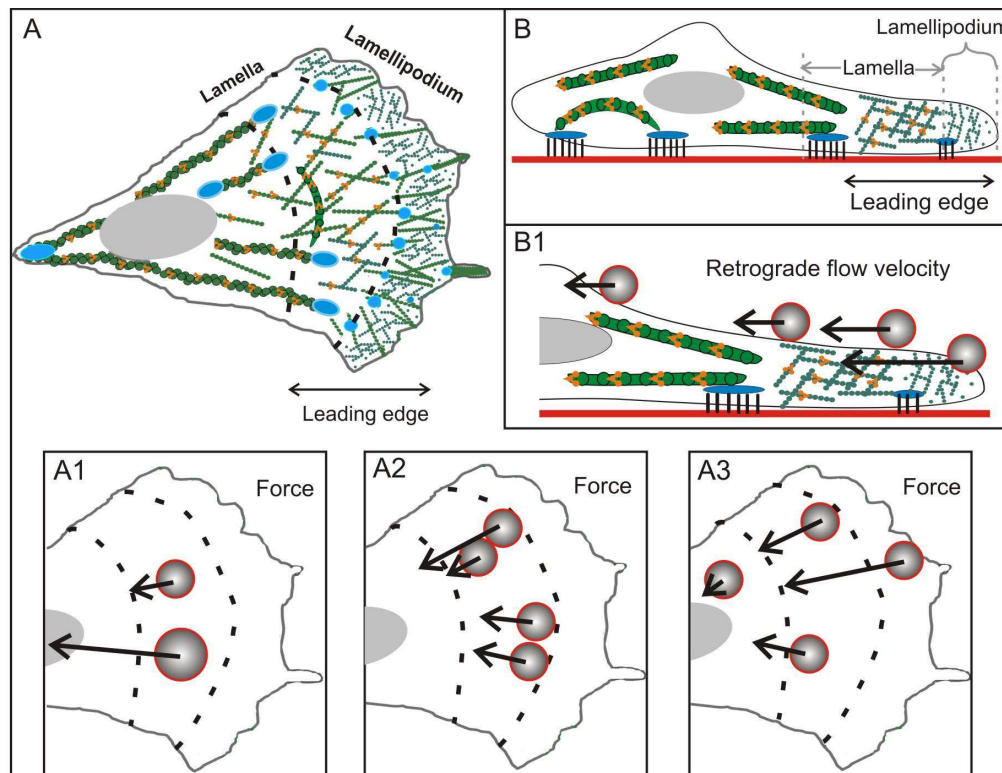


Fig. 4.1: Multiparametric study of force development and retrograde flow

Fibronectin-functionalized beads were arranged in the leading edge of the cell. A) Actin cytoskeleton (green) and adhesion sites (blue) of a polarized cell. The lamellipodium is comprised of a branched, gel-like actin network, while the distal area of the lamella features a contractile network of actin filaments interspersed with myosin motors. A1) Force development in adhesion sites of different size, mimicked by distinct bead dimensions. A2) Beads distributed throughout the leading edge and the cell body show a position-dependent force development. A3) Force development in neighboring adhesion sites arranged parallel and perpendicular to the membrane tip. B) Side view of a migrating cell. B1) Position-dependence of retrograde flow velocity.

4.2.4 Influence of Integrin Ligand Density on Cell Adhesion Behavior

Apart from geometrical limitations of cell adhesion sites, an essential parameter for force transduction is the presence of sufficient extracellular integrin ligands. Here, the type of ligand [Pierschbacher & Ruoslahti 1984, Petrie *et al.* 2006] as well as the provided density [Coussen *et al.* 2002, Engler *et al.* 2004, Geiger *et al.* 2009, Lagunas *et al.* 2011] and spacing of the ligand [Lehnert *et al.* 2004, Klein 2009, Malmström *et al.* 2010, Frith *et al.* 2012] regulate the adhesion formation. FN is a multiadhesive ECM protein, containing binding sites for a considerable number of different integrin types. Within the full length FN molecule distinctive binding sites were discovered over the last decades with the tripeptide RGD sequence in the FNIII₇₋₁₀ domain, constituting the shortest recognized adhesion motif (reviewed by [Pankov & Yamada 2002]). Petrie *et al.* compared RGD and FN functionalized substrates and concluded a higher binding affinity of cells to FN substrates from the evaluation of the adherent cell fraction. This raises the question of time-resolved adhesion development in response to these ligands, which was addressed with the ligand density study presented in chapter 3.2.2. Here, the influence of the FN macromolecule and of the RGD peptide on force development during adhesion assembly was evaluated. A cyclic RGD peptide (cRGDfk) was chosen for this comparison, as this conformation is supposed to mimic the native, loop-like sequence fold more accurately than a linear peptide configuration [Gao *et al.* 2002]. The application of functionalized beads (4.5 μm in diameter) with either ligand type to mouse embryonic fibroblasts resulted a force transmission depending on the ligand density on the bead surface. A linear relation between surface coverage and adhesion strength was deduced from force curves recorded for ligand densities ranging from 50 % to a complete monolayer of 100 % bead coverage (figure 3.3). This relation was valid for both FN and cRGDfk bead functionalization.

To determine whether adhesion reinforcement continued for even higher ligand amounts, a batch was prepared with a cRGDfk bead coverage of 150 %, corresponding to the formation of a ligand bilayer on the bead surface. With this ligand density, forces exerted onto the beads were of the same magnitude as for a ligand monolayer ($F_{mono} = 92 \pm 11 \text{ pN}$ and $F_{bi} = 90 \pm 16 \text{ pN}$). The occurrence of this saturation effect is possibly attributed to inhibited binding properties in the upper ligand layer: peptide-peptide interconnection is considered less stable than the interaction between the first peptide layer and the bead surface. Thus cRGDfk-cRGDfk binding provides less resistance to cellular traction forces probing the ligands and facilitates peptide detachment from the bead surface. As cells sense the ECM rigidity and respond to changes with a modification of adhesion complexes, the impaired tension resistance in the ligand bilayer might account for inhibited reinforcement. Another reason for the lack of additional reinforcement could be that the amount of ligand exceeds the spatial threshold for further enhanced integrin clustering. Due to the volume expansion of the integrins themselves, spatial restriction may result in a saturation of force transmission in the contact site. In a previous study, α_5 -integrin density within maturing adhesion sites was characterized with 900 integrins/ μm^2 , a number that is five-fold higher than in surrounding membrane areas [Wiseman *et al.* 2004]. Notably, this number is somewhat smaller than the number of integrin ligands per μm^2 , which was about 7-fold higher for a FN monolayer. This discrepancy could be due to

the contribution of further integrin subunits to adhesion formation, although it is unlikely that this accounts for the entire mismatch. As reported in chapter 3.2.2, the estimation of ligand density on the bead surface was rather inaccurate due to the limited sensitivity of the photospectrometer for unlabeled proteins. Here, the discussed development of linker molecules for the 1:1 coupling of fluophores and ligands (appendix A) would prove a beneficial tool for ligand density assessment in further investigations.

A comparative analysis of the distinct ligand types gave evidence to enhanced adhesion reinforcement at interface sites containing FN. With increasing ligand densities this effect became more pronounced. The preference for FN substrates was also demonstrated by Petrie *et al.* who attributed this phenomenon to the FN capacity to promote binding of a wider range of integrins. For example it was demonstrated that $\alpha_5\beta_1$ integrins mediate the binding of the FNIII₇₋₁₀ domain but cannot form complexes with the RGD adhesion motif alone [Petrie *et al.* 2006]. The investigation of the role of specific integrins on adhesion strength revealed that $\alpha_5\beta_1$ integrins are a key regulator for adhesion strength while the less stable $\alpha_v\beta_3$ integrins promote RGD binding and mediate signal transduction [Roca-Cusachs *et al.* 2009]. Thus, the observed reinforcement gain of FN-integrin complexes over cRGDfk-integrin adhesions might be attributed to the role of distinctive integrin subunits in adhesion regulation.

Summarizing the results from this study, a linear dependence of force transduction in early adhesion sites on ligand density was derived for both ligands if no more than a ligand monolayer was provided on the beads. With enough ligand to induce a bilayer assembly, force transmission did not increase but saturated.

Integrin complexes formed to a FN matrix developed stronger adhesion forces than cRGDfk mediated complexes, showing that RGD-binding integrins alone are not capable of triggering full adhesion strength.

An aspect that has not been discussed in this study is the influence of the basal substrate functionalization. MEF cells were plated and pre-incubated on FN-coated glass substrates. It is well-established that the substrate functionalization itself influences cellular integrin expression [Singer *et al.* 1988]. Additionally, it has been reported that cell morphology and motility are influenced by the chemical constitution of the growth substrate [Hakkinen *et al.* 2011]. In consequence, cells growing on FN-coated substrates might tend to express a higher number of $\alpha_5\beta_1$ integrins and other integrins primarily promoting binding to the FN macromolecule, while the expression of RGD ligating integrins could be downregulated. The enhanced amount of FN binding integrins compared to RGD associated integrins could also account for the increased force transmission observed on FN-functionalized beads. The cellular aptitude to adapt integrin expression to the external supply of ligands and the particular effect on adhesion reinforcement remain an issue for further investigation.

4.2.5 Force and Velocity Mapping: The Interdependence of Adhesion Forces, F-Actin Flow Velocity, and Cell Motility

Forces and retrograde F-actin flow have been demonstrated to be intrinsically coupled [Jurado *et al.* 2005, Medeiros *et al.* 2006, Gardel *et al.* 2008, Fournier *et al.* 2010]. The assembly of integrin clusters mediates the association of adhesion sites to the F-actin flow [Horwitz *et al.* 1986, Schmidt *et al.* 1993, Felsenfeld *et al.* 1996] and induces a reorganization of the underlying actin cytoskeleton [Grinnell & Geiger 1986, Forscher *et al.* 1992, Miyamoto *et al.* 1995a, Miyamoto *et al.* 1995b]. With the reorganization of the actin cytoskeleton, force generation by the actomyosin system and its transduction to the substrate is facilitated [Ahmed *et al.* 2010, Aratyn-Schaus *et al.* 2011]. Experiments using ECM protein-functionalized beads were among the first approaches to study cytoskeletal dynamics in fibroblasts [Schmidt *et al.* 1993, Choquet *et al.* 1997]. Furthermore, high spatial resolution actin flow mapping became feasible with the development of speckle and TIRF microscopy [Danuser & Oldenbourg 2000, Caspi *et al.* 2001b, Vallotton *et al.* 2004, Brown *et al.* 2006]. With these techniques, the retrograde F-actin flow was characterized and analyzed in detail, but still many aspects of the mechanisms driving rearward flow remained elusive.

In the study presented here, a velocity mapping of the F-actin flow in distinct spatial areas of the cell membrane was conducted. Of particular interest was the distribution of flow velocities in the highly dynamic leading edge. Complementary data were acquired for the adhesion strength of individual contacts in terms of a force mapping across the cell surface (chapter 3.2.3). To get insights into the general relation of intracellularly generated forces, F-actin dynamics, and cell motility, a cell type comprehensive study was conducted. Three cell lines were chosen for investigation, among them mouse embryonic fibroblasts, B16 mouse melanoma cells, and primary chicken fibroblasts.

Mouse embryonic fibroblasts were cultured for 2 h on FN-coated glass substrates for spreading. These cells were used for the force and velocity mapping across the entire cell surface. In addition, primary chicken fibroblasts were prepared for a closer investigation of the dynamic characteristics from the tip of the lamellipodium toward the lamella. For this purpose the primary fibroblasts were chosen, as they provided an extensive leading edge, ideally suited to visualize distinct velocity areas.

For all measurement types, well-spread cells were exposed to FN-functionalized beads of $4.5\mu\text{m}$ diameter. In the F-actin flow assay, beads were arranged with optical traps that were deactivated once the target position was attained. In contrast, optical traps in the force spectroscopy assay remained active for the entire measurement course.

The investigation of retrograde flow characteristics in the leading edge and lamella of primary chicken fibroblasts revealed exceedingly fast transport velocities at the very tip of the leading edge (figure 3.5). Analyzing the spatial dependence of F-actin velocity, a swift decline of the rapid F-actin flow was discovered with expanding displacements from the tip and eventually an area of stable, position-independent flow velocities was entered. The relation of actin flow and bead position was best characterized with a power-law regression.

It was observed that the force magnitude and retrograde flow dynamics correlated linearly within the distinctive spatial areas of the force and velocity mapping assays (figure 3.4). Close to the leading edge, adhesion sites transmitted the highest traction forces onto the beads. Concomitantly, these areas displayed the fastest bead transport toward the nuclear region. With increasing distance from the leading edge, both force transduction and F-actin flow velocity receded (figure 4.1 A3) and B1)).

This relation was derived on the scale of distinctive membrane areas within an individual cell. Analyzing force generation, and retrograde flow dynamics on the cellular scale, it was concluded that the direct correlation of force transmission and flow velocity applies accordingly. Here, the primary cells exhibited the strongest traction forces which coincided with the fastest F-actin flow rates measured throughout all cell lines. B16 melanoma cells developed the weakest adhesion forces which correlated with diminished F-actin dynamics. Although mouse embryonic fibroblasts and B16 cells assumed a similar shape and size upon spreading, their force and flow characteristics were well-distinguished. As the morphology of adhesion complexes of both cell are similar as well, neither cell form nor adhesion morphology could account for the strong distinctions. However, a well-defined discrepancy was observed with regard to the actin cytoskeletal organization. In mouse embryonic fibroblasts, the formation of dorsal F-actin bundles was prominent, whereas B16 cells assumed a rather randomly organized actin meshwork close to the leading edge. This hints at an essential role of the structure and organization of the actin cytoskeleton in force transduction.

As contractility and F-actin flow dynamics are intrinsically related to cellular motility, a migration assay was additionally conducted. The evaluation of cell motility data resulted an inverse correlation of locomotion with both force transduction and F-actin flow velocity.

Altogether, the force and velocity mapping approaches revealed a linear correlation of force and velocity, holding for both distinct cellular areas and distinct cell lines. In contrast, cell migration velocity showed an inverse proportionality toward force generation and F-actin dynamics.

In the literature, the relation of force transduction at adhesion sites and F-actin flow is controversially discussed. Some studies reported a biphasic correlation of traction stress and retrograde flow dynamics, with an inverse relation of force and F-actin translocation close to the tip of the leading edge and a direct relation holding for areas of more mature adhesion sites [Jurado *et al.* 2005, Gupta & Waterman-Storer 2006, Gardel *et al.* 2008]. While those studies attribute rather weak forces to newly assembled adhesion contacts in the leading edge, other groups presented traction force analyses identifying nascent adhesions as origins of strong force transduction that decreases with contact maturation [Benigno *et al.* 2001]. Yet another publication postulated that the formation of nascent adhesions switches F-actin flow from fast to slow [Alexandrova *et al.* 2008].

Analyzing the results concerning force and velocity mapping derived in the work presented here, it was concluded that areas of fast F-actin flow close to the tip of the leading edge are able to generate high forces in early adhesion formation. This corresponds to previous reports on force development in the lamellar region of motile cells [Gardel *et al.* 2008].

The power-law dependency of the F-actin flow velocity on the location with regard to the leading

edge tip is in good agreement with other studies concerning the F-actin flow in distinct cellular compartments [Vallotton *et al.* 2004, Brown *et al.* 2006, Gardel *et al.* 2010, Burnette *et al.* 2011]

Investigation of the adhesion forces, retrograde F-actin flow dynamics and motility of different cell types gained some additional information on the relation of those variables. Previous studies mainly considered the relation of only two quantities and were conducted for individual cell lines [Jurado *et al.* 2005, Guo & Wang 2007, Gardel *et al.* 2008, Fournier *et al.* 2010, Shih & Yamada 2010]. The study presented here confirms the conservation of the described relations for all three variables throughout distinct cell lines. Still, how exactly the correlation of actin dynamics, forces, and migration is balanced remains elusive. In the recent past, several theoretical mechanochemical models have been proposed to address the question of cellular mechanosensing, attributing a predominant importance on actin turnover rates and aggregation time scales [Kruse *et al.* 2006, Li *et al.* 2010, Walcott & Sun 2010].

4.3 Influence of Vinculin Recruitment on Actin Flow, Adhesion, and Motility

Vinculin is a multifaceted adhesion molecule containing known binding sites for more than 10 interaction partners (reviewed by [Ziegler *et al.* 2006, Mierke 2009, Carisey & Ballestrem 2011, Peng *et al.* 2011]). Although the structure of vinculin itself is well-characterized [Bakolitsa *et al.* 2004] and many details about protein interactions have been revealed in the last decade, the precise molecular architecture of cell adhesion sites is still unclear. The work presented in this thesis aims at further dissecting the mechanisms of vinculin-mediated force transmission in cell-matrix adhesions. Therefore, the role of native vinculin in force mediation is investigated and compared to the performance of several vinculin mutants afflicted with distinctive structural modifications. Optical tweezers (OT) and atomic force microscopy (AFM) force spectroscopy were performed on both individual adhesion sites and overall cell adhesion, respectively. All optical tweezers force spectroscopy data were obtained within the scope of this work, whereas the AFM single cell experiments were conducted and evaluated by the Nano-Biology group of Dr. Clemens Franz at the Center for Functional Nanostructures (CFN) and are included for a comparative analysis.

4.3.1 Role of Native Vinculin in Adhesion Reinforcement and Integrin-Actin Coupling

Cells expressing only low levels of vinculin or completely lacking vinculin exhibit modified growth, adhesiveness, motility, and proliferation characteristics [Fernández *et al.* 1993, Xu *et al.* 1998a, Coll *et al.* 1995, Baumann 2010]. Consistent with this observations, the vinculin deficient mouse embryonic fibroblasts (MEF $\text{vin}^{(-/-)}$) cultured for this study showed a more roundish morphology and enhanced motility compared to the wild type cell line (MEF WT).

Vinculin Deficiency Causes a Loss of Directionality in Actin Flow

To identify the relevance of native vinculin in promoting the mechanical link between cytosolic integrin domains and actin filaments, MEF $\text{vin}^{(-/-)}$ cells were compared to the respective wild type cell line (MEF WT). Cells were incubated on FN-coated glass substrates and were exposed to FN-functionalized beads of $4.5 \mu\text{m}$ diameter for a contact time of 300 seconds.

Evaluating the rearward bead translocation, it was concluded that the actin flow velocity in MEF $\text{vin}^{(-/-)}$ cells was doubled compared to MEF WT cells (figure 3.12). The finding that a vinculin deficiency effects the actin flow behavior was not reported so far and was further investigated with regard to the bead trajectories. Retrograde flow in MEF WT cells was following a fairly straight trajectory from the leading edge toward the nuclear region (figure 3.11). The analysis of bead trajectories on MEF $\text{vin}^{(-/-)}$ cells revealed a severe loss of directionality for the retrograde flow, resulting in some kind of a "zigzag" course. This occurred in both the long distance range and the short distance range of retrograde transport. A decline of directional persistence amounting 70 % was observed in vinculin deficient cells and coincided with a two-fold increase of retrograde flow velocity. The enhanced retrograde flow rates were observed in the lamella as well as in protrusions of the leading edge. However, using functionlaized beads as readout for the actin flow velocity, is a rather indirect estimate and requires further verification with direct imaging methods.

Former studies on purified actin and vinculin molecules did not report any changes in the rate of actin polymerization upon vinculin interaction [Goldmann *et al.* 1992, Götter *et al.* 1995]. However, studies addressing this question *in vitro* within the cell were not presented so far. Vinculin is known to accumulate into focal complexes [Rottner *et al.* 1999, Zaidel-Bar *et al.* 2003] but requires contractile forces for its recruitment [Riveline *et al.* 2001, Galbraith *et al.* 2002, Murthy & Wadsworth 2005, Pasapera *et al.* 2010]. The question of vinculin assembly at bead-membrane interfaces without external forces has been controversially discussed with some studies reporting the absence of vinculin recruitment [Grinnell & Geiger 1986] and others demonstrating its presence [Galbraith *et al.* 2002]. Galbraith *et al.* derived a more distinctive evaluation of vinculin recruitment, suggesting that a certain membrane-bead interaction area is required for force-independent vinculin assembly, whereas small interaction sites require the application of internal or external stimuli to induce vinculin accumulation.

In the work presented here, vinculin recruitment to adhesion sites was tested via the expression of vinculin-GFP fusion proteins in MEF WT cells. Analysis of fluorescence microscopy images revealed vinculin accumulation at membrane-bead interfaces without external force application. This suggests that the inertia of the applied beads offered a sufficient resistance to cellular traction to induce vinculin assembly. As the FN-coated beads were coupled to the retrograde F-actin flow and were not reinforced, the accumulation of vinculin at bead-membrane interfaces indicates a role of vinculin in mediating the link to the actin cytoskeleton even if no stabilization of the adhesion site occurs. The lack of vinculin in MEF $\text{vin}^{(-/-)}$ cells seemingly causes a stability reduction of

the integrin-mediated bead-cytoskeleton link. Possibly, this induces repeated partial ruptures in the actin-integrin association, which results in a kind of lateral rolling of the bead that might account for the observed zigzag course on long distance transport. The fluctuations observed in the short range might be attributed to a complete disassembly of the membrane-bead link, thereby causing bead detachment with subsequent Brownian motion of the bead. Consecutive recapturing of the bead restarts the rearward translocation, which can proceed along a different path.

Adhesion Force Development in Wild Type and Vinculin Deficient Cells

In a next step, the evolution of force transmission in MEF WT cells was compared to MEF $\text{vin}^{(-/-)}$ cells. The influence of vinculin on cell adhesiveness has been extensively studied and revealed a reduced substrate adhesion of MEF $\text{vin}^{(-/-)}$ cells [Coll *et al.* 1995, Xu *et al.* 1998a] as well as a diminished membrane stiffness and disruption resistance of adhesion sites [Goldmann *et al.* 1998a, Alenghat *et al.* 2000, Mierke & Kollmannsberger 2008]. Vinculin is recruited early into adhesion sites, but requires activation from its autoinhibited conformation to reveal cryptic binding sites for partner molecules such as talin, α -actinin and F-actin, enabling its participation in reinforcing adhesion sites [Kroemker *et al.* 1994, Johnson & Craig 1994, Johnson & Craig 1995, Gilmore & Burridge 1996, Margadant *et al.* 2011].

Here, a time-resolved study of force development in early adhesion sites is presented.

MEF WT and MEF $\text{vin}^{(-/-)}$ cells were incubated on FN-coated glass substrates and were exposed to 4.5 μm FN-functionalized beads for an interaction time of 300 seconds.

Evaluation of the adhesion morphology of wild type and MEF $\text{vin}^{(-/-)}$ cells demonstrated smaller adhesions in MEF $\text{vin}^{(-/-)}$ cells, which corresponds to previous studies on vinculin deficient cells [Coll *et al.* 1995, Xu *et al.* 1998a, Saunders *et al.* 2006].

Both cell lines showed the characteristic 3-phase development as described in paragraph 4.2.1 for different wild type cell lines, but MEF $\text{vin}^{(-/-)}$ cells remained far behind the traction force generation of MEF WT cells (figure 3.14). A force reduction of 50% was observed, with MEF $\text{vin}^{(-/-)}$ cells transmitting only $F_{\text{vin}^{(-/-)}} = 34 \pm 4 \text{ pN}$ compared to MEF WT cells with $F_{\text{WT}} = 84 \pm 4 \text{ pN}$ after 300 seconds. In the early phase of membrane-bead interaction (< 60 seconds), MEF $\text{vin}^{(-/-)}$ cells accomplished similar adhesion reinforcement rates as MEF WT cells. In contrast to WT cells they did not continue reinforcing the adhesion site but almost entirely stopped maturation at this force level. This demonstrates that vinculin does not play a significant role in the initial process of force generation but is a prerequisite for enhanced strengthening of adhesion sites. When a certain tension threshold is attained across the contact, force dependent recruitment of vinculin is triggered and regulates further reinforcement. This threshold force was traversed at $F_{\text{th}} \approx 20 \text{ pN}$.

The OT force spectroscopy approach gives insights into the time scale of vinculin recruitment and of vinculin-mediated reinforcements in early adhesion assembly. Here, vinculin accumulation and vinculin-mediated strengthening was deduced to occur within the time frame of 30 to 60 seconds after adhesion initiation. This finding corresponds to previous observations where vinculin was

demonstrated to be a prerequisite for enhanced force transmission but was not crucial for the initial formation of adhesion sites [Galbraith *et al.* 2002, Bershadsky *et al.* 2003, Cohen *et al.* 2005, Chen *et al.* 2006, Humphries *et al.* 2007, Choi *et al.* 2008, del Rio *et al.* 2009, Pasapera *et al.* 2010, Grashoff *et al.* 2010, Carisey & Ballestrem 2011, Yu *et al.* 2011].

A rescue of the mutant phenotype was successfully induced by re-expression of native, full length vinculin (vinFL). The expression of this protein restored adhesion morphology to wild type characteristics. Force spectroscopy with MEF vin^(-/-) cells expressing vinFL revealed nearly identical force development over the entire measurement interval and resulted in a force transmission of $F_{rescue} = 82 \pm 6 \text{ pN}$ after 300 seconds of bead interaction. This confirms the the diminished reinforcement of MEF vin^(-/-) adhesions was purely attributed to vinculin deficiency and was not induced by additional defect of this cell line.

Altogether, the OT force spectroscopy study gives insights into force development at individual adhesion sites and allows a time-resolved evaluation of early contact formation in MEF vin^(-/-) and MEF WT cell lines. However, OT only provide the means to assess force development in the pN regime of individual adhesions. For the evaluation of adhesion forces on the single cell level, an approach with access to the nN regime was required. To correlate adhesive behavior across distinctive force regimes, complementary data were acquired with AFM, focusing on single cell force spectroscopy (AFM-SCFS). This study was conducted and evaluated by Dr. Clemens Franz and his group at the Center for Functional Nanostructures (CFN). The aim of comparing the two studies was to infer on the relation of individual contact strength and the overall adhesion strength of an entire cell.

Evaluating AFM-SCFS measurements, it was concluded that the overall cell-substrate adhesion strength was reduced to about 20 % of wild type adhesion after 300 seconds of substrate contact. The reintroduction of vinculin into MEF vin^(-/-) cells successfully rescued the mutant phenotype and resulted in similar detachment forces as in MEF WT cells [Baumann 2010]. Hence, both force spectroscopy techniques showed the same tendency for detachment forces of entire cells as for reinforcement of individual adhesions. This supplies evidence that the initial cell-substrate contact formation follows the same dynamics as the assembly of isolated adhesion sites on well-spread cells and allows the cross-correlation of distinctive force and size scales.

4.3.2 Structural Mutations of Vinculin Modify Cell Adhesion Morphology and Force Development

Vinculin is a major component in cell adhesion sites and mediates adhesion reinforcement and force transmission to the substrate. The protein is comprised of distinct structural domains, namely a globular head domain, constituted by four organized helical bundles (D1 to D4), a flexible neck domain and a tail domain (D5) [Eimer *et al.* 1993, Winkler *et al.* 1996, Bakolitsa *et al.* 2004]. When vinculin is not incorporated into adhesion sites, it adopts a default autoinhibited conformation by binding of the head to the tail domain, which covers binding sites for several interaction partners

[Johnson & Craig 1994, Johnson & Craig 1995]. The complex structure of vinculin as well as the conformational switch from autoinhibited to active raises the question of how recruitment and force transmission are regulated by specific vinculin domains. Due to its presumed key function with regard to mechanosensing in adhesion sites, vinculin is one of the most extensively studied proteins. Nonetheless, many of the molecular mechanisms of vinculin interactions within adhesion sites remain unclear. In the presented study, the influence of structural mutations in specific vinculin domains on adhesion formation and force development is investigated.

Vinculin deficient mouse embryonic fibroblasts (MEF $\text{vin}^{(-/-)}$) were transfected to express mutated vinculin-GFP fusion proteins, such as the constitutively active protein **vinT12**, the autoinhibited **vinA50I** and a protein lacking the entire tail domain (**vin880**). Adhesion morphology and force transmission of these mutants were compared to MEF $\text{vin}^{(-/-)}$ cells expressing native full length vinculin (**vinFL**), which was demonstrated to completely rescue the mutant phenotype (detailed information on all vinculin constructs is provided in chapter 1.2.6).

Conformational Changes in Specific Vinculin Domains Manipulate Adhesion Assembly

Characterizing the adhesion morphology of the four vinculin mutants, it was derived that **vinFL** resembles the wild type morphology in all examined aspects (figure 3.15).

The constitutively active **vinT12** mutant exhibited adhesions of normal size in the cell periphery but featured extensive additional adhesion sites throughout the cell body. Notably, those adhesions were mostly smaller and more roundish than in the periphery. As this is an exclusive characteristic of this mutant, it is presumed that the enforced active conformation of the protein in the cytosolic pool facilitates the location-independent assembly of adhesion sites.

Expression of the autoinhibited **vinA50I** protein induced the assembly of wild type resembling adhesions, but these mutants produced a severe decrease in the number of adhesion sites. Instead, a large cytosolic pool of **vinA50I** molecules was formed, which was also reported in previous studies [Chen *et al.* 2005, Humphries *et al.* 2007, Diez *et al.* 2011]. This supplies evidence that the tightly closed conformation inhibits vinculin incorporation into adhesion sites.

Cells transfected to express **vin880**, a mutant comprising only head and neck domain, produced elongated but thin adhesion sites concomitant with an enhanced number of adhesion sites. The lack of the tail domain denotes a loss of binding sites for F-actin, paxillin, and PIP_2 (phosphatidylinositol 4,5-bisphosphate) and completely inhibits vinculin association to the cytoskeleton. Although F-actin-vinculin engagement is generally accomplished by the tail domain, these mutant adhesions were still able to establish a connection between the transmembrane integrins and the cytoskeleton [Humphries *et al.* 2007], which is possibly mediated by talin [Margadant *et al.* 2011]. Despite the truncation of the paxillin binding site, recruitment of **vin880** to adhesion sites was not inhibited. Paxillin was discussed as a promoter for vinculin recruitment in recent studies [Pasapera *et al.* 2010], whereas other investigators confirmed a paxillin-independent recruitment [Humphries *et al.* 2007]. While paxillin remains a candidate for mediating vinculin recruitment, a direct interaction of the proteins is apparently not mandatory for the association of vinculin with adhesion

sites. This holds at least for the expression of active protein conformations, whereas these results do not provide any information regarding the autoinhibited conformation.

Cells Expressing Vinculin Mutants Show Specific Alterations in Cell Adhesion Reinforcement

To exploit a correlation between cell adhesion morphology and strength, force spectroscopy assays were conducted on mutant expressing cells. The standard assay with FN-coated beads of $4.5\ \mu\text{m}$ diameter was followed and beads were applied close to the leading edge of well-spread, transfected MEF $\text{vin}^{(-/-)}$ cells.

Analysis of the OT force spectroscopy data (figure 3.16) revealed indistinguishable adhesion characteristics for all mutants (vinT12, vinA50I, vin880) after the initial 10 seconds of membrane-bead contact. Within the first 60 seconds all cells, independent of the mutant they were expressing, exhibited a similar gain in adhesion strength, demonstrating that vinculin does not influence the assembly of nascent adhesions. However, some differences for the various mutant expressing cells were observed over when considering the entire measurement interval of 300 seconds.

The tail truncated **vin880** mutant developed the least reinforcement of adhesion sites over the entire observation time of 300 seconds and exerted 50 % reduced traction forces compared to vinFL expressing cells. Comparing these results to MEF $\text{vin}^{(-/-)}$ cells, it was concluded that a rescue was not induced by this protein conformation although the adhesion size was larger than in MEF $\text{vin}^{(-/-)}$ cells.

Expression of the autoinhibited mutant **vinA50I** led to 30 % lower adhesion forces than observed in vinFL expressing cells. This indicates a partial rescue of the mutant phenotype, possibly evoked by the activation of a reduced number of vinA50I molecules. A recent study concerning the traction forces of vinA50I expressing cells on polyacrylamide gels came to a similar conclusion and reported a partial rescue with traction forces in an intermediate regime between MEF WT and MEF $\text{vin}^{(-/-)}$ cells [Diez *et al.* 2011]. The autoinhibited conformation of vinculin masks the cryptic binding site for talin and severely reduces talin-vinculin interaction [Johnson & Craig 1994, Bakolitsa *et al.* 2004]. It has been proposed that the association of talin to the vinculin head domain modifies the turnover dynamics of talin within adhesion sites towards elongated residency times [Cohen *et al.* 2006]. Taking these results together, the diminished talin affinity of the vinA50I mutant is assumed to limit talin detention time at the membrane-bead interface, causing a diminished cell adhesion stability compared to wild type adhesion sites.

Adhesion sites comprising constitutively active **vinT12** accomplished a full reinforcement recovery after 300 seconds of membrane-bead interaction. However, the development of the force-time curve of this mutant resembled the vinA50I characteristics in the first 120 seconds. Only afterwards did the reinforcement of vinT12 containing adhesion sites accelerate to match the native vinculin force transmission after about 180 seconds. This finding is particularly surprising as a protein in the constitutively active conformation was supposedly recruited more easily into adhesion sites. Analyzing the time-resolved results from the OT force spectroscopy, it was deduced that either vinT12 recruitment from the cytosolic pool was retarded in the initial contact phase or that the

incorporation of vinculin into the adhesion site was impeded. It was demonstrated in a previous study that the attenuation of head-to-tail binding, activated the assembly of vinculin-talin- β_1 integrin complexes at ectopic cellular regions [Cohen *et al.* 2006]. This might account for a retarded vinT12 recruitment and subsequently cause a delay in reinforcement. However, this hypothesis requires further investigation on vinculin mutant recruitment and turnover rates.

With the mutants tested in this study a possible correlation of the size of cell adhesions, formed during cell spreading between the basal membrane and FN-coated substrates, and the traction forces, exhibited at newly formed adhesions at membrane-bead interfaces, was evaluated. The overall examination of distinctive vinculin mutants concedes the case that the average size of individual cell-substrate adhesions does not allow a prediction of cellular traction forces.

A complementary AFM-SCFS study on overall detachment forces was conducted with identical vinculin constructs in the group of Dr. Clemens Franz and revealed the same tendencies as deduced with OT force spectroscopy. Detachment forces in the initial 5 seconds of cell-substrate contact were low but well within the sensitivity range of the cantilever. Surprisingly, at this very early stage of adhesion formation significantly higher adhesion forces were observed in vinT12 expressing cells compared to vin880 mutants. The initial nucleation of adhesion sites is supposed to originate from thermodynamically driven mutual encounters of integrins and extracellular ligands [Cohen *et al.* 2004] followed by ligation and accumulation of additional integrins. In vinT12 expressing cells pre-assembled vinculin-talin-integrin complexes exist [Cohen *et al.* 2006]. The amplification of force transmission, observed in an extremely early contact phase, might originate from random engagement of these complexes with the extracellular ligand. The hypothesis was derived that random complex-ligand interactions give the vinT12 mutant a slight advance on force generation in the initial contact phase.

After 300 seconds of cell-substrate contact, both vinFL and vinT12 expressing cells had developed high adhesion forces. In comparison, adhesion forces in vinA50I and vin880 expressing cells were reduced to 50 % and 45 %, respectively. A slight tendency was observed towards enhanced detachment forces in vinA50I expressing cells over vin880 mutants. This corresponds to the increased reinforcement of individual adhesion sites in vinA50I expressing cells derived from OT force spectroscopy.

Altogether, the employment of the two force spectroscopy methods, AFM and OT, allowed to obtain insights into the temporal development of overall cell attachment and individual cell adhesion forces. Comparing the results for the expression of various vinculin mutants, both methods draw similar conclusions on the functionality of distinct structural conformations of vinculin as is illustrated in figure 4.2. The introduction of vinFL into vinculin deficient cells triggered a complete rescue of the mutant phenotype (figure 4.2 C)). The constitutively active vinT12, lacking head/tail interaction, was likewise able to induce a full rescue (figure 4.2 D)). However, an indication of retarded recruitment or impaired incorporation into adhesion sites was provided by OT force spectroscopy. Due to the attenuation of head/tail affinity, cryptic binding sites for talin and other binding

partners are invariably exposed [Johnson & Craig 1994]. Previous reports gave evidence that the enforced active conformation of the protein leads to the formation of tripartite complexes with talin and β_1 integrin at ectopic cell sites. This possibly leads to a retardation in vinT12 recruitment to peripheral adhesion sites. Besides, the phenomenon of pre-existing tripartite complexes

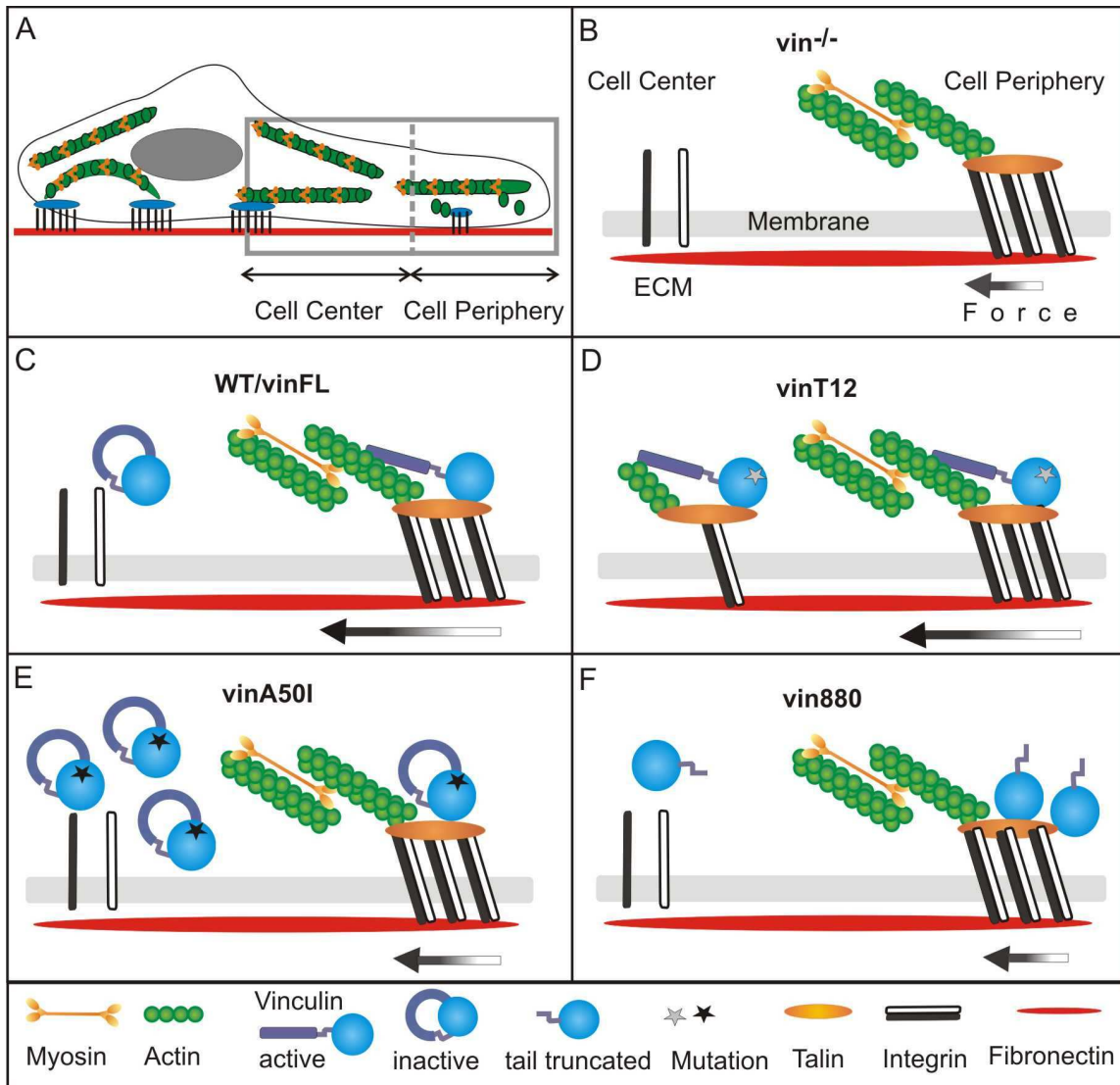


Fig. 4.2: Summary of the effect of vinculin mutations on force development

A) Sketch of the investigated cellular areas. B) Vinculin deficient cells show a weak force transmission to the extracellular matrix (ECM), as depicted by the arrow; the link between integrins and the actomyosin system is probably mediated by talin [Margadant *et al.* 2011]. C) The expression of native vinculin rescues the mutant phenotype and the interaction of the vinculin head with talin and the vinculin tail with actin allows for reinforcement of the adhesion site, which results in strong force transmission to the ECM. Adhesion sites are mainly formed in the cell periphery and rarely in the cell center. D) The constitutively active vinT12 leads to equal force transmission as the native protein, but auxiliary small adhesion sites are formed in the central cell body. E) Expression of the autoinhibited mutant vinA50I resulted in high cytosolic concentrations and reduced adhesions strength, compared to native vinculin expressing cells. F) In adhesions mediated by the tail truncated vin880 protein, adhesion strength is as low as in vinculin deficient cells, which is probably due to the missing interconnection with the actin cytoskeleton.

might account for the extensive formation of small roundish adhesion sites throughout the entire cell-substrate contact area.

The mutant vinA50I is engaged in a constitutively inhibited conformation with enhanced head-tail interaction and thus features a reduced binding affinity for talin and other vinculin head associated proteins. This was observed to induce a slight recovery of adhesion strength in vinA50I expressing cells compared to MEF vin^(-/-) cells and highlights the impact of talin binding to vinculin on force transmission (figure 4.2 E)). Furthermore, the expression of the autoinhibited protein led to the emergence of a large cytosolic pool, indicating that the closed vinculin conformation presented an obstruction to recruitment into adhesion sites.

Analyzing vin880 expressing cells, it was concluded that a protein comprising head and neck domain only, failed to restore the adhesion characteristics of wild type cells (figure 4.2 F)). Instead, this mutant retained the weak adhesion forces of MEF vin^(-/-) cells. This was observed although vin880 was recruited into adhesion sites, indicating that the incorporation of vinculin into adhesion sites is mediated by the head domain, most likely by talin binding [Gilmore & Burridge 1996, Chen *et al.* 2006].

Both vinT12 and vinA50I protein structures feature point mutations that manipulate the head-tail interaction of vinculin, causing a highly diverse response in cellular adhesion reinforcement. This gives evidence to a fundamental role attributed to the conformational switch integrated into the vinculin molecule, which is associated with an all-or-nothing response of cell adhesion strengthening.

4.3.3 Cellular Forces and Cytoskeletal Dynamics: A Comparison of Cell Types

Cell adhesion, retrograde F-actin flow, and cell motility are intrinsically interleaved phenomena observed within a large variety of cell types, in which the actomyosin system presents the driving force.

The results reported in the previous paragraphs were concerned with cellular traction forces and/or the retrograde transport dynamics of actin and were conducted in different cell types. To complement these data, an additional cell motility study was implemented for all cell types investigated so far. This enabled a cell type comprehensive study on the universal relation of cellular traction force, retrograde transport velocity and migration velocity. Here, the results from the investigation of three wild type (WT) cell lines, namely B16 mouse melanoma cells (B16), mouse embryonic fibroblasts (MEF WT), and primary chicken fibroblasts (PCF), were analyzed with respect to data obtained on the vinculin deficient MEF vin^(-/-) cells. This comparative study aims at describing a cell-type-independent relation between the three parameters force, actin flow, and migration speed. The incorporation of data on the vinculin deficient MEF vin^(-/-) cells, was driven by the intention to quantify the impact of vinculin on cellular forces and dynamics in a cell type comprehensive context.

It has been demonstrated in previous studies, that a biphasic correlation exists between traction stress and actin flow rate, depending on cell migration rates [Jurado *et al.* 2005] or on a threshold velocity of actin and F-actin flow [Gardel *et al.* 2008, Li *et al.* 2010]. Other studies reported a linear

relation of contractility and F-actin dynamics [Lin *et al.* 1996]. Furthermore, an inversely proportional behavior of F-actin flow and migration was observed [Jurado *et al.* 2005, Guo & Wang 2007] and recently data on a linear relation of traction stress and F-actin flow were published [Fournier *et al.* 2010]. However, these relations were determined within individual cell types (fish epidermal keratocytes, NIH3T3 mouse embryonic fibroblasts, rat kangaroo kidney epithelial cells PtK1) and usually only two of the three parameters were monitored.

Analyzing the force spectroscopy data, the retrograde flow, and the motility measurements, a linear correlation between traction force and actin flow (deduced from bead translocation), was demonstrated. Furthermore, an inverse relation of migration velocity and both traction force and actin flow was observed. This result was universally validated for all wild type cell lines (figure 3.9): highest traction force and exceeding retrograde transport dynamics were found in PCF cells and coincided with nearly stationary migration rates. In contrast, the slow actin flow in B16 cells was related to weak adhesion strength at the membrane-bead interface and concomitant with a fast migration. The symmetry of adhesion strength, retrograde actin flow and cell locomotion is illustrated in figure 4.3 A)) for fast migrating cells and in B) for slowly migrating cells.

The incorporation of vinculin deficient MEF $\text{vin}^{(-/-)}$ cells into the analysis revealed that this cell type was incompatible with the symmetries derived for WT cells. Significantly, MEF $\text{vin}^{(-/-)}$ cells exhibited comparatively low traction forces that coincided with exalted retrograde transport dynamics (figure 4.3 C)). While the relation of weak forces and enhanced motility agrees with the WT derived model, the retrograde actin dynamics are apparently incoherent with this model. The

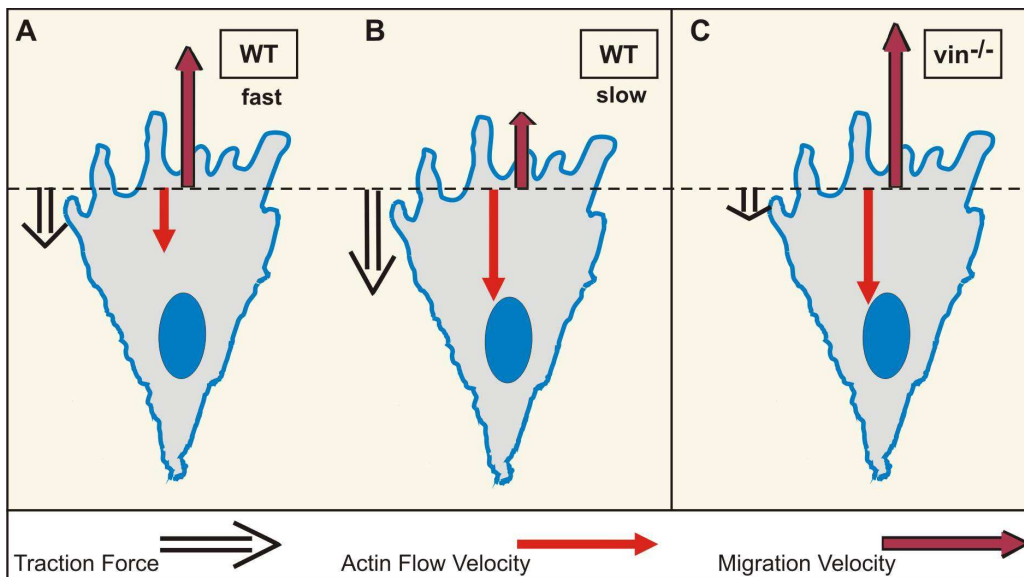


Fig. 4.3: Comparison of traction forces and actin dynamics in wild type and vinculin knockout cell lines

A) A fast migrating wild type (WT) cell exhibits weak forces at individual adhesion sites and features a slow retrograde actin flow. B) Slowly migrating WT cells display strong adhesion forces and fast actin dynamics. C) Vinculin deficiency ($\text{vin}^{(-/-)}$) leads to increased cell motility in combination with weak adhesiveness but enhanced retrograde actin flow.

mismatched relation of force and retrograde flow coupling emphasizes the impact of vinculin in mediating and stabilizing the association of integrin complexes with the actin cytoskeleton [Choquet *et al.* 1997, Galbraith *et al.* 2002]. In motile cells, actin flow rates in the lamellipodium are strongly enhanced compared to the lamella. The formation of focal adhesions is assumed to act as a barrier that modulate actin flow dynamics and accounts for the transition from fast to slow flow at the interface of lamellipodium and lamella [Hu *et al.* 2007, Alexandrova *et al.* 2008, Shemesh *et al.* 2009]. It remains a question for further investigation if the attenuated stability of vinculin deficient adhesions contributes to a limited deceleration of the rapid actin flow at this interface. Here, the comparison of retrograde flow behavior at the transition from lamellipodium and lamella in MEF WT and vinculin deficient MEF $\text{vin}^{(-/-)}$ cells could provide a first indication of a disturbance in the adhesion-induced slowdown of actin flow, which might account for the enhanced flow rates in MEF $\text{vin}^{(-/-)}$ cells.

The results of the cell type comprehensive study enabled the characterization of cell-type independent relations between the contractile force generation, retrograde actin dynamics, and cell motility. However, the detailed mechanisms of interdependence between these parameters are still poorly understood and require further investigation. With the comparative analysis of a vinculin deficient cell line, specific discrepancies with different wild type cell lines were elucidated and revealed once again the importance of vinculin in the regulation of the cytoskeletal association with integrin complexes.

4.4 Outlook

Cell adhesion formation has a crucial influence on cellular mechanosensing and mechanotransduction and is a key mediator of cell function and morphology. The presented work deals with the investigation of early adhesion formation (300 seconds) and was able to elaborate on several parameters regulating the force transmission at cell adhesion sites.

With the custom-build optical tweezers (OT) setup force measurements in the order of 10 to 190 pN were feasible. Especially the upper limit of applicable counterforces is a restraining element on further investigations. Cellular traction forces after the initial 300 seconds start to exceed the linear trap-force regime required for force spectroscopy evaluation. Especially the primary cell line exerted pulling forces on the order of maximum OT counterforces. Hence, an upgrade in OT generated forces would be useful to extend the conducted measurements to longer observation times and stronger primary cell lines. One method to achieve this is to intensify the applied laser power. However, this puts the cell samples at risk as it would lead to amplified heating in both the cell culture medium and the cells themselves. Another method is the modification of the force probes. In the conducted experiments, ligand-functionalized polystyrol beads were applied to the cells to mimic new contact sites. The reflective properties of polystyrol in aqueous solutions are not optimal for the generation of optical gradient forces. It has been demonstrated, that a bead coating with an anti-reflective layer (e.g. a silica layer on a polystyrol core) can enhance the efficiency of the optical trap and results in a two- to three-fold increase in optical gradient forces [Graf *et al.* 2003, Bormuth *et al.* 2008]. Implementing this method into the bead preparation routine could thus give rise to new possibilities in the study of cell adhesion maturation over extended time periods.

One parameter investigated with regard to cell adhesion development was the type of integrin ligand and ligand density. A comparison of the ECM constituent fibronectin (FN) with a cyclic peptide containing the adhesion motif RGD (cRGDfk) revealed a faster reinforcement and stronger overall attachment of cell adhesion sites formed to the ligand FN. This effect became more pronounced with enhanced coating densities. As the investigated cells were plated on a FN-coated glass substrates, the question arises whether this functionalization influences the ligand-dependent response. It is well-established that the chemical substrate characteristics influence the expression rate of several integrin types as well as cell morphology [Singer *et al.* 1988, Hakkinen *et al.* 2011]. Thus, additional experiments with cells plated on RGD-coated substrates and exposed to FN- and RGD-functionalized beads, respectively, could give insights into the cellular regulation of integrin expression.

Another aspect of the integrin ligand assay was the comparison of different functionalization densities and their effect on force transmission in developing cell adhesion sites. The experiments were conducted with one type of coating density applied per sample. As the various coating densities were optically indistinguishable, it was not possible to create ligand density gradients by geometrically arranging beads with different coating densities. This type of experiment would provide versatile additional information on cellular haptotaxis. Therefore, a fluorescent labeling of the lig-

and is essential for further investigations. As the direct labeling of a peptide with a fluorophor can easily change its recognition by the integrin family, an indirect labeling approach was developed in cooperation with the Nano-Devices group of Dr. Ljiljana Fruk. First, a cRGD peptide with a spacer chain of aminohexanoic acids was attached to the functional cRGDfk peptide to increase the distance to the fluorescent label. Second, a trifunctional linker was designed with the aim to crosslink one terminus to a fluorophor, another to the peptide and the remaining terminus to the bead. Although the basic concept of this method has already been established within the scope of this work, the actual coupling of the trifunctional linker with the peptide proved challenging. A future aim is to optimize the process of peptide-linker attachment by selecting a different set of functional groups at the linker and peptide spacer termini and to implement the peptide-linker-fluorophor construct in the standard bead-functionalization assay. With the availability of fluorescently labeled cRGDfk peptides, new experimental designs become feasible, such as the combination of ligand gradients generated by the arrangement of distinctively coated beads on the apical cell surface with micro contact printing adhesive gradients on the growth substrate.

The presented work showed fascinating insights into the influence of vinculin on adhesion development and retrograde flow characteristics. Strongly enhanced transport rates of surface attached beads were observed in vinculin deficient cells and point at a possible role of vinculin in actin flow regulation. However, a more direct analysis of actin flow dynamics and directionality is required to confirm this hypothesis. Fluorescent speckle microscopy and spatiotemporal image correlation spectroscopy have proven versatile tools for flow velocity mapping of various proteins in live cells [Valloton *et al.* 2004, Brown *et al.* 2006]. These methods could play an important role in the future evaluation of actin and vinculin flow dynamics in wild type and vinculin deficient cells.

APPENDIX

A Indirect Labeling of cyclic RGD Peptides

In the experiments described in chapter 3.2.2, different amounts of the integrin ligands fibronectin (FN) and the cyclic peptide cRGDfk were coupled to the bead surface for force spectroscopy. For each measurement, beads functionalized with one specific FN or cRGDfk density were applied to the investigated cells. The density of ligands attached to a bead surface was measured with UV-VIS spectroscopy, which allowed to characterize the average coating density of a sample containing a large number of beads. With this approach it was not possible to account for individual variabilities of beads functionalized under the same conditions. Neither was it feasible to simultaneously expose cells to beads with different ligand densities, as they were optically indistinguishable. To solve this problem, the cRGDfk peptides on the bead surface requires a fluorescent label to quantify ligand density by fluorescence microscopy. For an exact determination of the ligand density on a bead surface, a fluorescent labeling of the ligand with one dye molecule per ligand is a prerequisite.

Design of a Trifunctional Linker

First, a direct labeling approach of the RGD containing cyclic peptide cGRGDSPA (Bachem AG) with AlexaFluor488-succinimidyl (Life Technologies) was tested. The succinimidyl ester of the dye can be covalently coupled to the amino groups of the peptide. Although the peptide sequence was in a cyclic conformation, it was considered to feature a free amino group in one of its side chains. However, the establishment of a crosslink between the dye and the cGRGDSPA peptide was not successful. Probably the cyclic conformation inhibited the access of the succinimidyl ester to the amino group.

As a direct coupling of a dye to the peptide also risks to modify or impair its functionality as

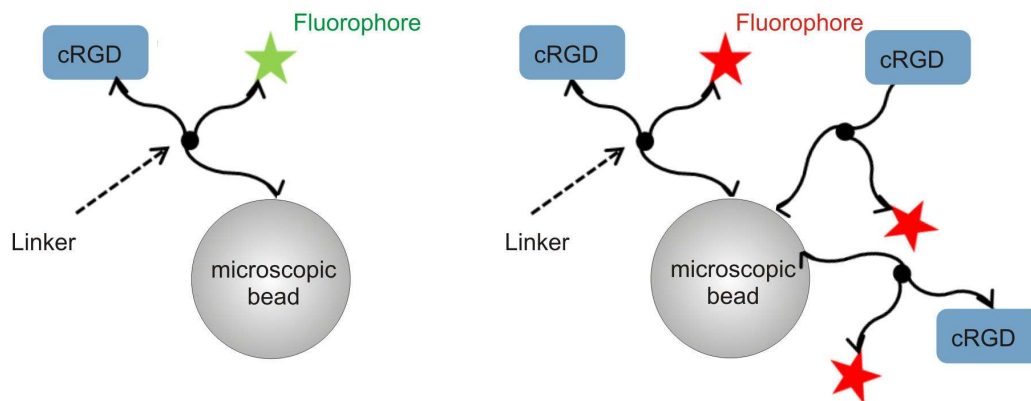


Fig. A.1: Indirect labeling of cRGD peptides

A trifunctional linker allows to couple different fluorophores together with a peptide to the microscopic beads used in force spectroscopy. The linker allows to label a peptide indirectly, which reduces the risk of unfavorable conformational changes in the peptide occurring with direct coupling.

adhesion motif, a new approach was developed in cooperation with Dr. Ljiljana Fruk and her group (Young Scientist Group Nano-Devices of the DFG-Center for Functional Nanostructures at the KIT). To accomplish an indirect labeling and to amplify the distance between the RGD adhesion motif of the peptide and the dye, a trifunctional lysine linker was designed and a modified peptide with an elongated spacer sequence was synthesized. One arm of the linker features a functional group to attach a fluorophore, while another is used to attach the peptide and the third terminus allows to couple the linker to the microscopic beads (figure A.1).

The trifunctional linker can be labeled with fluorophores emitting in distinct spectral regimes. This allows to mark specific ligand densities on the bead surface via linkers labeled by fluorophores emitting in different regimes. This approach allows to apply beads labeled with different ligand densities simultaneously to the cell samples. The actual ligand density can either be quantified during the OT force spectroscopy experiment via fluorescence illumination or after the experiments with confocal scanning microscopy for accurate density calculation. This opens the completely new opportunity to study the cellular traction response to different ligand densities and ligand gradients in close spatial correlation.

For this type of experiments a trifunctional linker is required, allowing to attach a fluorophore and a peptide and then couple the linker to the microscopic beads. The carboxylated surface of the beads allows to attach the linker via an amine functional group. In addition, fluorophores are commonly functionalized with NHS-esters targeting functional amine groups. This leads to the demand of a second amino group in the linker to crosslink the fluorophore. As only one single fluorophore molecule and one single peptide molecule are to be attached to each linker molecule, one of the functional amino groups has to be protected to block the binding site during peptide or fluorophore application.

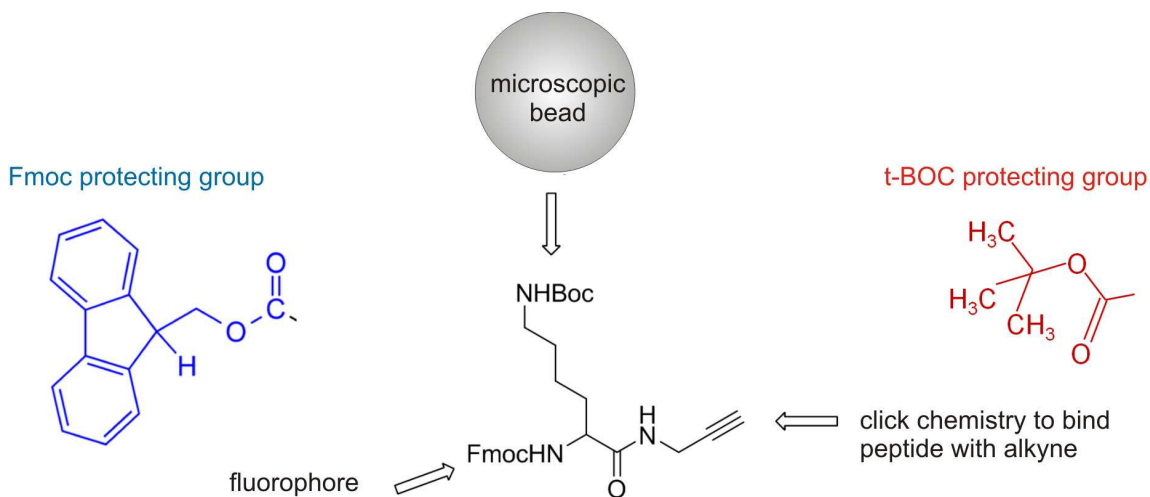


Fig. A.2: Trifunctional linker synthesis

A lysine linker was synthesized by Dr. Martina Altemöller and the two functional amino groups were protected with Fmoc and t-BOC groups. Fluorophores are coupled to the Fmoc protected amine and carboxylated beads to the BOC protected group. The third functional group is an azide to couple an alkyne modified cRGD peptide to the linker.

The linker designed for this purpose was a lysine linker featuring two protected amino groups and a terminal alkyne was synthesized by Dr. Martina Altemöller in the Nano-Devices group. Linker protection was realized by reacting one amino group with a Fmoc (fluorenylmethoxycarbonyl) protecting group and the other with a BOC (di-tert-butyl dicarbonate) protecting group. Fmoc and BOC can be used orthogonally, as Fmoc deprotection is achieved with base treatment while t-BOC is removed in acidic solution. The third arm of the linker was functionalized with an alkyne group to be crosslinked with the cRGD peptide (figure A.2).

Fmoc Cleavage

The dried lysine linker was dissolved in acetonitrile (ACN) containing 35 % piperidine (Carl Roth) to cleave the Fmoc protection and the success of the reaction was checked after 12 h with a thin layer chromatography approach. When the analysis showed a complete conversion of the reactant, the product was concentrated in a rotary evaporator. A test tube was analyzed with $^1\text{H-NMR}$ (nuclear magnetic resonance) spectroscopy, confirming the deprotection of one amino group of the lysine linker. The cleaved linker was purified by filtration through a silica gel prepacked suction filter and the purified linker was concentrated in a rotary evaporator for storage at 4°C .

Coupling of Fluorophor and Lysine Linker

The Fmoc cleaved lysine linker was coupled with the fluorophor Atto610-NHS (Atto-Tec): linker and fluorophor were dissolved in dimethyl sulfoxide (DMSO) and mixed with a molar ratio of 1:1 over night at room temperature. The labeled linker was purified using high pressure liquid chromatography (HPLC; Agilent 1200 series HPLC system) with a 30 min gradient from 0 % to 100 % ACN containing 0.1 % trifluoroacetic acid (TFA). Product sampling was performed for chromaog-

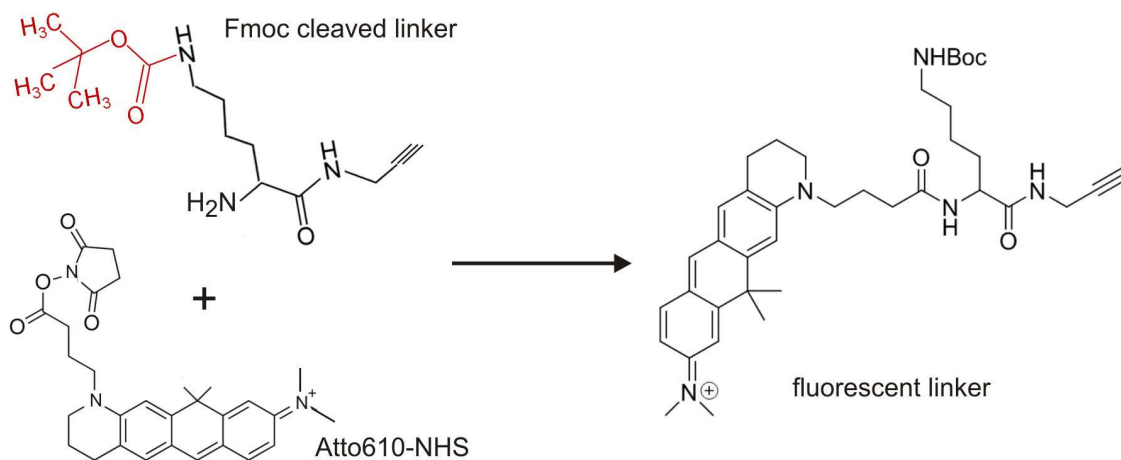


Fig. A.3: Coupling of fluorophor and linker

Reaction: $5\ \mu\text{l}$ lysine linker (34 mM) was added to $110\ \mu\text{l}$ Atto-NHS (1.7 mM) and incubated at room temperature over night. The product was purified via HPLC and analyzed with MALDI-TOF.

raphy peaks occurring simultaneously at 280 nm (absorption of proteins) and in the fluorescence channel at 615 nm (for details on the optical characteristics of Atto610 refer to table A.2). For mass confirmation, the HPLC sample containing the purified Atto-linker was applied onto a DHB (2,5-dihydroxybenzoic acid) matrix suitable for peptides and proteins below 10 kDa. As a control the Atto610 dye and the lysine linker were added onto separate panels. With matrix assisted desorption ionisation mass spectroscopy using time of flight measurements (MALDI-TOF) the molecular weight of the components was determined and compared to the computed values. The molecular weights obtained from MALDI-TOF were the following: $MW_{\text{linker}} = 283$; $MW_{\text{Atto}}=390$; $MW_{\text{AttoLinker}}=656$ and corresponded to the computed values referred to in table A.1. This analysis confirmed that all three components were separately sampled with the applied HPLC protocol. In figure A.3 the coupling of the Fmoc cleaved linker, which is still featuring a t-BOC protecting group with the Atto610 fluorophor, is depicted. The now deprotected amino group was reacted with the succinimidyl ester of the fluorophor and the resulting Atto-linker molecule was dried in a centrifugal evaporator (SpeedVac, Savant) and stored at 4°C for further use.

BOC Cleavage

Di-tert-butyl dicarbonate (BOC) was used to protect one of the amine functional groups of the lysine linker. The protecting group was removed by adding phosphoric acid and incubating the solution over night. The deprotected linker was purified with the HPLC protocol mentioned previously, using an ACN gradient from 0 % to 100 % over a time course of 30 min. The free amino group was subsequently used to couple the linker to the carboxylated beads. As t-BOC does not react to bases, it was used as orthogonal protection with Fmoc.

Click-Chemistry: Coupling of Peptide and Lysine Linker

To couple a cRGD peptide with the fluorescently labeled lysine linker, a Huisgen copper catalyzed azide-alkyne cycloaddition was performed. The working principle of the click reaction is depicted in figure A.4, where an organic azide is fused with a terminal alkyne, forming a 1,2,3-triazole.

Tab. A.1: Molecular weight (MW) of reactants for MALDI-TOF quantification

Name	MW [g/mol]
Linker, protected (BOC, Fmoc)	505.6
Linker, protected (BOC)	283.4
Linker, protected (Fmoc)	406.0
Linker(BOC)-Atto	656.0
Linker-Atto (deprotected)	556.8
cRGDfk peptide	1088
Atto-Linker-cRGD	1634

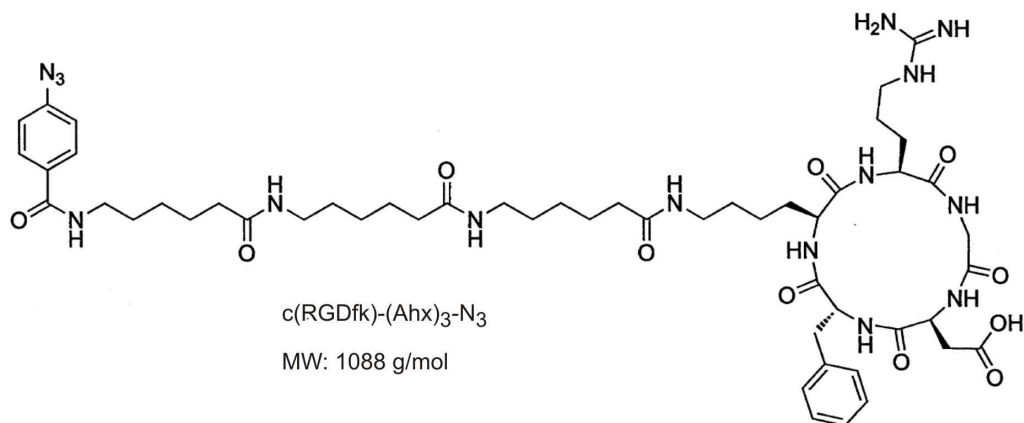


Fig. A.5: The cyclic RGD peptide cRGDfk

A cyclic cRGDfk peptide with a functional azide group was synthesized by C. Richter. The sequence of aminohexanoic acids was added as a spacer to protect the RGD adhesion motif from conformational changes due to crosslinking with the lysine linker molecule.

Even though a variety of conditions were tested (table A.3) the reaction was never successful. MALDI-TOF mass quantification resulted in the detection of the linker mass and of a changed peptide mass. This led to the assumption that either the peptide synthesis was not completely successful or the peptide was damaged during storage. Also, the free functional groups of the peptide (amines for example) possibly interfered with the cycloaddition process.

Due to this, the approach for linker and peptide synthesis had to be adapted: instead of attempting to attach the peptide via cycloaddition to the linker, a fluorophore featuring an alkyne functional group can be coupled to the azide group of the linker. The peptide was modified and synthesized with a maleimide group at the terminus of the aminohexanoic spacer. In addition, a modification of the lysine linker is planned: a sulfhydryl group will be newly introduced, replacing one of the amine groups. Via this functional group, the newly synthesized cRGDfk peptide will be crosslinked.

With the availability of the fluorescently marked linkers, it will be feasible to prepare sets of cRGDfk functionalized beads with different densities and distinct excitation/emission spectra. These beads can then simultaneously be added to a cell sample and ligand density can be tested by fluorescence imaging. New experiments deriving the cellular response to various ligand densities, gradients or patterns can be conducted within individual cells. This can give new insights into cellular behavior toward a complex extracellular environment containing various biochemical cues.

B Overview of Forces and Dynamics in All Examined Cell Types

Four cell types were studied with regard to their traction forces, retrograde transport dynamics and motility. Forces were obtained from OT force spectroscopy with $4.5\ \mu\text{m}$ FN-functionalized beads that were positioned in the leading edge of the cells. The force transmission onto the beads was evaluated after 300 s of bead-cell contact. In the retrograde transport assay FN-functionalized beads of $4.5\ \mu\text{m}$ diameter were deposited in the leading edge and bead velocity was evaluated after 20 min. Motility studies were performed by nucleus tracking of the migrating cells, which were monitored over 12 h to 16 h.

For all cell lines, force transmission at adhesion sites and migration velocity correlated reciprocally with MEF $\text{vin}^{(-/-)}$ cells exhibiting the lowest traction forces and the highest motility (figure B.1).

Regarding the retrograde actin flow, the rearward bead translocation dynamics correlated with the strength of adhesion reinforcement in all wild type cell lines. For MEF $\text{vin}^{(-/-)}$ cells this symmetry was broken: the low traction forces in these cells were linked to exalted retrograde transport dynamics.

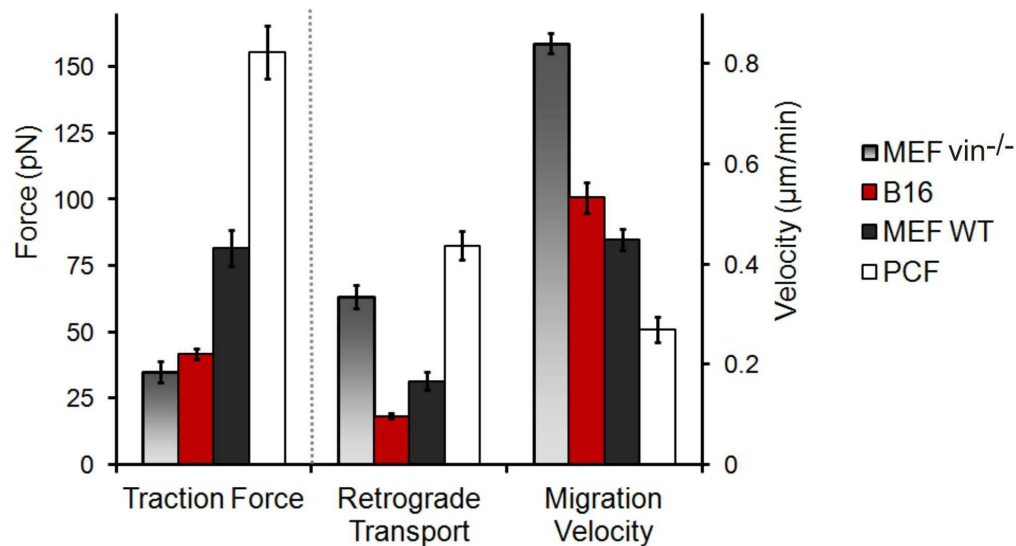


Fig. B.1: Force, retrograde transport and motility in B16, MEF WT, MEF $\text{vin}^{(-/-)}$ and PCF cells
Cell lines are arranged in ascending order regarding traction forces (black). MEF $\text{vin}^{(-/-)}$ cells showed a force-RT-migration relation distinct from the other observed cell lines: a higher RT velocity was linked to a reduced force transmission and enhanced motility.

Tab. B.1: Traction forces, retrograde transport velocity v_{RT} and migration velocity v_m in B16, PCF, MEF WT and MEF $\text{vin}^{(-/-)}$ cells. Forces were measured in the leading edge of the cells after a contact time of 300 s.

Cell type	Force [pN]	v_{rt} [$\mu\text{m}/\text{min}$]	v_m [$\mu\text{m}/\text{min}$]
B16	42 ± 2	0.097 ± 0.006	0.53 ± 0.03
PCF	155 ± 10	0.44 ± 0.03	0.27 ± 0.03
MEF WT	81 ± 7	0.17 ± 0.02	0.45 ± 0.02
MEF $\text{vin}^{(-/-)}$	34 ± 4	0.34 ± 0.06	0.84 ± 0.05

BIBLIOGRAPHY

- [Adler & Parmryd 2010] J Adler and I Parmryd. *Quantifying colocalization by correlation: the Pearson correlation coefficient is superior to the Mander's overlap coefficient*. Cytometry A, vol. 77, no. 8, pp 733–742, 2010.
- [Ahmed *et al.* 2010] WW Ahmed, T Wolfram, AM Goldyn, K Bruellhoff, BA Rioja, M Möller, JP Spatz, TA Saif, J Groll and R Kemkemer. *Myoblast morphology and organization on biochemically micro-patterned hydrogel coatings under cyclic mechanical strain*. Biomaterials, vol. 31, no. 2, pp 250–258, 2010.
- [Alenghat & Ingber 2002] FJ Alenghat and DE Ingber. *Mechanotransduction: all signals point to cytoskeleton, matrix, and integrins*. Sci STKE, vol. 2002, no. 119, p pe6, 2002.
- [Alenghat *et al.* 2000] FJ Alenghat, B Fabry, KY Tsai, WH Goldmann and DE Ingber. *Analysis of cell mechanics in single vinculin-deficient cells using a magnetic tweezer*. Biochem Biophys Res Commun, vol. 277, no. 1, pp 93–99, 2000.
- [Alexandrova *et al.* 2008] AY Alexandrova, K Arnold, S Schaub, JM Vasiliev, JJ Meister, AD Bershadsky and AB Verkhovskiy. *Comparative dynamics of retrograde actin flow and focal adhesions: formation of nascent adhesions triggers transition from fast to slow flow*. PLoS One, vol. 3, no. 9, p e3234, 2008.
- [Aota *et al.* 1994] S Aota, M Nomizu and KM Yamada. *The short amino acid sequence Pro-His-Ser-Arg-Asn in human fibronectin enhances cell-adhesive function*. J Biol Chem, vol. 269, no. 40, pp 24756–24761, 1994.
- [Aratyn-Schaus & Gardel 2010] Y Aratyn-Schaus and ML Gardel. *Transient frictional slip between integrin and the ECM in focal adhesions under myosin II tension*. Curr Biol, vol. 20, no. 13, pp 1145–1153, 2010.
- [Aratyn-Schaus *et al.* 2011] Y Aratyn-Schaus, PW Oakes and ML Gardel. *Dynamic and structural signatures of lamellar actomyosin force generation*. Mol Biol Cell, vol. 22, no. 8, pp 1330–1339, 2011.
- [Ashkin *et al.* 1986] A Ashkin, JM Dziedzic, JE Bjorkholm and S Chu. *Observation of a single-beam gradient force optical trap for dielectric particles*. Optics Letters, vol. 11, no. 5, pp 288–290, 1986.
- [Ashkin *et al.* 1987] A Ashkin, JM Dziedzic and T Yamane. *Optical trapping and manipulation of single cells using infrared laser beams*. Nature, vol. 330, pp 769–771, 1987.
- [Ashkin *et al.* 1990a] A Ashkin, K Schütze, JM Dziedzic, U Euteneuer and M Schliwa. *Force generation of organelle transport measured in vivo by an infrared laser trap*. Nature, vol. 348, pp 346–348, 1990.
- [Ashkin *et al.* 1990b] A Ashkin, K Schütze, JM Dziedzic, U Euteneuer and M Schliwa. *Force generation of organelle transport measured in vivo by an infrared laser trap*. Nature, vol. 348, no. 6299, pp 346–348, 1990.
- [Ashkin 1970] A Ashkin. *Acceleration and trapping of particles by radiation pressure*. Phys. Rev. Lett., vol. 24, pp 156–159, 1970.
- [Ashkin 1992] A Ashkin. *Forces of a single-beam gradient laser trap on a dielectric sphere in the ray optics regime*. Biophys. J. (Biophysical Society), vol. 61, pp 569–582, 1992.
- [Autenrieth 2008] T Autenrieth. *Zellpolarisierung im substratgebundenen Fibronektingradienten*. Master's thesis, Karlsruhe Institute of Technology (KIT), 2008.
- [Bailly *et al.* 2001] M Bailly, I Ichetovkin, W Grant, N Zebda, LM Machesky, JE Segall and J Condeelis. *The F-actin side binding activity of the Arp2/3 complex is essential for actin nucleation and lamellipod extension*. Curr Biol, vol. 11, no. 8, pp 620–625, 2001.
- [Bakolitsa *et al.* 2004] C Bakolitsa, DM Cohen, LA Bankston, AA Bobkov, GW Cadwell, L Jennings, DR Critchley, SW Craig and RC Liddington. *Structural basis for vinculin activation at sites of cell adhesion*. Nature, vol. 430, no. 6999, pp 583–586, 2004.

- [Balaban *et al.* 2001] NQ Balaban, US Schwarz, D Riveline, P Goichberg, G Tzur, I Sabanay, D Mahalu, S Safran, A Bershadsky, L Addadi and B Geiger. *Force and focal adhesion assembly: a close relationship studied using elastic micropatterned substrates*. Nat Cell Biol, vol. 3, no. 5, pp 466–472, 2001.
- [Ballestrem *et al.* 2000] C Ballestrem, B Wehrle-Haller, B Hinz and BA Imhof. *Actin-dependent lamellipodia formation and microtubule-dependent tail retraction control-directed cell migration*. Mol Biol Cell, vol. 11, no. 9, pp 2999–3012, 2000.
- [Bao & Suresh 2003] G Bao and S Suresh. *Cell and molecular mechanics of biological materials*. Nat Mat, vol. 2, no. 11, pp 715–725, 2003.
- [Barnhart *et al.* 2011] EL Barnhart, KC Lee, K Keren, A Mogilner and JA Theriot. *An adhesion-dependent switch between mechanisms that determine motile cell shape*. PLoS Biol, vol. 9, no. 5, p e1001059, 2011.
- [Baumann 2010] H Baumann. Investigating the role of vinculin during early adhesion formation using single-cell force spectroscopy. Master's thesis, Karlsruhe Institute of Technology (KIT), 2010.
- [Baumgartel 2007] J Baumgartel. *Colloids as model systems for condensed matter*. PhD thesis, Universität Stuttgart, 2007.
- [Bausch *et al.* 1998] AR Bausch, F Ziemann, AA Boulbitch, K Jacobson and E Sackmann. *Local measurements of viscoelastic parameters of adherent cell surfaces by magnetic bead microrheometry*. Biophys J, vol. 75, no. 4, pp 2038–2049, 1998.
- [Beck 1989] K Beck. *Structural model of vinculin: correlation of amino acid sequence with electron-microscopical shape*. FEBS Lett, vol. 249, no. 1, pp 1–4, 1989.
- [Beningo *et al.* 2001] KA Beningo, M Dembo, I Kaverina, JV Small and YL Wang. *Nascent focal adhesions are responsible for the generation of strong propulsive forces in migrating fibroblasts*. J Cell Biol, vol. 153, no. 4, pp 881–888, 2001.
- [Bershadsky *et al.* 2003] AD Bershadsky, NQ Balaban and B Geiger. *Adhesion-dependent cell mechanosensitivity*. Annu Rev Cell Dev Biol, vol. 19, pp 677–695, 2003.
- [Bershadsky *et al.* 2006] AD Bershadsky, C Ballestrem, L Carramusa, Y Zilberman, B Gilquin, S Khochbin, AY Alexandrova, AB Verkhovsky, T Shemesh and MM Kozlov. *Assembly and mechanosensory function of focal adhesions: experiments and models*. Eur J Cell Biol, vol. 85, no. 3-4, pp 165–173, 2006.
- [Binnig *et al.* 1986] Binnig, Quate and Gerber. *Atomic force microscope*. Phys Rev Lett, vol. 56, no. 9, pp 930–933, 1986.
- [Bleil *et al.* 2007] S Bleil, P Reimann and C Bechinger. *Directing Brownian motion by oscillating barriers*. Physical Review E, vol. 75, p 031117, 2007.
- [Boccafoschi *et al.* 2010] F Boccafoschi, M Bosetti, PM Sandra, M Leigheb and M Cannas. *Effects of mechanical stress on cell adhesion: a possible mechanism for morphological changes*. Cell Adh Migr, vol. 4, no. 1, pp 19–25, 2010.
- [Bordeleau *et al.* 2011] F Bordeleau, J Bessard, N Marceau and Y Sheng. *Measuring integrated cellular mechanical stress response at focal adhesions by optical tweezers*. J Biomed Opt, vol. 16, no. 9, p 095005, 2011.
- [Bormuth *et al.* 2008] V Bormuth, A Jannasch, M Ander, CM van Kats, A van Blaaderen, J Howard and E Schäffer. *Optical trapping of coated microspheres*. Opt Express, vol. 16, no. 18, pp 13831–13844, 2008.
- [Bormuth *et al.* 2009] V Bormuth, V Varga, J Howard and E Schäffer. *Protein friction limits diffusive and directed movements of kinesin motors on microtubules*. Science, vol. 325, no. 5942, pp 870–873, 2009.
- [Brenner *et al.* 2011] MD Brenner, R Zhou and T Ha. *Forcing a connection: impacts of single-molecule force spectroscopy on in vivo tension sensing*. Biopolymers, vol. 95, no. 5, pp 332–344, 2011.

- [Brown *et al.* 2006] CM Brown, B Hebert, DL Kolin, J Zareno, L Whitmore, AR Horwitz and PW Wiseman. *Probing the integrin-actin linkage using high-resolution protein velocity mapping*. J Cell Sci, vol. 119, no. 24, pp 5204–5214, 2006.
- [Brownell *et al.* 2010] WE Brownell, F Qian and B Anvari. *Cell membrane tethers generate mechanical force in response to electrical stimulation*. Biophys J, vol. 99, no. 3, pp 845–852, 2010.
- [Burnette *et al.* 2011] DT Burnette, S Manley, P Sengupta, R Sougrat, MW Davidson, B Kachar and J Lippincott-Schwartz. *A role for actin arcs in the leading-edge advance of migrating cells*. Nat Cell Biol, vol. 13, no. 4, pp 371–381, 2011.
- [Burrige & Chrzanowska-Wodnicka 1996] K Burrige and M Chrzanowska-Wodnicka. *Focal adhesions, contractility, and signaling*. Annu Rev Cell Dev Biol, vol. 12, pp 463–518, 1996.
- [Burton & Taylor 1997] K Burton and DL Taylor. *Traction forces of cytokinesis measured with optically modified elastic substrata*. Nature, vol. 385, no. 6615, pp 450–454, 1997.
- [Burton *et al.* 1999] K Burton, JH Park and DL Taylor. *Keratocytes generate traction forces in two phases*. Mol Biol Cell, vol. 10, no. 11, pp 3745–3769, 1999.
- [Capitano *et al.* 2007] M Capitano, R Cicchi and FS Pavone. *Continuous and time-shared multiple optical tweezers for the study of single motor proteins*. Optics and Lasers in Engineering, vol. 45, pp 450–457, 2007.
- [Carisey & Ballestrem 2011] A Carisey and C Ballestrem. *Vinculin, an adapter protein in control of cell adhesion signalling*. Eur J Cell Biol, vol. 90, no. 2-3, pp 157–163, 2011.
- [Caspi *et al.* 2001a] A Caspi, O Yeger, I Grosheva, AD Bershadsky and M Elbaum. *A new dimension in retrograde flow: Centripetal movement of engulfed particles*. Biophys. J., vol. 81, pp 1990–2000, 2001.
- [Caspi *et al.* 2001b] A Caspi, O Yeger, I Grosheva, AD Bershadsky and M Elbaum. *A new dimension in retrograde flow: centripetal movement of engulfed particles*. Biophys J, vol. 81, no. 4, pp 1990–2000, 2001.
- [Chan & Odde 2008] CE Chan and DJ Odde. *Traction dynamics of filopodia on compliant substrates*. Science, vol. 322, no. 5908, pp 1687–1691, 2008.
- [Cheezum *et al.* 2001] MK Cheezum, WF Walker and WH Guilford. *Quantitative comparison of algorithms for tracking single fluorescent particles*. Biophys J, vol. 81, no. 4, pp 2378–2388, 2001.
- [Chen & Singer 1982] WT Chen and SJ Singer. *Immunoelectron microscopic studies of the sites of cell-substratum and cell-cell contacts in cultured fibroblasts*. J Cell Biol, vol. 95, no. 1, pp 205–222, 1982.
- [Chen *et al.* 1997] CS Chen, M Mrksich, S Huang, GM Whitesides and DE Ingber. *Geometric control of cell life and death*. Science, vol. 276, no. 5317, pp 1425–1428, 1997.
- [Chen *et al.* 2005] H Chen, DM Cohen, DM Choudhury, N Kioka and SW Craig. *Spatial distribution and functional significance of activated vinculin in living cells*. J Cell Biol, vol. 169, no. 3, pp 459–470, 2005.
- [Chen *et al.* 2006] H Chen, DM Choudhury and SW Craig. *Coincidence of actin filaments and talin is required to activate vinculin*. J Biol Chem, vol. 281, no. 52, pp 40389–40398, 2006.
- [Choi *et al.* 2008] CK Choi, M Vicente-Manzanares, J Zareno, LA Whitmore, A Mogilner and AR Horwitz. *Actin and alpha-actinin orchestrate the assembly and maturation of nascent adhesions in a myosin II motor-independent manner*. Nat Cell Biol, vol. 10, no. 9, pp 1039–1050, 2008.
- [Choquet *et al.* 1997] D Choquet, DP Felsenfeld and MP Sheetz. *Extracellular matrix rigidity causes strengthening of integrin-cytoskeleton linkages*. Cell, vol. 88, no. 1, pp 39–48, 1997.
- [Clemen 2005] A Clemen. *Charakterisierung des molekularen Motors Myosin-V mittels Laser-Pinzette und Fluoreszenzmikroskopie*. PhD thesis, TU München, 2005.

- [Cohen *et al.* 2004] M Cohen, D Joester, B Geiger and L Addadi. *Spatial and temporal sequence of events in cell adhesion: from molecular recognition to focal adhesion assembly*. ChemBioChem, vol. 5, no. 10, pp 1393–1399, 2004.
- [Cohen *et al.* 2005] DM Cohen, H Chen, RP Johnson, B Choudhury and SW Craig. *Two distinct head-tail interfaces cooperate to suppress activation of vinculin by talin*. J Biol Chem, vol. 280, no. 17, pp 17109–17117, 2005.
- [Cohen *et al.* 2006] DM Cohen, B Kutscher, H Chen, DB Murphy and SW Craig. *A conformational switch in vinculin drives formation and dynamics of a talin-vinculin complex at focal adhesions*. J Biol Chem, vol. 281, no. 23, pp 16006–16015, 2006.
- [Coll *et al.* 1995] JL Coll, A Ben-Ze'ev, RM Ezzell, JLR Fernández, H Baribault, RG Oshima and ED Adamson. *Targeted disruption of vinculin genes in F9 and embryonic stem cells changes cell morphology, adhesion, and locomotion*. Proc Natl Acad Sci U S A, vol. 92, no. 20, pp 9161–9165, 1995.
- [Coppin *et al.* 1996] CM Coppin, JT Finer, JA Spudich and RD Vale. *Detection of sub-8-nm movements of kinesin by high-resolution optical-trap microscopy*. Proc Natl Acad Sci U S A, vol. 93, no. 5, pp 1913–1917, 1996.
- [Cortasio *et al.* 2011] CL Cortasio, LR Boateng, TM Piazza, DA Bennin and A Huttenlocher. *Calpain-mediated proteolysis of paxillin negatively regulates focal adhesion dynamics and cell migration*. J Biol Chem, vol. 286, no. 12, pp 9998–10006, 2011.
- [Coussen *et al.* 2002] F Coussen, D Choquet, MP Sheetz and HP Erickson. *Trimers of the fibronectin cell adhesion domain localize to actin filament bundles and undergo rearward translocation*. J Cell Sci, vol. 115, no. 12, pp 2581–2590, 2002.
- [Cramer *et al.* 1994] LP Cramer, TJ Mitchison and JA Theriot. *Actin-dependent motile forces and cell motility*. Curr Opin Cell Biol, vol. 6, no. 1, pp 82–86, 1994.
- [Cramer 1997] LP Cramer. *Molecular mechanism of actin-dependent retrograde flow in lamellipodia of motile cells*. Front Biosci, vol. 2, pp d260–d270, 1997.
- [Cukierman *et al.* 2001] E Cukierman, R Pankov, DR Stevens and KM Yamada. *Taking cell-matrix adhesions to the third dimension*. Science, vol. 294, no. 5547, pp 1708–1712, 2001.
- [Cukierman *et al.* 2002] E Cukierman, R Pankov and KM Yamada. *Cell interactions with three-dimensional matrices*. Curr Opin Cell Biol, vol. 14, no. 5, pp 633–639, 2002.
- [Dai & Sheetz 1995] J Dai and MP Sheetz. *Mechanical properties of neuronal growth cone membranes studied by tether formation with laser optical tweezers*. Biophys J, vol. 68, no. 3, pp 988–996, 1995.
- [Dai & Sheetz 1999] J Dai and MP Sheetz. *Membrane tether formation from blebbing cells*. Biophys J, vol. 77, no. 6, pp 3363–3370, 1999.
- [Danuser & Oldenbourg 2000] G Danuser and R Oldenbourg. *Probing f-actin flow by tracking shape fluctuations of radial bundles in lamellipodia of motile cells*. Biophys J, vol. 79, no. 1, pp 191–201, 2000.
- [del Rio *et al.* 2009] A del Rio, R Perez-Jimenez, R Liu, P Roca-Cusachs, J Fernandez and M Sheetz. *Stretching single talin rod molecules activates vinculin binding*. Science, vol. 323, p 638, 2009.
- [DeMali *et al.* 2002] KA DeMali, CA Barlow and K Burridge. *Recruitment of the Arp2/3 complex to vinculin: coupling membrane protrusion to matrix adhesion*. J Cell Biol, vol. 159, no. 5, pp 881–891, 2002.
- [DeMali *et al.* 2003] KA DeMali, K Wennerberg and K Burridge. *Integrin signaling to the actin cytoskeleton*. Curr Opin Cell Biol, vol. 15, no. 5, pp 572–582, 2003.
- [DesMarais *et al.* 2002] V DesMarais, I Ichetovkin, J Condeelis and SE Hitchcock-DeGregori. *Spatial regulation of actin dynamics: a tropomyosin-free, actin-rich compartment at the leading edge*. J Cell Sci, vol. 115, no. 23, pp 4649–4660, 2002.

- [Dessinges *et al.* 2002] MN Dessinges, B Maier, Y Zhang, M Peliti, D Bensimon and V Croquette. *Stretching Single Stranded DNA, a Model Polyelectrolyte*. Phys Rev Lett, vol. 89(24), p 248102, 2002.
- [Diez *et al.* 2011] G Diez, V Auernheimer, B Fabry and WH Goldmann. *Head/tail interaction of vinculin influences cell mechanical behavior*. Biochem Biophys Res Commun, vol. 406, no. 1, pp 85–88, 2011.
- [Discher *et al.* 2005] DE Discher, P Janmey and YL Wang. *Tissue cells feel and respond to the stiffness of their substrate*. Science, vol. 310, no. 5751, pp 1139–1143, 2005.
- [Dufresne & Grier 1998] ER Dufresne and DG Grier. *Optical tweezer arrays and optical substrates created with diffractive optics*. Rev Sci Instrum, vol. 69(5), pp 1974–1977, 1998.
- [Eimer *et al.* 1993] W Eimer, M Niermann, MA Eppe and BM Jockusch. *Molecular shape of vinculin in aqueous solution*. J Mol Biol, vol. 229, no. 1, pp 146–152, 1993.
- [Emiliani *et al.* 2004] V Emiliani, D Sanvitto, M Zahid, F Gerbal and M Coppey-Moisan. *Multi force optical tweezers to generate gradients of forces*. Opt Express, vol. 12, no. 17, pp 3906–3910, 2004.
- [Engel *et al.* 1981] J Engel, E Odermatt, A Engel, JA Madri, H Furthmayr, H Rohde and R Timpl. *Shapes, domain organizations and flexibility of laminin and fibronectin, two multifunctional proteins of the extracellular matrix*. J Mol Biol, vol. 150, no. 1, pp 97–120, 1981.
- [Engler *et al.* 2004] A Engler, L Bacakova, C Newman, A Hategan, M Griffin and D Discher. *Substrate compliance versus ligand density in cell on gel responses*. Biophys J, vol. 86, no. 1, pp 617–628, 2004.
- [Engler *et al.* 2006] AJ Engler, S Sen, HL Sweeney and DE Discher. *Matrix elasticity directs stem cell lineage specification*. Cell, vol. 126, no. 4, pp 677–689, 2006.
- [Ermilov *et al.* 2007] SA Ermilov, DR Murdock, F Quian, WE Brownell and B Anvari. *Studies of plasma membrane mechanics and plasma membrane-cytoskeleton interactions using optical tweezers and fluorescence imaging*. J. Biomech., vol. 40, pp 476–480, 2007.
- [Farré *et al.* 2010] A Farré, A van der Horst, GA Blab, BPB Downing and NR Forde. *Stretching single DNA molecules to demonstrate high-force capabilities of holographic optical tweezers*. J Biophotonics, vol. 3, no. 4, pp 224–233, 2010.
- [Fazal & Block 2011] FM Fazal and SM Block. *Optical tweezers study life under tension*. Nat Photonics, vol. 5, pp 318–321, 2011.
- [Felgner *et al.* 1995] H Felgner, O Müller and M Schliwa. *Calibration of light forces in optical tweezers*. Applied Optics, vol. 34(6), pp 977–982, 1995.
- [Felsenfeld *et al.* 1996] DP Felsenfeld, D Choquet and MP Sheetz. *Ligand binding regulates the directed movement of beta1 integrins on fibroblasts*. Nature, vol. 383, no. 6599, pp 438–440, 1996.
- [Felsenfeld *et al.* 1999] DP Felsenfeld, PL Schwartzberg, A Venegas, R Tse and MP Sheetz. *Selective regulation of integrin–cytoskeleton interactions by the tyrosine kinase Src*. Nat Cell Biol, vol. 1, no. 4, pp 200–206, 1999.
- [Fernández *et al.* 1993] JLR Fernández, B Geiger, D Salomon and A Ben-Ze'ev. *Suppression of vinculin expression by antisense transfection confers changes in cell morphology, motility, and anchorage-dependent growth of 3T3 cells*. J Cell Biol, vol. 122, no. 6, pp 1285–1294, 1993.
- [Fidler & Kripke 1977] IJ Fidler and ML Kripke. *Metastasis results from preexisting variant cells within a malignant tumor*. Science, vol. 197, no. 4306, pp 893–895, 1977.
- [Fidler 1973] IJ Fidler. *Selection of successive tumour lines for metastasis*. Nat New Biol, vol. 242, no. 118, pp 148–149, 1973.
- [Finer *et al.* 1994] JT Finer, RM Simmons and JA Spudich. *Single myosin molecule mechanics: piconewton forces and nanometre steps*. Nature, vol. 368, pp 113–119, 1994.

- [Fällman *et al.* 2004] E Fällman, S Schedin, J Jass, M Andersson, BE Uhlin and O Axner. *Optical tweezers based force measurement system for quantitating binding interactions: system design and application for the study of bacterial adhesion*. Biosensors and Bioelectronics, vol. 19, pp 1429–1437, 2004.
- [Forscher & Smith 1988] P Forscher and SJ Smith. *Actions of cytochalasins on the organization of actin filaments and microtubules in a neuronal growth cone*. J Cell Biol, vol. 107, no. 4, pp 1505–1516, 1988.
- [Forscher *et al.* 1992] P Forscher, CH Lin and C Thompson. *Novel form of growth cone motility involving site-directed actin filament assembly*. Nature, vol. 357, no. 6378, pp 515–518, 1992.
- [Fournier *et al.* 2010] MF Fournier, R Sausser, D Ambrosi, JJ Meister and AB Verkhovskiy. *Force transmission in migrating cells*. J Cell Biol, vol. 188, no. 2, pp 287–297, 2010.
- [Fraley *et al.* 2010] SI Fraley, Y Feng, R Krishnamurthy, DH Kim, A Celedon, GD Longmore and D Wirtz. *A distinctive role for focal adhesion proteins in three-dimensional cell motility*. Nat Cell Biol, vol. 12, no. 6, pp 598–604, 2010.
- [Franz & Puech 2008] C Franz and PH Puech. *Atomic Force Microscopy: A Versatile Tool for Studying Cell Morphology, Adhesion and Mechanics*. Cellular and Molecular Bioengineering, vol. 1, pp 289–300, 2008.
- [Franz *et al.* 2007] CM Franz, A Taubenberger, PH Puech and DJ Muller. *Studying integrin-mediated cell adhesion at the single-molecule level using AFM force spectroscopy*. Sci STKE, vol. 2007, no. 406, p p15, 2007.
- [Friedrichs *et al.* 2010] J Friedrichs, J Helenius and DJ Muller. *Quantifying cellular adhesion to extracellular matrix components by single-cell force spectroscopy*. Nat Protoc, vol. 5, no. 7, pp 1353–1361, 2010.
- [Frith *et al.* 2012] JE Frith, RJ Mills and JJ Cooper-White. *Lateral spacing of adhesion peptides influences human mesenchymal stem cell behaviour*. J Cell Sci, vol. 125, no. 2, pp 317–327, 2012.
- [Fuente *et al.* 2007] LDL Fuente, E Montanes, Y Meng, Y Li, TJ Burr, HC Hoch and M Wu. *Assessing adhesion forces of type I and type IV pili of xylella fastidiosa bacteria by use of a microfluidic flow chamber*. Applied and Environmental Microbiology, vol. 73(8), pp 2690–2696, 2007.
- [Fujiwara & Pollard 1976] K Fujiwara and TD Pollard. *Fluorescent antibody localization of myosin in the cytoplasm, cleavage furrow, and mitotic spindle of human cells*. J Cell Biol, vol. 71, no. 3, pp 848–875, 1976.
- [Fukui *et al.* 1999] Y Fukui, T Kitanishi-Yumura and S Yumura. *Myosin II-independent F-actin flow contributes to cell locomotion in dictyostelium*. J Cell Sci, vol. 112, no. 6, pp 877–886, 1999.
- [Galbraith & Sheetz 1997] CG Galbraith and MP Sheetz. *A micromachined device provides a new bend on fibroblast traction forces*. Proc Natl Acad Sci U S A, vol. 94, no. 17, pp 9114–9118, 1997.
- [Galbraith *et al.* 2002] CG Galbraith, KM Yamada and MP Sheetz. *The relationship between force and focal complex development*. J Cell Biol, vol. 159, no. 4, pp 695–705, 2002.
- [Gao *et al.* 2002] M Gao, D Craig, V Vogel and K Schulten. *Identifying unfolding intermediates of FN-III(10) by steered molecular dynamics*. J Mol Biol, vol. 323, no. 5, pp 939–950, 2002.
- [Gardel *et al.* 2008] ML Gardel, B Sabass, L Ji, G Danuser, US Schwarz and CM Waterman. *Traction stress in focal adhesions correlates biphasically with actin retrograde flow speed*. J Cell Biol, vol. 183, no. 6, pp 999–1005, 2008.
- [Gardel *et al.* 2010] ML Gardel, IC Schneider, Y Aratyn-Schaus and CM Waterman. *Mechanical integration of actin and adhesion dynamics in cell migration*. Annu Rev Cell Dev Biol, vol. 26, pp 315–333, 2010.
- [Gauthier *et al.* 2011] NC Gauthier, MA Fardin, P Roca-Cusachs and MP Sheetz. *Temporary increase in plasma membrane tension coordinates the activation of exocytosis and contraction during cell spreading*. Proc Natl Acad Sci U S A, vol. 108, no. 35, pp 14467–14472, 2011.

- [Geiger & Bershadsky 2001] B Geiger and A Bershadsky. *Assembly and mechanosensory function of focal contacts*. *Curr Opin Cell Biol*, vol. 13, no. 5, pp 584–592, 2001.
- [Geiger & Bershadsky 2002] B Geiger and A Bershadsky. *Exploring the neighborhood: adhesion-coupled cell mechanosensors*. *Cell*, vol. 110, no. 2, pp 139–142, 2002.
- [Geiger *et al.* 2001] B Geiger, A Bershadsky, R Pankov and KM Yamada. *Transmembrane crosstalk between the extracellular matrix–cytoskeleton crosstalk*. *Nat Rev Mol Cell Biol*, vol. 2, no. 11, pp 793–805, 2001.
- [Geiger *et al.* 2009] B Geiger, JP Spatz and AD Bershadsky. *Environmental sensing through focal adhesions*. *Nat Rev Mol Cell Biol*, vol. 10, no. 1, pp 21–33, 2009.
- [Geiger 1979] B Geiger. *A 130K protein from chicken gizzard: its localization at the termini of microfilament bundles in cultured chicken cells*. *Cell*, vol. 18, no. 1, pp 193–205, 1979.
- [Ghislain *et al.* 1994] LP Ghislain, NA Switz and WW Webb. *Measurement of small forces using an optical trap*. *Rev Sci Instrum*, vol. 65, no. 9, pp 2762–2768, 1994.
- [Giannone *et al.* 2003] G Giannone, G Jiang, DH Sutton, DR Critchley and MP Sheetz. *Talin1 is critical for force-dependent reinforcement of initial integrin-cytoskeleton bonds but not tyrosine kinase activation*. *J Cell Biol*, vol. 163, no. 2, pp 409–419, 2003.
- [Giannone *et al.* 2004] G Giannone, BJ Dubin-Thaler, HG Döbereiner, N Kieffer, AR Bresnick and MP Sheetz. *Periodic lamellipodial contractions correlate with rearward actin waves*. *Cell*, vol. 116, no. 3, pp 431–443, 2004.
- [Giannone *et al.* 2007] G Giannone, BJ Dubin-Thaler, O Rossier, Y Cai, O Chaga, G Jiang, W Beaver, HG Döbereiner, Y Freund, G Borisy and MP Sheetz. *Lamellipodial actin mechanically links myosin activity with adhesion-site formation*. *Cell*, vol. 128, no. 3, pp 561–575, 2007.
- [Gillespie & Walker 2001] PG Gillespie and RG Walker. *Molecular basis of mechanosensory transduction*. *Nature*, vol. 413, no. 6852, pp 194–202, 2001.
- [Gilmore & Burridge 1996] AP Gilmore and K Burridge. *Regulation of vinculin binding to talin and actin by phosphatidyl-inositol-4-5-bisphosphate*. *Nature*, vol. 381, no. 6582, pp 531–535, 1996.
- [Goldmann *et al.* 1992] WH Goldmann, V Niggli, S Kaufmann and G Isenberg. *Probing actin and liposome interaction of talin and talin-vinculin complexes: a kinetic, thermodynamic and lipid labeling study*. *Biochemistry*, vol. 31, no. 33, pp 7665–7671, 1992.
- [Goldmann *et al.* 1998a] WH Goldmann, R Galneder, M Ludwig, W Xu, ED Adamson, N Wang and RM Ezzell. *Differences in elasticity of vinculin-deficient F9 cells measured by magnetometry and atomic force microscopy*. *Exp Cell Res*, vol. 239, no. 2, pp 235–242, 1998.
- [Goldmann *et al.* 1998b] WH Goldmann, Z Guttenberg, JX Tang, K Kroy, G Isenberg and RM Ezzell. *Analysis of the F-actin binding fragments of vinculin using stopped-flow and dynamic light-scattering measurements*. *Eur J Biochem*, vol. 254, no. 2, pp 413–419, 1998.
- [Goldyn 2009] A Goldyn. *The spatiotemporal response of cells and their cytoskeleton to cyclic stretching*. PhD thesis, Ruperto-Carola University of Heidelberg, 2009.
- [Gosse & Croquette 2002] C Gosse and V Croquette. *Magnetic tweezers: micromanipulation and force measurement at the molecular level*. *Biophys J*, vol. 82, no. 6, pp 3314–3329, 2002.
- [Gouesbet 1994] G Gouesbet. *Generalized lorenz-mie theory and applications*. *Particle & Particle Systems Characterization*, vol. 11, no. 1, pp 22–34, 1994.
- [Graf *et al.* 2003] C Graf, DLJ Vossen, A Imhof and A van Blaaderen. *A General Method To Coat Colloidal Particles with Silica*. *Langmuir*, vol. 19, no. 17, pp 6693–6700, 2003.
- [Grashoff *et al.* 2010] C Grashoff, BD Hoffman, MD Brenner, R Zhou, M Parsons, MT Yang, MA McLean, SG Sligar, CS Chen, T Ha and MA Schwartz. *Measuring mechanical tension across vinculin reveals regulation of focal adhesion dynamics*. *Nature*, vol. 466, no. 7303, pp 263–266, 2010.

- [Grier 2003] DG Grier. *A revolution in optical manipulation*. Nature, vol. 424, pp 810–816, 2003.
- [Grinnell & Geiger 1986] F Grinnell and B Geiger. *Interaction of fibronectin-coated beads with attached and spread fibroblasts. Binding, phagocytosis, and cytoskeletal reorganization*. Exp Cell Res, vol. 162, no. 2, pp 449–461, 1986.
- [Gross *et al.* 2000] SP Gross, MA Welte, SM Block and EF Wieschaus. *Dynein-mediated cargo transport in vivo: A switch controls travel distance*. J Cell Biol, vol. 148, pp 945–955, 2000.
- [Gross 2003] SP Gross. *Application of optical traps in vivo*. Methods in Enzymology, vol. 361, pp 162–174, 2003.
- [Götter *et al.* 1995] R Götter, WH Goldmann and G Isenberg. *Internal actin filament dynamics in the presence of vinculin: a dynamic light scattering study*. FEBS Lett, vol. 359, no. 2-3, pp 220–222, 1995.
- [Guo & Wang 2007] WH Guo and YL Wang. *Retrograde fluxes of focal adhesion proteins in response to cell migration and mechanical signals*. Mol Biol Cell, vol. 18, no. 11, pp 4519–4527, 2007.
- [Gupton & Waterman-Storer 2006] SL Gupton and CM Waterman-Storer. *Spatiotemporal feedback between actomyosin and focal-adhesion systems optimizes rapid cell migration*. Cell, vol. 125, no. 7, pp 1361–1374, 2006.
- [Gupton *et al.* 2007] SL Gupton, K Eisenmann, AS Alberts and CM Waterman-Storer. *mDia2 regulates actin and focal adhesion dynamics and organization in the lamella for efficient epithelial cell migration*. J Cell Sci, vol. 120, no. 19, pp 3475–3487, 2007.
- [Hakkinen *et al.* 2011] KM Hakkinen, JS Harunaga, AD Doyle and KM Yamada. *Direct comparisons of the morphology, migration, cell adhesions, and actin cytoskeleton of fibroblasts in four different three-dimensional extracellular matrices*. Tissue Eng Part A, vol. 17, no. 5-6, pp 713–724, 2011.
- [Hamill & Martinac 2001] OP Hamill and B Martinac. *Molecular basis of mechanotransduction in living cells*. Physiol Rev, vol. 81, no. 2, pp 685–740, 2001.
- [Harada & Asakura 1996] Y Harada and T Asakura. *Radiation forces on a dielectric sphere in the Rayleigh scattering regime*. Optics Communications, vol. 124, pp 529–541, 1996.
- [Harris 1994] AK Harris. *Locomotion of tissue culture cells considered in relation to ameboid locomotion*. Int Rev Cytol, vol. 150, pp 35–68, 1994.
- [Helenius *et al.* 2008] J Helenius, CP Heisenberg, HE Gaub and DJ Muller. *Single-cell force spectroscopy*. J Cell Sci, vol. 121, no. 11, pp 1785–1791, 2008.
- [Henson *et al.* 1999] JH Henson, TM Svitkina, AR Burns, HE Hughes, KJ MacPartland, R Nazarian and GG Borisy. *Two components of actin-based retrograde flow in sea urchin coelomocytes*. Mol Biol Cell, vol. 10, no. 12, pp 4075–4090, 1999.
- [Hochmuth *et al.* 1996] FM Hochmuth, JY Shao, J Dai and MP Sheetz. *Deformation and flow of membrane into tethers extracted from neuronal growth cones*. Biophys J, vol. 70, no. 1, pp 358–369, 1996.
- [Hoffman *et al.* 2011] BD Hoffman, C Grashoff and MA Schwartz. *Dynamic molecular processes mediate cellular mechanotransduction*. Nature, vol. 475, no. 7356, pp 316–323, 2011.
- [Hopkins *et al.* 2004] RJ Hopkins, L Mitchem, AD Ward and JP Reid. *Control and characterisation of a single aerosol droplet in a single-beam gradient-force optical trap*. Phys Chem Phys, vol. 6, p 4924, 2004.
- [Hormeno & Arias-Gonzalez 2006] S Hormeno and JR Arias-Gonzalez. *Exploring mechanochemical processes in the cell with optical tweezers*. Biol Cell, vol. 98, pp 679–695, 2006.
- [Horwitz *et al.* 1986] A Horwitz, K Duggan, C Buck, MC Beckerle and K Burridge. *Interaction of plasma membrane fibronectin receptor with talin – a transmembrane linkage*. Nature, vol. 320, no. 6062, pp 531–533, 1986.
- [Hotulainen & Lappalainen 2006] P Hotulainen and P Lappalainen. *Stress fibers are generated by two distinct actin assembly mechanisms in motile cells*. J Cell Biol, vol. 173, no. 3, pp 383–394, 2006.

- [Hu *et al.* 2007] K Hu, L Ji, KT Applegate, G Danuser and CM Waterman-Storer. *Differential transmission of actin motion within focal adhesions*. Science, vol. 315, no. 5808, pp 111–115, 2007.
- [Huang *et al.* 2004] H Huang, RD Kamm and RT Lee. *Cell mechanics and mechanotransduction: pathways, probes, and physiology*. Am J Physiol Cell Physiol, vol. 287, no. 1, pp C1–C11, 2004.
- [Humphries *et al.* 2006] JD Humphries, A Byron and MJ Humphries. *Integrin ligands at a glance*. J Cell Sci, vol. 119, no. 19, pp 3901–3903, 2006.
- [Humphries *et al.* 2007] JD Humphries, P Wang, C Streuli, B Geiger, MJ Humphries and C Ballestrem. *Vinculin controls focal adhesion formation by direct interactions with talin and actin*. J Cell Biol, vol. 179, no. 5, pp 1043–1057, 2007.
- [Icard-Arcizet *et al.* 2008] D Icard-Arcizet, O Cardoso, A Richert and S Hénon. *Cell stiffening in response to external stress is correlated to actin recruitment*. J. Biophys., vol. 94, pp 2906–2913, 2008.
- [Ichetovkin *et al.* 2002] I Ichetovkin, W Grant and J Condeelis. *Cofilin produces newly polymerized actin filaments that are preferred for dendritic nucleation by the Arp2/3 complex*. Curr Biol, vol. 12, no. 1, pp 79–84, 2002.
- [Ingber 1997] DE Ingber. *Tensegrity: the architectural basis of cellular mechanotransduction*. Annu Rev Physiol, vol. 59, pp 575–599, 1997.
- [Ingber 2003] DE Ingber. *Tensegrity II. How structural networks influence cellular information processing networks*. J Cell Sci, vol. 116, no. 8, pp 1397–1408, 2003.
- [Ingber 2004] DE Ingber. *The mechanochemical basis of cell and tissue regulation*. Mech Chem Biosyst, vol. 1, no. 1, pp 53–68, 2004.
- [Irimura *et al.* 1981] T Irimura, R Gonzalez and GL Nicolson. *Effects of tunicamycin on B16 metastatic melanoma cell surface glycoproteins and blood-borne arrest and survival properties*. Cancer Res, vol. 41, pp 3411–3418, 1981.
- [Iwasa & Mullins 2007] JH Iwasa and RD Mullins. *Spatial and temporal relationships between actin-filament nucleation, capping, and disassembly*. Curr Biol, vol. 17, no. 5, pp 395–406, 2007.
- [Izard *et al.* 2004] T Izard, G Evans, RA Borgon, CL Rush, G Bricogne and PRJ Bois. *Vinculin activation by talin through helical bundle conversion*. Nature, vol. 427, no. 6970, pp 171–175, 2004.
- [Jackson 1999] JD Jackson. Classical electrodynamics. Wiley, New York, 1999.
- [Janmey & McCulloch 2007] PA Janmey and CA McCulloch. *Cell mechanics: integrating cell responses to mechanical stimuli*. Annu Rev Biomed Eng, vol. 9, pp 1–34, 2007.
- [Jeney *et al.* 2004] S Jeney, EHK Stelzer, H Grubmüller and EL Florin. *Mechanical properties of single motor molecules studied by three-dimensional thermal force probing in optical tweezers*. ChemPhysChem, vol. 5, no. 8, pp 1150–1158, 2004.
- [Jeney *et al.* 2010] S Jeney, F Mor, R Koszali, L Forró and VT Moy. *Monitoring ligand-receptor interactions by photonic force microscopy*. Nanotechnology, vol. 21, no. 25, p 255102, 2010.
- [Jiang *et al.* 2003] G Jiang, G Giannone, DR Critchley, E Fukumoto and MP Sheetz. *Two-piconewton slip bond between fibronectin and the cytoskeleton depends on talin*. Nature, vol. 424, no. 6946, pp 334–337, 2003.
- [Johnson & Craig 1994] RP Johnson and SW Craig. *An intramolecular association between the head and tail domains of vinculin modulates talin binding*. J Biol Chem, vol. 269, no. 17, pp 12611–12619, 1994.
- [Johnson & Craig 1995] RP Johnson and SW Craig. *F-actin binding site masked by the intramolecular association of vinculin head and tail domains*. Nature, vol. 373, no. 6511, pp 261–264, 1995.
- [Jones *et al.* 1989] P Jones, P Jackson, GJ Price, B Patel, V Ohanion, AL Lear and DR Critchley. *Identification of a talin binding site in the cytoskeletal protein vinculin*. J Cell Biol, vol. 109, no. 6, pp 2917–2927, 1989.

- [Jurado *et al.* 2005] C Jurado, JR Haserick and J Lee. *Slipping or gripping? Fluorescent speckle microscopy in fish keratocytes reveals two different mechanisms for generating a retrograde flow of actin.* Mol Biol Cell, vol. 16, no. 2, pp 507–518, 2005.
- [Kanchanawong *et al.* 2010] P Kanchanawong, G Shtengel, AM Pasapera, EB Ramko, MW Davidson, HF Hess and CM Waterman. *Nanoscale architecture of integrin-based cell adhesions.* Nature, vol. 468, no. 7323, pp 580–584, 2010.
- [Kegler *et al.* 2007] K Kegler, M Salomo and F Kremer. *Forces of interaction between DNA-grafted colloids: An optical tweezer measurement.* Phys. Rev. Lett., vol. 98, p 058304, 2007.
- [King *et al.* 2004] MD King, KC Thompson and AD Ward. *Laser tweezers Raman study of optically trapped aerosol droplets of seawater and oleic acid reacting with ozone: implications for cloud-droplet properties.* J Am Chem Soc, vol. 126, no. 51, pp 16710–16711, 2004.
- [Klein *et al.* 2010] F Klein, T Striebel, J Fischer, Z Jiang, CM Franz, G von Freymann, M Wegener and M Bastmeyer. *Elastic fully three-dimensional microstructure scaffolds for cell force measurements.* Adv Mater, vol. 22, no. 8, pp 868–871, 2010.
- [Klein 2009] F Klein. *Der Einfluss von 2D- und 3D-Substratgeometrien und Flexibilität auf Zellform und Zellverhalten.* PhD thesis, Universität Karlsruhe (TH), 2009.
- [Kobayashi & Sokabe 2010] T Kobayashi and M Sokabe. *Sensing substrate rigidity by mechanosensitive ion channels with stress fibers and focal adhesions.* Curr Opin Cell Biol, vol. 22, no. 5, pp 669–676, 2010.
- [Kroemker *et al.* 1994] M Kroemker, AH Rüdiger, BM Jockusch and M Rüdiger. *Intramolecular interactions in vinculin control alpha-actinin binding to the vinculin head.* FEBS Lett, vol. 355, no. 3, pp 259–262, 1994.
- [Kruse *et al.* 2006] K Kruse, JF Joanny, F Jülicher and J Prost. *Contractility and retrograde flow in lamellipodium motion.* Phys Biol, vol. 3, no. 2, pp 130–137, 2006.
- [Kubow & Horwitz 2011] KE Kubow and AR Horwitz. *Reducing background fluorescence reveals adhesions in 3D matrices.* Nat Cell Biol, vol. 13, no. 1, pp 3–5, 2011.
- [Kuo & Sheetz 1992] SC Kuo and MP Sheetz. *Optical tweezers in cell biology.* Trends in Cell Biology, vol. 2, pp 116–118, 1992.
- [Kuo & Sheetz 1993] SC Kuo and MP Sheetz. *Force of single kinesin molecules measured with optical tweezers.* Science, vol. 260, no. 5105, pp 232–234, 1993.
- [Kuo 2001] SC Kuo. *Using optics to measure biological forces and mechanics.* Traffic, vol. 2, no. 11, pp 757–763, 2001.
- [Lagunas *et al.* 2011] A Lagunas, J Comelles, E Martínez, E Prats-Alfonso, GA Acosta, F Albericio and J Samitier. *Cell adhesion and focal contact formation on linear RGD molecular gradients: study of non-linear concentration dependence effects.* Nanomedicine, 2011.
- [Lai *et al.* 2008] FPL Lai, M Szczodrak, J Block, J Faix, D Breitsprecher, HG Mannherz, TEB Stradal, GA Dunn, JV Small and K Rottner. *Arp2/3 complex interactions and actin network turnover in lamellipodia.* EMBO J, vol. 27, no. 7, pp 982–992, 2008.
- [Langevin 1908] P Langevin. *On the Theory of Brownian Motion.* C. R. Acad. Sci (Paris), vol. 146, 1908.
- [Larsen *et al.* 2006] M Larsen, VV Artym, JA Green and KM Yamada. *The matrix reorganized: extracellular matrix remodeling and integrin signaling.* Curr Opin Cell Biol, vol. 18, no. 5, pp 463–471, 2006.
- [Lauffenburger & Horwitz 1996] DA Lauffenburger and AF Horwitz. *Cell migration: a physically integrated molecular process.* Cell, vol. 84, pp 359–369, 1996.
- [Laukaitis *et al.* 2001] CM Laukaitis, DJ Webb, K Donais and AF Horwitz. *Differential dynamics of alpha 5 integrin, paxillin, and alpha-actinin during formation and disassembly of adhesions in migrating cells.* J Cell Biol, vol. 153, no. 7, pp 1427–1440, 2001.

- [Laurent *et al.* 2002] VM Laurent, S Hénon, E Planus, R Fodil, M Balland, D Isabey and F Gallet. *Assessment of mechanical properties of adherent living cells by bead micromanipulation: comparison of magnetic twisting cytometry vs optical tweezers.* J Biomech Eng, vol. 124, no. 4, pp 408–421, 2002.
- [Lawson *et al.* 2012] C Lawson, ST Lim, S Uryu, XL Chen, DA Calderwood and DD Schlaepfer. *FAK promotes recruitment of talin to nascent adhesions to control cell motility.* J Cell Biol, vol. 196, no. 2, pp 223–232, 2012.
- [Lazarides & Burridge 1975] E Lazarides and K Burridge. *Alpha-actinin: immunofluorescent localization of a muscle structural protein in nonmuscle cells.* Cell, vol. 6, no. 3, pp 289–298, 1975.
- [Leahy *et al.* 1996] DJ Leahy, I Aukhil and HP Erickson. *2.0 A crystal structure of a four-domain segment of human fibronectin encompassing the RGD loop and synergy region.* Cell, vol. 84, no. 1, pp 155–164, 1996.
- [Lehnert *et al.* 2004] D Lehnert, B Wehrle-Haller, C David, U Weiland, C Ballestrem, BA Imhof and M Bastmeyer. *Cell behaviour on micropatterned substrata: limits of extracellular matrix geometry for spreading and adhesion.* J Cell Sci, vol. 117, no. 1, pp 41–52, 2004.
- [Lele *et al.* 2008] TP Lele, CK Thodeti, J Pendse and DE Ingber. *Investigating complexity of protein-protein interactions in focal adhesions.* Biochem Biophys Res Commun, vol. 369, no. 3, pp 929–934, 2008.
- [Levayer & Lecuit 2012] R Levayer and T Lecuit. *Biomechanical regulation of contractility: spatial control and dynamics.* Trends Cell Biol, vol. 22, no. 2, pp 61–81, 2012.
- [Li *et al.* 2010] Y Li, P Bhimalapuram and AR Dinner. *Model for how retrograde actin flow regulates adhesion traction stresses.* J. Phys.: Cond. Mat., vol. 22, p 194113, 2010.
- [Liang *et al.* 1996] H Liang, KT Vu, P Krishnan, TC Trang, D Shin, S Kimel and MW Berns. *Wavelength dependence of cell cloning efficiency after optical trapping.* Biophys J, vol. 70, pp 1529–1533, 1996.
- [Liesener *et al.* 2000] J Liesener, M Reicherter, T Haist and HJ Tiziani. *Multi-functional optical tweezers using computer-generated holograms.* Optics Communications, vol. 185, pp 77–82, 2000.
- [Lin & Forscher 1995] CH Lin and P Forscher. *Growth cone advance is inversely proportional to retrograde F-actin flow.* Neuron, vol. 14, no. 4, pp 763–771, 1995.
- [Lin *et al.* 1996] CH Lin, EM Espreafico, MS Mooseker and P Forscher. *Myosin drives retrograde F-actin flow in neuronal growth cones.* Neuron, vol. 16, no. 4, pp 769–782, 1996.
- [Liu *et al.* 2010] Z Liu, JL Tan, DM Cohen, MT Yang, NJ Sniadecki, SA Ruiz, CM Nelson and CS Chen. *Mechanical tugging force regulates the size of cell-cell junctions.* Proc Natl Acad Sci U S A, vol. 107, no. 22, pp 9944–9949, 2010.
- [Luca *et al.* 2007] ACD Luca, G Volpe, AM Drets, MI Geli, G Pesce, G Rusciano, A Sasso and D Petrov. *Real-time actin-cytoskeleton depolymerization detection in a single optical tweezers.* Optics Express, vol. 15, no. 13, pp 7922–7932, 2007.
- [Machesky *et al.* 1999] LM Machesky, RD Mullins, HN Higgs, DA Kaiser, L Blanchoin, RC May, ME Hall and TD Pollard. *Scar, a WASp-related protein, activates nucleation of actin filaments by the Arp2/3 complex.* PNAS, vol. 96, no. 7, pp 3739–3744, 1999.
- [Mahamdeh *et al.* 2011] M Mahamdeh, CP Campos and E Schäffer. *Under-filling trapping objectives optimizes the use of the available laser power in optical tweezers.* Opt Express, vol. 19, no. 12, pp 11759–11768, 2011.
- [Maheu *et al.* 1988] B Maheu, G Gouesbet and G Grehan. *A concise presentation of the generalized Lorenz-Mie theory for arbitrary location of the scatterer in an arbitrary incident profile.* Journal of Optics, vol. 19, no. 2, p 59, 1988.
- [Malmström *et al.* 2010] J Malmström, B Christensen, HP Jakobsen, J Lovmand, R Foldbjerg, ES Sørensen and DS Sutherland. *Large area protein patterning reveals nanoscale control of focal adhesion development.* Nano Lett, vol. 10, no. 2, pp 686–694, 2010.

- [Manders *et al.* 1992] EM Manders, J Stap, GJ Brakenhoff, R van Driel and JA Aten. *Dynamics of three-dimensional replication patterns during the S-phase, analysed by double labelling of DNA and confocal microscopy.* J Cell Sci, vol. 103, no. 3, pp 857–862, 1992.
- [Margadant *et al.* 2011] F Margadant, LL Chew, X Hu, H Yu, N Bate, X Zhang and M Sheetz. *Mechanotransduction In Vivo by Repeated Talin Stretch-Relaxation Events Depends upon Vinculin.* PLoS Biol, vol. 9, no. 12, p e1001223, 2011.
- [Maruthamuthu *et al.* 2010] V Maruthamuthu, Y Aratyn-Schaus and ML Gardel. *Conserved F-actin dynamics and force transmission at cell adhesions.* Curr Opin Cell Biol, vol. 22, no. 5, pp 583–588, 2010.
- [McCauley & Williams 2007] MJ McCauley and MC Williams. *Mechanisms of DNA binding determined in optical tweezers experiments.* Biopolymers, vol. 85, pp 154–168, 2007.
- [McGrath *et al.* 1998] JL McGrath, Y Tardy, CF Dewey, JJ Meister and JH Hartwig. *Simultaneous measurements of actin filament turnover, filament fraction, and monomer diffusion in endothelial cells.* Biophys J, vol. 75, no. 4, pp 2070–2078, 1998.
- [McGrath *et al.* 2000] JL McGrath, EA Osborn, YS Tardy, CF Dewey and JH Hartwig. *Regulation of the actin cycle in vivo by actin filament severing.* Proc Natl Acad Sci U S A, vol. 97, no. 12, pp 6532–6537, 2000.
- [Medeiros *et al.* 2006] NA Medeiros, DT Burnette and P Forscher. *Myosin II functions in actin-bundle turnover in neuronal growth cones.* Nat Cell Biol, vol. 8, no. 3, pp 215–226, 2006.
- [Mejean *et al.* 2009] CO Mejean, AW Schaefer, EA Millman, P Forscher and ER Dufresne. *Multiplexed force measurements on live cells with holographic optical tweezers.* Opt Express, vol. 17, no. 8, pp 6209–6217, 2009.
- [Möhl *et al.* 2009] C Möhl, N Kirchgessner, C Schäfer, K Küpper, S Born, G Diez, WH Goldmann, R Merkel and B Hoffmann. *Becoming stable and strong: the interplay between vinculin exchange dynamics and adhesion strength during adhesion site maturation.* Cell Motil Cytoskeleton, vol. 66, no. 6, pp 350–364, 2009.
- [Möhl *et al.* 2012] C Möhl, N Kirchgessner, C Schäfer, B Hoffmann and R Merkel. *Quantitative mapping of averaged focal adhesion dynamics in migrating cells by shape normalization.* J Cell Sci, vol. 125, no. 1, pp 155–165, 2012.
- [Mierke & Kollmannsberger 2008] C Mierke and P Kollmannsberger. *Mechano-Coupling and Regulation of Contractility by the Vinculin Tail Domain.* Biophys J, vol. 94, pp 661–670, 2008.
- [Mierke 2009] CT Mierke. *The role of vinculin in the regulation of the mechanical properties of cells.* Cell Biochem Biophys, vol. 53, no. 3, pp 115–126, 2009.
- [Milam 1985] LM Milam. *Electron microscopy of rotary shadowed vinculin and vinculin complexes.* J Mol Biol, vol. 184, no. 3, pp 543–545, 1985.
- [Mitchison & Cramer 1996] TJ Mitchison and LP Cramer. *Actin-based cell motility and cell locomotion.* Cell, vol. 84, no. 3, pp 371–379, 1996.
- [Miyamoto *et al.* 1995a] S Miyamoto, SK Akiyama and KM Yamada. *Synergistic roles for receptor occupancy and aggregation in integrin transmembrane function.* Science, vol. 267, pp 883–885, 1995.
- [Miyamoto *et al.* 1995b] S Miyamoto, H Teramoto, OA Coso, JS Gutkind, PD Burbelo, SK Akiyama and KM Yamada. *Integrin function: molecular hierarchies of cytoskeletal and signaling molecules.* J Cell Biol, vol. 131, no. 3, pp 791–805, 1995.
- [Müller & Dufrêne 2011] DJ Müller and YF Dufrêne. *Atomic force microscopy: a nanoscopic window on the cell surface.* Trends Cell Biol, vol. 21, no. 8, pp 461–469, 2011.
- [Molloy *et al.* 1995a] JE Molloy, JE Burns, J Kendrick-Jones, RT Tregear and DCS White. *Movement and force produced by a single myosin head.* Nature, vol. 378, pp 209–212, 1995.

- [Molloy *et al.* 1995b] JE Molloy, JE Burns, JC Sparrow, RT Tregear, JK Kendrick-Jones and DCS White. *Single-Molecule mechanics of heavy meromyosin and S1 interacting with rabbit or drosophila actins using optical tweezers*. *Biophys J*, vol. 68, pp 298s–305s, 1995.
- [Molony & Burridge 1985] L Molony and K Burridge. *Molecular shape and self-association of vinculin and metavinculin*. *J Cell Biochem*, vol. 29, no. 1, pp 31–36, 1985.
- [Mullins *et al.* 1998] RD Mullins, JA Heuser and TD Pollard. *The interaction of Arp2/3 complex with actin: nucleation, high affinity pointed end capping, and formation of branching networks of filaments*. *Proc Natl Acad Sci U S A*, vol. 95, no. 11, pp 6181–6186, 1998.
- [Munevar *et al.* 2001] S Munevar, Y Wang and M Dembo. *Traction force microscopy of migrating normal and H-ras transformed 3T3 fibroblasts*. *Biophys J*, vol. 80, no. 4, pp 1744–1757, 2001.
- [Murthy & Wadsworth 2005] K Murthy and P Wadsworth. *Myosin-II-dependent localization and dynamics of F-actin during cytokinesis*. *Curr Biol*, vol. 15, no. 8, pp 724–731, 2005.
- [Nakamura *et al.* 2002] K Nakamura, N Yoshikawa, Y Yamaguchi, S Kagota, K Shinozuka and M Kunitomo. *Characterization of mouse melanoma cell lines by their mortal malignancy using an experimental metastatic model*. *Life Sci*, vol. 70, no. 7, pp 791–798, 2002.
- [Neuman & Block 2004] KC Neuman and SM Block. *Optical trapping*. *Rev Sci Inst*, vol. 75, no. 9, pp 2787–2809, 2004.
- [Neuman & Nagy 2008] KC Neuman and A Nagy. *Single-molecule force spectroscopy: optical tweezers, magnetic tweezers and atomic force microscopy*. *Nat Methods*, vol. 5, no. 6, pp 491–505, 2008.
- [Neuman *et al.* 1999] KC Neuman, EH Chadd, GF Liou, K Bergman and SM Block. *Characterization of Photodamage to Escherichia coli in optical traps*. *Biophys. J.*, vol. 77, pp 2856–2863, 1999.
- [Neuman *et al.* 2003] KC Neuman, EA Abbondanzieri, R Landick, J Gelles and SM Block. *Ubiquitous transcriptional pausing is independent of RNA polymerase backtracking*. *Cell*, vol. 115, no. 4, pp 437–447, 2003.
- [Nicolas *et al.* 2004] A Nicolas, B Geiger and SA Safran. *Cell mechanosensitivity controls the anisotropy of focal adhesions*. *PNAS*, vol. 101, no. 34, pp 12520–12525, 2004.
- [Nishizaka *et al.* 2000] T Nishizaka, Q Shi and MP Sheetz. *Position-dependent linkages of fibronectin-integrin-cytoskeleton*. *PNAS*, vol. 97, no. 2, pp 692–697, 2000.
- [Oakes *et al.* 2012] PW Oakes, Y Beckham, J Stricker and ML Gardel. *Tension is required but not sufficient for focal adhesion maturation without a stress fiber template*. *J Cell Biol*, vol. 196, no. 3, pp 363–374, 2012.
- [O’Callaghan *et al.* 2011] R O’Callaghan, KM Job, RO Dull and V Hlady. *Stiffness and heterogeneity of the pulmonary endothelial glycocalyx measured by atomic force microscopy*. *Am J Physiol Lung Cell Mol Physiol*, vol. 301, no. 3, pp L353–L360, 2011.
- [Oddershede *et al.* 2001] L Oddershede, S Grego, SF Norrelykke and K Berg-Sorensen. *Optical Tweezers: Probing Biological Surfaces*. *Probe Microscopy*, vol. 2, pp 129–137, 2001.
- [Oliver *et al.* 1999] T Oliver, M Dembo and K Jacobson. *Separation of propulsive and adhesive traction stresses in locomoting keratocytes*. *J Cell Biol*, vol. 145, no. 3, pp 589–604, 1999.
- [Omori *et al.* 1997] R Omori, T Kobayashi and A Suzuki. *Observation of a single-beam gradient-force optical trap for dielectric particles in air*. *Opt Lett*, vol. 22, no. 11, pp 816–818, 1997.
- [Palecek *et al.* 1997] SP Palecek, JC Loftus, MH Ginsberg, DA Lauffenburger and AF Horwitz. *Integrin-ligand binding properties govern cell migration speed through cell-substratum adhesiveness*. *Nature*, vol. 385, pp 537–540, 1997.
- [Pankov & Yamada 2002] R Pankov and KM Yamada. *Fibronectin at a glance*. *J Cell Sci*, vol. 115, no. 20, pp 3861–3863, 2002.

- [Papusheva & Heisenberg 2010] E Papusheva and CP Heisenberg. *Spatial organization of adhesion: force-dependent regulation and function in tissue morphogenesis*. EMBO J, vol. 29, no. 16, pp 2753–2768, 2010.
- [Paramanathan *et al.* 2012] T Paramanathan, I Vladescu, MJ McCauley, I Rouzina and MC Williams. *Force spectroscopy reveals the DNA structural dynamics that govern the slow binding of Actinomycin D*. Nucleic Acids Res, 2012.
- [Parsons *et al.* 2010] JT Parsons, AR Horwitz and MA Schwartz. *Cell adhesion: integrating cytoskeletal dynamics and cellular tension*. Nat Rev Mol Cell Biol, vol. 11, no. 9, pp 633–643, 2010.
- [Pasapera *et al.* 2010] AM Pasapera, IC Schneider, E Rericha, DD Schlaepfer and CM Waterman. *Myosin II activity regulates vinculin recruitment to focal adhesions through FAK-mediated paxillin phosphorylation*. J Cell Biol, vol. 188, no. 6, pp 877–890, 2010.
- [Peng *et al.* 2011] X Peng, ES Nelson, JL Maiers and KA DeMali. *New insights into vinculin function and regulation*. Int Rev Cell Mol Biol, vol. 287, pp 191–231, 2011.
- [Perez *et al.* 2008] TD Perez, M Tomada, MP Sheetz and WJ Nelson. *Immediate-early signaling induced by E-cadherin engagement and adhesion*. J. of Biological Chemistry, vol. 283, no. 8, pp 5014–5022, 2008.
- [Petrie *et al.* 2006] TA Petrie, JR Capadona, CD Reyes and AJ García. *Integrin specificity and enhanced cellular activities associated with surfaces presenting a recombinant fibronectin fragment compared to RGD supports*. Biomaterials, vol. 27, no. 31, pp 5459–5470, 2006.
- [Pierschbacher & Ruoslahti 1984] MD Pierschbacher and E Ruoslahti. *Cell attachment activity of fibronectin can be duplicated by small synthetic fragments of the molecule*. Nature, vol. 309, no. 5963, pp 30–33, 1984.
- [Pollard *et al.* 2000] TD Pollard, L Blanchoin and RD Mullins. *Molecular mechanisms controlling actin filament dynamics in nonmuscle cells*. Annu Rev Biophys Biomol Struct, vol. 29, pp 545–576, 2000.
- [Pollard 2004] TD Pollard. *Molecular mechanisms regulating actin filament dynamics at the leading edge of motile cells*, chapter 1, pp 1–17. John Wiley & Sons, Ltd, 2004.
- [Pollard 2007] TD Pollard. *Regulation of actin filament assembly by Arp2/3 complex and formins*. Annu Rev Biophys Biomol Struct, vol. 36, pp 451–477, 2007.
- [Ponti *et al.* 2004] A Ponti, M Machacek, SL Gupton, CM Waterman-Storer and G Danuser. *Two distinct actin networks drive the protrusion of migrating cells*. Science, vol. 305, pp 1782–1786, 2004.
- [Prager-Khoutorsky *et al.* 2011] M Prager-Khoutorsky, A Lichtenstein, R Krishnan, K Rajendran, A Mayo, Z Kam, B Geiger and AD Bershadsky. *Fibroblast polarization is a matrix-rigidity-dependent process controlled by focal adhesion mechanosensing*. Nat Cell Biol, vol. 13, no. 12, pp 1457–1465, 2011.
- [Prass *et al.* 2006] M Prass, K Jacobson, A Mogilner and M Radmacher. *Direct measurement of the lamellipodial protrusive force in a migrating cell*. J Cell Biol, vol. 174, no. 6, pp 767–772, 2006.
- [Rape *et al.* 2011] AD Rape, WH Guo and YL Wang. *The regulation of traction force in relation to cell shape and focal adhesions*. Biomaterials, vol. 32, no. 8, pp 2043–2051, 2011.
- [Raucher & Sheetz 2000] D Raucher and MP Sheetz. *Cell Spreading and Lamellopodial Extension Rate is Regulated by Membrane Tension*. J Cell Biol, vol. 148, no. 1, pp 127–136, 2000.
- [Reicherter *et al.* 1999] M Reicherter, T Haist, EU Wagemann and HJ Tiziani. *Optical particle trapping with computer-generated holograms written on a liquid-crystal display*. Opt Lett, vol. 24, no. 9, pp 608–610, 1999.
- [Riveline *et al.* 2001] D Riveline, E Zamir, NQ Balaban, US Schwarz, T Ishizaki, S Narumiya, Z Kam, B Geiger and AD Bershadsky. *Focal contacts as mechanosensors: externally applied local mechanical force induces growth of focal contacts by an mDia1-dependent and ROCK-independent mechanism*. J Cell Biol, vol. 153, no. 6, pp 1175–1186, 2001.

- [Robinson *et al.* 2001] RC Robinson, K Turbedsky, DA Kaiser, JB Marchand, HN Higgs, S Choe and TD Pollard. *Crystal structure of Arp2/3 complex*. *Science*, vol. 294, no. 5547, pp 1679–1684, 2001.
- [Roca-Cusachs *et al.* 2009] P Roca-Cusachs, NC Gauthier, AD Rio and MP Sheetz. *Clustering of alpha(5)beta(1) integrins determines adhesion strength whereas alpha(v)beta(3) and talin enable mechanotransduction*. *PNAS*, vol. 106, no. 38, pp 16245–16250, 2009.
- [Rohde *et al.* 1980] H Rohde, HP Bächinger and R Timpl. *Characterization of pepsin fragments of laminin in a tumor basement membrane. Evidence for the existence of related proteins*. *Hoppe Seylers Z Physiol Chem*, vol. 361, no. 11, pp 1651–1660, 1980.
- [Rohrbach & Stelzer 2002] A Rohrbach and EHK Stelzer. *Trapping forces, force constants, and potential depths for dielectric spheres in the presence of spherical aberrations*. *Applied Optics*, vol. 41, no. 13, pp 2494–2507, 2002.
- [Rohrbach 2005] A Rohrbach. *Switching and measuring a force of 25 femtoNewtons with an optical trap*. *Optics Express*, vol. 13, no. 24, pp 9695–9701, 2005.
- [Rottner & Stradal 2011] K Rottner and TEB Stradal. *Actin dynamics and turnover in cell motility*. *Curr Opin Cell Biol*, vol. 23, no. 5, pp 569–578, 2011.
- [Rottner *et al.* 1999] K Rottner, A Hall and JV Small. *Interplay between Rac and Rho in the control of substrate contact dynamics*. *Curr Biol*, vol. 9, no. 12, pp 640–648, 1999.
- [S. Yang 2005] TS S. Yang. *Micromachined force sensors for the study of cell mechanics*. *Rev Sci Instrum*, vol. 76, p 044301, 2005.
- [Sagvolden *et al.* 1999] G Sagvolden, I Giaever, EO Pettersen and J Feder. *Cell adhesion force microscopy*. *PNAS*, vol. 96, pp 471–476, 1999.
- [Saunders *et al.* 2006] RM Saunders, MR Holt, L Jennings, DH Sutton, IL Barsukov, A Bobkov, RC Liddington, EA Adamson, GA Dunn and DR Critchley. *Role of vinculin in regulating focal adhesion turnover*. *Eur J Cell Biol*, vol. 85, no. 6, pp 487–500, 2006.
- [Scales & Parsons 2011] TME Scales and M Parsons. *Spatial and temporal regulation of integrin signalling during cell migration*. *Curr Opin Cell Biol*, vol. 23, no. 5, pp 562–568, 2011.
- [Schäfer *et al.* 2010] C Schäfer, S Born, C Möhl, S Houben, N Kirchgeßner, R Merkel and B Hoffmann. *The key feature for early migratory processes: Dependence of adhesion, actin bundles, force generation and transmission on filopodia*. *Cell Adh Migr*, vol. 4, no. 2, 2010.
- [Schäffer *et al.* 2007] E Schäffer, SF Norrelykke and J Howard. *Surface forces and drag coefficients of microspheres near a plane surface measured with optical tweezers*. *American Chemical Society*, vol. 23, pp 3654–3665, 2007.
- [Schmidt *et al.* 1993] CE Schmidt, AF Horwitz, DA Lauffenburger and MP Sheetz. *Integrin-cytoskeletal interactions in migrating fibroblasts are dynamic, asymmetric, and regulated*. *J Cell Biol*, vol. 123, no. 4, pp 977–991, 1993.
- [Schönherr 2012] H Schönherr. *AFM to study bio/nonbio interactions*. *Methods Mol Biol*, vol. 811, pp 179–192, 2012.
- [Schwartz 2004] M Schwartz. *Rho signalling at a glance*. *Journal of Cell Science*, vol. 117, no. 23, pp 5457–5458, 2004.
- [Shank *et al.* 2010] EA Shank, C Cecconi, JW Dill, S Marqusee and C Bustamante. *The folding cooperativity of a protein is controlled by its chain topology*. *Nature*, vol. 465, no. 7298, pp 637–640, 2010.
- [Sheetz *et al.* 1998] MP Sheetz, DP Felsenfeld and CG Galbraith. *Cell migration: regulation of force on extracellular-matrix-integrin complexes*. *Trends Cell Biol*, vol. 8, no. 2, pp 51–54, 1998.
- [Shemesh *et al.* 2005] T Shemesh, B Geiger, AD Bershadsky and MM Kozlov. *Focal adhesions as mechanosensors: a physical mechanism*. *PNAS*, vol. 102, no. 35, pp 12383–12388, 2005.

- [Shemesh *et al.* 2009] T Shemesh, AB Verkhovsky, TM Svitkina, AD Bershadsky and MM Kozlov. *Role of focal adhesions and mechanical stresses in the formation and progression of the lamellipodium-lamellum interface*. Biophys J, vol. 97, no. 5, pp 1254–1264, 2009.
- [Shih & Yamada 2010] W Shih and S Yamada. *Myosin IIA dependent retrograde flow drives 3D cell migration*. Biophys J, vol. 98, no. 8, pp L29–L31, 2010.
- [Silva *et al.* 2011] MS Silva, M Depken, B Stuhmann, M Korsten, FC MacKintosh and GH Koenderink. *Active multistage coarsening of actin networks driven by myosin motors*. PNAS, vol. 108, no. 23, pp 9408–9413, 2011.
- [Simmons *et al.* 1996] RM Simmons, JT Finer, S Chu and JA Spudich. *Quantitative measurements of force and displacement using an optical trap*. Biophysical Journal, vol. 70, pp 1813–1822, 1996.
- [Singer *et al.* 1988] II Singer, S Scott, DW Kawka, DM Kazazis, J Gailit and E Ruoslahti. *Cell surface distribution of fibronectin and vitronectin receptors depends on substrate composition and extracellular matrix accumulation*. J Cell Biol, vol. 106, no. 6, pp 2171–2182, 1988.
- [Small & Resch 2005] JV Small and GP Resch. *The comings and goings of actin: coupling protrusion and retraction in cell motility*. Curr Opin Cell Biol, vol. 17, no. 5, pp 517–523, 2005.
- [Small *et al.* 1978] JV Small, G Isenberg and JE Celis. *Polarity of actin at the leading edge of cultured cells*. Nature, vol. 272, no. 5654, pp 638–639, 1978.
- [Small *et al.* 1996] JV Small, K Anderson and K Rottner. *Actin and the coordination of protrusion, attachment and retraction in cell crawling*. Biosci Rep, vol. 16, no. 5, pp 351–368, 1996.
- [Small *et al.* 1998] J Small, K Rottner, I Kaverina and K Anderson. *Assembling an actin cytoskeleton for cell attachment and movement*. Biochimica et Biophysica Acta, vol. 1404, no. 3, pp 271–281, 1998.
- [Small 1988] JV Small. *The actin cytoskeleton*. Electron Microsc Rev, vol. 1, no. 1, pp 155–174, 1988.
- [Stewart *et al.* 2011] MP Stewart, Y Toyoda, AA Hyman and DJ Muller. *Force probing cell shape changes to molecular resolution*. Trends Biochem Sci, vol. 36, no. 8, pp 444–450, 2011.
- [Straube *et al.* 2011] AV Straube, AA Louis, J Baumgartl, C Bechinger and RPA Dullens. *Pattern formation in colloidal explosions*. EPL (Europhysics Letters), vol. 94, no. 4, p 48008, 2011.
- [Stricker *et al.* 2011] J Stricker, Y Aratyn-Schaus, PW Oakes and ML Gardel. *Spatiotemporal constraints on the force-dependent growth of focal adhesions*. Biophys J, vol. 100, no. 12, pp 2883–2893, 2011.
- [Sun *et al.* 2010] SX Sun, S Walcott and CW Wolgemuth. *Cytoskeletal cross-linking and bundling in motor-independent contraction*. Curr Biol, vol. 20, no. 15, pp R649–R654, 2010.
- [Svitkina & Borisy 1999] TM Svitkina and GG Borisy. *Arp2/3 complex and actin depolymerizing factor/cofilin in dendritic organization and treadmilling of actin filament array in lamellipodia*. J Cell Biol, vol. 145, no. 5, pp 1009–1026, 1999.
- [Svitkina *et al.* 1986] TM Svitkina, AA Neyfakh and AD Bershadsky. *Actin cytoskeleton of spread fibroblasts appears to assemble at the cell edges*. J Cell Sci, vol. 82, pp 235–248, 1986.
- [Svitkina *et al.* 1997] TM Svitkina, AB Verkhovsky, KM McQuade and GG Borisy. *Analysis of the actin-myosin II system in fish epidermal keratocytes: mechanism of cell body translocation*. J Cell Biol, vol. 139, no. 2, pp 397–415, 1997.
- [Svoboda & Block 1994a] K Svoboda and SM Block. *Biological Applications of optical forces*. Annu Rev Biophys Biomol Struct, vol. 23, p 247, 1994.
- [Svoboda & Block 1994b] K Svoboda and SM Block. *Force and velocity measured for single kinesin molecules*. Cell, vol. 77, no. 5, pp 773–784, 1994.
- [Svoboda *et al.* 1993] K Svoboda, CF Schmidt, BJ Schnapp and SM Block. *Direct observation of kinesin stepping by optical trapping interferometry*. Nature, vol. 365, no. 6448, pp 721–727, 1993.
- [Symons & Mitchison 1991] MH Symons and TJ Mitchison. *Control of actin polymerization in live and permeabilized fibroblasts*. J Cell Biol, vol. 114, no. 3, pp 503–513, 1991.

- [Tamariz & Grinnell 2002] E Tamariz and F Grinnell. *Modulation of fibroblast morphology and adhesion during collagen matrix remodeling*. Mol Biol Cell, vol. 13, no. 11, pp 3915–3929, 2002.
- [Tan *et al.* 2003] JL Tan, J Tien, DM Pirone, DS Gray, K Bhadriraju and CS Chen. *Cells lying on a bed of microneedles: an approach to isolate mechanical force*. PNAS, vol. 100, no. 4, pp 1484–1489, 2003.
- [Tang *et al.* 2009] J Tang, AM Jofre, RB Kishore, JE Reiner, ME Greene, GM Lowman, JS Denker, CCC Willis, K Helmerson and LS Goldner. *Generation and mixing of subfemtoliter aqueous droplets on demand*. Anal Chem, vol. 81, no. 19, pp 8041–8047, 2009.
- [Theriot & Mitchison 1991] JA Theriot and TJ Mitchison. *Actin microfilament dynamics in locomoting cells*. Nature, vol. 352, no. 6331, pp 126–131, 1991.
- [Thompson *et al.* 2002] RE Thompson, DR Larson and WW Webb. *Precise nanometer localization analysis for individual fluorescent probes*. Biophys J, vol. 82, no. 5, pp 2775–2783, 2002.
- [Titushkin & Cho 2006] I Titushkin and M Cho. *Distinct membrane mechanical properties of human mesenchymal stem cells determined using laser optical tweezers*. Biophys J, vol. 90, no. 7, pp 2582–2591, 2006.
- [Urban *et al.* 2010] E Urban, S Jacob, M Nemethova, GP Resch and JV Small. *Electron tomography reveals unbranched networks of actin filaments in lamellipodia*. Nat Cell Biol, vol. 12, no. 5, pp 429–435, 2010.
- [Vallotton *et al.* 2004] P Vallotton, SL Gupton, CM Waterman-Storer and G Danuser. *Simultaneous mapping of filamentous actin flow and turnover in migrating cells by quantitative fluorescent speckle microscopy*. PNAS, vol. 101, no. 26, pp 9660–9665, 2004.
- [Verkhovskiy *et al.* 1995] AB Verkhovskiy, TM Svitkina and GG Borisy. *Myosin II filament assemblies in the active lamella of fibroblasts: their morphogenesis and role in the formation of actin filament bundles*. J Cell Biol, vol. 131, no. 4, pp 989–1002, 1995.
- [Verkhovskiy *et al.* 1997] AB Verkhovskiy, TM Svitkina and GG Borisy. *Polarity sorting of actin filaments in cytochalasin-treated fibroblasts*. J Cell Sci, vol. 110, no. 15, pp 1693–1704, 1997.
- [Vicente-Manzanares & Horwitz 2011] M Vicente-Manzanares and AR Horwitz. *Adhesion dynamics at a glance*. J Cell Sci, vol. 124, no. 23, pp 3923–3927, 2011.
- [Vicente-Manzanares *et al.* 2009] M Vicente-Manzanares, CK Choi and AR Horwitz. *Integrins in cell migration—the actin connection*. J Cell Sci, vol. 122, no. 2, pp 199–206, 2009.
- [Visscher *et al.* 1993] K Visscher, GJ Brakenhoff and JJ Krol. *Micromanipulation by multiple optical traps created by a single fast scanning trap integrated with the bilateral confocal scanning laser microscope*. Cytometry, vol. 14, pp 105–114, 1993.
- [Visscher *et al.* 1996] K Visscher, SP Gross and SM Block. *Construction of multiple-beam optical traps with nanometer-resolution position sensing*. IEEE J Quantum Electron, vol. 2, no. 4, pp 1066–1076, 1996.
- [Visscher *et al.* 1999] K Visscher, MJ Schnitzer and SM Block. *Single kinesin molecules studied with a molecular force clamp*. Nature, vol. 400, no. 6740, pp 184–189, 1999.
- [Vogel & Sheetz 2006] V Vogel and M Sheetz. *Local force and geometry sensing regulate cell functions*. Nature Rev., vol. 7, pp 265–275, 2006.
- [Volberg *et al.* 1995] T Volberg, B Geiger, Z Kam, R Pankov, I Simcha, H Sabanay, JL Coll, E Adamson and A Ben-Ze'ev. *Focal adhesion formation by F9 embryonal carcinoma cells after vinculin gene disruption*. J Cell Sci, vol. 108, no. 6, pp 2253–2260, 1995.
- [Voss & Jockusch 1996] GC Voss and H Jockusch. *New testis-specific expressed genes on mouse Chromosome 11*. Mamm Genome, vol. 7, no. 2, p 163, 1996.
- [Wagner *et al.* 2011] C Wagner, C Olbrich, H Brutzer, M Salomo, U Kleinekathöfer, UF Keyser and F Kremer. *DNA condensation by TmHU studied by optical tweezers, AFM and molecular dynamics simulations*. J Biol Phys, vol. 37, no. 1, pp 117–131, 2011.

- [Walcott & Sun 2010] S Walcott and SX Sun. *A mechanical model of actin stress fiber formation and substrate elasticity sensing in adherent cells*. PNAS, vol. 107, no. 17, pp 7757–7762, 2010.
- [Walter *et al.* 2006] N Walter, C Selhuber, H Kessler and JP Spatz. *Cellular unbinding forces of initial adhesion processes on nanopatterned surfaces probed with magnetic tweezers*. Nano Lett, vol. 6, no. 3, pp 398–402, 2006.
- [Wang & Thampatty 2006] JHC Wang and BP Thampatty. *An introductory review of cell mechanobiology*. Biomech Model Mechanobiol, vol. 5, no. 1, pp 1–16, 2006.
- [Wang & Uhlenbeck 1945] MC Wang and GE Uhlenbeck. *On the theory of the Brownian motion II*. Reviews of modern physics, vol. 17, pp 323–342, 1945.
- [Wang *et al.* 1993] N Wang, JP Butler and DE Ingber. *Mechanotransduction across the cell surface and through the cytoskeleton*. Science, vol. 260, no. 5111, pp 1124–1127, 1993.
- [Wang *et al.* 1995] Z Wang, S Khan and MP Sheetz. *Single cytoplasmic dynein molecule movements: characterization and comparison with kinesin*. Biophys J, vol. 69, no. 5, pp 2011–2023, 1995.
- [Wang *et al.* 1998] MD Wang, MJ Schnitzer, H Yin, R Landick, J Gelles and SM Block. *Force and velocity measured for single molecules of RNA polymerase*. Science, vol. 282, no. 5390, pp 902–907, 1998.
- [Wang 1985] YL Wang. *Exchange of actin subunits at the leading edge of living fibroblasts: possible role of treadmilling*. J Cell Biol, vol. 101, no. 2, pp 597–602, 1985.
- [Wang 2007] YL Wang. *Flux at focal adhesions: slippage clutch, mechanical gauge, or signal depot*. Sci STKE, vol. 2007, no. 377, p pe10, 2007.
- [Watanabe & Mitchison 2002] N Watanabe and TJ Mitchison. *Single-molecule speckle analysis of actin filament turnover in lamellipodia*. Science, vol. 295, no. 5557, pp 1083–1086, 2002.
- [Watanabe *et al.* 2010] TM Watanabe, AH Iwane, H Tanaka, M Ikebe and T Yanagida. *Mechanical characterization of one-headed myosin-V using optical tweezers*. PLoS One, vol. 5, no. 8, p e12224, 2010.
- [Webb *et al.* 2002] DJ Webb, JT Parsons and AF Horwitz. *Adhesion assembly, disassembly and turnover in migrating cells – over and over and over again*. Nat Cell Biol, vol. 4, no. 4, pp E97–100, 2002.
- [Wehrle-Haller & Imhof 2002] B Wehrle-Haller and B Imhof. *The inner lives of focal adhesions*. Trends Cell Biol, vol. 12, no. 8, pp 382–389, 2002.
- [Wehrle-Haller & Imhof 2003] B Wehrle-Haller and BA Imhof. *Actin, microtubules and focal adhesion dynamics during cell migration*. Int J Biochem Cell Biol, vol. 35, no. 1, pp 39–50, 2003.
- [Wehrle-Haller 2012] B Wehrle-Haller. *Structure and function of focal adhesions*. Curr Opin Cell Biol, vol. 24, no. 1, pp 116–124, 2012.
- [Welch & Mullins 2002] MD Welch and RD Mullins. *Cellular control of actin nucleation*. Annu Rev Cell Dev Biol, vol. 18, pp 247–288, 2002.
- [Welch *et al.* 1997] MD Welch, AH DePace, S Verma, A Iwamatsu and TJ Mitchison. *The human Arp2/3 complex is composed of evolutionarily conserved subunits and is localized to cellular regions of dynamic actin filament assembly*. J Cell Biol, vol. 138, no. 2, pp 375–384, 1997.
- [Winkler *et al.* 1996] J Winkler, H Lünsdorf and BM Jockusch. *The ultrastructure of chicken gizzard vinculin as visualized by high-resolution electron microscopy*. J Struct Biol, vol. 116, no. 2, pp 270–277, 1996.
- [Wiseman *et al.* 2004] PW Wiseman, CM Brown, DJ Webb, B Hebert, NL Johnson, JA Squier, MH Ellisman and AF Horwitz. *Spatial mapping of integrin interactions and dynamics during cell migration by image correlation microscopy*. J Cell Sci, vol. 117, no. 23, pp 5521–5534, 2004.
- [Wolfenson *et al.* 2011] H Wolfenson, A Bershadsky, YI Henis and B Geiger. *Actomyosin-generated tension controls the molecular kinetics of focal adhesions*. J Cell Sci, vol. 124, no. 9, pp 1425–1432, 2011.

- [Woodside *et al.* 2008] MT Woodside, C García-García and SM Block. *Folding and unfolding single RNA molecules under tension*. *Curr Opin Chem Biol*, vol. 12, no. 6, pp 640–646, 2008.
- [Wu *et al.* 2005] CC Wu, HW Su, CC Lee, MJ Tang and FC Su. *Quantitative measurement of changes in adhesion force involving focal adhesion kinase during cell attachment, spread, and migration*. *Biochem Biophys Res Commun*, vol. 329, no. 1, pp 256–265, 2005.
- [Wu *et al.* 2011] Y Wu, D Sun and W Huang. *Force and motion analysis for automated cell transportation with optical tweezers*. *Intelligent Control and Automation*, vol. 9, pp 839–843, 2011.
- [Wu *et al.* 2012] C Wu, SB Asokan, ME Berginski, EM Haynes, NE Sharpless, JD Griffith, SM Gomez and JE Bear. *Arp2/3 is critical for lamellipodia and response to extracellular matrix cues but is dispensable for chemotaxis*. *Cell*, vol. 148, pp 973–987, 2012.
- [Xu *et al.* 1998a] W Xu, H Baribault and ED Adamson. *Vinculin knockout results in heart and brain defects during embryonic development*. *Development*, vol. 125, no. 2, pp 327–337, 1998.
- [Xu *et al.* 1998b] W Xu, JL Coll and ED Adamson. *Rescue of the mutant phenotype by reexpression of full-length vinculin in null F9 cells; effects on cell locomotion by domain deleted vinculin*. *J Cell Sci*, vol. 111, no. 11, pp 1535–1544, 1998.
- [Yamada & Nelson 2007] S Yamada and WJ Nelson. *Localized zones of Rho and Rac activities drive initiation and expansion of epithelial cell-cell adhesion*. *J Cell Biol*, vol. 178, no. 3, pp 517–527, 2007.
- [Yin *et al.* 1995] H Yin, MD Wang, K Svoboda, R Landick, SM Block and J Gelles. *Transcription against an applied force*. *Science*, vol. 270, no. 5242, pp 1653–1657, 1995.
- [Yu *et al.* 2011] CH Yu, JBK Law, M Suryana, HY Low and MP Sheetz. *Early integrin binding to Arg-Gly-Asp peptide activates actin polymerization and contractile movement that stimulates outward translocation*. *PNAS*, vol. 108, no. 51, pp 20585–20590, 2011.
- [Zaidel-Bar *et al.* 2003] R Zaidel-Bar, C Ballestrem, Z Kam and B Geiger. *Early molecular events in the assembly of matrix adhesions at the leading edge of migrating cells*. *J Cell Sci*, vol. 116, no. 22, pp 4605–4613, 2003.
- [Zaidel-Bar *et al.* 2004] R Zaidel-Bar, M Cohen, L Addadi and B Geiger. *Hierarchical assembly of cell-matrix adhesion complexes*. *Biochem Soc Trans*, vol. 32, no. 3, pp 416–420, 2004.
- [Zamir & Geiger 2001] E Zamir and B Geiger. *Components of cell-matrix adhesions*. *J Cell Sci*, vol. 114, no. 20, pp 3577–3579, 2001.
- [Zicha *et al.* 2003] D Zicha, IM Dobbie, MR Holt, J Monypenny, DYH Soong, C Gray and GA Dunn. *Rapid actin transport during cell protrusion*. *Science*, vol. 300, no. 5616, pp 142–145, 2003.
- [Ziegler *et al.* 2006] WH Ziegler, RC Liddington and DR Critchley. *The structure and regulation of vinculin*. *Trends Cell Biol*, vol. 16, no. 9, pp 453–460, 2006.
- [Zimmermann *et al.* 2010] J Zimmermann, M Enculescu and M Falcke. *Leading-edge-gel coupling in lamellipodium motion*. *Phys Rev E*, vol. 82, no. 5, p 051925, 2010.
- [Zimmermann *et al.* 2012] J Zimmermann, C Brunner, M Enculescu, M Goegler, A Ehrlicher, J Käs and M Falcke. *Actin filament elasticity and retrograde flow shape the force-velocity relation of motile cells*. *Biophys J*, vol. 102, no. 2, pp 287–295, 2012.

LIST OF ABBREVIATIONS

AFM	Atomic Force Microscopy
AOD	Acousto-Optic Deflector
B16	Mouse Melanoma Cell Line
DAPI	4',6-diamidino-2-phenylindole,dihydrochloride
DIC	Differential Interference Contrast
DMEM	Dulbecco's Modified Eagle Medium
ECM	Extracellular Matrix
F12	Cell culture medium for PCFs
FACS	Fluorescence Assisted Cell Sorting
FCS	Fetal Calf Serum
FFT	Fast Fourier Transformation
FN	Fibronectin
GFP	Green Fluorescent Protein
MEF	Mouse Embryonic Fibroblast
MEF ^{vin-/-}	Vinculin deficient MEF cells
OT	Optical Tweezers
PBS	Phosphate Buffered Saline
PCF	Primary Chick Fibroblast
PLL	Poly-l-lysine
SCFS	Single-Cell Force Spectroscopy
SEM	Standard Error of the Mean
WT	Wild type

ACKNOWLEDGEMENTS - DANKSAGUNG

An dieser Stelle möchte ich mich bei allen bedanken die fachlich und persönlich zum guten Gelingen dieser Arbeit beigetragen haben.

Ein besonderer Dank gebührt Prof. Dr. Martin Bastmeyer, der mir die Möglichkeit gegeben hat an diesem spannenden Thema zwischen Biologie und Physik zu arbeiten und der mir viel Zeit ließ mir meinen optischen Versuchsaufbau zusammen zu basteln. Exzellent war auch die Einbettung der Arbeit in die KSOP und das CFN.

Ein großer Dank geht an Prof. Dr. Ulrich Nienhaus für die freundliche Übernahme des Co-Referats im Rahmen der KSOP.

Bei Prof. Dr. Clemens Bechinger möchte ich mich dafür bedanken, dass er sein Fachwissen über Optische Pinzetten so bereitwillig zur Verfügung stellte und mir die Gelegenheit gab mich gründlich in die experimentellen Details einzuarbeiten.

Besonders bedanke ich mich auch bei Dr. Franco Weth, der dieses Projekt als KSOP-Mentor begleitet hat, immer einen guten Überblick über sämtliche KSOP "Pflichtveranstaltungen" hatte und jederzeit auch für fachliche Fragen zur Verfügung stand.

Ich möchte mich bei Dr. Clemens Franz ganz herzlich für die "Vinculin-Kooperation" bedanken, sowie für seine fachliche Unterstützung, die Diskussionen und die vielen Anregungen zu diesem Projekt.

Ein großes Dankeschön geht auch an Dr. Ljiljana Fruk, die mir einen Platz in ihrem Chemielabor eingeräumt und mir mit großer Geduld diverse chemische Verfahren näher gebracht hat.

Ganz besonders herzlich möchte ich mich bei Dr. Alexandra Greiner für ihre hervorragende Unterstützung bedanken sowie für die vielen anregenden Diskussionen die meine Arbeit entscheidend voranbrachten. Ein großer Extradank gebührt ihr auch für die selbstlose Bereitschaft große Teile meiner Arbeit Korrektur zu lesen.

Mein großer Dank gilt Tanja Landmann für ihre großartige Unterstützung im Labor und ihre bewundernswerte Gelassenheit.

Der größte Dank gilt der gesamten Arbeitsgruppe für die vielen kreativen Kaffeepausen, die einen großen Erkenntnisgewinn auch außerhalb der fachlichen Dimensionen brachten. Meinen Bürokollegen Philipp, Michael, Steffi, Wolfgang, Felix und Siyka danke ich für die entspannte Arbeitsatmosphäre, die vielen Diskussionen und die immer gute Stimmung.

Mein ganz persönlicher Dank gilt meinen Eltern und meiner Schwester, die mich in jeder Hinsicht unterstützen haben und die sich immer wieder freiwillig als Erholungsort zur Verfügung stellten.

Nicht zuletzt Danke ich meinem Freund Simon der eine ganz besonders wichtige Stütze für diese Arbeit und für mich persönlich war und ist. Vielen Dank für das kritische Korrekturlesen meiner Arbeit und für die liebevolle moralische Unterstützung während unserer gesamten gemeinsamen Zeit.

